

NON-INVASIVE INVESTIGATION OF CARDIAC TISSUE COMPARTMENTS AND  
COMPONENTS USING MR MICROSCOPY

By

MIN SIG HWANG

A DISSERTATION PRESENTED TO THE GRADUATE SCHOOL  
OF THE UNIVERSITY OF FLORIDA IN PARTIAL FULFILLMENT  
OF THE REQUIREMENTS FOR THE DEGREE OF  
DOCTOR OF PHILOSOPHY

UNIVERSITY OF FLORIDA

2010

© 2010 Min Sig Hwang

To my wife, Jung Eun Kim for all her support and encouragement

## ACKNOWLEDGMENTS

I believe there are few experiences as exhilarating as watching a seemingly meager daily harvest of only a graph, a table or a half page gradually blossoming into a full-fledged thesis – it was truly amazing experience. Of course, every single work in this thesis could not have been accomplished without the help of a great many people.

First and foremost, I would like to thank Dr. John R. Forder for his support, patience, mentoring over the last years. Working with him, I learned how to be independent, how to enjoy the work, how to become a good colleague, and when to retreat for a better tomorrow. Just as he was my pride when I joined the Forder lab, so am I hoping to be his pride. I would like to thank Dr. Stephen Blackband for all his counsel and valuable advice. From him, I learned how to think critically about MRI and how to appreciate achievement in MRI field. I would like to Dr. Baba Vemuri for his encouraging words and advice. My appreciation also goes to Dr. Rosalind Sadleir for her valuable advice and patience.

I would like to thank Dr. Angelos Barmoutis for his help with the fanDTasia and valuable discussion. It was great luck to work with him. I would also like to thank Melvin Clark for all his help with hardware setup for cardiac MRI. Without him, the tissue compartment studies and a RF coil fabrication could not have been accomplished. I would like to thank Dr. Jeremy Flint for proofreading of chapters in this thesis with valuable comment and for providing what was necessary for the animal experiment. I would like to thank my lab colleagues, Saurav Chandra and Dr. Vijay Antharam for their help in my endeavors. My thanks also go to Dan Plant, Barbara Beck, and Kelley Jenkins in the AMRIS of the UF Brain Institute. I would also like to thank Gary Blaskowski, a former AMRIS staff. With their help I could acquire the MR images used in this thesis. I would like to thank Dr. William O. Ogle and Philip Barish for their aids in emulsifying the Perfluorocarbons solution. I would also like to thank Drs. Gideon Koren

and Bum-Rak Choi of the Brown University for providing isolated hearts and giving valuable discussion. I would like to thank Dr. Thomas H. Mareci for his teaching at early years of my graduate study.

I would like to acknowledge six people without whom I could never have made it through graduate school. I would like to thank my parents and my parents-in-law for their endless love and support. I want to recognize my daughters, Michelle Hwang and Lauren Hwang. They have truly been my joy all the time since they arrived during my graduate study. Last, but not least, I want to thank my wife, Jung Eun Kim for loving me, standing always by my side, consistently reminding me of smile, and encouraging me.

# TABLE OF CONTENTS

	<u>page</u>
ACKNOWLEDGMENTS .....	4
LIST OF TABLES .....	9
LIST OF FIGURES .....	10
ABSTRACT.....	14
CHAPTER	
1 INTRODUCTION AND BACKGROUND .....	16
Introduction.....	16
Background.....	17
Water in Biological Systems .....	17
Diffusion Measurement of Water Molecules Using MR .....	18
Basic Principles of Diffusion-Weighted Imaging .....	20
From Diffusion Coefficient to Diffusion Tensor.....	22
Extracting Information from DTI data .....	24
Mean diffusivity .....	25
Fractional anisotropy.....	25
High Angular Resolution Diffusion Imaging .....	26
Optimization of the Diffusion Sensitizing Factor .....	27
Effect of Imaging Gradients to the Diffusion Sensitizing Factor.....	29
Apparent Diffusion Coefficient: An Outstanding Issue .....	31
Water Compartmentalization in Cardiac Tissue.....	36
Cell Volume Regulation in Cardiac Tissue .....	37
Diffusion Tensor Imaging of the Myocardium .....	38
Magnetic Resonance Microscopy of the Cardiac Conduction System .....	40
2 HARDWARE FOR CARDIAC DIFFUSION WEIGHTED MR IMAGING .....	50
Introduction.....	50
Diffusion Gradient System .....	51
A Linear Birdcage RF Coil.....	52
Perfusion System for Diffusion-Weighted Imaging .....	53
A Long Cradle Immune to Gradient-induced Motion .....	55
3 CONTRIBUTION OF CARDIAC TISSUE COMPARTMENTS TO THE MR DIFFUSION SIGNAL.....	68
Introduction.....	68
Materials and Method .....	72
Isolated Perfused Heart Preparation .....	72

Heart Slice Procurement.....	73
Placement of Heart Slices into the Multislice Perfusion Chamber .....	74
The Emulsified Perfluorocarbons Preparation .....	75
Diffusion Magnetic Resonance Imaging .....	75
Heart slices .....	75
Vascular replacement with the PFC emulsion .....	76
Change of the flow rate of the STH perfusate.....	77
Data Analysis.....	78
Results.....	79
Discussion.....	82
Modified Vasculature .....	82
Effect of the Direct Flow Rate Change .....	84
Effect of the Vascular Replacement with PFC Emulsion .....	85
Heart Slice in Hypotonicity .....	88
Possibility of the Triexponential Fitting Model .....	89
4 NON-INVASIVE VISUALIZATION OF THE CARDIAC CONDUCTION SYSTEM USING MR MICROSCOPY .....	115
Introduction.....	115
Materials and Method .....	117
Isolated and Fixed Heart Preparation .....	117
Magnetic Resonance Imaging .....	118
Data Analysis.....	119
Results.....	119
Discussion.....	120
Visualization of Free-running Purkinje Fiber Network.....	121
The Left Bundle Branching Forming Fan-like Structure .....	123
MR Images of the Connecting Bundle .....	124
Anatomical Complexity in the Ventricular Muscular Interseptum .....	124
Non-invasive Visualization of the Intramural Purkinje Fibers.....	125
5 MICROSCOPIC HIGH ANGULAR RESOLUTION DIFFUSION IMAGING OF ISOLATED RABBIT HEART .....	136
Introduction.....	136
Materials and Methods .....	138
Isolated and Fixed Heart Preparation .....	138
Microscopic High Angular Resolution Diffusion Imaging .....	139
Data Analysis.....	140
Results.....	140
Discussion.....	142
Diffusion Parameters Depending on B-values .....	142
Diffusion MR Imaging of the Free-running Purkinje Fibers.....	144
Diffusion MR Imaging of the Ventricular Muscular Interseptum.....	145

6	NON-INVASIVE MONITORING OF MORPHOLOGICAL ALTERATIONS IN THE RABBIT HEART WITH AGING .....	166
	Introduction.....	166
	Materials and Method .....	168
	Isolated Heart Preparation .....	168
	Magnetic Resonance Imaging .....	169
	Data Analysis.....	170
	Results.....	170
	Morphological Change in the Purkinje Fiber Network .....	170
	Change in MR Diffusion Characteristics .....	171
	Discussion.....	172
7	CONCLUSIONS .....	181
	LIST OF REFERENCES .....	185
	BIOGRAPHICAL SKETCH .....	198

## LIST OF TABLES

<u>Table</u>	<u>page</u>
2-1	Gradient system suitable for heavy diffusion weighted imaging.....58
3-1	Estimates of the diffusion parameters in heart slices buffered with iso-osmotic and hypotonic solution.....92
3-2	Estimates of the diffusion parameters in isolated hearts. The vascular space filled with the STH was replaced with the PFC emulsion.. .....92
3-3	Change in the diffusion parameters of isolated hearts with direct flow (1mL/min).....92
3-4	Estimates of the diffusion parameters in myocardial fibers parallel to the diffusion gradient with direct flow .....93
3-5	Estimates of the diffusion parameters in myocardial fibers orthogonal to the diffusion gradient with direct flow.....93
3-6	Estimates of the diffusion parameters in Papillary muscle fibers nearly orthogonal to the diffusion gradient with direct flow.....94
3-7	Percentile decrease of averaged ADC after the PFC replacement of vascular space with the six diffusion weighted directions in spherical coordinate.....95
5-1	Diffusion parameters depending on b-values at various regions in the LV.....149
6-1	Diffusion parameters of the papillary muscles in the left ventricles of young and old rabbit hearts.....176

## LIST OF FIGURES

<u>Figure</u>	<u>page</u>
1-1	A diffusion imaging pulse sequence using a spin echo and diagram showing the overall phase shifts of protons by diffusion.....44
1-2	A schematic diagram showing procedure extracting information from diffusion weighted images.....45
1-3	Diffusion sensitizing factor modulated by the imaging gradients and the cross terms. ....46
1-4	A schematic diagram of relative distribution of tissue compartments and their elements in the heart. ....47
1-5	A schematic diagram showing compartmentalization and transport of the water molecules in the cardiac tissue.....48
1-6	A schematic diagram showing the specific aims to achieve the goal in this thesis. ....49
2-1	A schematic transverse view showing configuration of components for imaging within the gradient coil, the BGA6-S. ....59
2-2	A schematic procedure to fabricate a linear birdcage RF coil for diffusion MR imaging of isolated rabbit heart. ....60
2-3	Perfusion system for isolated rabbit heart preparation. ....61
2-4	Portable perfusion system for diffusion imaging of the isolated, perfused rabbit heart. ...62
2-5	Diffusion weighted MR images of a fresh rabbit heart showing motion that occurs during diffusion measurements.....63
2-6	Motion-free MR images of a fixed rabbit heart isolated by the long cradle.....64
2-7	A schematic diagram of a long cradle isolated from both the gradient and the magnet bore in the horizontal 11 T magnet system. ....65
2-8	A long cradle for cardiac diffusion weighted imaging and a birdcage RF coil mounted on the cradle.....66
2-9	DTI of isolated rabbit heart measured using a b value of $2000 \text{ s/mm}^2$ and HARDI of in vivo rat brain measured with a b value of $850 \text{ s/mm}^2$ . ....67
3-1	Schematics of experimental setup for DWI of isolated heart. ....96
3-2	Vascular replacement of the STH perfusate with the PFC emulsion.....97

3-3	Primary eigen vector map and 3D fiber tracking map of a short axis view.....	98
3-4	Representative diffusion weighted images of an isolated heart perfused with STH using 10 diffusion sensitizing (b-values) factors. ....	99
3-5	A representative plot of the logarithmic signal intensity as a function of b-values for an isolated rabbit heart.. ....	100
3-6	Normalized signal attenuation and its logarithmic normalized signal attenuation with modification of the vascular space, collapsed, replacement, and direct flow. Direct flow rate of perfusate was 1 mL/min. ....	101
3-7	Normalized signal attenuation and its logarithmic normalized signal attenuation with changes in perfusate flow in a free wall in the LV .....	103
3-8	Normalized signal attenuation and its logarithmic normalized signal attenuation with changes in perfusate flow in a free wall in the LV .....	104
3-9	Normalized signal attenuation and its logarithmic normalized signal attenuation with changes in perfusate flow in a papillary muscle in the LV .....	105
3-10	Temporal evolution of the apparent diffusion coefficient (ADC) of control hearts. ....	106
3-11	The ADC sensitivity to six diffusion encoding directions in a Free Wall region in the LV when the vascular space is filled with the STH perfusate and replaced with the PFC emulsion.....	107
3-12	The ADC decrease when the vascular space filled with the STH perfusate is replaced with the PFC emulsion.....	108
3-13	Schematic presentations of the tissue compartments.....	110
3-14	Relaxation times depending on the direct flow rate in various regions in an isolated heart.....	111
3-15	Representative MR images of an isolated rabbit heart under the STH perfusate and under the PFC perfusate.....	112
3-16	Comparison between <sup>1</sup> H MR image and <sup>19</sup> F MR image after the vascular space was replaced with PFC emulsion. ....	113
3-17	Normalized signal attenuation measured.....	114
4-1	Examples of sagittal MRI slices.. ....	128
4-2	A representative volume rendered 3D MR image to visualize the conduction paths and anatomical features in an isolated heart.. ....	129

4-3	A left bundle branch bulging out of the ventricular septum and its outline in an enlarged view of the small region enclosed in the dotted red box.....	130
4-4	Demonstration of the details of polygonal free-running Purkinje fiber network in the left and right ventricular cavities.. .....	131
4-5	Volume rendered images that may show septal attachment of a free-running Purkinje fiber in the RV and its continuation in the ventricular interseptum.....	132
4-6	Demonstration of fan-like division of the left bundle branch of an isolated heart.. .....	133
4-7	A volume rendered 3D MR image showing anatomical complexity in the interseptum contiguous to the right ventricle.....	134
4-8	Striped patterns found intramurally in the ventricular interseptum... .....	135
5-1	Spin echo MR images revealing anatomical details of the heart depending on the resolutions employed.. .....	150
5-2	Diffusion weighted images of a HARDI data set measured in twenty one collinear diffusion encoding directions with 1000 s/mm <sup>2</sup> of b value.. .....	151
5-3	Diffusion tensor component images and images derived with the diffusion tensor components of b values of 1000 s/mm <sup>2</sup> .....	153
5-4	Parameter images derived from the diffusion tensor components shown in the Figure 5-3.. .....	154
5-5	Diffusion tensor images and images derived with the diffusion tensor component of b values of 2000 s/mm <sup>2</sup> .....	155
5-6	Parameter images derived from the diffusion tensor components shown in the Figure 5-5.. .....	156
5-7	Diffusion tensor images and parameter images derived with the diffusion tensor component of b values of 1000 s/mm <sup>2</sup> .....	157
5-8	Diffusion tensor images and parameter images derived with the diffusion tensor component of b values of 2000 s/mm <sup>2</sup> .....	158
5-9	MR images revealing structural complexity in the ventricular interseptum.....	159
5-10	Diffusion parameter images showing components in the ventricular interseptum.....	160
5-11	A long axis view MR images showing the ventricular interseptum in the vicinity of the right ventricular cavity.....	161
5-12	Diffusion parameter maps implying proximity at distance between the perforating artery and the right bundle branch. ....	163

5-13	The Free-running Purkinje fibers in the left ventricular chamber..	164
5-14	Plot of the logarithmic signal intensity as a function of b-values for an isolated rabbit heart.....	165
6-1	Volume rendered transverse images and manual segmentation (magnified) of the free-running Purkinje fiber network in the LV of a young rabbit heart and an old rabbit heart. ....	177
6-2	Diffusion parameter maps from MHARDI and a volume rendered image of the interseptum of a young rabbit heart. ....	178
6-3	Diffusion parameter maps from MHARDI and a volume rendered image of the interseptum of an old rabbit heart. ....	179
6-4	Logarithmic normalized diffusion signal attenuation depending on aging. Blue and red colors correspond to the ROIs in the papillaries of young and old hearts, respectively. ....	180

Abstract of Dissertation Presented to the Graduate School  
of the University of Florida in Partial Fulfillment of the  
Requirements for the Degree of Doctor of Philosophy

NON-INVASIVE INVESTIGATION OF CARDIAC TISSUE COMPARTMENTS AND  
COMPONENTS USING MR MICROSCOPY

By

Min Sig Hwang

April 2010

Chair: John R Forder  
Major: Biomedical Engineering

The heart responds to the ever-changing demands that the whole body places on the cardiovascular system. This life-time pump expels the blood out by generating a forceful and efficient contraction. The homogeneous function is the orchestrated outcome of morphologic, electrophysiological, molecular constituents that exhibit prominent heterogeneity in the heart. Non-invasive imaging of anatomical structure of the whole heart has increasing demand for the understanding of its role to normal function and pathological development.

Our hypothesis is that magnetic resonance imaging at high magnetic fields can distinguish different tissue compartments and cellular components in the mammalian heart and monitor their pathophysiological alterations, in-situ. In this thesis, we investigate non-invasively tissue compartments and cellular components comprising the rabbit heart using 17.6 T and 11.1 T magnets. The attenuation of MR diffusion signal intensity is used to reflect change in the tissue compartments. Magnetic resonance micro images contrasted by diffusion and transverse relaxation time of water molecules reveal anatomical features previously unavailable. Besides the myocardium, we visualize anatomical details of the cardiac conduction system from the bundle of His to terminal ramification of the Purkinje fibers in the ventricles using three-dimensional high resolution MR imaging and microscopic high angular resolution diffusion

imaging (MHARDI). Anatomical relationship of constituents in the ventricular muscular interseptum is explored. The combined investigative technique of microscopic three-dimensional high resolution MRI and MHARDI is observed to be an effective method of monitoring morphological changes occurring in cardiac tissue with advancing age.

## CHAPTER 1 INTRODUCTION AND BACKGROUND

### **Introduction**

The heart functions to respond to changing demands that the whole body places on the cardiovascular system (Katz and Katz, 1989; Katz, 1977). This life-time pump expels the blood out by generating a forceful and efficient contraction (Katz, 1977). The homogeneous function is the orchestrated outcome of morphologic, electrophysiological, molecular components that exhibit prominent heterogeneity in the heart (Baumgarten, 2006). The complex heterogeneity resembles structural heterogeneities of the trireme, a Greek warship that led the Greek naval victory in the 5<sup>th</sup> century BC (Katz and Katz, 1989). As the functional homogeneity in the trireme, traveling long distance at high speed, depends on heterogeneity in structure of oars, the functional homogeneity in the heart, delivering less turbulent blood to the extremity of the body, depends on heterogeneity in structure. In particular, the orderly spread of the depolarization wave through the heart and subsequent synchrony of contraction and relaxation in the ventricular walls are all facilitated by complex specializations in the myocardium. The heterogeneity plays essential roles in the well-coordinated electro-mechanical coupling of the heart (Katz and Katz, 1989). Conversely, abnormality in the well-coordinated heterogeneity might result in drastic cascade into failure of the homogenous cardiac function (Oxenham and Sharpe, 2003; Katz, 1977).

The ability to visualize anatomical connections between different parts of the heart, non-invasively, has opened a new era in the field of cardiac MRI (Bishop et al., , 2010; Burton et al., 2006; Forder and Pohost, 2003; Goodyer et al., 2007; Plank et al., 2009). This important breakthrough for cardiology and related clinical field has also developed through the advance of diffusion magnetic resonance imaging (Beck et al., 2002; Croisille, 2009). Currently, DTI is the

only non-invasive approach available to track the myocardial muscle fiber without myocardial MR tagging, or phase tracking. Complex architecture in the contracting ventricular myocardium has successfully been approached using Cardiac DTI. For example, overlapping spiral muscle fiber orientation, having different orientations depending on their location, could be identified using the primary eigen vector map generated from diffusion tensor (Hsu and Henriquez, 2001; Hsu et al., 1998a; Scollan et al., 1998; Scollan et al., 2000). DTI has also showed the great potential of providing data on heart contractility using diffusion anisotropy (Collins et al., 2007). In contrast, non-invasive investigation of electrophysiological heterogeneity is, at most, at an initial stage. To date, the techniques most commonly employed to study the cardiac conduction system depends upon destructive procedures that are also extremely time-consuming. Consequently, the need for a non-invasive method suitable to describe the conduction system and the anatomical features of the heart makes magnetic resonance imaging (MRI) an especially promising modality (Bishop et al., 2010; Plank et al., 2009).

In this thesis, we introduce MR imaging of the cardiac conduction pathways including the Purkinje fibers as a result of effort made to illustrate the heterogeneous conduction system non-invasively. The in-situ conduction pathways in the heart will be explored using three-dimensional high resolution MRI and microscopic high angular resolution diffusion imaging (MHARDI). In the following section, background on general diffusion, diffusion MRI and DTI as well as MRM will be briefly reviewed.

## **Background**

### **Water in Biological Systems**

While appearing as static to the naked eye, water molecules in liquid are in constant random motion termed as Brownian motion (Brown, 1827). This phenomenon called as

diffusion is caused by thermal agitation of the water molecules at the microscopic scale and shows the Gaussian displacement distribution (Einstein, 1906).

When placed in biological tissue, the liquid water does not function as an inert solvent (Finney, 2004; Le Bihan, 2007). Instead, the water molecules are involved in a variety of biochemical events and play essential roles in the biological processes (Aliev et al., 2002). The free diffusion of the water molecules is modulated by many tissue compartments, such as cell membranes, cytoskeleton, macromolecules, fibers, and vasculature (Bammer, 2003). For example, diffusion molecules can be restricted or bounced off in closed spaces, such as cells. The morphology and permeability of membrane and other natural barriers may have a significant effect upon the amount of restriction. Diffusion might also be hindered by obstacles that result in tortuous pathways. Exchange between compartments also slows down molecular displacements. Thus the apparent diffusion coefficient (ADC), usually reduced in comparison with rate of free diffusion, is necessary to depict the true water diffusion in the tissue. The non-invasive measurement of the water diffusion-driven displacement distribution will provide unique clues to the fine structural features and geometrical organization in biological tissues, and also to changes in these features with physiological and pathological states.

### **Diffusion Measurement of Water Molecules Using MR**

Nuclear magnetic resonance (NMR) phenomenon was discovered in 1946 (Bloch, 1946; Bloch et al., 1946; Purcell et al., 1946). Eight years later, effect of molecular self diffusion on NMR was first observed (Carr and Purcell, 1954). At an NMR experiment using a spin echo developed by Hahn (Hahn, 1950), measured transverse relaxation times (T<sub>2</sub>) for the water molecules were found to be abnormally low, and the effect was exacerbated by lack in homogeneity of the magnet at that time. These results implied significant contribution of diffusing water molecules to the MR signal under the gradients. The diffusion effect on

magnetization in a magnetic field could be solved using a modified Bloch equation, which includes self-diffusion terms of a particle described by the second Fick's law (Fick, 1855; Torrey, 1956; Callaghan, 1991; Callaghan, 1997). After that, Edward Stejskal and John Tanner introduced an idea to pulse the two symmetrical diffusion field gradients rather than continuous application of a single gradient for the diffusion measurement of a fluid. This Stejskal-Tanner method led to their widely cited 1965 publication (Stejskal and Tanner, 1965) and becomes still the workhorse of all diffusion imaging.

However, the discovery of the NMR phenomenon and the early diffusion measurement using the MR had not created a big impact in the medical field until magnetic resonance imaging was first published in 1973 (Lauterbur, 1973; Mansfield and Grannell, 1973), which opened the door for the non-invasive NMR in medical imaging. This Nobel-prize winning achievement simply utilized gradients in the magnetic fields that have linearly varying strength so as to distinguish a position in space, generating a two-dimensional image. In mid 1980s, Wesbey et al. introduced the Stejskal-Tanner method into MR imaging, which laid the ground work for the subsequent diffusion MR imaging (Wesbey et al., 1984a, 1984b). Moseley et al. (1990a, 1990b) also found that diffusion MRI could be utilized in early detection of ischemic stroke. This finding caused explosive interest in diffusion MRI. Since then, with technological advance occurred in related fields, this powerful investigative technique has become one of the best non-invasive imaging modalities.

The contrast underlying conventional anatomical MRI results from the 'relaxation times', called T1 and T2, which depend roughly on the intrinsic nature of the tissue (Purcell et al., 1956, Bloembergen et al., 1948). The longitudinal relaxation time (T1) characterizes how fast water magnetization returns to the equilibrium after the perturbation induced by electromagnetic waves

having the same resonant frequency. The transverse relaxation time (T2) is a measure of how fast the initial transverse magnetization created by the electromagnetic pulses is perturbed by interaction with adjacent magnetization. Whereas, contrast of diffusion MRI results from the diffusion path of water molecules shaped by the obstacles in the tissues. The next section shows how MR signal can be sensitive to the shaped diffusion path, consequently generating diffusion MR image.

### **Basic Principles of Diffusion-Weighted Imaging**

Since the water molecules are ubiquitous in living organisms and reflect intrinsic properties of the tissue, they are the most convenient species for diffusion measurement using MR. A precise estimation of water content and diffusion characteristics of the water molecules is essential to understand what occurs in biological tissues or organs (Basser, 1995; Basser and Pierpaoli, 1996). Diffusion-weighted magnetic resonance imaging (MRI) is deeply rooted in the powerful concept that the randomly moving water molecules probe tissue structure at a microscopic scale well beyond the usual image resolution (Le Bihan, 1995a, 1995b, , 2006, , 2007; Le Bihan et al., 2001). Diffusion-weighted MRI tags the hydrogen nuclei (protons) of the water molecules using pulsed gradient magnetic fields.

After random jumps during some time, a water molecule originally at a given position can be found at another position distant at the diffusion distance (RMS, root mean square displacement), given by the Einstein equation. Under a linear constant gradient, transport of a proton that is carried by the water molecule of interest into a region where the applied field is slightly different brings about change in the rate of nuclear precession, and results in a discrepancy in phase.

Figure 1-1 shows a common approach to perform the diffusion MRI using a standard spin echo pulse sequence. A spin echo MR signal can be made sensitive to diffusion of the water

molecules by using a pair of pulsed magnetic field gradients played out before and after the 180 degree refocusing pulse. The first gradient pulse magnetically ‘labels’ proton spins by means of minute differences in the Larmor frequency according to their spatial location as, for a short time, the magnetic field slowly varies along one direction. The second pulse having the same duration is introduced after the refocusing RF pulse to detect change in the location of the protons. In the presence of this gradient pulse, spins without translational motion would be completely rephased. Change in location of a proton nucleus carried by a diffusing water molecules results in change of the magnetic field seen by the proton. Thus the resulting phase shift is proportional to the spin displacement in the direction that the diffusion encoding gradients are applied in. At the time when a spin echo is formed, total phase shift of the spin is

$$\phi(TE) = \gamma \int_{t_1}^{t_1+\delta} G(t') \cdot x(t') dt' - \gamma \int_{t_1+\Delta}^{t_1+\Delta+\delta} G(t') \cdot x(t') dt', \quad (1-1)$$

where  $x(t)$  is the random displacement function of the water molecules.

Considering a great number of diffusing water molecules in a voxel, random phase shifts of all individual protons will contribute MR signal attenuation. Fast diffusing protons will bring about a large distribution of phase shifts, resulting in a large MR signal attenuation. Similarly, slow diffusing protons will bring about a small distribution of phase shifts, resulting in a small MR signal attenuation. Thus overall effect is a statistical diffusion process by the corresponding protons that experience change in the magnetic fields. The statistical displacement distribution will be reflected in the distribution of the phase shifts of the corresponding protons. This yields ultimately an attenuated MR signal that is less than a MR signal that is obtained without the pulsed magnetic gradient fields. Degree of the signal attenuation is quantitatively linked to intensity, arrangement in time, and shape of the pulsed gradient fields. This is represented by the

diffusion sensitizing factor called as ‘b-value’. Therefore, the effect of the MR signal attenuation can be expressed as

$$S = S_0 \exp(-b \cdot D), \quad (1-2)$$

where  $S$  is the signal intensity,  $S_0$  is the signal intensity in the absence of the pulsed magnetic gradients,  $D$  is the apparent diffusion coefficient (ADC) of the water molecules. The diffusion sensitizing factor ( $b$ ) can be expressed as

$$b = \gamma^2 G^2 \delta^2 (\Delta - \delta/3), \quad (1-3)$$

Here,  $\delta$  is duration of one pulsed gradient,  $\Delta$  is the time interval between the leading edges of the pulsed gradients,  $G$  is the strength of each diffusion gradient, and  $\gamma$  is the gyromagnetic ratio. b-value will be discussed in detail in a following section.

### **From Diffusion Coefficient to Diffusion Tensor**

From the characteristic signal equation of diffusion, the apparent diffusion coefficient can be calculated from two measurements with different diffusion attenuation. However, complex heterogeneity observed in biological tissues makes the real diffusion fully an anisotropic process. In the presence of the anisotropy, diffusion can no longer be characterized by a single scalar coefficient since outcome of diffusion measurement could vary depending on choice of diffusion encoding gradient direction, where diffusion weighted imaging is only an approximation of the actual diffusion sensitivity of an anisotropic sample. Hence information must be obtained in three-dimensional space in order to fully describe the anisotropic molecular mobility. In other words, a matrix of diffusion values in several directions is necessary in order to visualize the three dimensional diffusion properties.

A much improved estimation could be achieved by measuring an apparent diffusion tensor (ADT) (Basser et al., 1994a), which is based on the diffusion coefficients in various

directions. Figure 1-2 shows a general method that acquires the complete apparent diffusion tensor of measured MR diffusion (Basser et al., 1994a). Basser and colleagues have formulated diffusion tensor MRI (DTI) that employs a second order, positive definite, symmetric diffusion tensor to represent the local tissue structure (Basser et al., 1994a; Basser and Pierpaoli, 1998). In particular, the simple diffusion ellipsoid obtained from DTI could provide information about diffusion anisotropy and its orientation (Basser, 1995; Basser and Pierpaoli, 1998).

As mentioned in the previous section, diffusion in anisotropic media is characterized by Fick's law (Fick, 1855). When the diffusion term is added, a modified Bloch equation about the transverse magnetization, so-called Bloch-Torrey equation (Torrey, 1956), is expressed as;

$$\frac{\partial \psi_{(r,t)}}{\partial t} = -i\gamma(r \cdot G)\psi_{(r,t)} + \nabla^T (-D)\nabla \psi_{(r,t)}, \quad (1-4)$$

where G (gradient) and D (the apparent diffusion tensor) are matrices.

A solution of the differential equation of (2-1) can be expressed,

$$\psi_{(r,t)} = A(t) \exp(-i\gamma(r \cdot F)), \quad F = \int_0^t G(t') \partial t', \quad (1-5)$$

where A(t) corresponds to diffusion weighting effect on the measured MR signal.

From a solved form of Eq. (1-5),

$$A = A_0 \exp\left(-\sum_{i=x,y,z} \sum_{j=x,y,z} \gamma^2 \int_0^t F_i F_j \partial t' D_{ij}\right) = A_0 \exp\left(-\sum_{i=x,y,z} \sum_{j=x,y,z} b_{ij} D_{ij}\right), \quad (1-6)$$

$$\text{where } b_{ij} = \gamma^2 \int_0^t F_i F_j.$$

Since the measured diffusion weighted signal is sensitive only along the direction that the diffusion gradient is applied, positive and negative displacement of diffusing agents are indistinguishable. The opposite pole symmetry of the diffusion tensor and b matrix is required;  $D_{xy}$  term is equal to  $D_{yx}$ ,  $D_{yz}$  equal to  $D_{zy}$ , and  $D_{xz}$  equal to  $D_{zx}$ . Similarly,  $b_{xy}$ ,  $b_{yz}$ , and  $b_{xz}$  are

equal to  $b_{yx}$ ,  $b_{zy}$ , and  $b_{zx}$ , respectively. A diffusion encoding gradient applied in an arbitrary direction determines an antipodal symmetric  $b$  matrix. From  $b$  matrices of a diffusion tensor imaging data set with a minimum of 6  $b$ -value directions, the complete diffusion tensor components can be derived (Figure 1-2). The estimated diffusion tensor provides a complete description of the three-dimensional translational diffusion of the water molecules in a voxel. The diffusion tensor can be diagonalized to provide a simpler description of the self diffusion (Basser et al., 1994a; Basser and Pierpaoli, 1998; Mori and Zhang, 2006; Yoneda et al., 1999). The final diagonalized diffusion tensor provides the three eigen values and the three eigen vectors, which represent the rates of diffusion in three orthogonal directions and defines the diffusion ellipsoid. For instance, the primary eigen vector indicates the predominant direction of water diffusion in an image voxel (Mori and van Zijl, 2002).

### **Extracting Information from DTI data**

Diffusion data can be used to derive parameter images that provide meaningful information on tissue microstructure and architecture for each voxel (Basser, 1995; Basser and Pierpaoli, 1996; Pierpaoli and Basser, 1996). This may resemble histological stains that characterize features inherent to tissue microstructure. Diffusion tensor invariants including anisotropy indices have been proposed to characterize the measured diffusion signals. The invariant indices can be computed in terms of the three eigen values of the diffusion tensor ( $\lambda_1$ ,  $\lambda_2$ , and  $\lambda_3$ ). This makes the generated parameters objective and insensitive to choice of coordinate system. Most useful are the rotationally independent measures such as mean diffusivity and fractional anisotropy (Basser and Jones, 2002; Le Bihan, 1995b; Le Bihan et al., 2001).

## Mean diffusivity

To obtain an overall assessment of diffusion in a voxel, anisotropic effect should be avoided and the result should be orientation-independent measure of water diffusion. Mean diffusivity, averaged rate of water diffusion, characterizes the overall mean-squared displacement of the water molecules and the overall presence of obstacle to diffusion. When the trace of the diffusion tensor,  $\text{Tr}(\underline{\mathbf{D}})$ , is represented by the sum of the three eigen values ( $\lambda_1$ ,  $\lambda_2$ , and  $\lambda_3$ ), the mean diffusivity is then given by  $\text{Tr}(\underline{\mathbf{D}})/3$  (Gill, 1991; Le Bihan, 1995b; Le Bihan et al., 2001; Le Bihan et al., 1992).

## Fractional anisotropy

Fractional anisotropy (FA) is one of the most widely used indices of diffusion anisotropy (Le Bihan et al., 2001; Le Bihan and van Zijl, 2002; Pierpaoli et al., 1996; Pierpaoli and Basser, 1996), written as

$$FA = \frac{\sqrt{3[(\lambda_1 - \langle \lambda \rangle)^2 + (\lambda_2 - \langle \lambda \rangle)^2 + (\lambda_3 - \langle \lambda \rangle)^2]}}{\sqrt{2(\lambda_1^2 + \lambda_2^2 + \lambda_3^2)}}, \quad (1-7)$$

where  $\langle \lambda \rangle = (\lambda_1 + \lambda_2 + \lambda_3)/3$ .

Fractional anisotropy measures orientation-independently the fraction of the “magnitude” of the ADC that can be ascribed to anisotropic diffusion. Fractional anisotropy varies between 0 (isotropic diffusion) and 1 (infinite anisotropy). A main advantage of diffusion tensor imaging lies in this quantitative measure of anisotropy. Fractional anisotropy may highlight subtle anomalies in the organization of myocardial fiber track or contractility of the muscle cells otherwise not visible with other modalities (Mori and Zhang, 2006). Particularly, a measure of muscle contractility by the FA may predict viability in non-beating donor hearts transported under global ischemic condition (Collins et al., 2007).

## High Angular Resolution Diffusion Imaging

When the tissue of interest has a complicated geometry in a voxel, a simple diffusion tensor that presumes a homogeneous structure in each voxel might yield incorrect assumption about the actual heterogeneity of muscle or nerve fiber orientation. The statistical diffusion process in the heterogeneous voxel violates the assumption of Gaussian probability model implicit in the conventional DTI. For instance, two fibers crossing at  $90^\circ$  in a voxel may lead the primary eigen vector that does not fit with any of the actual fiber direction. The primary eigen vector does not represent the underlying fiber orientation. Thus the conventional and relatively simple DT model fails to describe more realistic, multiple fiber structures in a given voxel. To overcome this shortcoming of the conventional diffusion tensor model, both a number of advanced image acquisition strategies and more sophisticated reconstruction methods have been proposed.

High angular resolution diffusion imaging (HARDI) evaluates the apparent diffusion coefficients along many diffusion gradient orientations independently without the data fitted to the Stejskal-Tanner expression (Frank, 2002; Tuch et al., 2002). The HARDI method introduces the diffusivity profile that represents an angular distribution of the apparent diffusivities by acquiring diffusion weighted images with a number of non-collinear diffusion encoding directions effectively sampling the sphere around a point (Tuch et al., 2002). Several studies showed that the diffusivity profile has a complicated structure in voxels having the orientationally heterogeneous fibers (Tuch et al., 2002; von dem Hagen and Henkelman, 2002). The resulting shape of the ADC or diffusion ellipsoid from such a measurement could represent underlying multiple fiber structure in a voxel. With the multidirectional measurement from HARDI, the spherical harmonic transformation (Frank, 2002) and the generalized diffusion

tensor model (Ozarslan and Mareci, 2003; Ozarslan et al., 2005) have been employed to represent the diffusivity profiles of the intravoxel orientational heterogeneity (IVOH).

However, peaks of the diffusivity profile from the HARDI method, assuming Gaussian distribution, do not necessarily coincide with ones of the diffusion probability profile that corresponds to distinct fiber orientations (Jiang et al., 2004; Ozarslan et al., 2006). Thus computational methods have been employed to remove the erroneous fiber structure interpretation from HARDI data (Barmpoutis et al., 2009; Barmpoutis et al., 2007a; Barmpoutis et al., 2008; Ozarslan et al., 2006; Tuch, 2004; Wedeen et al., 2005; Wedeen et al., 2008). Ozarslan et al. (2006) introduced so-called the diffusion orientation transform (DOT) that describes a robust and fast transformation of apparent diffusivity to diffusion probability profile, without employing any model. Several studies employed the multi-compartmental model to characterize the diffusion-attenuated MR signal from the HARDI (Barmpoutis et al., 2009; Barmpoutis et al., 2007a; Barmpoutis et al., 2008; Barmpoutis et al., 2007b; Jiang et al., 2004). Techniques handling HARDI data prior to analysis or visualization is currently an object of intensive research in the medical imaging field.

### **Optimization of the Diffusion Sensitizing Factor**

As shown in the Eq. (1-2), the attenuated signal ( $S$ ) observed in the diffusion MR image does not only depend on the statistical integration of all the microscopic displacement distributions of the water molecules present in the voxel ( $D$ ), but also other experimental, technical parameters, most of which are incorporated in the diffusion sensitizing factor ( $b$ -value). Optimal diffusion sensitizing factor becomes the key to desired diffusion MR imaging. Hence elements that are associated with the  $b$ -value should be well understood to interpret the diffusion MR signal or the estimate the diffusion tensor correctly (Norris and Niendorf, 1995). Optimization of the  $b$ -value largely depends on experimental priority. Among elements to be

generally considered for optimum b-value are the signal to noise ratio (SNR) of diffusion weighted image and gradient power available for the desired diffusion weighting, the accuracy of diffusion measurement, intrinsic property of tissue (relaxation times), and imaging artifacts arising from non-diffusional motion. However, all of these elements are correlated or compete with each other.

Due to signal reduction by T2 weighting, a pulse sequence using spin echo for diffusion weighting should have an upper limit to the echo time (TE) (Figure 1-1). The selection of TE may be complicated by effect of the transverse relaxation time (T2) on diffusion signal. Previous studies demonstrated change in diffusion signal attenuation curve as a function of echo time, suggesting that a difference in T2 of the intracellular and extracellular compartments might contribute to the observed change in the ADC curve. Due to the morphological complexity within the cell, the T2 of intracellular compartment is likely to be shorter than that of the extracellular compartment (Buckley et al., 1999a). Thus due to the T2 difference among tissue compartments and the signal loss issue, a shorter echo time will be favored for diffusion weighted MR imaging using a spin echo.

A short echo time will then restrict space and duration for a pair of the pulsed diffusion encoding gradients, which determine the diffusion time ( $\tau, \Delta - \delta/3$ ). In cardiac tissue that contains at least two compartments, typically intracellular, interstitial, and vascular water, the MR signal attenuation by the translational diffusion of water molecules would depend on the rate of water exchange between the tissue compartments that occurs during the diffusion time. Hence the diffusion time determines sensitivity of the MR diffusion experiment to restriction of diffusion. When a short diffusion time is used, the majority of spins may not reach the barriers of the system but remain in one or the other of the compartments (the limit of slow exchange).

The diffusion measurement will integrate relatively genuine diffusion phenomenon within each compartment. By the way, as the diffusion time increases the amount of spins that interact with the barriers will also increase. Water diffusion will appear to be restricted (the intermediate condition of water exchange) and this condition is encountered in most practical diffusion experiments (Buckley et al., 1999a; Buckley et al., 1999b; Karger et al., 1988). In case the diffusion time is long enough to diffuse over a length of local anisotropy, the anisotropic biological tissue will appear isotropic diffusion. All of the water molecules within a voxel also can diffuse through the compartments (the limit of fast exchange). The signal attenuation will then be mono-exponential and the ADC will simply be expressed as a sum of relative contribution of each compartment (Buckley et al., 1999a; Buckley et al., 1999b).

From the diffusion time, diffusion gradient intensity will be determined to give the desired b-value, of course within a maximal power the system permits. Therefore, b-values should always be selected under consideration of both the purpose of desired diffusion imaging and limitation of the magnet system to be employed (Niendorf et al., 1996; Norris, 2001; Norris and Niendorf, 1995; Norris et al., 1994).

### **Effect of Imaging Gradients to the Diffusion Sensitizing Factor**

Equation (1-6) suggests that the diffusion sensitizing factor reflects contribution from all the time varying gradients used for spatial mapping of water diffusion characteristic. The time varying gradients do not include just the diffusion encoding gradients played before and after the refocusing RF pulse, but also include the imaging gradients (Figure 1-1). Thus the actual diffusion sensitizing factor seen by diffusing protons consists of 1) contribution by the diffusion gradients alone, 2) contribution by the interaction between imaging gradients alone (the imaging terms), and 3) contribution by the interaction between the imaging gradients and the diffusion gradients (the cross terms) (Neeman et al., 1991a). Ignoring contribution of imaging gradients

may result in severe overestimation of the apparent diffusion coefficient (Neeman et al., 1991a; Neeman et al., 1991b).

Likewise the diffusion encoding gradients, signal attenuation by the imaging gradients depends on the strength and duration of the imaging gradients. The imaging gradient intensity (Hz/mm) in the read-out (frequency encoding) direction is determined by a ratio of the sampling bandwidth during acquisition and the field of view (FOV). And the imaging gradient intensity (Hz/mm) in the slice selective direction is determined by a ratio of the bandwidth of the refocusing RF pulse and the selected slice thickness. Thus as a voxel resolution increases, contribution from the imaging gradients becomes more significant. This means that high resolution MR imaging contains a considerable degree of diffusion weighting in acquired image even without the diffusion weighted gradients. The imaging gradients tend to attenuate selectively signal from the fast moving molecules in the tissue, which is called as the imaging filter effect. Effect of the imaging gradients can not be eliminated but be minimized 1) by using relatively short RF pulses in combination with a strong and short slice selection gradient, and 2) by placing the dephasing read-out gradient using a gradient pulse of opposite polarity immediately prior to data acquisition.

The cross terms can result in significant deviation from dependence of the MR signal intensity on the diffusion gradients alone. Effect of the cross terms may become severe for strong imaging gradients and low diffusion gradient. Since the effect might be substantially different depending on axes, orientation dependence of the cross terms should be considered particularly in measurement of diffusion anisotropy (Mattiello et al., 1997). Pulse sequences without the cross terms can be designed by using bipolar diffusion gradients in the same

direction or by acquiring two data sets with diffusion gradients of opposite polarity (Neeman et al., 1991a; Neeman et al., 1991b).

In addition to the cross terms and the imaging terms, contribution of the crusher gradients to the effective b values may be significant particularly in microscopic diffusion imaging. This may be another type of the cross-terms produced by the crusher gradients. When a pulse sequence contains imperfect refocusing RF pulse (i.e., flip angle is not  $180^\circ$ ), multiple signal pathways, including free induction decay (FID) and stimulated echo, can be produced in addition to the spin echoes (Bernstein et al., 2004). These signals can map incorrectly the spatial information encoded in their phase, resulting in image artifact by errors in the acquired k-space. Crusher gradients are generally applied just before and just after the refocusing RF pulse to preserve the desired signal pathways while removing the interfering ones (Figure 1-1).

Figure 1-3 shows dependence of effective b-values on duration of the crusher gradients in HARDI using the b-value of  $1300 \text{ s/mm}^2$ . When the crusher gradients are applied for 2 ms with half of a maximum strength available, the effective b-values, actually seen by protons, vary significantly depending on the diffusion gradient directions. As a consequence, with the b value inconsistent in each direction, the estimated diffusion tensor might lead to incorrect information about diffusion directionality and diffusion anisotropy. Therefore, effect of the crusher gradients to the diffusion signal should be kept at a minimum.

### **Apparent Diffusion Coefficient: An Outstanding Issue**

Since water molecules in different tissues and subcellular structures play essential roles of biochemical reactions (Aliev et al., 2002), the energy fluxes between the cellular compartments, the concentration gradients of ion, and the membrane potential, a precise spatial mapping of the apparent diffusion coefficient (ADC) of the water molecules would provide important physiological information within the related tissue with water motility,

compartmentalization, and diffusion anisotropy. For example, in pathological situations, such as ischemia, cells undergo significant cellular edema due to increase in cellular osmolarity. Cell swelling causes stretch and/or deformation of cell membrane and of the underlying cytoskeletal network. Hence relating alterations in the cellular hydration to the ADC is attractive to monitor change or abnormality in the tissue.

With the phenomenal technical advance to date, the window the MRI permits us to look into tissues has been enhanced to sub-millimetric resolutions (Le Bihan, 2007; Le Bihan et al., 2006a; Mori and Zhang, 2006). However, since the mean diffusion path of water molecules is well beyond the typical imaging resolution, the signal of each voxel in diffusion MRI integrates all microscopic displacements from involved tissue compartments (Le Bihan, 2007; Le Bihan et al., 2001; Mori and Zhang, 2006).

Since a sharp drop in the apparent diffusion coefficient (ADC) of water, just minutes after an onset of the ischemic event in the infarcted region of brain was reported in the early 1990s (Moseley et al., 1990), the origin of the MR signal of water diffusion observed in the biological tissues has been of outstanding interest to MR researchers (Assaf and Cohen, 1998b; Buckley et al., 1999a; Buckley et al., 1999b; Norris, 2001). Hence there have been a large number of publications to make indirect inferences on the microstructure from the macroscopic ADC of water molecules in biological tissues, especially in the brain. The subsequent studies speculated that cell swelling due to cytotoxic edema plays a major role in the observed change in the ADC.

The early ADC measurements that were made as a function of b-values indicated that diffusion is a mono-exponential phenomenon (Basser et al., 1994b; Norris et al., 1994). These measurements were performed largely with b-values ranging  $0 \sim 1500 \text{ s/mm}^2$  due to limitations

to the diffusion gradient power available. However, when measured with sufficiently high  $b$  values up to  $40,000 \text{ s/mm}^2$ , the ADC of water in tissues was observed to be inherently non-monoexponential (Buckley et al., 1999b; Bui et al., 1999; Niendorf et al., 1996; Pfeuffer et al., 1999). Interestingly, most experimental data have been very well fitted with a biexponential function corresponding to two water diffusion pools with a fast and a slow diffusion coefficient in slow exchange assumption (i.e. when the water molecules remain in each compartment during the diffusion time), written as (Assaf and Cohen, 1998b; Buckley et al., 1999a; Buckley et al., 1999b; Niendorf et al., 1996):

$$S = S_0 [f_{slow} \cdot \exp(-b \cdot D_{slow}) + f_{fast} \cdot \exp(-b \cdot D_{fast})], \quad (1-8)$$

where  $f_{slow}$  and  $f_{fast}$  are the volume fractions of the slow and the fast components. Similarly,  $D_{slow}$  and  $D_{fast}$  are the ADCs of the slow and the fast component.

Previous studies describing water diffusion in tissue compartments using modeling tools proposed that restriction in the intracellular space with high viscosity, transport of water into cells resulting in intracellular/extracellular volume changes, a concomitant change in extracellular tortuosity, membrane permeability, water exchange, and geometrical features (cell size distribution or directional distribution of cell) might cause principal changes in diffusion characteristics (Latour et al., 1994; Norris, 2001; Stanisz et al., 1997; Szafer et al., 1995). Some experimental works using other tracer molecules than water molecules suggested that variations in the tortuosity within the extracellular space might be at the origin of the ADC change (Norris, 2001; Sehy et al., 2002; Stanisz et al., 1997). Tortuosity describes how barriers within a biological system reduce the diffusion coefficient compared with the coefficient without such barriers. In the presence of impermeable obstacles, spins in the interstitial space exhibit unrestricted diffusion if the spins are able to diffuse around the impermeable barriers. The mean

path between two points is thereby shortened and the measured ADC is lowered compared with an identical measurement in a medium without barriers. This aspect of hindered diffusion is described by the concept of tortuosity. Dominant factors affecting tortuosity are the size, shape, and density of the cellular obstacles. In biological systems a change in the extracellular volume fraction will be the largest effect on changes in tortuosity. A decrease in the extracellular space will increase the effects of cellular obstacles.

On the other hand, an ensemble of experimental studies demonstrated that the change in volume fractions of the intracellular and the extracellular compartments resulting from cellular swelling or shrinking always led to variations of the ADC (Assaf and Cohen, 1998a, 1998b; Buckley et al., 1999a; Buckley et al., 1999b). They also discussed that effect of tortuosity and exchange rate between the two compartments observed in previous studies might be overestimated.

Buckley et al. (1999b) observed that the global ADC decrease in perfused rat hippocampal slices treated with ouabain, acting as an agent that promotes cell swelling by blocking the membrane-bound Na-K ATPase. Interestingly, from the bi-exponentially fitted diffusion curves, the observed ADC decrease was found to come from the relative increase of the slow diffusion component, rather than from the change of the slow and the fast diffusion coefficients. The early view led to hypothesize that the fast and the slow diffusion components might correspond directly to the intracellular and the extracellular compartments - or at least provide an index of those compartment sizes and their changes under perturbation.

However, studies performed by Niendorf et al. (1996) and Buckley et al. (1999b) showed an important similarity in a sense that estimates of the fractional volumes of the fast component and the slow component do not directly match with the fractional volumes of the real

extracellular and the intracellular compartments. The subsequent studies using N-acetyl aspartate (NAA) (Nicholson and Sykova, 1998) and the oocyte (Sehy et al., 2002) suggested that even the intracellular space has two populations of the fast and slow components, which might be a convincing explanation for disagreement between the calculated volumes of intracellular and extracellular compartments with accepted values shown in the early studies.

Le Bihan et al. (2007) proposed that ‘the highly structured water’ resulting from the strong interactions between polarized water, hydrophilic proteins and phospholipids at the interface with membranes as well as within the cytoplasm might be the predominant factor responsible for the slow diffusion component. By calculating using the conceptual model frame, he hypothesized that the ADC decrease observed in tissues containing swollen cell resulted from the increase of the membrane-bound structured water at the expense of free water in the intracellular compartment and extracellular compartment. But assumptions used in this model are still matter of discussion. No signal enhancement around the membrane was observed in diffusion weighted images of a single cell (Aguayo et al., 1986; Bowtell et al., 1995; Grant et al., 2000; Grant et al., 2001; Hsu et al., 1997)

From the literature reviewed, until now there is no final agreement on two tissue compartments as the sources responsible for the ADC change. A convincing yet speculative explanation about the ADC issue is that the fast and the slow diffusion components obtained from the bi-exponential fitting of the attenuated signal intensity would correspond to two water pools, both existing partly in the intracellular compartment and partly in the extracellular compartment. Relative distribution of the fast and the slow diffusing pools to each compartment is still under investigation.

If the vascular space is extracted from the extracellular space, leaving the interstitial space, the picture becomes further complicated. Recently, diffusion weighted MR imaging has been used to detect transient morphological change occurring in close connection with neural activation (Flint et al., 2009a; Jin and Kim, 2008; Le Bihan, 2006, , 2007; Le Bihan et al., 2006b). Several studies attributed the ADC change observed in activated neural tissues to cellular volume increase related to neural activation (Le Bihan et al., 2006b) or to increased vascular flow in the region of tissue (Jin and Kim, 2008; Jin et al., 2006; Miller et al., 2007). Flint et al. (2009a) employed hippocampal slices in absence of vasculature to detect only effect of morphological changes induced by neural activation on signal intensity as a function of b-value. Hence this study, eliminating the contribution of residual vascular space and flow, could describe that the lack of ADC resulted only from the cell swelling occurring during activation. However it remains unclear how the vascular space contributes to the ADC or MR signal intensity.

### **Water Compartmentalization in Cardiac Tissue**

Figure 1-4 shows relative volume fraction of compartments or elements comprising the heart (Aliev et al., 2002; Cieslar et al., 1998; Dobson and Cieslar, 1997; Frank and Langer, 1974). Space for diffusing water in the cardiac tissue is proportional to the size occupied by individual tissue compartment and its elements (Aliev et al., 2002; Cieslar et al., 1998). Water molecules within the cardiac tissue diffuse passively between the tissue compartments through specialized channels known as aquaporin (Boron and Boulpaep, 2005). The water molecules transport across a capillary endothelial wall until the oncotic pressure and the hydrostatic pressure between the interstitial compartment and the intravascular space are equal (Figure 1-5). On the other hand, the diffusion of water in and out of myocytes is driven only by the osmolarity difference at either part of the non-rigid cellular membrane. Water into the cell by this osmotic

gradient dilutes the cellular contents and generates cell swelling (Boron and Boulpaep, 2005). Under the assumption that the exchange rate between the compartments is negligible (Buckley et al., 1999a; Forder et al., 2001), diffusion between the tissue compartments is likely to result in the fractional changes of water having diffusion characteristic inherent to each compartment. This implies that the controlled perturbation studies using MR can follow non-invasively the changes in compartments in cardiac tissue.

### **Cell Volume Regulation in Cardiac Tissue**

Cells regulate their volume by interplay of passive  $\text{Na}^+$ ,  $\text{K}^+$ , and  $\text{Cl}^-$  fluxes and active transport, ion channels and transporters that have voltage dependence, etc. (Baumgarten, 2006). In particular, a central mechanism to maintain cell volume is made by the active transport process by the Na-K ATPase that extrudes the  $\text{Na}^+$ , the primary extracellular permeant cation, that leaks into the cells. Because of its key role, the inhibition of the pump results in cell swelling. And the predicted cell swelling was observed in the brain tissue treated with ouabain, the Na-K pump inhibitor.

In contrast, swelling of cardiac muscles such as the ventricular myocytes and the papillary muscles are, at most, modest after the Na-K pump inhibition. This implies that cardiac cells may have another system to regulate cell volume. Simulation and experimental studies revealed that the plasma membrane  $\text{Ca}^{2+}$ -ATPase (PMCA) works in concert with  $\text{Na}^+$ - $\text{Ca}^+$  exchanger (Baumgarten, 2006). In inhibition of the Na-K pump, the PMCA keeps intracellular  $\text{Ca}^{2+}$  relatively low. This will activate exchange between intracellular  $\text{Na}^+$  and extracellular  $\text{Ca}^{2+}$ . By this cooperative work, surplus cellular  $\text{Na}^+$  is extruded and the driving force for water transport, osmotic gradient, is reduced. This mechanism makes the cardiac muscle cells behave like a leaky boat that has a bilge pump. Therefore the greater efficient yet complex volume

regulatory mechanism should be taken into account when designing study to understand the physiological sources responsible for the MR diffusion signal in the cardiac tissue.

### **Diffusion Tensor Imaging of the Myocardium**

Ventricular myocardium is not a uniformly connected structure but a composite of discrete muscle layers which run radially across the ventricular wall from subendocardium to subepicardium, accommodating local muscle fiber orientation (Legrice et al., 1997). The myocardial muscle fiber orientation and laminar architecture play important roles in both mechanical and electrical function of the ventricles, influencing electrical depolarization, tissue perfusion, and myocardial contraction (Helm et al., 2005; Kanai and Salama, 1995; Scollan et al., 2000; Waldman et al., 1988). This underlies the importance of diffusion tensor imaging to reveal the structure of the myocardium in a non-invasive and efficient fashion previously unavailable as a potential diagnostic aid for management of the related patients (Hsu and Henriquez, 2001; Hsu et al., 1998a; Reese et al., 1995; Scollan et al., 1998).

Myocardial diffusion tensor imaging (DTI) has been successfully used to provide information regarding anatomic microstructure of the myocardium by correlating the principle eigen vector of water diffusion with myocardial fiber orientation (Hsu and Henriquez, 2001; Hsu et al., 1998a; Reese et al., 1995) and the tertiary directions of the water diffusion with the laminar sheet structure of the specialized cardiac muscle layers (Dou et al., 2003; Helm et al., 2005). Its direct clinical application has also been proposed (Collins et al., 2007; Wu et al., 2006). Moreover, fractional anisotropy, a MR parameter indicating cellular integrity orientation independently, has recently been proposed to be a rapid and useful method to predict myocardial viability in non-beating donor hearts after warm global ischemia (Collins et al., 2007). Forder et al. (Forder et al., 2001) has confirmed that the multi-exponential behavior of water diffusion observed in other tissues exists in the heart as well. Unlike the brain, delayed ADC reduction of

water diffusion after myocardial ischemia was observed in the isolated heart model measured with b values below 1,000 s/mm<sup>2</sup> (Hsu et al., 1998b).

In myocardial diffusion weighted imaging, the complicated diffusion profile may come from the special circulation network feeding this life-long muscle pump. The capillary surface area, as a formidable oxygen delivery system necessary for the sustained high energy turnover of the cardiac muscle, comprises 14~22% of heart tissue (Olivetti et al., 1990; Poole and Mathieu-Costello, 1990), which is significantly larger than that of the brain, 3~4%. Contribution of the vascular compartment to the very fast and/or fast component of the ADC has strongly been suspected (Forder et al., 2001; Hsu et al., 2001; Hsu et al., 1998b). The intravascular incoherent motion (IVIM) in the capillary vasculature may cause the incorrect estimation of the global ADC and fraction of water pools (Le Bihan et al., 1988; Le Bihan et al., 1986). The contribution of the IVIM to the fast pseudo-diffusion coefficient, usually observed at b values less than 600 s/mm<sup>2</sup>, may be extended to a b value of 1000 s/mm<sup>2</sup> due to the significant volume of the vasculature (Le Bihan et al., 1988). This suggests additional factors should be considered when analyzing the clinical diffusion MR data that might be biased to the fast component usually around 1000 s/mm<sup>2</sup>.

In the early stages of cardiac ischemia, cardiac myocytes undergo cell swelling caused by increase in cellular osmolarity. This implies that the global ADC, volume fraction, and the ADC of each water pool obtained from MR diffusion measurement may be specific to the structural states of myocardial tissue in the pathological conditions.

Therefore, a clear understanding of the sources of MR diffusion signals observed in the heart, which remains to be identified, is believed to be the pivotal key to a greater understanding of tissue structure and function, which will provide the foundation for suitable models of

diffusion coefficients in normal and diseased tissues. Interpretation of existing myocardial diffusion MRI data without clear knowledge of its origin can lead to incorrect inferences. Development of controlled perturbation studies will ultimately aid in generation of accurate and meaningful mathematical models to predict correctly the physiological changes of the myocardial ischemia and can be used to assess the effectiveness of clinical treatments.

### **Magnetic Resonance Microscopy of the Cardiac Conduction System**

The cardiac conduction system functions to generate spontaneous electrical impulses and deliver them to the contractile muscles of the whole heart . The Purkinje fibers, named after its discoverer in 1845, were the first part to be found of the cardiac conduction system (Ansari et al., 1999; Eliska, 2006). This specialized fibers play a major role in electrical conduction and propagation of impulse to the ventricular muscle (Dun and Boyden, 2008). Knowledge of the cardiac conduction system was significantly expanded after Tawara (2000) had demonstrated outstanding histological work concerning the morphological unit of conduction transfer from the atrioventricular node (AV node) to the bundle of His, bundle branching, and Purkinje fibers.

At present, the cardiac conduction system is known to start at the sino-atrial node, situated at the junction of the anterior circumference of the superior vena cava and the right auricle (Eliska, 2006). The conduction pathways then reach the AV node by so-called specialized internodal tracts. The AV node is usually found between the coronary sinus and the septal leaflet of the tricuspid valve in the Koch triangle. At the apex of the Koch triangle, the penetrating connecting bundle (bundle of His) passes through the central fibrous body where the aortic valve and the mitral valve meet. This relatively short bundle is a direct extension of the compact AV node, enabling conduction activity at the atrium to be conveyed to the ventricles.

The emergence of this bundle of His is directly related to the membranous part of the atrioventricular interseptum. Hence the bundle of His is sandwiched between the membranous

septum and the supercrest of the muscular ventricular interseptum. At a short distance, the connecting bundle bifurcates into the left and the right bundle branches (Sheets et al., 1983). The left bundle branch largely fans out as it descends in the sub-endocardium of the septal inner surface of the left ventricle. In contrast, the right bundle branch is relatively thin and cordlike, and descends through the musculature of the ventricular interseptum only to emerge in the subendocardium at the base of the medial papillary muscle and then run into the septomarginal trabeculation.

The left bundle and the right bundle branch as the Purkinje fibers. These fibers run in the subendocardium and into the myocardium forming a network (Tawara, 2000). These can be traced crossing the ventricular cavities in tendinous cords, so-called the free-running Purkinje fibers. Finally the conduction pathways terminate at the Purkinje–ventricular muscular junction within the ventricular myocardium (Nakamura et al., 1986). This His-Purkinje system, a network of rapidly conducting cardiac muscle cells, synchronizes activation of more slowly conducting contractile ventricular myocardial cells.

This impulse-conducting system that coordinates the cardiac cycle has a feature of highly heterogeneous structure. The anatomical make-up of the system has intrinsic differences in cell size and cell type distribution. (Katz and Katz, 1989; Kohl, 2003). The harmonious interplay of heterogeneous components is required for the conduction system to accomplish synchronous and reliable delivery to contractile muscles. Thus, detailed insight into the anatomy of the complex conduction system would be greatly essential to understand the homogeneous cardiac performance arising from well-coordinated electro-mechanical activity and further for the investigation of cardiac function and morphology in both normal and abnormal (pathophysiologic) states (Goodyer et al., 2007).

To date, the techniques most commonly employed to study the cardiac conduction system include mapping from the histological serial sectioning (usually only a few micrometers in thickness), micro-dissection, endocardial staining, and direct ink injections (Burton et al., 2006). However, these techniques are invasive, and use intrinsically destructive procedures. Furthermore, three dimensional reconstruction of the Purkinje fiber network using histological data is extremely difficult and time consuming. Until now, the in-situ anatomical details of the whole conduction system are rarely done. As a consequence, the need for a non-invasive method suitable to describe the conduction system of the whole heart makes magnetic resonance imaging an especially promising modality (Beg et al., 2004). Magnetic resonance microscopy (MRM) enabling a high resolution at a subcellular level (several tens of  $\mu\text{m}$ ) in at least one dimension has the potential to visualize the conduction pathways as well as anatomical details in the heart (Benveniste and Blackband, 2002; Benveniste and Blackband, 2006; Bishop et al., 2010; Burton et al., 2006; Vadakkumpadan et al., 2009).

We believe that magnetic resonance imaging at high magnetic fields can distinguish different tissue compartments and cellular components in the mammalian heart and monitor their pathophysiological alterations, in-situ. In this thesis, we aim to discern non-invasively tissue compartments and cellular components comprising the rabbit heart using 17.6 T magnet and 11.1 T magnet (Beck et al., 2002). The specific aims to achieve the goal are schematically represented in Figure 1-6.

First, the attenuation of MR diffusion signal intensity of water molecules as a function of the diffusion sensitizing factor is used to reflect change in the tissue compartments. We propose to use a modified hardware setup that enables to perform the heavy diffusion weighted imaging of isolated rabbit heart at the horizontal 11.1 T magnet (Chapter 2). Using this experimental

setup, physiological sources responsible for the cardiac diffusion MR signal will be investigated using isolated perfused rabbit hearts and heart slices (Chapter 3). We conduct controlled perturbation studies using tissue compartmentalization of water molecules, which will distinguish responses from different compartments. In particular, contribution of the vascular compartment to attenuated diffusion MR signal intensity, hence the apparent diffusion coefficient, will be examined in terms of replacing the vascular space and altering the direct perfusate flow in the vascular space.

Second, we utilize three-dimensional high resolution MRI (Chapter 4) and microscopic high angular resolution diffusion imaging (Chapter 5) to visualize the Purkinje fibers, specialized muscle cells comprising the cardiac conduction system. Since the Purkinje fibers have different cellular shape and distribution from the contractile muscle cells, we reason that this component can be highlighted by the high resolution MRI and MHARDI, which generate image contrast by T2 relaxation time and diffusion of water in the tissue.

Third, we monitor morphological changes in aging heart using three-dimensional high resolution MRI, microscopic high angular resolution diffusion imaging, as well as diffusion-weighted imaging using b-values up to  $6500 \text{ s/mm}^2$  (Chapter 6). We will use the investigative techniques achieved from the specific aims described above. We propose to relate the MR findings with age-related changes observed in the heart, such as cellular hypertrophy, myocardial fibrosis, and slowing in conduction velocity. Histochemical staining will be used to validate our analysis.

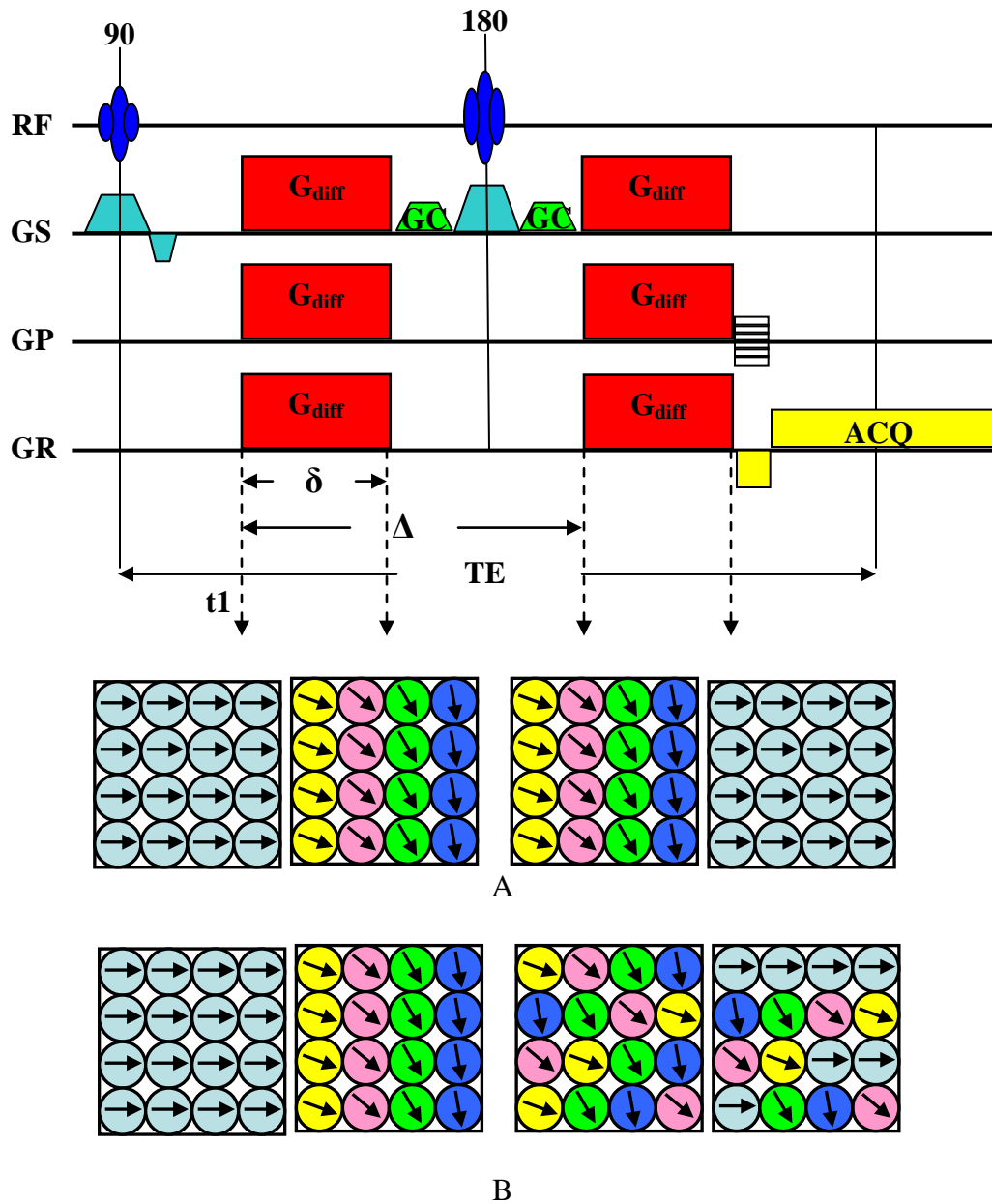


Figure 1-1. A diffusion imaging pulse sequence using a spin echo (top) and diagram showing the overall phase shifts of protons by diffusion (bottom, adopted from Mori et al., 2002). A) Without translational random motion. B) With translational random motion. Diffusion occurring at the diffusion gradient duration is ignored. Contribution of the phase encoding gradients is negligible. Note that the rephrasing gradient in the phase encoding direction is applied after the acquisition is done. With this gradient pulse, hypothetical motionless spins would be completely rephased. Change in location of a proton nucleus carried by a diffusing water molecules results in overall phase shift. RF: radio frequency electromagnetic pulse; GR: gradient in the frequency encoding direction; GP: gradient in the phase-encoding direction; GS: gradient in the slice selective direction; GC: crusher gradients; ACQ: data acquisition.

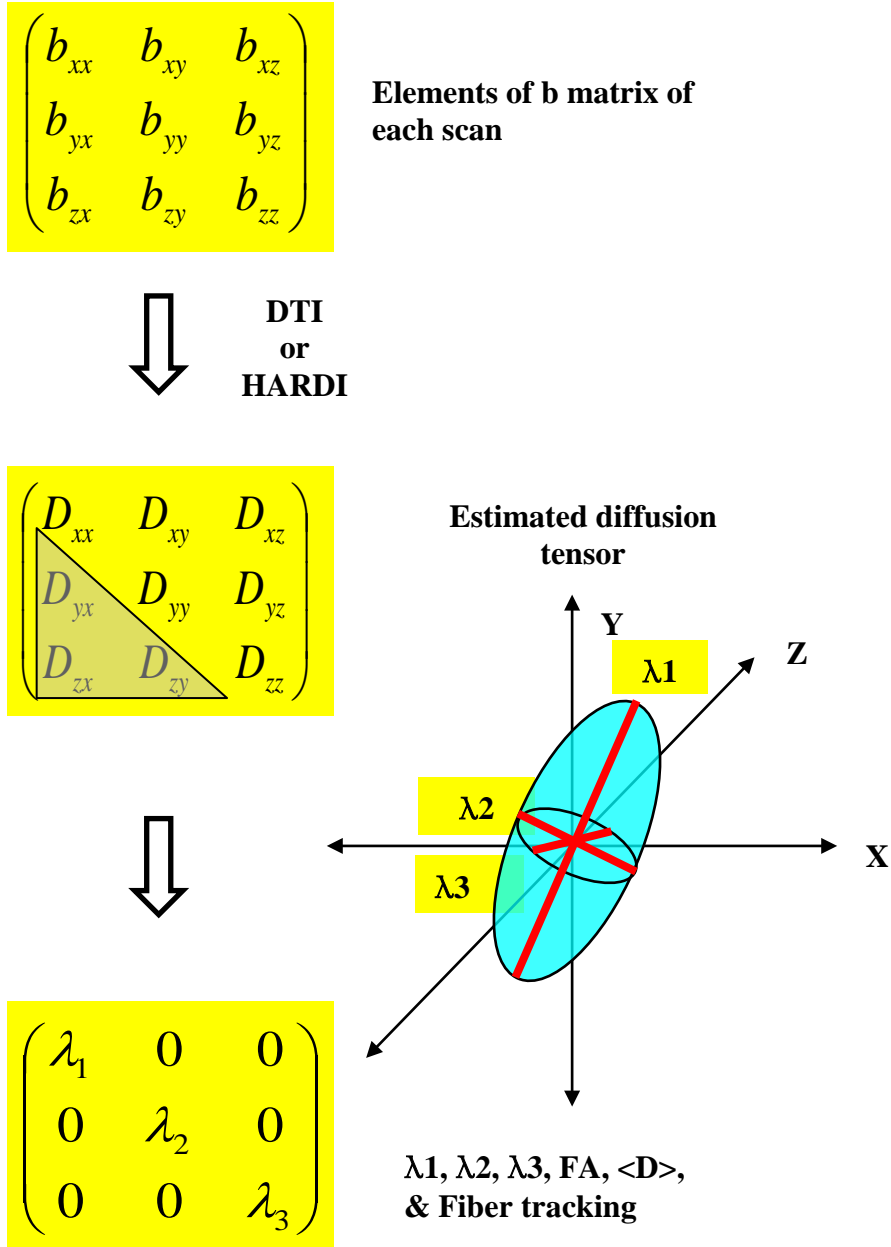


Figure 1-2. A schematic diagram showing procedure extracting information from diffusion weighted images. Since positive and negative displacement of diffusing agents are indistinguishable, the opposite pole symmetry of the diffusion tensor and b matrix is required. A diffusion encoding gradient applied in an arbitrary direction determines an antipodal symmetric b matrix. Seven scans including a minimum of 6 b-value directions are required to generate the complete diffusion tensor.

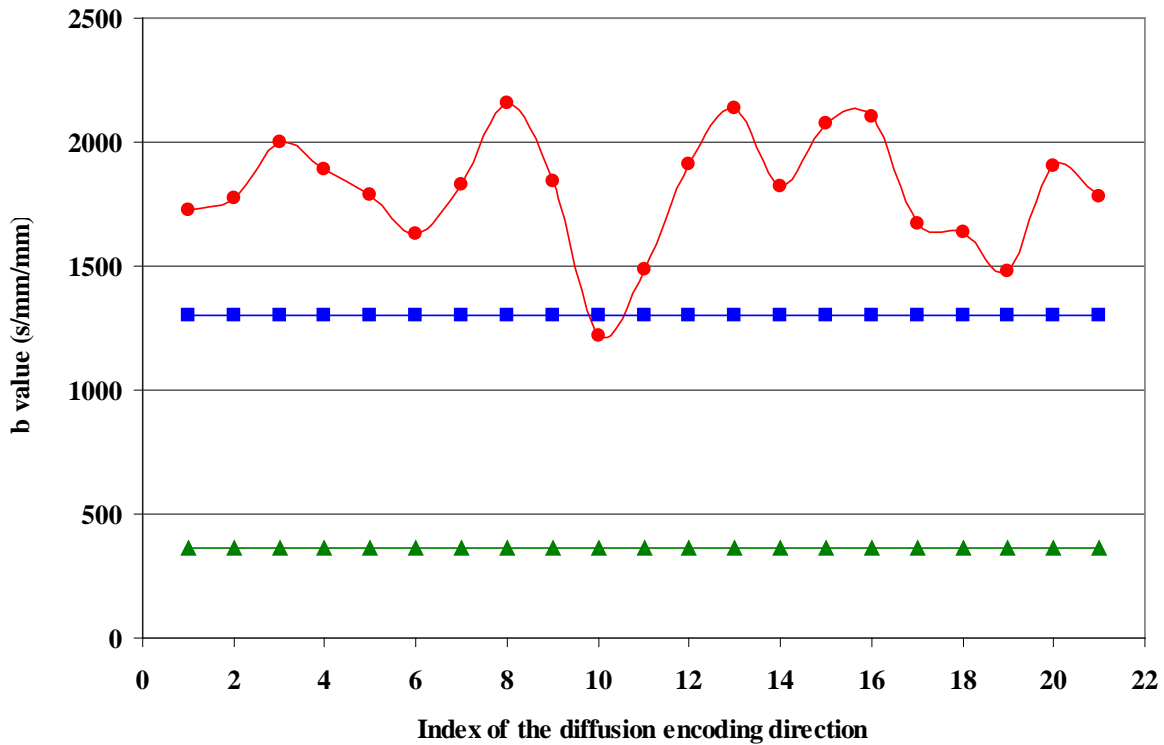


Figure 1-3. Diffusion sensitizing factor modulated by the imaging gradients and the cross terms. Red (circle) is the effective b-values seen by protons during diffusion experiment. Blue (square) is the b values determined by the diffusion encoding gradient alone ( $\Delta = 13.4$  ms,  $\delta = 1.8$  ms). Green (triangle) represents contribution of imaging gradients alone, determined by the RF pulse of 2 ms to achieve a high resolution of  $60 \mu\text{m} \times 60 \mu\text{m} \times 500 \mu\text{m}$  (slice thickness). Duration and strength for each crusher gradient are 2 ms and 50 % of a maximum intensity available, respectively.

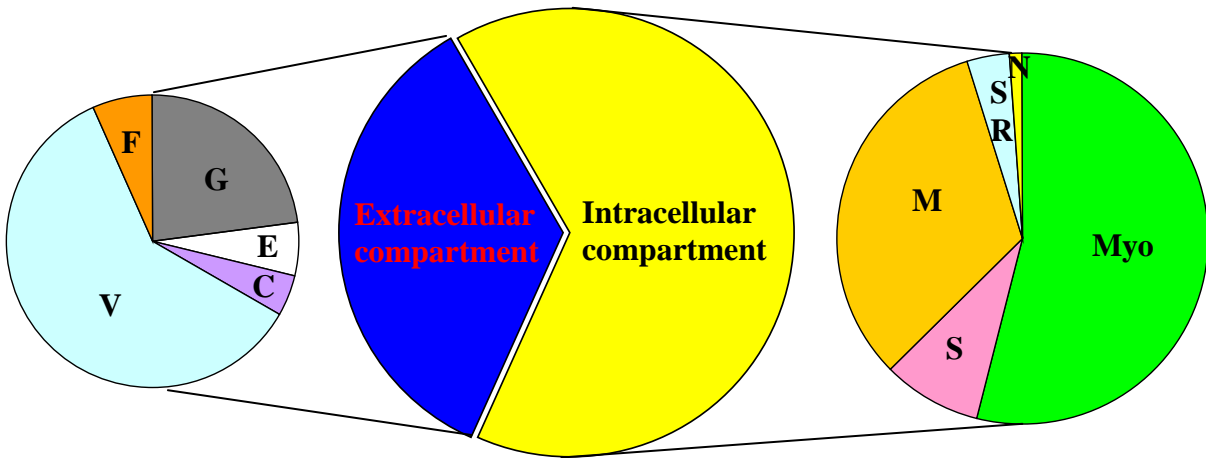


Figure 1-4. A schematic diagram of relative distribution of tissue compartments and their elements in the heart. V: vascular space; F: connective tissue; G: ground substance; E: empty space; C: collagen in the extracellular space. Myo: myofibrils; S: sarcoplasm; M: mitochondria; SR: sarcoplasmic reticulum; N: nucleus in the intracellular space

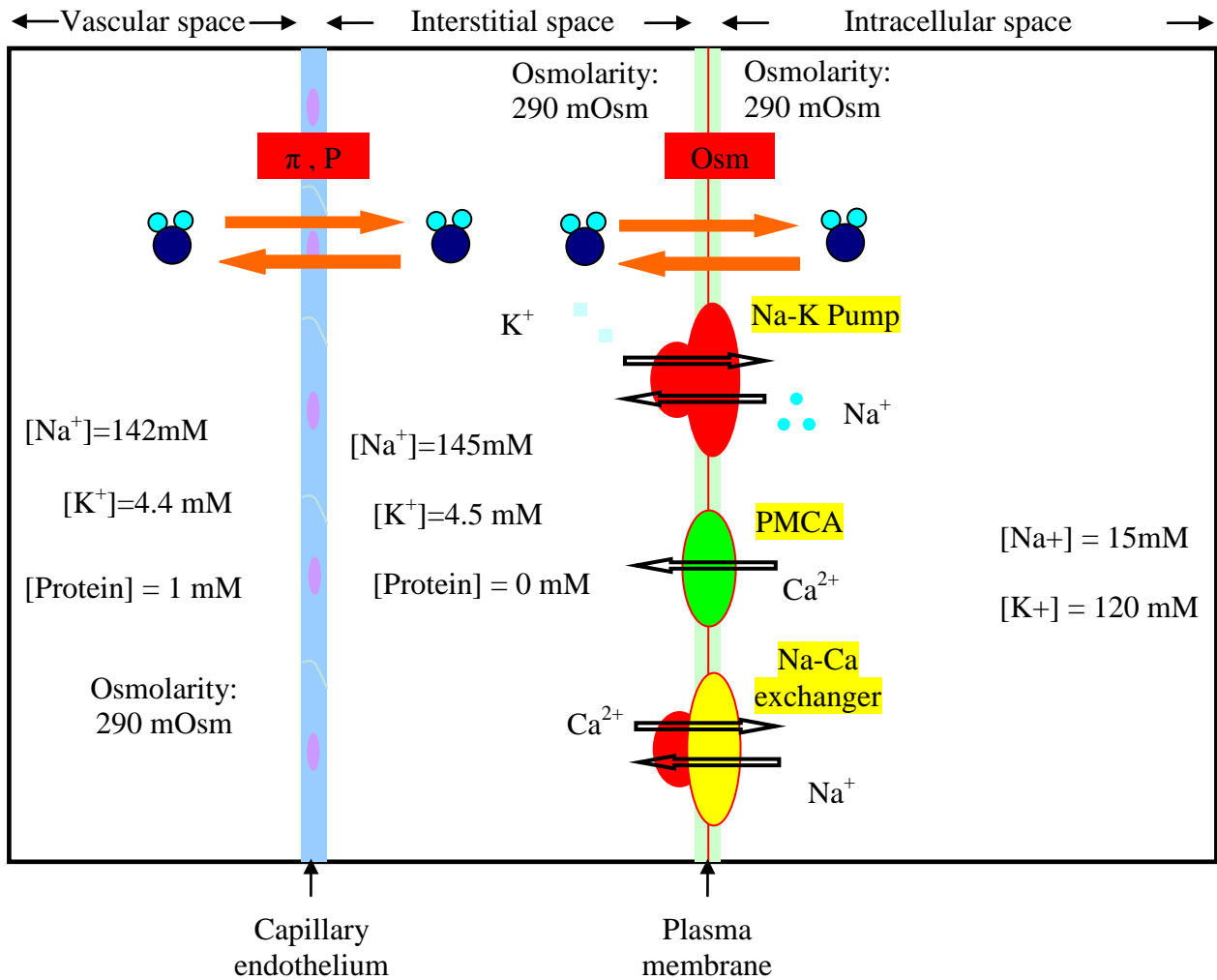


Figure 1-5. A schematic diagram showing compartmentalization and transport of the water molecules in the cardiac tissue.  $\pi$ : oncotic pressure across capillary endothelium, P: hydrostatic pressure across capillary endothelium, Osm: osmolarity, PMCA: plasma membrane  $Ca^{2+}$  ATPase.

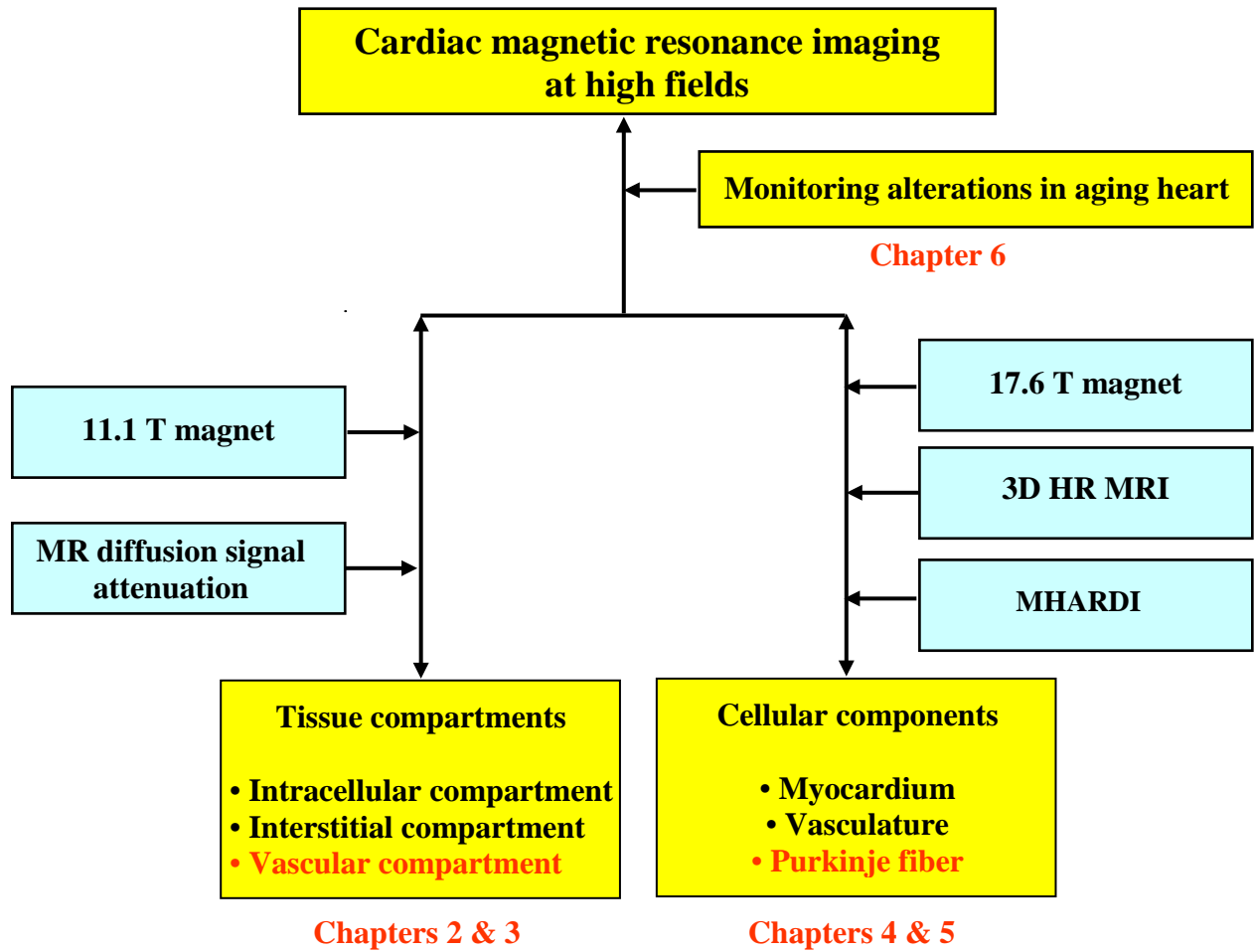


Figure 1-6. A schematic diagram showing the specific aims to achieve the goal in this thesis.

## CHAPTER 2 HARDWARE FOR CARDIAC DIFFUSION WEIGHTED MR IMAGING

### **Introduction**

Diffusion-weighted magnetic resonance (MR) imaging using a spin echo places two diffusion encoding gradients on either side of the refocusing radio frequency (RF) pulse in order to relate the randomly moving water molecules to the microstructure in cardiac tissue. As stated in the previous chapter, the apparent diffusion coefficient (ADC) in cardiac tissue shows the multi-exponential behavior as a function of b-values. Thus heavy diffusion weighting is required to conduct the experiment to examine the tissue compartmental sources responsible for the ADC (Inglis et al., 2001). Since the heavy diffusion-weighted imaging gathers significantly low signal from the region of interest and is susceptible to non-diffusional motion, resulting in incorrect interpretation of the acquired signal, methods to prevent or correct those problems should be employed (Clark et al., 2000). Perfusion system is an indispensable part to maintain the tissue viability during diffusion imaging and further to control direct flow in the vascular space of isolated rabbit heart (Aliev et al., 2002; Forder et al., 2001; Gamcsik et al., 1996).

In this chapter, we introduce an experimental setup that is developed to perform the desired diffusion-weighted MR imaging of isolated rabbit hearts using the horizontal-bore 11 T magnet (Magnex Instrument Inc., UK; Bruker Instrument console, Billerica, MA). This setup contains 1) a birdcage RF coil giving acceptable signal to noise ratio (SNR) with appropriate filling factor for the isolated rabbit hearts, 2) a compact, reusable, and portable perfusion system equipped with a temperature controller and a flow controller, 3) and a long cradle fitted with a minimum margin into a gradient coil allowing sufficient diffusion gradient strength to obtain desired images.

## Diffusion Gradient System

Because of the central role of the diffusion encoding gradients, there is a need for hardware that is capable of providing stable gradients of the utmost intensity for proton diffusion-weighted MR imaging. The degree of diffusion weighting is primarily determined by the diffusion gradient intensity and the diffusion gradient duration. From the Stejskal and Tanner expression (Stejskal and Tanner, 1956), the diffusion gradient duration and the diffusion time contributes significantly to the calculated b-value. Hence to control the time appears to be no less effective approach than to do the intensity. However, since long diffusion time is likely to result in too much signal loss in the pulsed gradient spin echo (PGSE) sequence, measurement of the restricted diffusion, and complicated effect of different transverse relaxation times of the tissue compartments, short diffusion time should be favored. In addition, a long diffusion gradient can produce additional phase shifts by diffusion occurring during the gradient duration, which is usually ignored. Consequently, increasing diffusion gradient strength is an effective approach to avoid the attenuated signal from being complicated to analyze at the same time of obtaining desired high b-values.

Since individual gradient has a limit to a maximally tolerable gradient strength determined depending on its own configuration, the b-value that each gradient can provide also has an upper limit. Accordingly, the gradient intensity may run short of the desired heavy diffusion weighting. Table 2-1 compares the two gradients, the BGA12-S and the BGA6-S, which are available for cardiac diffusion imaging using the 11.1 T magnet. The BGA12-S allows only b values up to  $2000 \text{ s/mm}^2$  with 13.4 ms of big delta and 1.8 ms of small delta. Given the diffusion gradient timing, a maximal b value that the BGA6-S permits is approximately 2.8 times as large as one that the BGA12-S permits. Thus BGA6-S was selected for diffusion-weighted imaging to discern change in cardiac tissue compartments. The

subsequent lack of gradient power could be compensated by using somewhat long gradient pulses. But the resulting effects upon echo time, and diffusion mixing time (detailed in chapter 1) would need to be addressed.

### **A Linear Birdcage RF Coil**

As an antenna transmitting the B1 excitatory field to the sample and receiving the signal generated by the Faraday induction, sensitivity and homogeneity of the radio frequency (RF) coil are key factors for diffusion-weighted MR imaging. The thumb of rule with respect to the RF coil is one specifically optimized coil to accomplish an individual imaging project. Thus we fabricated a RF coil to achieve our aim for the understanding of tissue compartments perform the desired diffusion MR imaging. Even though high signal to noise ratio (SNR) is always preferred, we intended to fabricate an RF coil that fits geometrically the gradient selected for diffusion weighted imaging with an acceptable SNR at the heavy diffusion weighting up to 6500 s/mm<sup>2</sup>. Sufficiency of field homogeneity zone, providing adequate field of view, was checked using a phantom.

Figure 2-1 shows an RF coil fitted within the 60 mm inner diameter that the BGA6-S gradient permits to other elements comprising the diffusion experimental setup. The B1 field from the RF coil was configured to be orthogonal to the main magnetic field direction. A linear birdcage RF coil with a 32 mm diameter, geometrically fitting the isolated heart to a perfusion container, was designed both to transmit the B1 field and to receive the proton MR signal from the tissue.

Figure 2-2 shows schematically the procedure to fabricate the linear birdcage coil. The RF coil has eight legs and a length-diameter ratio of 0.7, achieving the maximum sensitivity of the coil in the middle plane (Figure 2-7, B) (Hasse et al., 2000). The coil thus could give an acceptable SNR and B1 field homogeneity within the desired field of view (FOV). Sixteen

capacitors of 2.17 pf were soldered to connect either end of the eight legs and the end ring segments made up of 3 mm wide copper tapes, which make the RF coil a low pass birdcage type (Tropp, 1997). As a result, the homogeneous mode of the linear low-pass type birdcage RF coil could be tuned to 470 MHz. The impedance of the RF coil was then matched to 50  $\Omega$  using an LC matching circuit that serially connected to a leg with one end. Since tuning and matching the RF coil to the desired resonance frequency is very sensitive to loading condition of the measured sample in the magnet, the phantom or isolated rabbit heart that was immersed in the STH cardioplegic solution was used continuously during the bench work. The tuned/matched RF coil was coated with a sealing spray to prevent failure of the circuit caused by any perfusate leak that might occur during the imaging and was mounted firmly on the carrying cradle with a hardened epoxy. The SNR from tissue at diffusion weighting of b-value of 6500 s/mm<sup>2</sup> was examined to avoid an incorrect estimation of the fast and slow components, caused by a too low diffusion-weighted MR signal.

### **Perfusion System for Diffusion-Weighted Imaging**

The perfusion system that previously used to prepare an isolated working heart was utilized with a modification (Gamcsik et al., 1996) to isolate rabbit heart (Figure 2-3) and to perform its diffusion-weighted MR imaging (Figure 2-4). In order to maintain aortic pressure under conditions closely mimicking the in vivo environment, the perfusion system was equipped with a membrane oxygenator, a flow controller, and a temperature controller (Figure 2-3). The oxygenator is composed of three sections: the coil prewarming of the perfusate, the silicone membrane semipermeable to the gas, and a bubble trap. These enable the oxygenator to sustain a isolated heart with minimal loss of physiological performance. During the rabbit heart, the nutrient buffer solution, the Krebs-Henseleit solution, was saturated continuously with 95% O<sub>2</sub>/5% CO<sub>2</sub> gases to maintain oxygen tension at >600 torr, and keep pH at 7.4. The performance of

the heart could be continually monitored by a pressure transducer and a flow meter. Due to the sensitivity of diffusion imaging of the beating heart, the isolated rabbit heart was arrested by switching the buffer solution with the STH cardioplegic solution before it was moved into the magnet.

Then the isolated arrested heart was promptly delivered into a perfusate container in a portable perfusion system (Figure 2-4). This portable perfusion system continuously perfused with the STH cardioplegic solution could carry the isolated heart into the magnet room without rendering global ischemic condition. The system enabled to control the direct perfusate flow at the same time of maintaining tissue viability throughout the diffusion experiment. This experimental setup was also equipped with a compact, reusable membrane oxygenator, a flow controller, and a temperature controller with appropriate tubing connected. With this perfusion system, the distance from the oxygenator to the perfused isolated heart could be kept at a minimum. This would keep oxygenation and warming of the perfusate immediately prior to delivery to the tissue relatively constant, therefore eliminating problems with heat or oxygen loss that may result from a long perfusion line. This perfusion system enabled diffusion-weighted imaging of isolated rabbit heart, maintaining viability, for up to eight hours.

A reward using the portable perfusion system equipped with a bubble trap is to prevent tissue from being embolized due to air bubble formation. The gas solubility of the buffer that immersed the sample within the magnet bore (21°C) and one of perfusate at exit (39°C) from a reservoir were estimated to be 8.98 and 6.65 mg/L, respectively, using an empirical equation (Schumpe et al., 2004). The solubility gap of 2.33 mg/L might result in bubble formation. In addition, microbubbles in the perfusate or the reservoir may converge by a pulsed flow controller. If these happen, the bubbles within the perfusate tube could easily enter the left

ventricle through the cannulated aorta and might bring about an ischemic condition in the ventricular wall. The trapped bubbles also interferes with the magnetic field applied to the surrounding tissue, resulting in image artifacts caused by a susceptibility mismatch at the discrete boundaries. With water at 39°C circulating through the water jacket in the membrane oxygenator, which was placed as close to the isolated heart as possible, no bubble formation was found during the diffusion measurements. This system was also versatile for diffusion-weighted imaging of heart slices using the 14.1 T or 17.6 T vertical bore magnet (Bruker console, Billerica, MA) with simple modifications.

### **A Long Cradle Immune to Gradient-induced Motion**

Image artifact induced by the gradients is a problem inherent to MRI (Clark et al., 2000; Dou et al., 2002; Ma et al., 2008). In comparison with the imaging gradients used for spatial mapping of the MR signal, the diffusion encoding gradient intensity is applied much stronger (Le Bihan, 1995). A common artifact of diffusion-weighted MR imaging springs from non-diffusional motion caused by vibrating or jiggling diffusion gradients (Gamper et al., 2007; Leemans and Jones, 2009; Ma et al., 2008). When heavy diffusion weighting is required, the dark effect of the diffusion encoding gradients becomes more significant, spoiling the reconstructed MR images. Further, the local eddy currents by steep increase of the diffusion gradient may interfere with the homogeneous magnetic field, resulting in low image quality. The eddy currents can be removed or eliminated by using the diffusion gradients that has a decent slew rate or compensatory shapes to make the eddy currents even out (Le Bihan, 1995).

Figure 2-5 shows sample movement that was observed in diffusion weighted MR images. Diffusion weighted images measured with b values above 2000 s/mm<sup>2</sup> show the change in ventricular shape of a transverse slice or shift of interested pixels. Under the diffusion gradient intensity of 500 mT/m giving a b value of 2000 mm<sup>2</sup>/s, microscopically diffusing water

molecules in track might be liberated from a pixel of interest because of the macroscopic movement. This might lead to an incorrect estimation of the fast/slow components of the diffusion signal. Since phase modification might vary depending on individual diffusion encoding directions, the motion can cause an incorrect estimation of the diffusion tensor. A post-imaging correction algorithm, including translation and rotation, might be a solution to handle the motion during the imaging. However, how to register individual diffusion weighted images is still left to be solved. The b matrix of a shifted pixel might also need to be corrected (Leemans and Jones, 2009; Wedeen et al., 1994).

Imaging gradients might also cause signal contamination associated with sample motion during refocusing of the excited slice and data acquisition. Imaging gradients (Hz/mm) in read-out direction and in slice direction are determined by the ratio of the sampling bandwidth (Hz) and the field of view (FOV; mm), and the ratio between bandwidth of the refocusing RF pulse (Hz) and slice thickness (mm), respectively. These parameters are handled by expert users within a tolerable minimum FOV and a minimum slice thickness. The Bruker console also has set a maximum gradient strength, 62,300 Hz/mm (1470 mT/m). Moreover, the possibility of motion may increase as resolution increases.

An initial diffusion MR imaging using a short cradle, tightly fitted to the inner surface of the gradient coil, was not of success because it could still vibrate coherently with the gradients. An animal positioning system was previously designed to provide robust support to an animal cradle and a RF coil against acoustic vibrations generated by the gradients and other sources (Ma et al., 2008). A long bore tube of the system was supported at either end via brackets attached directly to the exterior of the bore magnet. Four foam 'donut' shaped gaskets were also used to dampen acoustically induced vibrations of the bore tube (Ma et al., 2008). This design could

place consistently the region of interest within the homogeneous center of the magnetic field. However, since mechanical works such as drilling and threading would require modification of exterior sides of the bore magnet, we instead tried to isolate the cradle of a perfusate chamber and a RF coil from both the gradients and the bore magnet in order to eliminate motion induced problems during diffusion-weighted MR imaging, which could ensure diffusion-weighted MR signal from a biological sample immune to jiggling or vibrating gradients. A mechanical arm such as a cantilever, fixed in an exterior side of the bore magnet, was also avoided due to a long length of the horizontal magnet (2.7 m), which might result in a bended arm inside the gradients.

Motion-free imaging was achieved using the fiberglass tubes (Max-Gain Systems, Marietta, GA) a little longer than the magnet bore (Figure 2-7). Due to special delivery issues of a cradle longer than 2.43 m, two fiberglass tubes each having a length of 0.56 m and 2.43 m had to be joined together with an epoxy (West System, Bay City, MI) with a third and smaller cradle sleeved to give strong support and prevent bending of the joined cradle. The joined cradle, with a length of 3.75 m and a width of 8.9 cm, could isolate the isolated hearts and perfusion line from the gradient coil (Figure 2-8). The setup could also be detached from the magnet bore using a modified tripod at either end of the horizontal magnet bore. Part of a length of 30 cm in the middle of the cradle was cut a in-plane half out to mount a RF coil and connect the perfusion tube into a chamber holding a isolated heart. As a result, diffusion weighted images measured using 6 b values up to  $5000 \text{ s/mm}^2$  showed no shift of selected ROIs (Figure 2-6). No movement was observed during high resolution diffusion tensor MR imaging (DTI) of isolated and fixed rabbit heart measured using a b value of  $2000 \text{ s/mm}^2$  and the high angular resolution diffusion imaging (HARDI) of in vivo rat brain measured using a b value of  $1000 \text{ s/mm}^2$  (Figure 2-9).

Table 2-1. Gradient system suitable for heavy diffusion weighted imaging.

	Inner diameter (mm)	Maximum tolerable intensity on an axis (mT/m)	b value benefit (no unit)
BGA6-S	60	350	2.8
BGA12-S	116	210	1.0

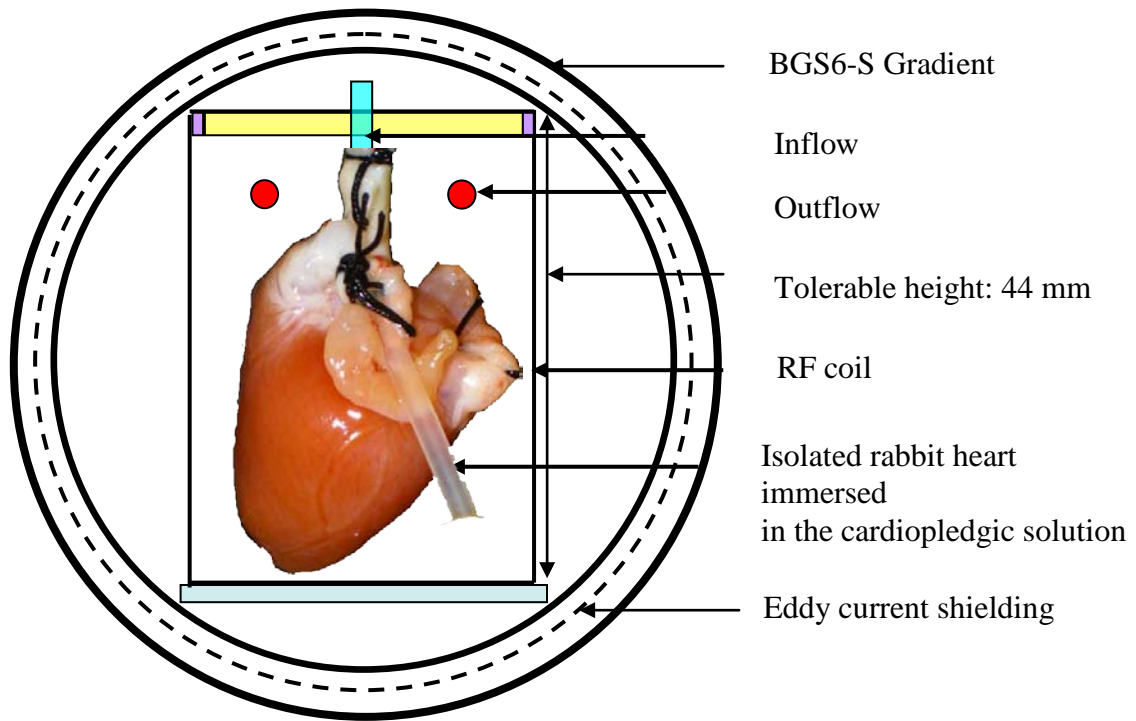


Figure 2-1. A schematic transverse view showing configuration of components for imaging within the gradient coil, the BGA6-S.

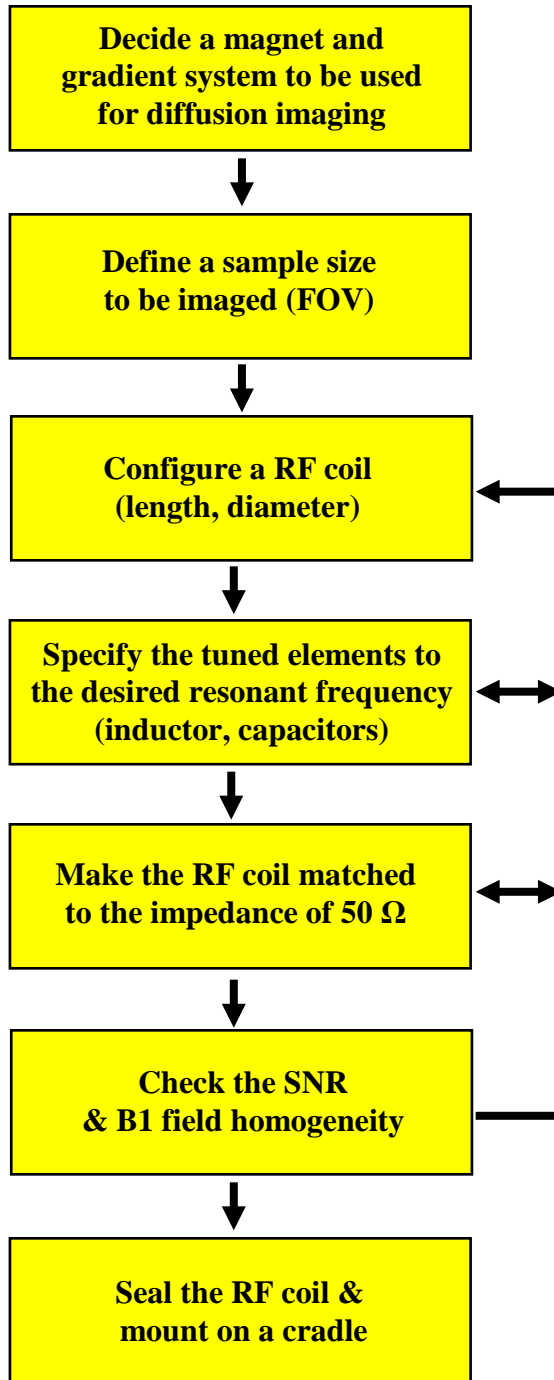


Figure 2-2. A schematic procedure to fabricate a linear birdcage RF coil for diffusion MR imaging of isolated rabbit heart.

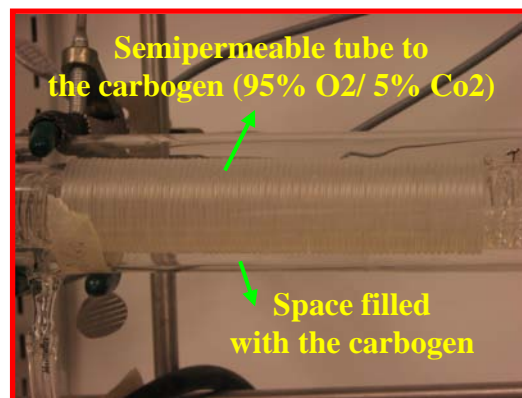
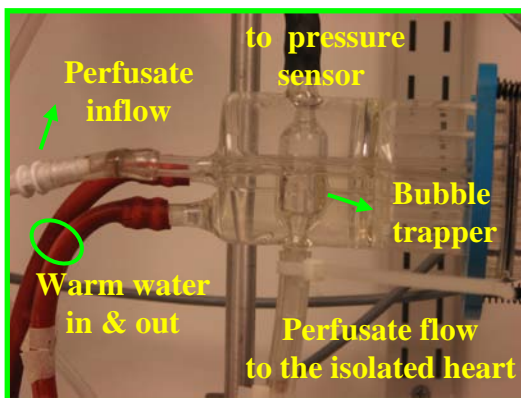
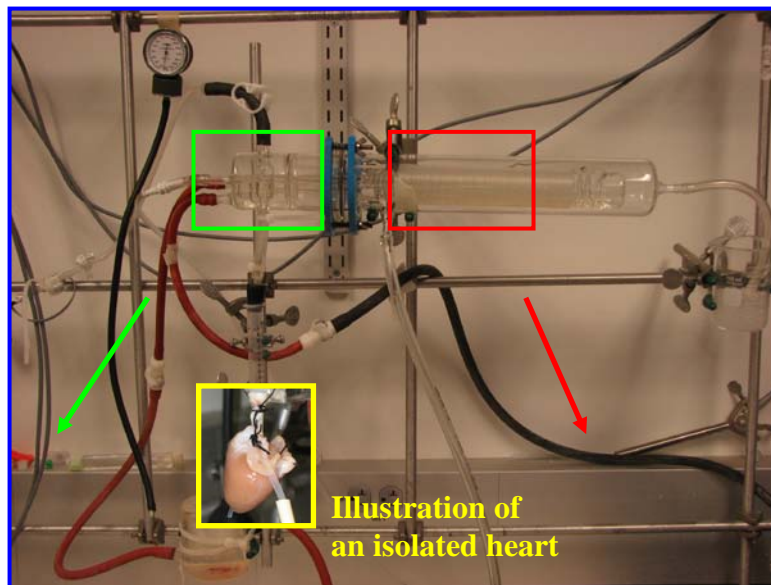
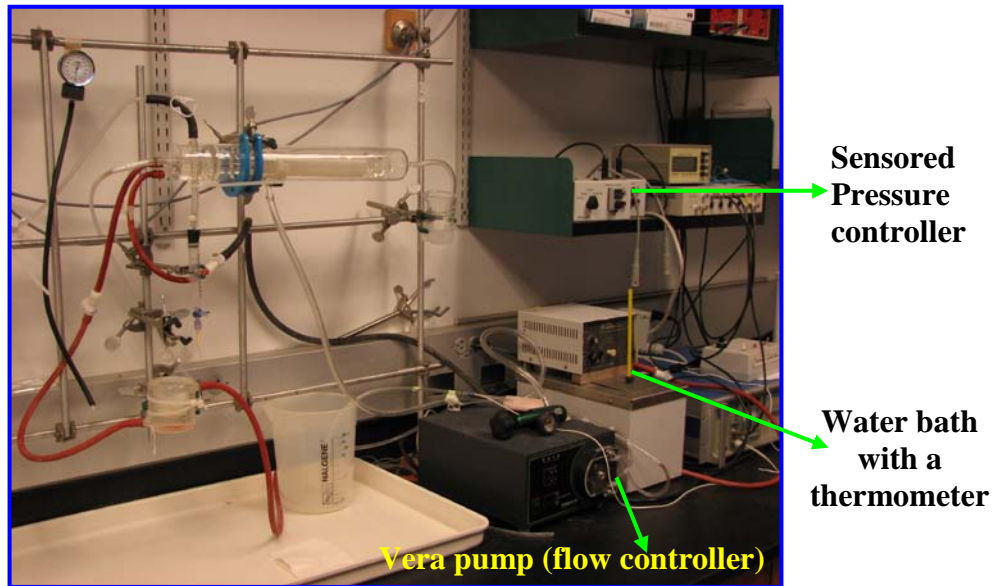


Figure 2-3. Perfusion system for isolated rabbit heart preparation.

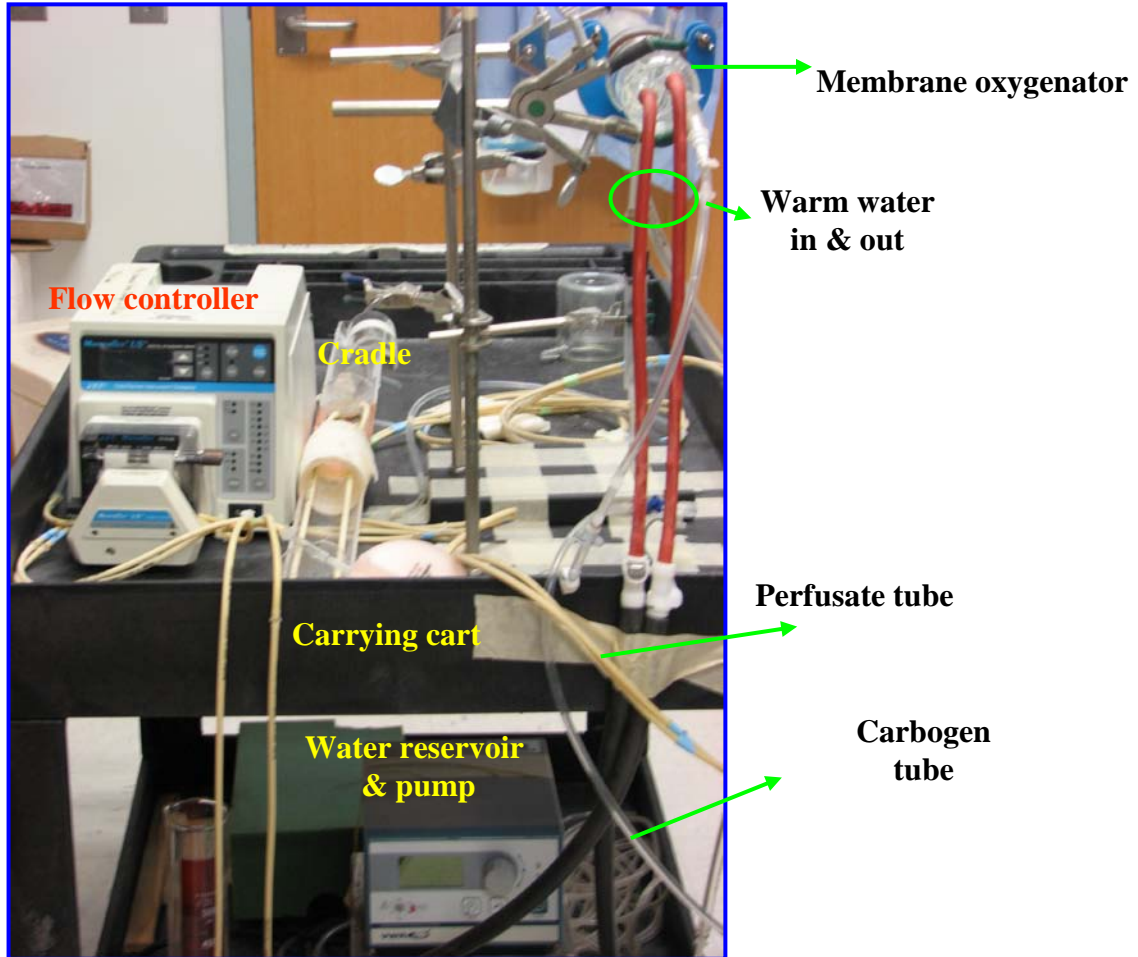


Figure 2-4. Portable perfusion system for diffusion imaging of the isolated, perfused rabbit heart.

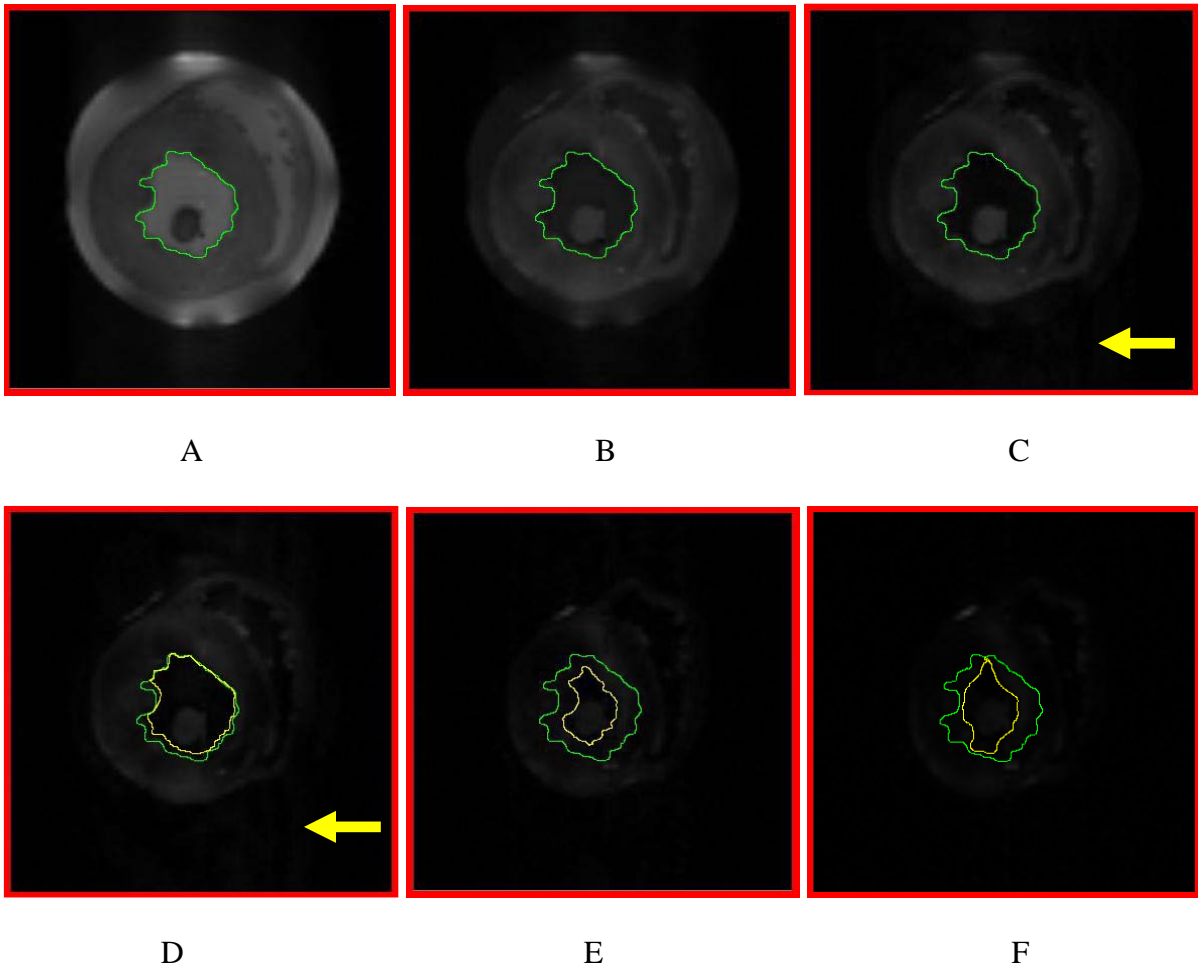


Figure 2-5. Diffusion weighted MR images of a fresh rabbit heart showing motion that occurs during diffusion measurements. A) Image measured without the diffusion gradients. B) Image using b value of  $1000 \text{ s/mm}^2$ . C) Image using b value of  $1400 \text{ s/mm}^2$ . D) Image using b value of  $2000 \text{ s/mm}^2$ . E) Image using b value of  $3000 \text{ s/mm}^2$ . F) Image using b value of  $4500 \text{ s/mm}^2$ . Note image D at  $b = 2000 \text{ s/mm}^2$  shows motion-induced artifact in the vertical phase encoding direction (yellow arrow). Images A, B, and C show the left ventricular space kept unaffected (arbitrary shape in green). Images E and F show significant changes in the size and shape of the left ventricular chamber (arbitrary shape in yellow).

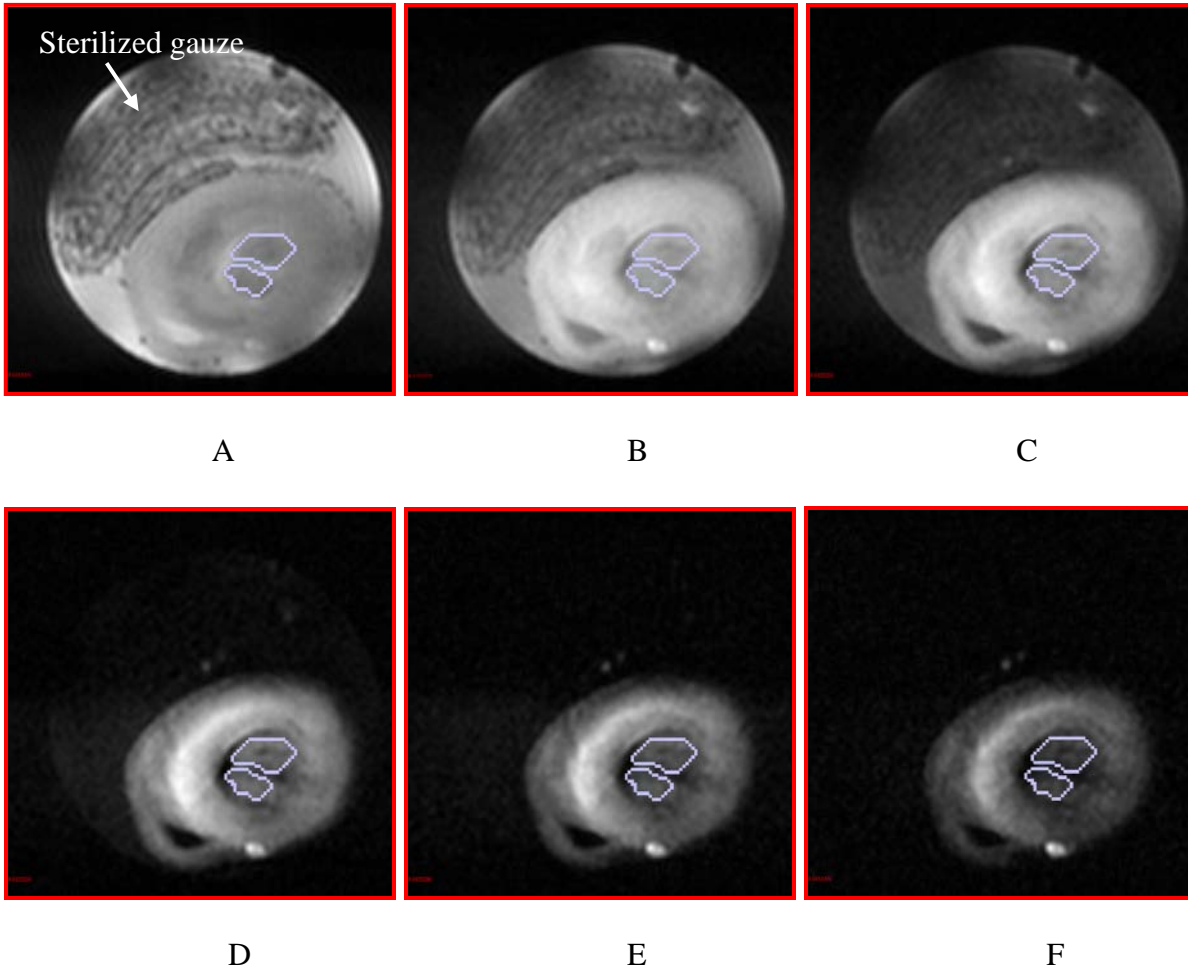


Figure 2-6. Motion-free MR images of a fixed rabbit heart isolated by the long cradle. A) Image measured without the diffusion gradients. B) Image using b value of  $620 \text{ s/mm}^2$ . C) Image using b value of  $1000 \text{ s/mm}^2$ . D) Image using b value of  $2000 \text{ s/mm}^2$ . E) Image using b value of  $3000 \text{ s/mm}^2$ . F) Image using b value of  $4500 \text{ s/mm}^2$ . The ROIs were selected from the two papillary muscles in the left ventricle. Sterilized gauze was used to prevent isolated heart from moving or floating in the perfused bath. A bright spot shown in the bottom of each image is suspected as fat tissue that exists in the inter-ventricular groove.

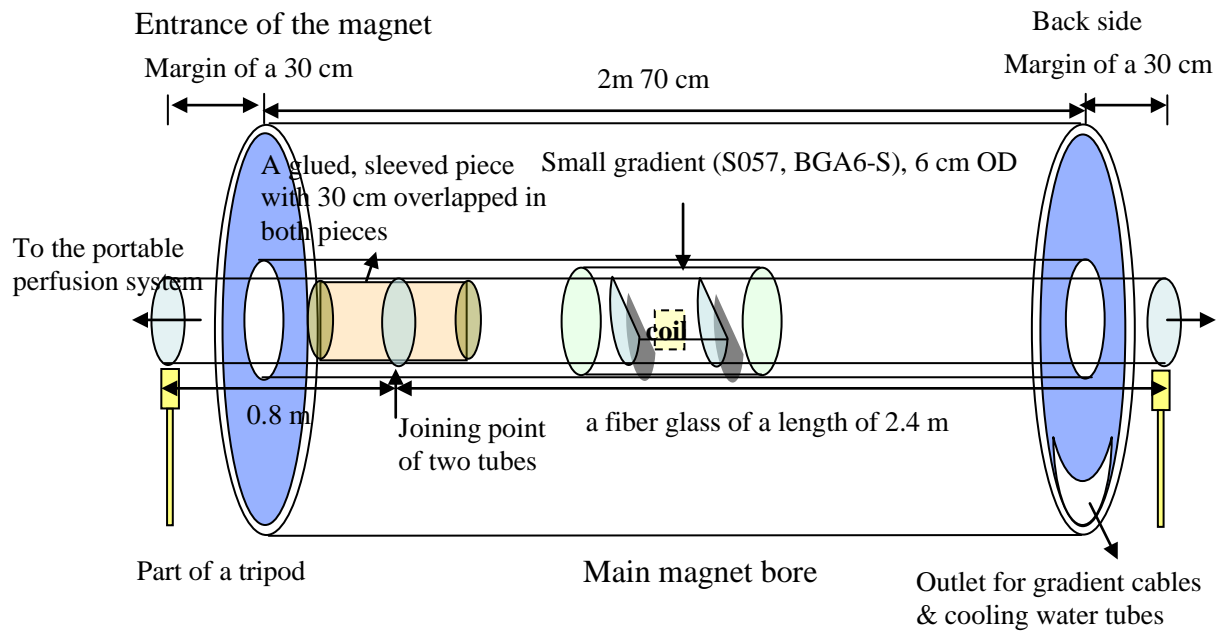


Figure 2-7. A schematic diagram of a long cradle isolated from both the gradient and the magnet bore in the horizontal 11 T magnet system.

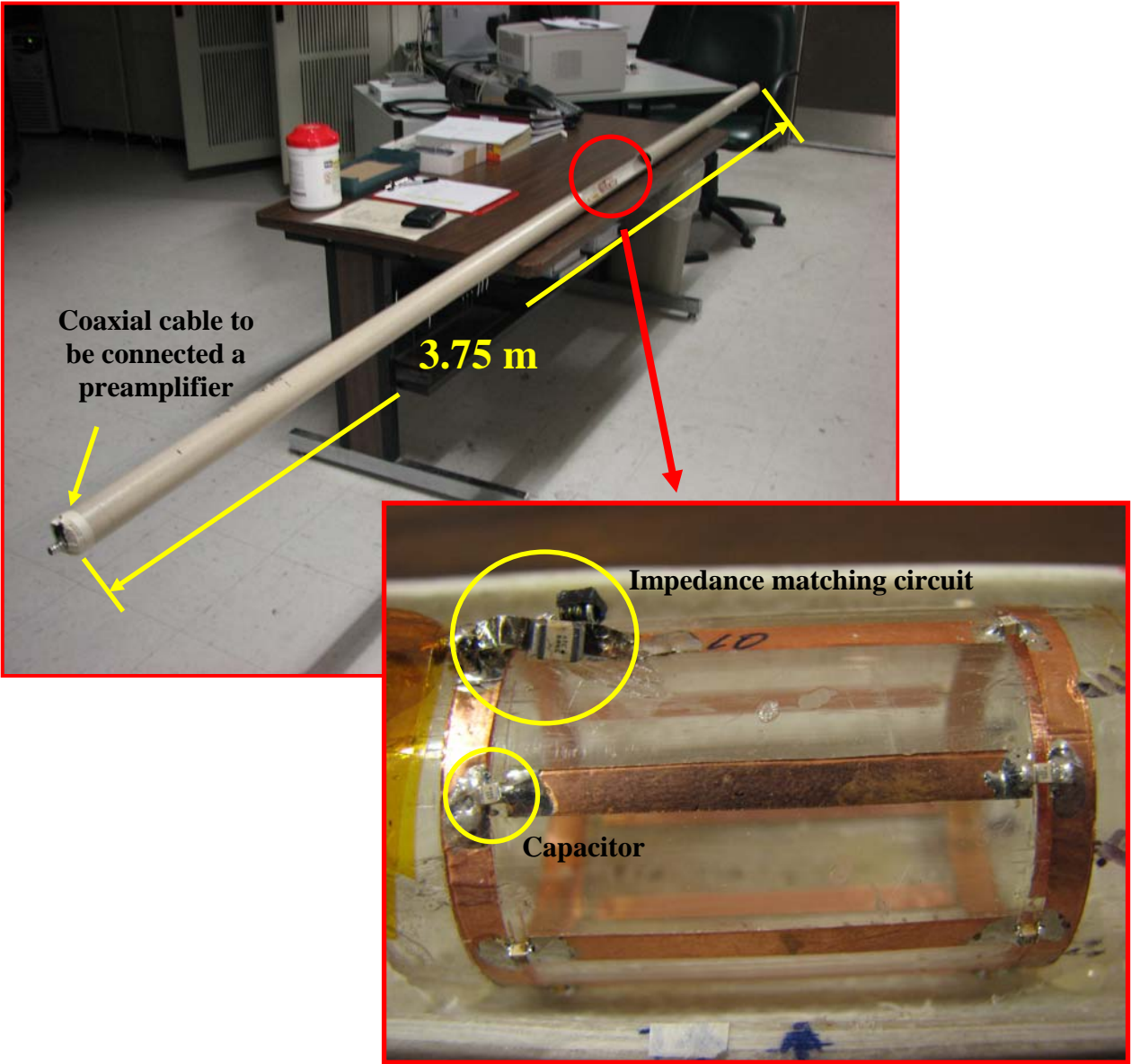


Figure 2-8. A long cradle for cardiac diffusion weighted imaging and a birdcage RF coil mounted on the cradle.

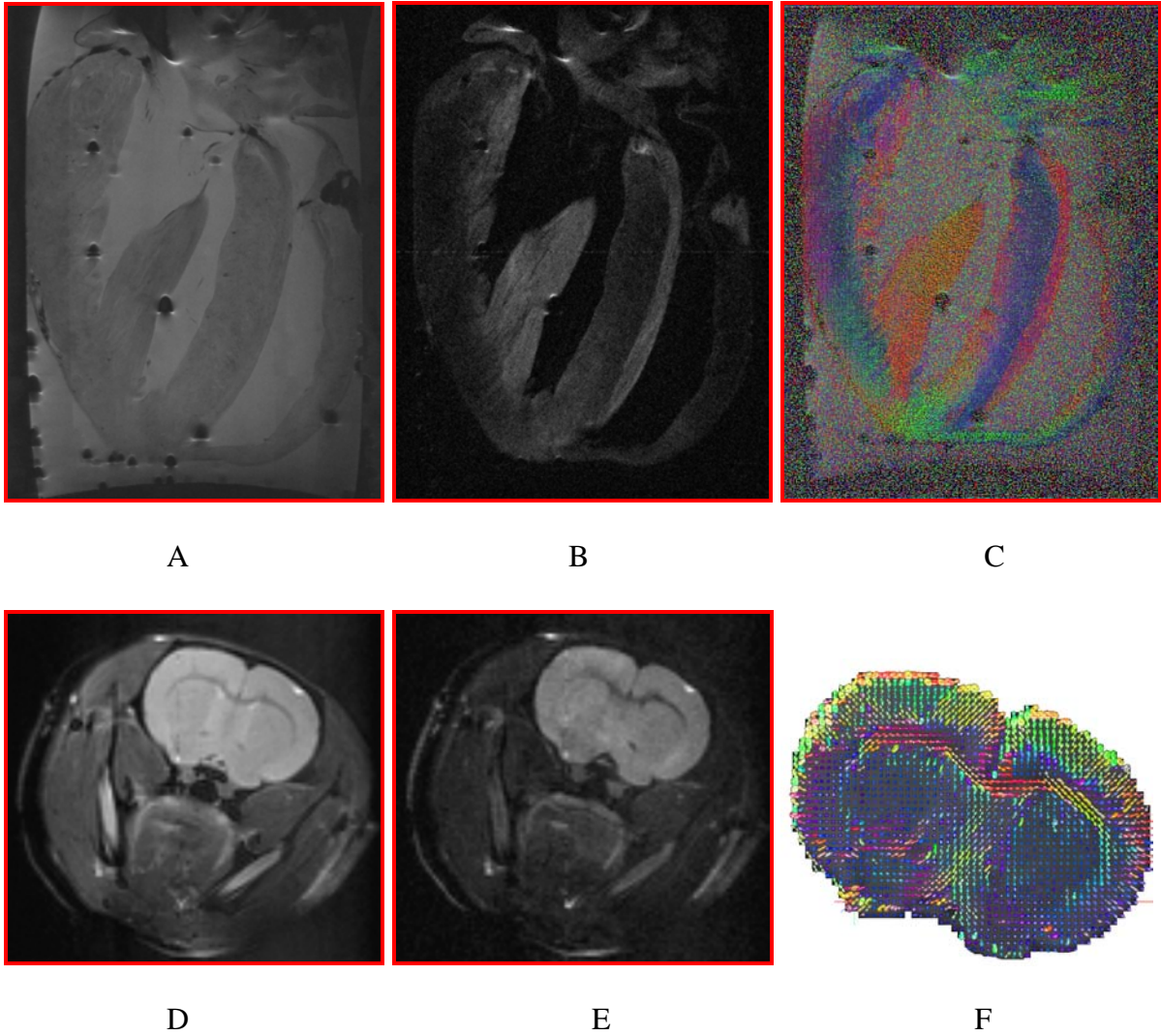


Figure 2-9. DTI of isolated rabbit heart measured using a b value of  $2000 \text{ s/mm}^2$  and HARDI of in vivo rat brain measured with a b value of  $850 \text{ s/mm}^2$ . A) An intensity image without diffusion gradient of an isolated rabbit heart. B) Diffusion weighted image of an isolated rabbit heart. C) Primary eigen vector map of an isolated rabbit heart. D) An intensity image without diffusion gradient of a rat brain. E) Diffusion weighted image of a rat brain. F) Primary eigen vector map of a rat brain.

## CHAPTER 3 CONTRIBUTION OF CARDIAC TISSUE COMPARTMENTS TO THE MR DIFFUSION SIGNAL

### **Introduction**

Imaging the diffusion of water molecules in biological tissues by magnetic resonance (MR) has emerged as a powerful imaging tool. The macroscopic and quantitative diffusion maps of water molecules provided by diffusion magnetic resonance imaging (MRI) infer non-invasively information about the microstructure in the biological tissues. Recent reports have shown that multi-compartmental diffusion imaging may eventually have direct clinical application (Collins et al., 2007; Wu et al., 2006). Diffusion MRI also reveals the details of anatomic microstructure of the myocardium, contractile cardiac tissue that plays important roles in both mechanical and electrical functions of the ventricles, influencing electrical depolarization, tissue perfusion, and myocardial contraction (Helm et al., 2005; Kanai and Salama, 1995; Scollan et al., 2000) in a non-invasive and efficient method previously unavailable. It correlates the primary eigen vector of water diffusion with myocardial fiber orientation (Hsu and Henriquez, 2001; Hsu et al., 1998a) and the secondary direction of the water diffusion with the laminar structure (Dou et al., 2003; Helm et al., 2005).

Since a sharp drop in the apparent diffusion coefficient (ADC) of water, just minutes after an onset of the ischemic event in the infarcted region of brain was reported in the early 1990s (Moseley et al., 1990; Moseley et al., 1990b), the origin of the MR signal of water diffusion observed in the biological tissues has been of considerable interest to MR researchers (Assaf and Cohen, 1998b; Buckley et al., 1999a; Buckley et al., 1999b; Norris, 2001). Hence, many experimental studies to date have been performed using a variety of biological tissues, i.e., brain neural tissues, cell aggregates, and myocardium.

It has been reported that the ADC of water in tissues is non-monoexponential in nature when measured with sufficiently high  $b$  values up to  $40,000 \text{ s/mm}^2$  (Buckley et al., 1999a; Bui et al., 1999; Niendorf et al., 1996; Pfeuffer et al., 1999). Interestingly, most data contributing to an understanding of the mechanism of diffusion have been very well fitted with a biexponential function corresponding to two water diffusion pools with a fast and a slow diffusion coefficient in slow exchange assumption (i.e., when the water molecules remain in each compartment during the diffusion time) (Assaf and Cohen, 1998b; Buckley et al., 1999a; Buckley et al., 1999b; Niendorf et al., 1996). An ensemble of experimental findings have demonstrated that the change of volume fractions of the intracellular and extracellular spaces that results from cellular swelling and shrinking always leads to variations of the ADC (Assaf and Cohen, 1998a, 1998b; Buckley et al., 1999a; Buckley et al., 1999b). For instance, Buckley et al. (1999a) observed the global ADC decrease in perfused rat hippocampal slices treated with ouabain, a polycyclic glycoside that promotes cell swelling by inhibition of the membrane-bound Na-K ATPase, and showed that the overall decrease results from the relative increase of the slow diffusion component rather than from the change of the slow and fast diffusion coefficients.

The early view that the fast and slow diffusion components might correspond to the intracellular and extracellular compartments--or at least provide an index of those compartment sizes and their changes under perturbation--became more complicated by research conducted using N-acetyl aspartate (NAA) (Assaf and Cohen, 1998a) and the oocyte (Sehy et al., 2002). The results suggested that the intracellular space has two populations of the fast and slow components, which is a convincing explanation for the disagreement between the calculated volumes of intracellular and extracellular compartments with accepted values shown in the early studies. Le Bihan (2007) hypothesized through a conceptual model that the ADC decrease

observed in tissues containing swollen cells might result from the increase of “the membrane-bound highly structured water,” which may be principally responsible for the slow diffusion component at the expense of unbound water in the intracellular/extracellular spaces. But the boundary layer of slow diffusion at the membrane of the cell was not observed in diffusion weighted imaging of a single cell (Aguayo et al., 1986; Bowtell et al., 1995; Grant et al., 2000; Grant et al., 2001; Hsu et al., 1997). Hence, assumptions used in the model are still matter of discussion.

Other studies describing water diffusion in tissue have also proposed that restriction in the highly viscous intracellular space, a shift of water to the intracellular space resulting in intracellular/extracellular volume changes, a concomitant change in extracellular tortuosity, membrane permeability, water exchange, and geometrical features (cell size distribution or directional distribution of cell) cause changes in diffusion characteristics (Latour et al., 1994; Norris, 2001; Stanisz et al., 1997; Szafer et al., 1995).

From the literature reviewed, until now there is no final agreement on two tissue compartments as the sources responsible for the ADC change. With dissimilarity among biological tissues considered, a simplified, very convincing speculation about the sources of the ADC is that the fast and slow diffusion components obtained from the bi-exponential fitting of the MR signals of water diffusion would correspond to two different water pools, both existing partly in the intracellular and partly in the extracellular spaces, rather than tissue compartments. If the vascular space is extracted from the extracellular space, leaving the interstitial space, the picture becomes further complicated.

Recent studies attributed the ADC change observed in activated neural tissues to cellular volume increase related to neural activation (Le bihan et al., 2006) or to increased vascular flow

in the region of tissue (Jin et al., 2006, Miller et al., 2007; Jin and Kim, 2008). This finding implies that the vascular compartment should be included to tissue compartments responsible for the diffusion signal. Flint et al. (2009a) used hippocampal slices in absence of vasculature only to detect effect of morphological changes induced by neural activation on signal intensity as a function of b-value. This study, eliminating the contribution of residual vascular space and flow, could describe that the lack of ADC resulted only from the cell swelling occurring during activation. However it remains unclear how the vascular space contributes to the ADC or MR signal intensity.

It was confirmed that the bi-exponential behavior of water diffusion reported for other known tissues exists in the isolated heart and the heart slice as well. In myocardial diffusion weighted imaging, the complicated diffusion profile may come from the special circulation network feeding this life-long muscle pump. The capillary surface area, as a formidable oxygen delivery system necessary for the sustained high energy turnover of the cardiac muscle, comprises 14~22% of heart tissue (Olivetti et al., 1990; Poole and Mathieu-Costello, 1990), which is significantly larger than that of the brain, 4~5%.

The intravascular incoherent motion (IVIM) due to complex capillary geometry and/or randomized water diffusion within the vasculature may cause incorrect estimations of the global ADC and fraction of water pools (Le Bihan et al., 1988; Le Bihan et al., 1986). Moreover, the contribution of the IVIM to the fast pseudo-diffusion coefficient, usually observed at b values less than  $600 \text{ s/mm}^2$ , may be extended to a b value of  $1000 \text{ s/mm}^2$  due to the significant volume of the vasculature (Le Bihan et al., 1988; Le Bihan et al., 1986). This suggests additional factors should be considered when analyzing the clinical diffusion data that were biased to the fast component usually around  $1000 \text{ s/mm}^2$  and optimized at approximately  $b \cdot \text{ADC} = 1$ . Thus in

addition to interstitial and intracellular spaces, vascular spaces need to be considered in order to understand the physiological compartmentalization responsible for the origin of the diffusion signals measured by MR. The contribution of the vascular compartment to the measured diffusion also needs to be quantified in order to avoid incorrect assumptions about myocardial fiber orientation derived from myocardial diffusion measurements. As a result, pathologies that result in altered vascular architecture may lead to incorrect assumptions about myocardial fiber orientation if contributions from this compartment are ignored because the vascular orientation may not always follow the myocardial fiber orientation.

In this experimental study using 11.1 T and 17.6 T magnets, we investigated the contribution of vasculature to the MR water diffusion signal observed in the myocardial tissue:

- by collapsing the vascular space with sliced tissue;
- by replacing the vascular space with the perfluorocarbon-emulsion (PFC);
- and by changing the vascular flow rate of a modified St. Thomas' Hospital (STH) cardioplegic solution.

Since most myocardial diffusion experiments are performed on fixed or cardioplegic-arrested preparations, the contribution of the vascular compartment to the measured diffusion may be substantial. The results of this study may then be employed to infer the contribution of the vascular space of other tissues, each having their own volume fraction, to the MR diffusion signal.

## **Materials and Method**

All animal protocols were in accordance to the guidelines approved by the Institutional Animal Care and Use Committee (IACUC) at the University of Florida.

### **Isolated Perfused Heart Preparation**

Isolated, then arrested hearts were used for this experiment (Jennings, 1976). New Zealand White male rabbits (N = 12, 2-3kg body weight, Harlan) were anesthetized using a

mixture of ketamine/xylazine (40mg/kg : 10mg/kg, i.m.) followed by heparin (1000 U/kg, i.v.), and then were exsanguinated. After sternosection, heart and lungs were excised and placed in a bath of cold (4°C) cardioplegic solution. They were transferred to a Langendorff apparatus and perfused retrogradely. After the descending aorta was cannulated, the lungs were ligated and removed rapidly. Tissue and perfusate were maintained at 37°C via a water-filled heat exchange unit. The perfusate was continually equilibrated with a 95% O<sub>2</sub>-5% CO<sub>2</sub> gas mixture using a membrane oxygenator. The initial perfusate was a modified Krebs Henseleit buffer, containing (in mM) 118.0 NaCl, 25.0 NaHCO<sub>3</sub>, 5.0 dextrose, 4.6 KCl, 2.5 CaCl<sub>2</sub>, 1.2 KH<sub>2</sub>PO<sub>4</sub>, 1.0 MgSO<sub>4</sub>, and insulin (50 mU/ml). An initial perfusion period of 10 min was used to wash the red blood cells out of the vascular space, permit the heart to contract normally, and the aortic valve to seat properly. A thin (1mm-OD) polyethylene tube was inserted in the left ventricle (LV) serving as a vent to avoid excess hydrostatic pressure accumulation and distension of the LV from Thebesian flow. Due to the sensitivity of diffusion weighted images to motion, the heart was arrested prior to imaging by switching perfusate to a modified St. Thomas' Hospital (STH) cardioplegic solution that consists of (in mM) 110.0 NaCl, 16.0 MgCl<sub>2</sub>, 16.0 KCl, 10.0 NaHCO<sub>3</sub>, 5.0 dextrose, and 1.2 CaCl<sub>2</sub>. These experiments were run at room temperature (18 - 19°C), and equilibrated continuously with a 95% O<sub>2</sub>- 5% CO<sub>2</sub> gas mixture resulting in a pH of 7.4.

### **Heart Slice Procurement**

In heart tissue slices, the cells are intact, but the vascular compartment is no longer an essential compartment of the system. The intermediate structural integration afforded by tissue slices not only offers a great opportunity to study some aspects of cell function, particularly cell volume control and transport of water molecules across cell membranes, but also provides considerable advantage over the intact heart for studies of ischemic effects on myocardial cells.

Since myocardium is quite rigid, the method of slice preparation may affect the structural and functional integrity of heart slices.

In this experiment, heart slices (N = 12) were procured from two isolated hearts by freehand slicing to minimize the mechanical trauma due to compression during slice preparation, resulting in the preservation of cell volume, extracellular space, and fine cellular structures (Ganote et al., 1976).

After an isolated perfused heart was prepared, dextrose (5 mM) and adenosine (1 mM) were added to improve the long term viability. The first sectioning was conducted perpendicularly to the long axis of the left ventricle using a double edge razor blade on a Teflon plate. A section of the left ventricular free wall was isolated and coarsely sectioned into a block of tissue approximately  $5 \times 5 \times 3 \text{ mm}^3$ . This block was subsequently finely sectioned into several 500- $\mu\text{m}$ -thick slices spanning the transmural direction of the left ventricular free wall. Papillary muscle was also sectioned in a similar way. Myocardial slices were immersed in ice-cold STH solution for 1 h to minimize preparation-induced ischemic damage, and warmed gradually to room temperature for MR imaging experiment.

### **Placement of Heart Slices into the Multislice Perfusion Chamber**

A multislice perfusion chamber was used for MR imaging after undergoing some modifications (Shepherd et al., 2002). The top and bottom support rings were designed to allow unhampered perfusate flow into the chamber which itself is fitted inside a 10 mm NMR tube. Eight spacers were made by gluing polypropylene mesh (0.5 mm pore size) to the underside of a Delrin ring. One slice was carefully positioned on the mesh surface of each spacer with placement in the NMR tube alternating between tissue slices and spacers. After the last tissue slice was inserted, a top supporting ring covered the perfusion assembly. The completed perfusion chamber was pushed to the bottom of the NMR tube and the outflow tube was placed

above the assembly. The tube was finally sealed with a slotted cap and parafilm before the chamber was perfused and loaded into the magnet. The temperature was maintained at 19°C and the perfusion rate was adjusted to 1ml/min. The flow stopped during diffusion-weighted imaging to minimize motion artifacts.

### **The Emulsified Perfluorocarbons Preparation**

In a 0°C ice bath, 0.475g of L-a-Lecithin (Calbiochem, San Diego, CA) was added to 3 ml of a cold modified St. Thomas' Hospital (STH) cardioplegic solution. The mixture was sonicated for 30 sec. at 500 watts (probe type sonicator Hewlett Packard, Palo Alto, CA). After an interval of 1 min., the sonication was repeated 2 more times. To this aqueous dispersion of lecithin, 2ml of Fluorinert™ (FC-43, 3M, St. Paul, MN) was added. The solution was then sonicated for 30 sec at 500 watts and repeated a total of ten times with a 1 min interval between each sonication. The temperature of the emulsion was measured during each sonication. Finally, the resulting milky-white emulsion was filtered through a 0.8 µm pore size membrane filter (Nalgene, Rochester, NY) and then a 0.45 µm pore size membrane filter (Corning®, Corning, NY), resulting in emulsion particles smaller than 0.45 µm. The procedure was repeated until the amount necessary for this experiment (~ 30 mL) was collected. The amount of 30 ml was estimated from calculations based on values found in the literature regarding capillary volume.

### **Diffusion Magnetic Resonance Imaging**

#### **Heart slices**

MR experiments were performed on a 14.1 T/ 51 mm vertical wide-bore magnet (Bruker instrument's spectrometer and console, Billerica, MA) using a 10 mm birdcage coil. The temperature in the magnet was maintained at 19°C. All MR images were acquired using a multislice imaging sequence. The pilot images with 3 orthogonal planes were collected first to

localize the heart slices in the chamber and check for air bubbles. Diffusion-weighted images were acquired by applying the gradients to give diffusion sensitizing factors (b values) of 180, 490, 1016, 1768, 2582, 3725, 4938, and 6324 s/mm<sup>2</sup> in six directions with a pulsed gradient spin echo sequence. Imaging parameters were TR = 1.5 s, TE = 20 ms, 1 average for all scans using  $\Delta = 12$  ms and  $\delta = 3.5$  ms. All scans were obtained at a slice thickness of 0.2 mm, each with an in-plane resolution of  $0.156 \times 0.156$  mm<sup>2</sup> and a data matrix of  $64 \times 64$ . At the end of each perfusion period, another image was acquired to monitor slice movement. Twelve heart slices from the two isolated hearts were used for the data analysis.

### **Vascular replacement with the PFC emulsion**

MR experiments were performed on an 11.1 T/ 40cm horizontal clear bore magnet (Magnex Instrument's Inc. UK; Bruker Instrument's console, Billerica, MA) with a loop-gap coil (32mm diameter, 40mm height) dual tuned to <sup>1</sup>H/<sup>19</sup>F resonances (Figure 3-1). The temperature in the magnet was 18 ~19°C. The pulmonary artery was cannulated and elevated to produce 10 cm of venous hydrostatic pressure in order to prevent the vascular compartment from collapsing. During the entire time before the injection of the PFC emulsion, coronary vasculature was flushed every 20 mins with fresh perfusate.

Proton diffusion weighted images of the arrested rabbit hearts (N = 5) with the vascular compartment filled with STH were acquired by applying the monopolar pulsed gradients to give diffusion sensitizing factors (b values) of 80, 160, 250, 350, 460, 580, 710, 850, and 1000, in six directions with a standard spin echo pulse sequence. Imaging parameters were TR = 1.5 s, TE = 29 ms, 1 average for all scans using  $\Delta = 16.5$  ms and  $\delta = 5.5$  ms. Thus, a total of 55 scans of 2 hour length were obtained per slice of 2 mm thickness each with an in-plane resolution of  $0.5 \times 0.5$  mm<sup>2</sup> and a data matrix of  $80 \times 80$ . Proton diffusion weighted imaging of an isolated heart (N = 1) was acquired with the six b values of 250, 650, 2000, 3500, and 5000 in a diffusion

encoding direction. Imaging parameters were TR = 2.5 s, TE = 37.7 ms, 1 average for all scans using  $\Delta = 19.3$  ms,  $\delta = 11.7$  ms.

Finally the six hearts underwent substitution of the STH in the coronary vascular space with 30 cc perfluorocarbon (PFC) emulsion through the cannulated aorta by bolus injection (< 1 mL/min), and the DTI was repeated after an equilibration period of 15 min to permit the return of the previously established heart shape. The images perfused with the STH were compared to the ones with the PFC emulsion to examine the shape change of hearts during infusion. The existence of the PFC emulsions in the vasculature was identified after the entire duration of imaging (Figure 3-2). T1 and T2 relaxation times under both perfusates were measured. Three hearts served as time-varying controls, and the ADCs were measured every 15 min for four hours in order to follow changes due to the intermittent global ischemic condition that occurs over time during this non-perfusion experiment. The first two hours were measured using 5cc modified St. Thomas' Hospital (Oosthoek et al.) cardioplegic solution infused every 30 min. The next two hours were measured without the periodic infusion. This would indirectly measure the metabolic deficiencies during the period as compared to the hearts infused with STH buffer.

### **Change of the flow rate of the STH perfusate**

MR experiments were performed on an 11.1 T/ 40 cm clear bore magnet (Magnex Instrument's Inc. UK; Bruker Instrument's console, Billerica, MA) with a birdcage coil (28 mm diameter, 30 mm height) (Figure 3-1). Diffusion weighted images of four isolated hearts were acquired by applying the gradients to give diffusion sensitizing factors (b values) of 30, 70, 140, 270, 430, 680, 1000, 1400, 2000, 3000, 4500, and 6500 s/mm<sup>2</sup> in six directions with a pulsed gradient spin echo sequence. Imaging parameters were TR = 1.5 s, TE = 27.3 ms, NA = 1,  $\Delta = 11.59$  ms, and  $\delta = 3.8$  ms. All scans were obtained at a slice thickness of 2 mm, each with an in-plane resolution of  $0.5 \times 0.5$  mm<sup>2</sup>. Flow rate varied from 0 mL/min to 5 mL/min using a flow

controller (Master Flex L/S, Barrington, OH), and  $^1\text{H}$  DWI was repeated after each flow rate change. Viability was maintained in the zero flow rate state by brief periods of perfusion in between image acquisitions.

### **Data Analysis**

In cardiac muscle, straight and unbranched capillaries comprise more than 80% of total capillary length and run parallel to the myocardial fiber, which enables quantification of the coherent vascular contribution by manually selecting the ROIs having the same primary eigen vector to track the fiber in an efficient fashion previously unavailable. Thus, pixel-based analysis of selected ROIs from a variety of regions (free wall in the LV, interventricular septum, and papillary muscles in the left ventricular cavity) was conducted on a map of the primary eigen vectors (Figure 3-3) of diffusion tensor following myocardial fibers using fanDTasia™ (©2008, Barmpoutis). Calculation of logarithmic, normalized diffusion-weighted signal intensity with b values and linear regression analysis were performed using Matlab (MathSoft, Cambridge, MA), to derive apparent diffusion coefficients (ADCs) under vascular replacement with the PFC. The logarithmic, normalized signal attenuation with vascular flow change within the manually selected ROIs was fitted to a biexponential function using Levenberg-Marquardt non-linear least squares fitting routines (Shepherd et al., 2002) formulated as,

$$S = S_0 (f_1 \cdot \exp(-bD_1) + f_2 \cdot \exp(-bD_2)),$$

where  $f_1$  and  $f_2$  are the volume fractions of the fast and slow components. Similarly,  $D_1$  and  $D_2$  are the ADCs of each component, respectively. Then  $f_1$ ,  $f_2$ ,  $D_1$  and  $D_2$  of each voxel were estimated. Individual data were then averaged among the hearts/slices measured and compared with the zero-mean hypothesis using the Student's t-test (Hsu et al., 1998b). A value of  $p < 0.05$  was considered to be statistically significant.

## Results

Diffusion weighted images in Figure 3-4 clearly demonstrate varying diffusion weighting effect depending on the fiber orientation in the right ventricle, left ventricle, and papillary muscles. At the heavy diffusion weightings, the MR signals were observed only from the heart tissue itself. The diffusion signals were best-fitted into the bi-exponential function (Figure 3-5).

Figure 3-6 shows significant change of normalized signal attenuations as a function of  $b$  values up to  $6500 \text{ mm}^2/\text{s}$  depending on controlled modification in the tissue compartments. Vascular capillaries were collapsed by slicing the isolated heart (diamond, rectangle), their space in the isolated heart was filled with the STH perfusate (crossed) and replaced by the PFC emulsion (triangle), and finally the space was perfused continually with the direct flow of  $1 \text{ ml}/\text{min}$  during the diffusion measurement (circle). Intracellular and interstitial spaces were modified by lowering tonicity of the perfusate by 20 % (rectangle). The normalized diffusion signals show the most significant variation between the heart slice (rectangle) and the continually perfused isolated heart. Volume fractions and ADCs for the fast components and slow components are tabulated in Table 3-1 ~ Table 3-3. The averaged ADC measured in the heart slices in the iso-osmotic STH buffer was  $0.687 \pm 0.08 \times 10^{-3} \text{ mm}^2/\text{s}$  for the fast component, and  $0.08 \pm 0.02 \times 10^{-3} \text{ mm}^2/\text{s}$  for the slow component with an  $R^2$  of 0.999. The relative distribution of the fast component was  $0.518 \pm 0.06$ . In the hypotonic buffer, the ADC of the fast component decreased to  $0.469 \pm 0.09 \times 10^{-3} \text{ mm}^2/\text{s}$ .

When the secured vasculature in isolated rabbit was filled with the STH perfusate, the ADC for the fast component was  $1.21 \pm 0.05 \times 10^{-3} \text{ mm}^2/\text{s}$ , and its relative fraction was  $0.956 \pm 0.016$ . With the STH being perfused into the vascular space at a rate of  $1 \text{ mL}/\text{min}$ , the ADC of the fast component increased significantly to  $1.49 \pm 0.13 \times 10^{-3} \text{ mm}^2/\text{s}$ . However, the volume fraction of the fast component in the perfused isolated heart appeared to be kept relatively

constant at  $0.949 \pm 0.016$ . The diffusion signal in the isolated heart filled with the PFC emulsion was attenuated intermediately between the one in the STH-filling heart and the one in heart slice. The vascular replacement decreased the ADC of the fast component.

When direct perfusate flow in the vascular space was controlled ( 0 ~ 5 mL/min ), the bi-exponential diffusion signal attenuation in the selected ROIs was fully sensitive depending on angular relations between the primary eigen vectors of the ROIs and the diffusion encoding direction (Figure 3-7 ). In Free Wall -1, where the diffusion weighting gradient was applied parallel to the primary eigen vectors ( $\Delta\alpha = 0 \sim 10^\circ$ ), the bi-exponential decline in signal intensity changed significantly with the direct flow rates, especially 1mL/min to 2mL/min. Interestingly, the effect of direct flow in the parallel Free Wall-1 was reversed as the flow rate increased to >3 mL/min. Conversely, in Free Wall-2 and papillary muscle, having the orthogonal primary eigen vectors to the diffusion encoding direction ( $\Delta\alpha = 80 \sim 90^\circ$ ), the diffusion signal attenuation did not alter significantly with change in direct flow rate. (Figure 3-8, and Figure 3-9). Volume fractions and ADCs for the fast components and slow components are tabulated in Table 3-4 ~ Table 3-6. Note that the relative distribution of two water pools and the ADC for the slow component were kept relatively constant in Free Wall-1, Free Wall-2, and papillary muscles.

As mentioned in the Materials and Method section, the ADCs of various regions in the isolated heart were examined every 15min for 4h in order to estimate changes due to the global ischemic condition that happens during the non-perfusion MR experiment of this vascular substitution with the PFC emulsion. Figure 3-10 demonstrates the averaged ADC changes of two isolated hearts used for time-varying control over the whole time course of the MR diffusion measurement in this section. The first two hours were measured with 5cc of STH infused every 30 min (shaded in green) and the next two hours without the STH infusion (shaded in yellow).

The temporary increase of the ADC just after the periodic STH infusions was shown during early two hours on the graph. The ADCs were calculated from the two region of interest (ROIs) templates in the left ventricular free wall. The averaged ADCs in the controlled hearts decreased by  $11.1 \pm 2.4\%$  and  $8.9 \pm 2.7\%$  in the two ROIs. The ADCs of the perfusate filling the left ventricular cavity remain relatively constant over time ( $2.04 \pm 0.12 \times 10^{-3} \text{ mm}^2/\text{s}$ ), which favorably matches the self-diffusion coefficient of  $2.15 \times 10^{-3} \text{ mm}^2/\text{s}$  in  $20^\circ\text{C}$ , the temperature of the MR diffusion measurement in this study. When STH and PFC emulsion phantoms were measured with diffusion weighting (b-values of 0-1000  $\text{s}/\text{mm}^2$ ), ADC was isotropic and measured  $2.23 \times 10^{-3} \text{ mm}^2/\text{s}$  and  $1.39 \times 10^{-3} \text{ mm}^2/\text{s}$ , respectively.

Figure 3-11-a shows that a representative logarithmic normalized signal of a free wall region in the LV decreases linearly with b values up to  $1000 \text{ s}/\text{mm}^2$  in six non-collinear diffusion encoding directions. The calculated slope at relatively low b values represents the apparent diffusion coefficient of fast moving water molecules in the myocardial tissue. The apparent diffusion coefficient decreases significantly up to 42.5% depending on the angular relation between the primary eigen vector and the diffusion encoding direction. When the diffusion encoding gradient is applied parallel to the primary eigen vector, the apparent diffusion coefficient is as high as  $1.4 \times 10^{-3} \text{ mm}^2/\text{s}$  (blue), but it is as low as  $0.8 \times 10^{-3} \text{ mm}^2/\text{s}$  under an orthogonally applied diffusion gradient.

Figure 3-11-b plots a logarithmic normalized signal attenuation of the free wall region in the LV after the vascular space was replaced with the PFC emulsion particles ( $\sim 450 \text{ nm}$  in OD, 30 cc). The ADC variations were similar to the initial measurements using the STH depending on the six diffusion encoded directions. The measured apparent diffusion coefficient into the

long myocardial fiber direction is as high as  $1.1 \times 10^{-3} \text{ mm}^2/\text{s}$  (blue) and the water motion into the short axis of the fiber is as low as  $0.7 \times 10^{-3} \text{ mm}^2/\text{s}$ .

Figure 3-12 shows the change of logarithmic normalized signals of myocardial fibers parallel and orthogonal to the diffusion encoding direction with b-values up to  $1000 \text{ s}/\text{mm}^2$  in the inter-ventricular septum (A), free wall in the LV (B), and papillary muscle in the LV (C) after isolated hearts were infused with 30 cc of the PFC emulsion. The ADC in the parallel and orthogonal myocardial fibers in the inter-ventricular septum decreased significantly. The ADC in the parallel and orthogonal fibers in the free wall in the LV also decreased significantly. Papillary muscle nearly orthogonal to the diffusion encoding direction decreased significantly. Table 3-7 summarizes percentile decreases of the averaged ADC with the six diffusion weighted directions in spherical coordinate over five isolated hearts.

### **Discussion**

These data demonstrate for the first time how the compartments in cardiac tissues contribute the cardiac MR diffusion signals when the water molecules are measured with a pair of mono-polar pulsed field gradients at  $20^\circ\text{C}$ . In particular, isolated rabbit heart model could give understanding of contribution of the vascular compartment to the diffusion MR signal.

### **Modified Vasculature**

Figure 3-13 represents schematically the tissue compartments that exist in the isolated heart (A) and heart slice (B) used for the MR diffusion measurement. Vascular space in the life-long muscle pump tissue could be modified by collapsing (heart slice), or by replacing (isolated heart), or by perfusing with direct flow (isolated heart). Drained, blood free capillaries flushed with a exchanging and nutrimental cardiopledgic solution could remove a region of modified magnetic field caused by paramagnetic deoxyhemoglobin within the capillary, and keep the arrested cardiac tissue fresh at the same time to maintain the structural integrity of the

vasculature over the time course of the MR diffusion measurement. Thus, this system having the preserved vasculature using perfused isolated heart would certainly have made it possible to investigate the vascular contribution to the diffusion signal in the cardiac tissue, which has not been available in other tissues such as brain.

The vascular volume present in the coronary circulation, 10% ~ 25%, appears to be enough to show the significant changes in the MR water diffusion characteristics. The diffusion parameters estimated from the bi-exponential function (Table 3-2) clearly indicate that the vasculature contributes to the diffusion characteristics of the water molecules in the isolated hearts by increasing both the volume fraction and the ADC for the fast component. The volume fraction and the ADC of the fast component increased by 0.438 and  $0.566 \times 10^{-3}$  ( $\text{mm}^2/\text{s}$ ) between the heart slice in the iso-osmotic STH buffer and the isolated heart filled with the STH buffer. Since the intracellular and the interstitial compartments are known as having both the fast component and the slow component in their MR diffusion signals, the tissue compartments responsible for the ADC for the fast component in biological tissues are still a challenge to clarify. In this study, the vascular space where the blood cells and proteins in the plasma are washed out is likely to have only the fast component. Cellular water content in isolated heart should remain constant because the STH perfusate was iso-osmotic to cardiomyocytes. Thus increase in the ADC and the volume fraction of the fast component, for the most part, comes from the existence of the secured vascular space.

On the other hand, due to experimental limitation imposed on this MR diffusion measurement, attention should also be paid when interpreting significant change in normalized diffusion signal observed the isolated heart. First, the longitudinal and transverse relaxation times ( $T_1$  &  $T_2$ ) of the intracellular/interstitial compartments in heart slice and isolated heart

were not measured. Furthermore, the fast moving water molecules in the vascular space would have a shorter spin-spin relaxation time than ones in the intracellular/interstitial compartments. Thus, the variation of the T2 relaxation times in tissue compartments might affect the diffusion signal, largely the fast component. Second, whereas the MR diffusion measurement of isolated heart was performed using 11.1 T (470 MHz for proton) magnet, the water diffusion of heart slice was measured using 14.1 T (600 MHz for proton) magnet. Since the spin-spin relaxation time is known to be shortened with increase of magnetic field strength, the effect of the two magnets on the T2 relaxation time should be taken into account as well. Measurement of relaxation times in the tissue compartments will be of necessity for accurate estimates of the MR diffusion signals. Single cell imaging using a micro-RF coil will give the measures. This is planned in a future study. Water diffusion measurement using stimulated echoes (STEAM pulse sequence) might be another way to remove contamination by the T2 relaxation time only if the signal reduction is acceptable (Fischer et al., 1995).

### **Effect of the Direct Flow Rate Change**

In specific regions where the capillaries largely follow the myocardial fibers, the diffusion MR signal was fully sensitive to direct flow rates. Interestingly, the effect of direct flow in the parallel capillary-fiber region was reversed as the flow rate increased to  $>3$  mL/min. This appears to correlate with an increase of the laminar flow in the vasculature at those flow rates. Since the flow rate in the tiny capillary vessels would increase in directly proportion to the fourth power of vessel radius, according to the Poiseuille's law, the randomly moving protons in those flow rates ( $>3$ mL/min) might become too fast to be traced in the window that a diffusion time of 12 ms offers. The spins labeled by the first diffusion gradient might be liberated from the bondage before the second diffusion encoding gradient is applied. Thus direct flow effect apparently would not be reflected in the measured diffusion weighted signal.

The longitudinal (T1) and transverse (T2) relaxation times of various regions in the myocardium of an isolated heart were examined (Figure 3-14). The transverse relaxation times did not exhibit significant change depending on the flow rate. This means that the relaxation times, in particular the transverse relaxation time (T2), might not be a confounding factor to the MR diffusion signal measured under the direct flow.

Compared to the flow rate (150 mL/min at rest) of averaged human male heart (280.4 ~ 340.2 g), flow rates up to 5 mL/min through the cannulated aorta in the isolated hearts (~ 5g) would lie within a meaningful range for clinical relevance. Hence, the sensitivity of the diffusion attenuation curve and diffusion parameters to the flow rate in the capillaries may be clinically promising indicators that help accurate diagnosis. For instance, decreased blood flow rate and increased cell volume in the region under an ischemic condition may be detected using the diffusion MR measurement used in this study.

The angular dependence of the MR diffusion signal measured with direct flow implies the possibility that the diffusion tensor in perfused isolated heart may be estimated incorrectly. Six non-collinear diffusion encoding directions at a minimum are required for the diffusion tensor estimation. At a given b value, each diffusion weighted image may include the varying vascular contribution to the diffusion signal. This may result in overestimation of the primary eigen value and the diffusion parameters such as the fractional anisotropy and the averaged rate of water diffusion. Degree of the overestimation is currently under investigation. This may be crucial for the correct estimation of the clinical diffusion tensor data.

### **Effect of the Vascular Replacement with PFC Emulsion**

MR diffusion measurement using the PFC emulsion demonstrates that the relatively slowly moving agent within secured vasculature in the isolated heart would contribute the ADC

for the fast component as well as the volume fraction for the fast component, with intermediate values between the heart slice with collapsed vasculature and the isolated heart with direct flow. In order to understand in depth the effect of the vascular space on the ADC for the fast component, the diffusion measurement was performed with relatively low  $b$  values up to  $1000 \text{ s/mm}^2$ . The decrease of ADC up to 40% in diffusion encoded directions observed in the PFC emulsion perfused hearts could come from the intrinsic low rate of water diffusion of the replaced perfusate inside the vascular space, in particular myocardial capillaries.

The emulsified PFC, which has been used as an artificial blood substitute carrying oxygen efficiently, provides great stability to subcellular structures and maintained metabolism in a more intact and functional state than other perfusates. Moreover, based on the previous studies, the PFC stays inside the vasculature when administered intravenously, similar to a non-diffusible tracer. Presuming that the PFC emulsion does not perturb as much affect the interstitial space (which accounts for another 20% of myocardial volume), the percentile ADC decrease in each pixel of  $500 \times 500 \mu\text{m}^2$  would be estimated approximately 10%. However, the measured ADC decrease in our study was larger than the estimated decrease by around 20%. This might result from the intermittent ischemia within periodically perfused tissue. The ADC in time varying control hearts decreased up to 6%, and 10% in the case without perfusion (Figure 3-10). Since the T1 and T2 relaxation times did not change after the replacement, diffusion signal contamination from the the relaxation times might not be significant.

The left ventricular free wall of hearts filled with STH perfusate showed significant variations in the ADC depending on six applied diffusion gradient directions. Compared to the orthogonal gradient, the ADC measured in the parallel gradient increased by 42.9% in the same ROI. Since these data indicate that the ADC for the fast component should always be taken into

account together with the geometrical information of the selected ROI so as to avoid incorrect assumptions by direct comparison to averaged ADC. The primary eigen vector of isolated heart in STH perfusate matched well with one in the PFC emulsion, which implies that the passive capillaries keeps equivalent degrees of structural orientation during infusion of STH perfusate and the denser PFC.

Considering uniformly distributed capillaries feed the heart, the overall reduction in the selected regions seems to be reasonable. And the percentile decrease of the ADC in the PFC emulsion appears to be insensitive to the six diffusion encoding directions. This orientation independent decrease might result from the mean diffusion path (6.43  $\mu\text{m}$ ) of water molecules in the PFC emulsion, which is about 40 % slower than STH perfusate. The diffusion of the water molecules inside the capillaries ( $\sim 5 \mu\text{m}$ ) would approach the slow diffusion limit.

Vascular replacement with the PFC emulsion ( $\sim 450 \text{ nm}$  in OD) could be verified by performing the bench test (Figure 3-2) and by using the MRI (Figure 3-15). The bench test clearly demonstrates that the infused PFC emulsion stays inside the coronary vasculatures and its branches (see arrows pointing to the left descending coronary artery) in an isolated heart. Since the large coronary vessels that supply the cardiac tissues are found subepicardially, the presence of the milky-white PFC emulsion enabled identification.

Since the MR diffusion was measured with a loop-gap RF coil double tuned to the  $^1\text{H}/^{19}\text{F}$ ,  $^{19}\text{F}$  MR imaging was performed to accurately locate the PFC emulsion in the myocardium as soon as the emulsion was infused. However, the effort to locate the  $^{19}\text{F}$  in selected ROIs was not successful due to chemical shifting caused by the four adjacent resonances, signal decreases induced by the lower Larmor frequency of  $^{19}\text{F}$ , and its low sensitivity to small dose molecules (Figure 3-16). Fluorine MRI using a chemical that has only one resonance, like the perfluoro-

15-crown-5-either (Flogel et al., 2008), is currently being scheduled as a future study. The administration of the milky-white PFC perfusate through a cannulated coronary artery may be used to avoid the potential valvular insufficiency that sometimes may arise with arrested preparations. This may also prevent the misregistration of ROIs due to a dilated/elongated heart that results from the denser PFC emulsion accumulation in the ventricular cavities (Buckberg, 2005; Flogel et al., 2008; Judd et al., 1992)

### **Heart Slice in Hypotonicity**

Hypotonic solution and ouabain increases the cellular volume in biological tissue by adjusting the osmolarity across the plasma membrane and by inhibition of the Na-K pump in the plasma membrane. The MR diffusion attenuation of heart slice in hypotonic buffer appears to reflect relative increase in intracellular volume. The MR diffusion signal of heart slice varied similarly as one of hippocampal slices in hypotonic solution or ouabain-treated hippocampal slice. However, unlike the previous papers that reported largely relative increase of volume fraction, this measurement showed decrease in the ADC of the fast component. This may imply the relative increase of the slow diffusing water in the expanded cell. However, as described, T2 relaxation time and its change in hypotonic solution was not considered.

Calcium ion plays essential roles of cardiac excitation-contraction from the electrical excitation of the myocyte to contraction of heart (Bers, 2002). Due to the importance of ubiquitous second messenger in cardiac function, the plasma membrane  $\text{Ca}^{2+}$  ATPase (PMCA) and the  $\text{Na}^{+}$ - $\text{Ca}^{+}$  exchanger are major cell volume regulators in cardiac tissue (Figure 3-13) (Baumgarten, 2006; Bers, 2002). This implies that blockage of the  $\text{Ca}^{2+}$  pump and/or the  $\text{Na}^{+}$ - $\text{Ca}^{+}$  exchanger might be necessary in ouabain-treated heart slice to impose the cell volume increase in cardiac tissue. Since a crucial protein involved in the ion exchanger, CoQ10, is very temperature sensitive, temperature change may be an effective method to bring about cellular

volume change (Kumar et al., 2009). This is a subject of future study regarding the tissue compartmentalization in the MR diffusion signal.

### **Possibility of the Triexponential Fitting Model**

Due to presence of the very fast pseudo-diffusion coefficient by the randomized capillary geometry or randomized diffusion of the water molecules in the capillary, a third very fast component in low b value regions ( $\sim 600 \text{ s/mm}^2$ ) was reported in previous studies, mostly dealing with brain tissue (Le Bihan et al., 1988; Norris, 2001). The effect of the very fast component to the diffusion signal can be extended to higher b value regions in proportion to the volume the vascular space occupies (Le Bihan and van Zijl, 2002). Forder et al. (2001) also speculated about the possibility of a tri-exponential fitting model for the MR diffusion by the decreased ADC ( $0.72 \pm 0.07 \times 10^{-3} \text{ mm}^2/\text{s}$ ) observed in their heart slices. The decreased ADC of the fast component in the heart slices was observed in our measurements ( $0.56 \pm 0.08 \times 10^{-3} \text{ mm}^2/\text{s}$ ), which supports the significant effect of the intact vasculature as reported in previous studies (Gamcsik et al., 1996; Hsu et al., 2001). The diffusion attenuation with direct flow (0 mL/min  $\sim$  1 mL/min) in isolated hearts with b values up to  $6500 \text{ s/mm}^2$  was well fitted to the bi-exponential function. This means that the vasculature contributes to the diffusion signal by being merged into the fast component, rather than generating a new third component at the time of measurement during a diffusion time of 12.8 ms.

In the cardiac muscle, the degree of randomized capillary tortuosity and branching, even if it may be considerable, provides only up to 20% of total capillary length. This means that most capillaries, straight and unbranched, have relatively coherent geometry that runs parallel to the myocardial fiber. However, it needs to be identified whether microscopic water motion in the capillaries would be merged into the preexisting fast component or would generate the very fast component that has a pseudo-diffusion coefficient by intravascular incoherent motion

(IVIM). Figure 3-17 suggests the possibility of diffusion attenuation being fitted to the tri-exponential function. Whereas the heart slices did not fit the tri-exponential function, diffusion parameters that have the third component were found in isolated hearts continuously perfused with 1 mL/min with a similar  $R^2$  as one in the bi-exponential function.

Hereafter, study to identify the third component as the vascular contribution will be undertaken in two ways. First, from the point of view of pulse sequence, if the diffusion - encoding time is reduced by applying two pairs of pulsed bipolar diffusion gradients at either side of the refocusing RF pulse, it is possible that the very fast component might be identified in the diffusion attenuation measurement. This work will be performed using the 17.6 T magnet system. An alternative method may be to perfuse such agents as Gd-DTPA or deuterium oxide ( $D_2O$ ). A high dosage, gadolinium-based agent (Gd-DTPA) will effectively knock out the MR signal from the vascular compartment by shortening the T2 relaxation time. Time evolution of the diffusion signal by inter-compartmental movement following the flow rate change may be measured with the  $D_2O$  perfusate because it will remove the signal from space that it moves into, with the tissue viability maintained.

In conclusion, diffusion MR imaging of isolated hearts and heart slices from rabbits demonstrates the vascular compartment of the myocardium is a significant contributor to the fast moving water pool of water diffusion signal that demonstrates bi-exponential behaviour. Hence, interpretation of existing myocardial diffusion MRI data without clear knowledge of the vascular effect to the global ADC can lead to incorrect inferences.

First, from the MR diffusion measurements using the PFC emulsion, the existence of the secured vasculature in the isolated heart contributes to the ADC for the fast component as well as the volume fraction for the fast component.

Second, from the MR diffusion measurement with direct flow, attenuation of signal intensity with b values up to  $6500 \text{ s/mm}^2$  appears to be modulated by vascular flow, especially at lower flow rates. The variation of the vascular flow rate contributes to the ADC for the fast component rather than the volume fraction for the fast component.

This has important implications under pathophysiological conditions, where hypoperfusion and ischemia may predominate. Furthermore, this study will help to understand the vascular contribution to the diffusion signal in the other tissues or organ. For a clear understanding of the sources of MR diffusion signals observed in the heart, studies to alter the interstitial volume by altered vascular permeability and/or oncotic pressure using a fast diffusion imaging sequence will be necessary.

Table 3-1. Estimates of the diffusion parameters in heart slices buffered with iso-osmotic and hypotonic solution. n is the number of heart slices. F1: volume fraction of the fast component; D1: the ADC of the fast component; D2: the ADC of the slow component. Mean (SD).

	f1 (no units)	D1 (X 10 <sup>-3</sup> mm <sup>2</sup> /s)	D2 (X 10 <sup>-3</sup> mm <sup>2</sup> /s)	R <sup>2</sup>
Heart slice in the hypotonic STH (n=7)	0.612 (0.08)	0.469 (0.09)	0.04 (0.03)	0.998
Heart slice in the iso-osmotic STH (n=7)	0.518 (0.08)	0.687 (0.18)	0.08 (0.02)	0.999

Table 3-2. Estimates of the diffusion parameters in isolated hearts. The vascular space filled with the STH was replaced with the PFC emulsion. n is the number of selected slices. F1: volume fraction of the fast component, D1: the ADC of the fast component, D2: the ADC of the slow component. Mean (SD).

	f1 (no units)	D1 (X 10 <sup>-3</sup> mm <sup>2</sup> /s)	D2 (X 10 <sup>-3</sup> mm <sup>2</sup> /s)	R <sup>2</sup>
Isolated heart filled with the PFC (n=6)	0.866 (0.023)	1.15 (0.06)	0.052 (0.021)	0.999
Isolated heart filled with the STH (n=13)	0.956 (0.016)	1.21 (0.05)	0.046 (0.029)	0.999

Table 3-3. Change in the diffusion parameters of isolated hearts with direct flow (1mL/min). n is the number of selected slices. F1, volume fraction of the fast component; D1, the ADC of the fast component; D2, the ADC of the slow component. Mean (SD)

	f1 (no units)	D1 (X 10 <sup>-3</sup> mm <sup>2</sup> /s)	D2 (X 10 <sup>-3</sup> mm <sup>2</sup> /s)	R <sup>2</sup>
Isolated heart filled with the STH (n=13)	0.956 (0.016)	1.21 (0.049)	0.046 (0.029)	0.999
Isolated heart perfused with the STH (n=13)	0.949 (0.016)	1.49 (0.129)	0.059 (0.012)	0.999

Table 3-4. Estimates of the diffusion parameters in myocardial fibers parallel to the diffusion gradient with direct flow (Free Wall -1). F1, volume fraction of the fast component; D1, the ADC of the fast component; D2, the ADC of the slow component. Mean (SD).

Flow rate of the perfusate	F1 (no units)	D1 (X 10 <sup>-3</sup> mm <sup>2</sup> /s)	D2 (X 10 <sup>-3</sup> mm <sup>2</sup> /s)	R <sup>2</sup>
0 mL/min	0.956 (0.016)	1.21 (0.049)	0.046 (0.012)	0.999
1 mL/min	0.949 (0.016)	1.49 (0.129)	0.059 (0.012)	0.999
2 mL/min	0.941 (0.029)	1.37 (0.092)	0.057 (0.011)	0.999
3 mL/min	0.951 (0.021)	1.27 (0.085)	0.045 (0.031)	0.999
5 mL/min	0.953 (0.021)	1.24 (0.055)	0.056 (0.027)	0.999

Table 3-5. Estimates of the diffusion parameters in myocardial fibers orthogonal to the diffusion gradient with direct flow. F1, volume fraction of the fast component; D1, the ADC of the fast component; D2, the ADC of the slow component. Mean (SD).

Flow rate of the perfusate	F1 (no units)	D1 (X 10 <sup>-3</sup> mm <sup>2</sup> /s)	D2 (X 10 <sup>-3</sup> mm <sup>2</sup> /s)	R <sup>2</sup>
0 mL/min	0.877 (0.02)	0.756 (0.136)	0.064 (0.011)	0.999
1 mL/min	0.875 (0.03)	0.734 (0.249)	0.056 (0.02)	0.998
2 mL/min	0.905 (0.06)	0.789 (0.172)	0.065 (0.01)	0.996
3 mL/min	0.890 (0.01)	0.750 (0.15)	0.060 (0.03)	0.999
5 mL/min	0.904 (0.02)	0.75 (0.14)	0.059 (0.01)	0.999

Table 3-6. Estimates of the diffusion parameters in Papillary muscle fibers nearly orthogonal to the diffusion gradient with direct flow. F1, volume fraction of the fast component; D1, the ADC of the fast component; D2, the ADC of the slow component. Mean (SD).

Flow rate of the perfusate	F1 (no units)	D1 ( $\times 10^{-3}$ mm <sup>2</sup> /s)	D2 ( $\times 10^{-3}$ mm <sup>2</sup> /s)	R <sup>2</sup>
0 mL/min	0.891 (0.02)	0.89 (0.137)	0.053 (0.011)	0.999
1 mL/min	0.893 (0.03)	0.85 (0.219)	0.060 (0.02)	0.998
2 mL/min	0.899 (0.06)	0.73 (0.162)	0.067 (0.01)	0.999
3 mL/min	0.892 (0.01)	0.70 (0.14)	0.051 (0.02)	0.997
5 mL/min	0.857 (0.02)	0.81 (0.14)	0.068 (0.01)	0.999

Table 3-7. Percentile decrease of averaged ADC after the PFC replacement of vascular space with the six diffusion weighted directions in spherical coordinate,  $\times 10^{-3} \text{ mm}^2/\text{s}$ . Manually selected ROIs are from the inter-ventricular septum, Free Wall in the LV, papillary muscles in the LV, and the STH or PFC isotropic solution with which the left ventricular spaces were filled. Percentile data were calculated based on the ADC obtained from linear regression analysis in MATLAB. Each datum corresponds to the mean of the selected ROIs.

	ROI	090	630	6372	63144	63216	63288
Heart #1	Inter-septum	20.3	21.2	21.9	19.8	21.7	13.9
	Free wall	10.7	23.4	16.6	19.5	33.2	30.1
	Papillary	21.0	26.0	25.7	29.5	26.3	21.1
	Muscle						
Heart #2	Inter-septum	19.7	30.23	34.3	7.0	40.5	7.8
	Free wall	18.8	5.9	26.9	25.3	9.1	0.3
	Papillary	38.4	40.1	36.6	42	18	32.8
	Muscle						
Heart #3	Inter-septum	9.3	18.6	21.5	22.7	25.4	25.9
	Free wall	22.2	17.6	46.3	21.0	18.5	20.5
	Papillary	13.3	6.6	10.3	11.3	12.1	18.9
	Muscle						
Heart #4	Inter-septum	12.7	6.8	5.1	14.9	14.2	8.1
	Free wall	18.1	10.5	22.4	8.6	26.0	7.2
	Papillary	-10.9	0.1	25.1	-0.9	22.6	20.6
	Muscle						
Heart #5	Inter-septum	22.9	23.0	24.0	22.4	30.4	31.2
	Free wall	30.6	28.5	37.1	34.2	31.3	33.4
	Papillary	22.8	25.1	28.0	33.5	15.4	32.0
	Muscle						

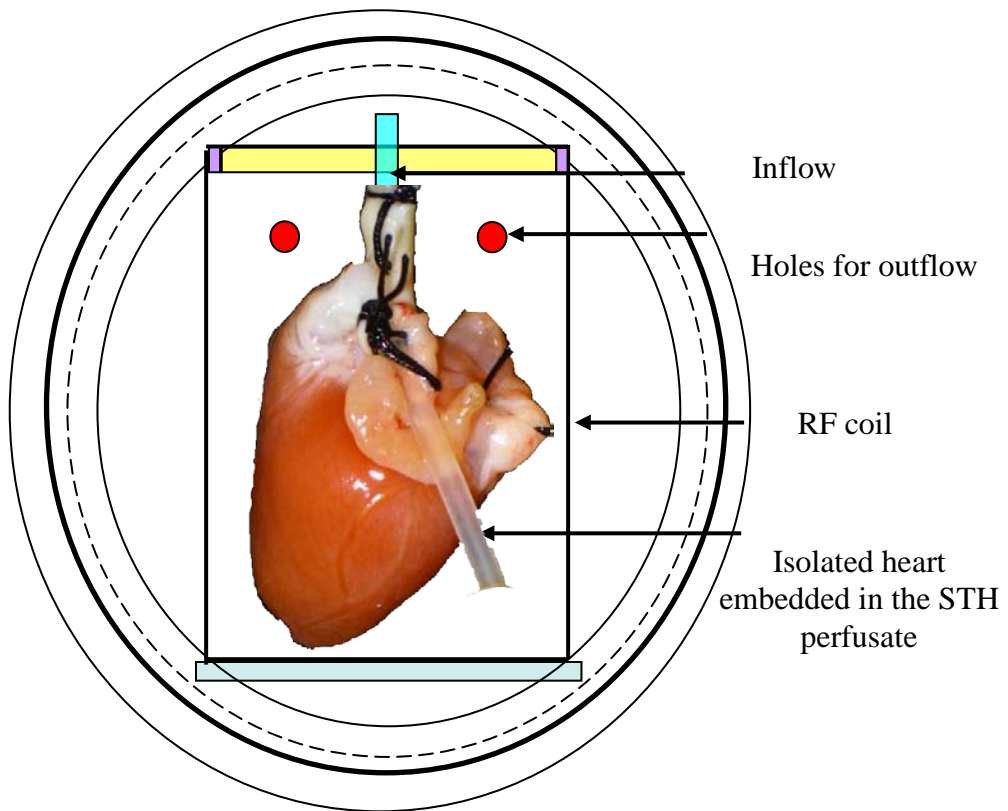
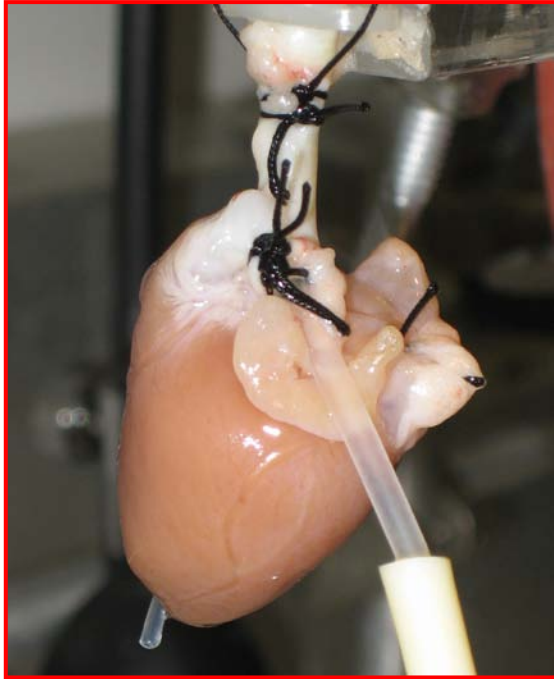
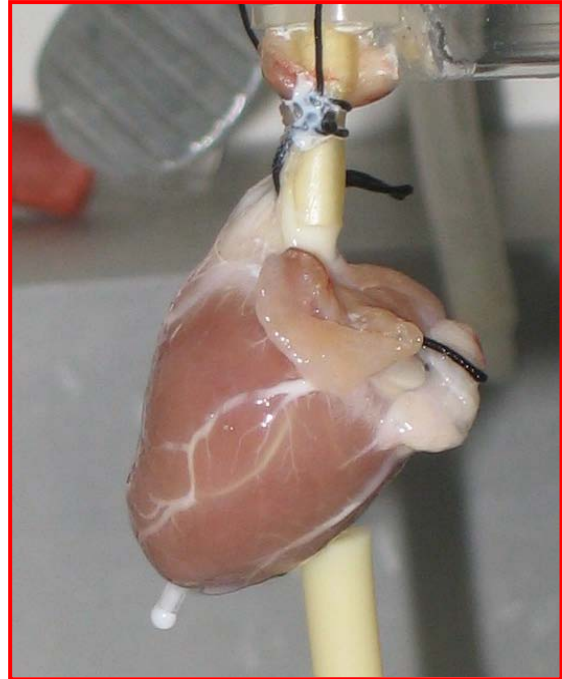


Figure 3-1. A schematic diagram of experimental setup for DWI of isolated heart.

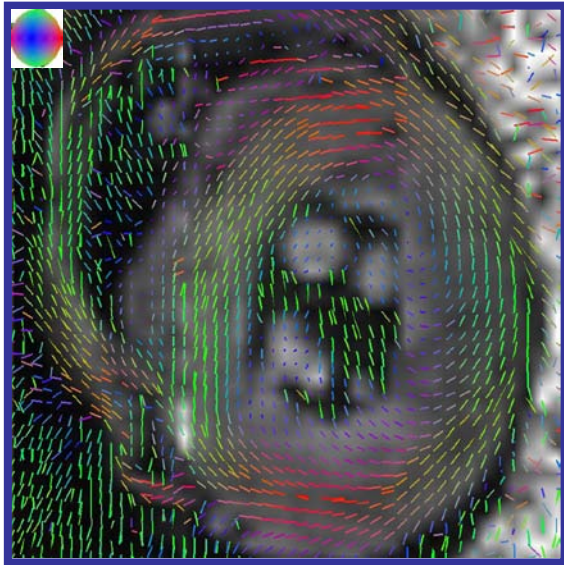


A

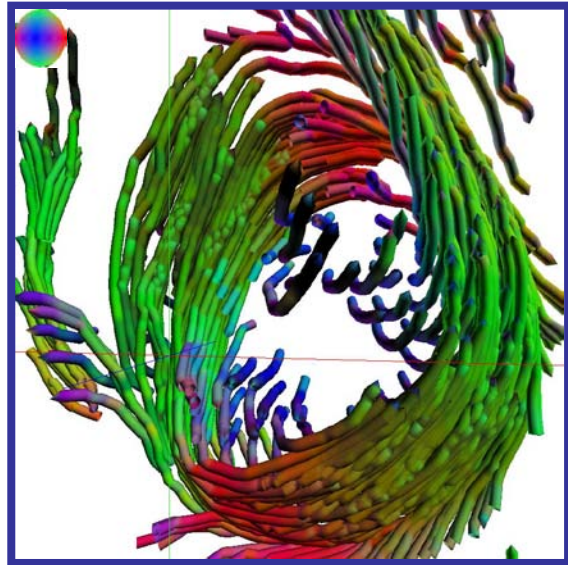


B

Figure 3-2. Vascular replacement of the STH perfusate with the PFC emulsion. A) Picture was taken during arresting the isolated, but still beating, heart with the STH cardioplegic solution at room temperature. B) Picture was taken as soon as the whole MR imaging experiment was completed. Left and right coronary arteries and their circumflex branches are matched in the two pictures and clearly show they are filled with the milky-white PFC emulsion. Note that small branches from the great vessels are also filled with the emulsion.



A



B

Figure 3-3. Primary eigen vector map (A) and 3D fiber tracking map (B) of a short axis view. This provides templates for the manual selection of ROIs, and enables examination of vascular flow that follows myocardial fibers.

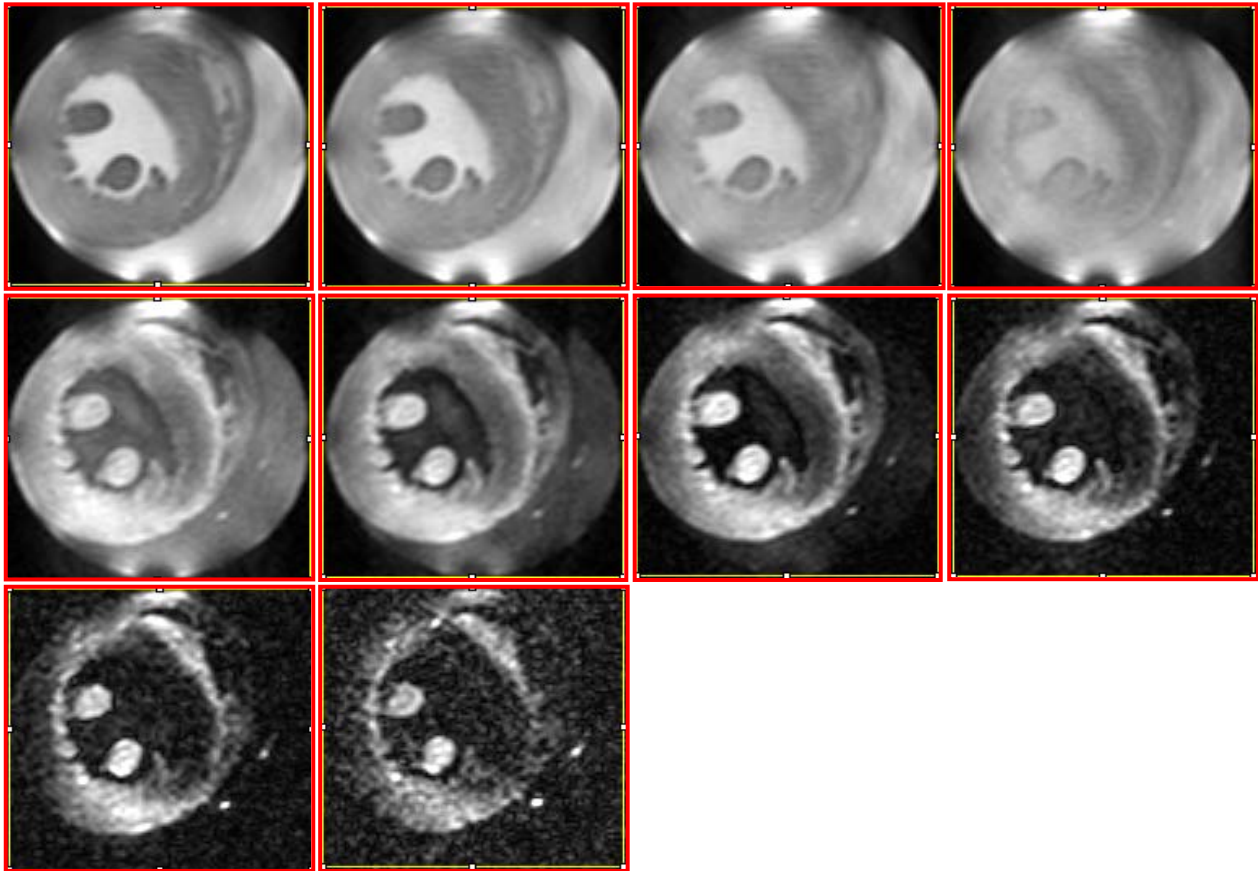


Figure 3-4. Representative diffusion weighted images of an isolated heart perfused with STH using 10 diffusion sensitizing (b-values) factors. From left in the top row: 0, 140, 270, 430  $\text{s/mm}^2$ . From left in the middle row: 1000, 1400, 2000, 3000  $\text{s/mm}^2$ . From left in the bottom row: 4500, and 6500  $\text{s/mm}^2$ . Each image has approximately a 28 mm x 28 mm field of view. This isolated heart was perfused continuously with the perfusate of 1ml/min while the diffusion imaging is performed. Images clearly demonstrate the weighted effect of water diffusion depending on the fiber orientation in the right ventricle, the left ventricle, and the papillary muscles. At the heavy diffusion weightings, the observed signal seems likely to come only from the heart tissue itself.

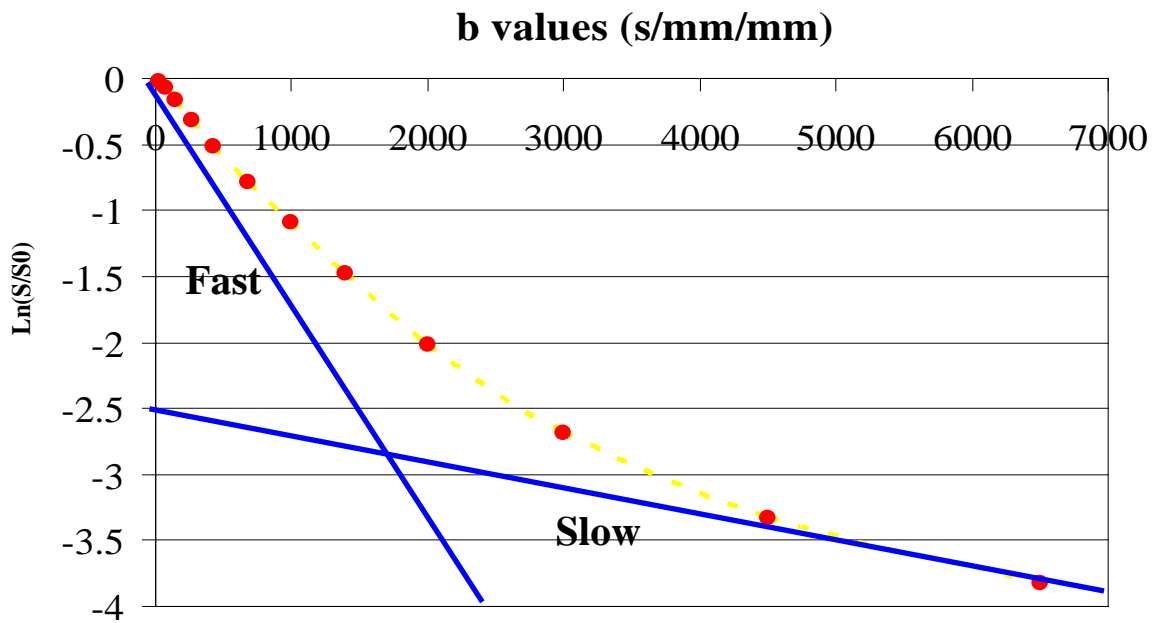
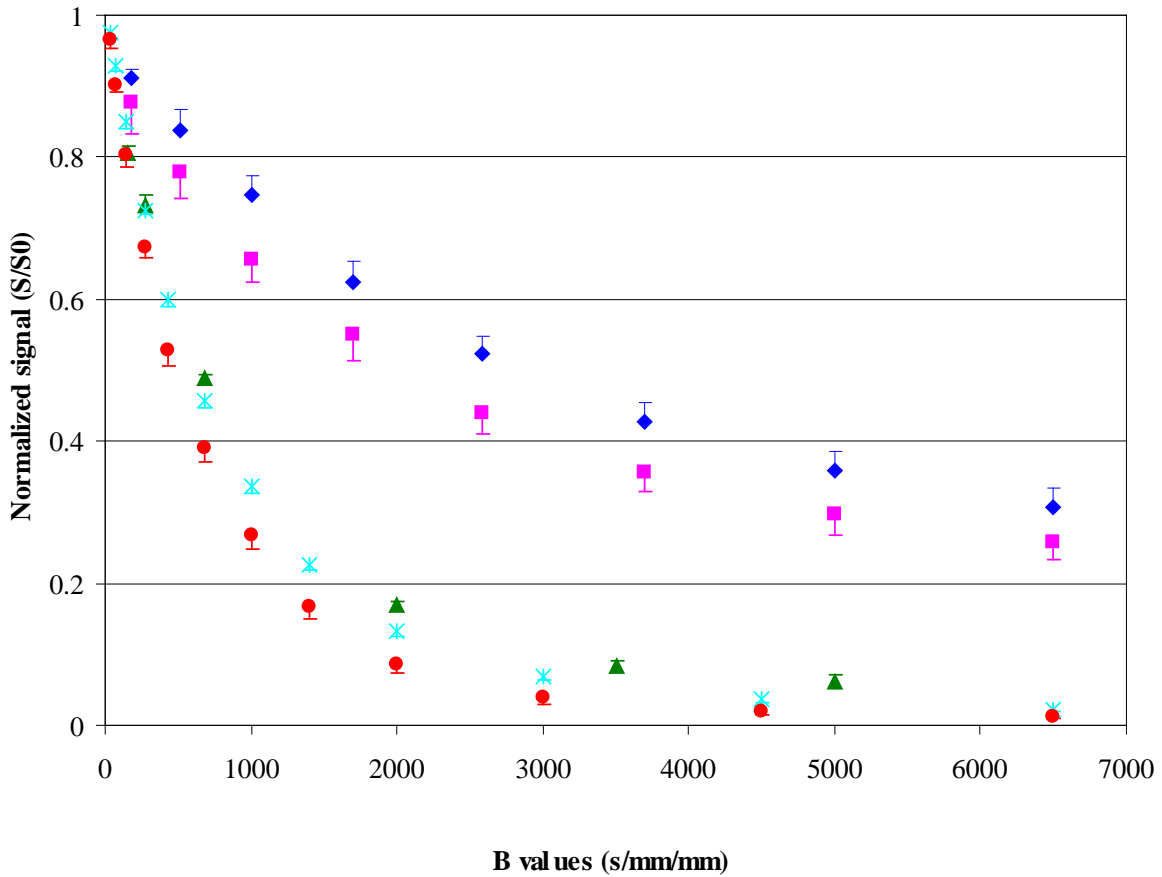


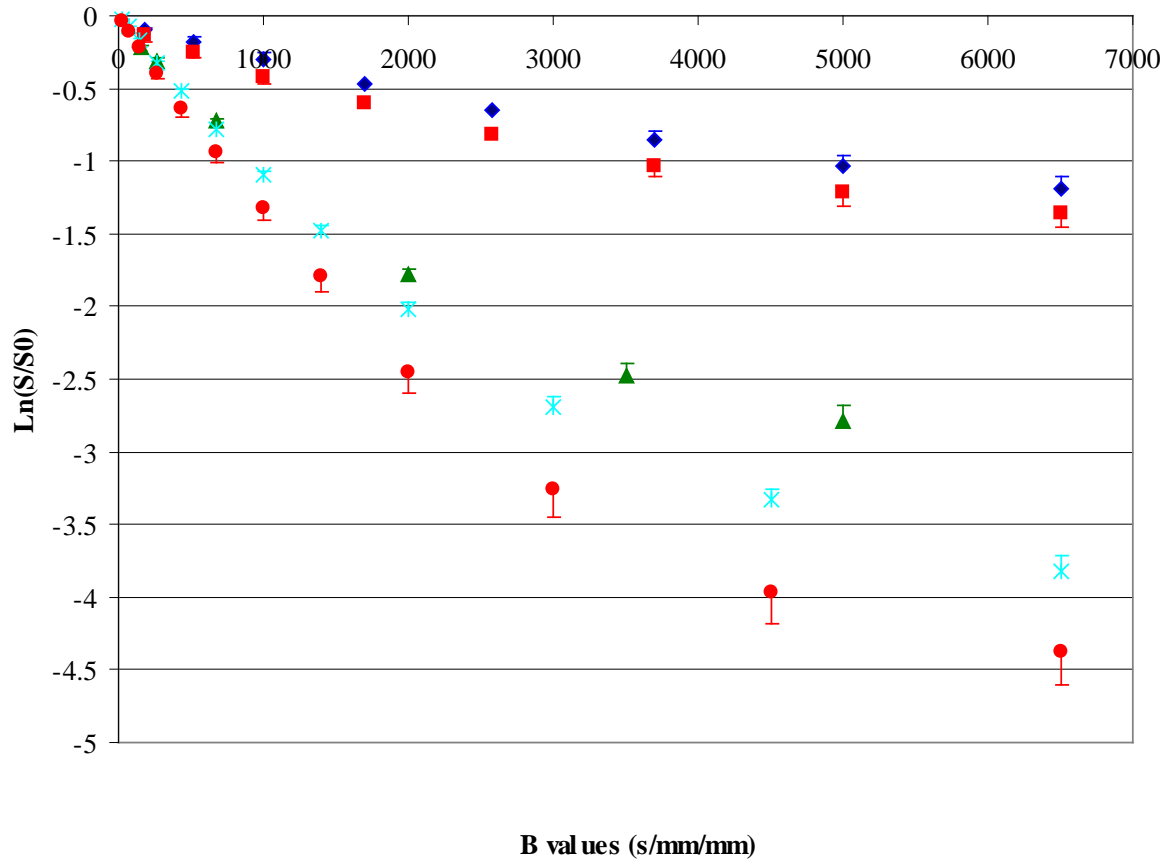
Figure 3-5. A representative plot of the logarithmic signal intensity as a function of b-values for an isolated rabbit heart. Dotted yellow line represents a bi-exponential function that is best-fitted with parameters of the fast and the slow components (Blue lines).



- ◆ Heart slice superfused in hypotonic buffer
- Heart slice superfused in the normo-osmotic STH buffer
- ▲ Isolated heart filled with the PFC emulsion
- \* Isolated heart filled with the iso-osmotic STH buffer
- Isolated heart perfused continuously with the iso-osmotic STH buffer

A

Figure 3-6. Normalized signal attenuation and its logarithmic normalized signal attenuation with modification of the vascular space, collapsed, replacement, and direct flow. Direct flow rate of perfusate was 1 mL/min.



B

Figure 3-6. Continued

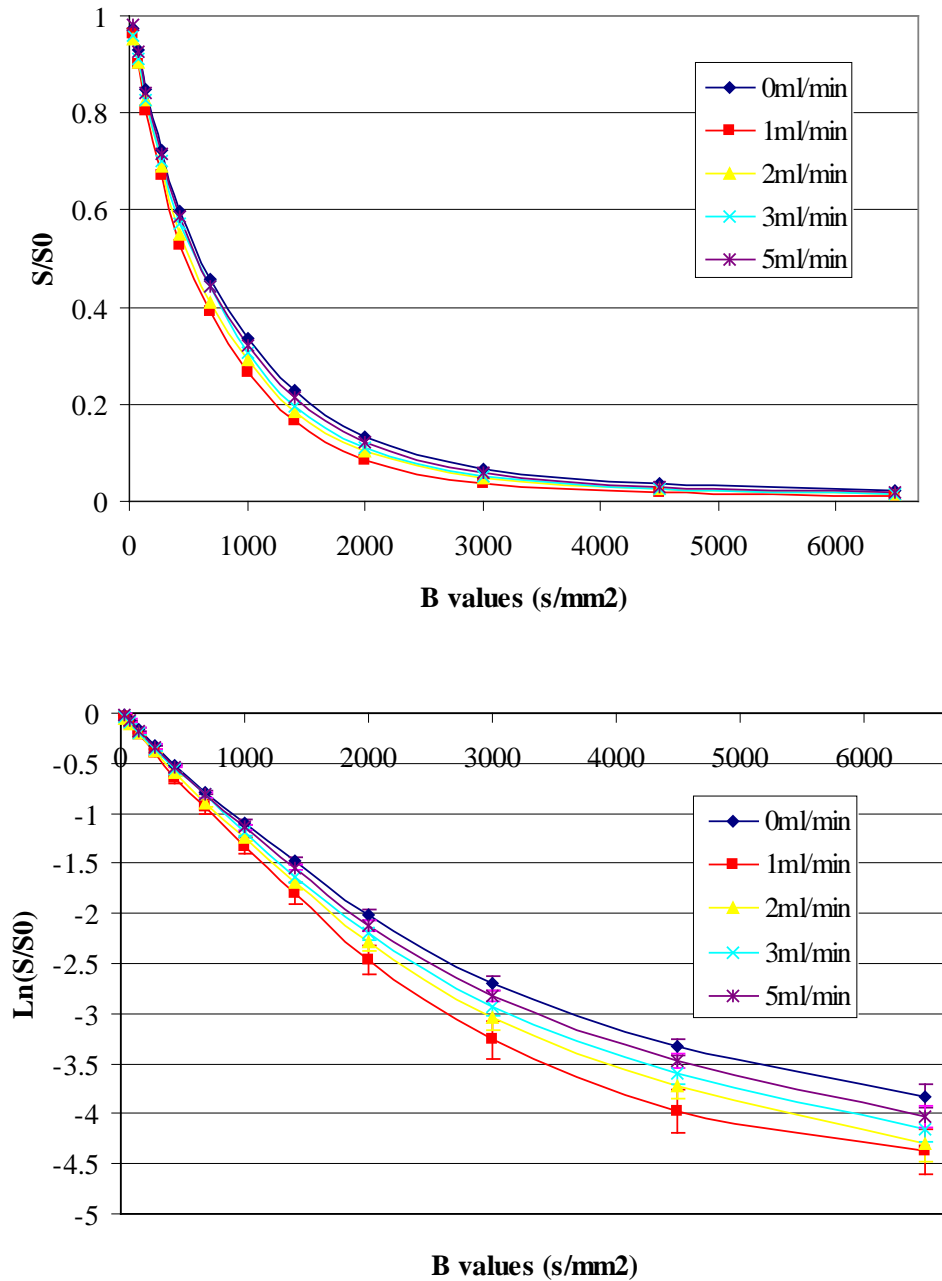


Figure 3-7. Normalized signal attenuation and its logarithmic normalized signal attenuation with changes in perfusate flow in a free wall in the LV. Angular relation between primary eigen vector and diffusion weighted direction is nearly parallel ( $\Delta\alpha = 0 \sim 10^\circ$ ).

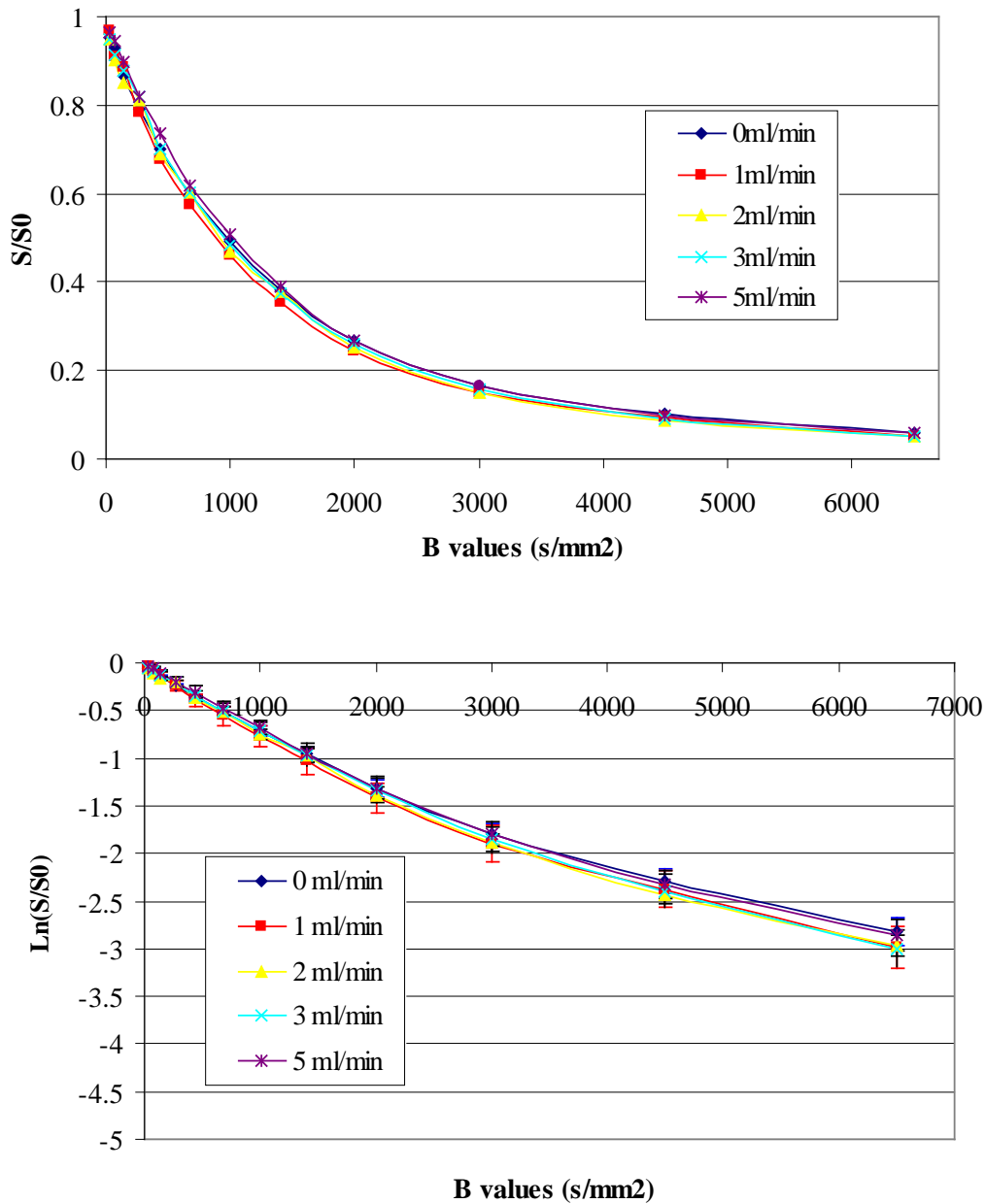


Figure 3-8. Normalized signal attenuation and its logarithmic normalized signal attenuation with changes in perfusate flow in a free wall in the LV. Angular relation between primary eigen vector and diffusion weighted direction is nearly orthogonal ( $\Delta\alpha = 80 \sim 90^\circ$ ).

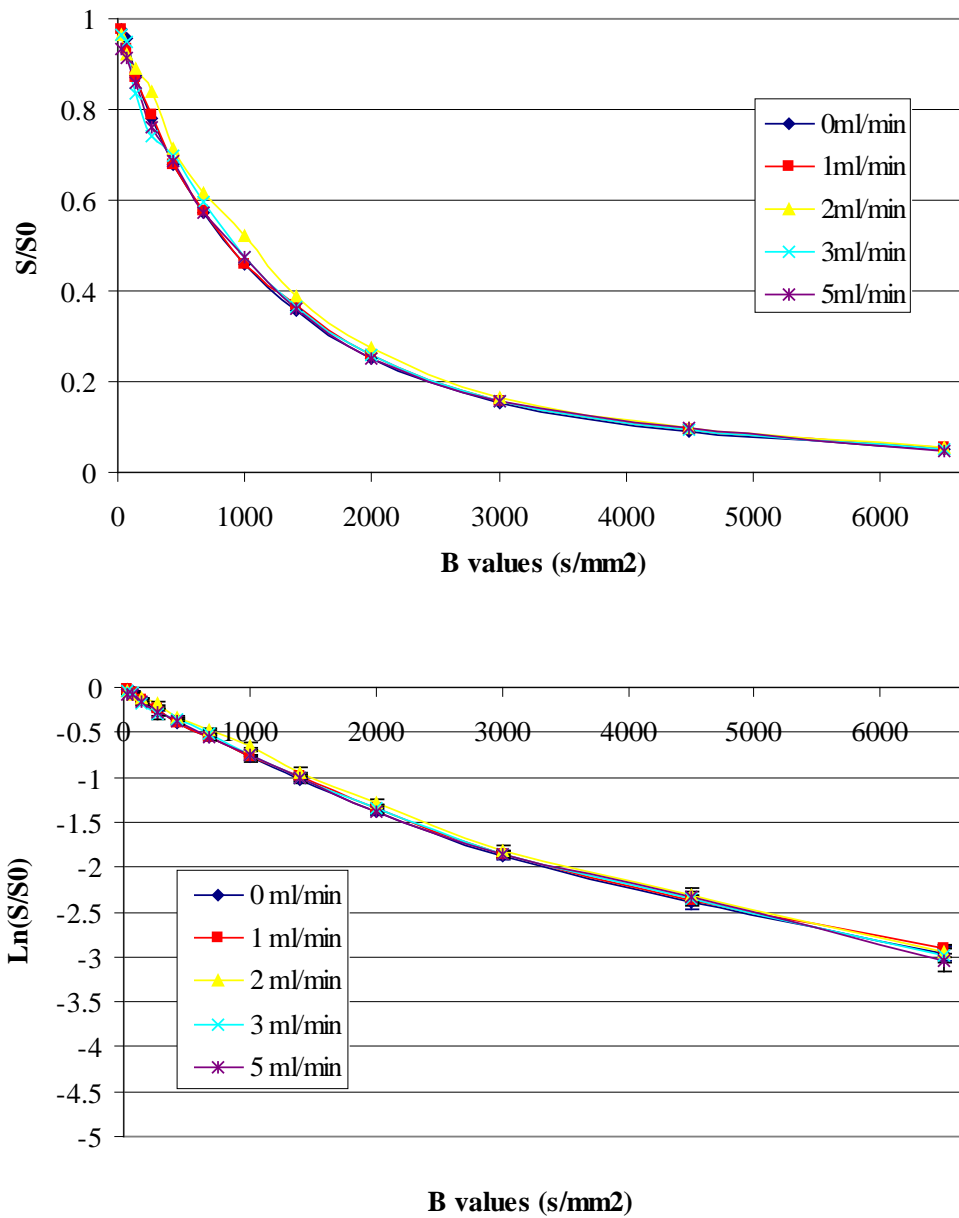


Figure 3-9. Normalized signal attenuation and its logarithmic normalized signal attenuation with changes in perfusate flow in a papillary muscle in the LV. Angular relation between primary eigen vector and diffusion weighted direction is nearly orthogonal ( $\Delta\alpha = 80 \sim 90^\circ$ ).

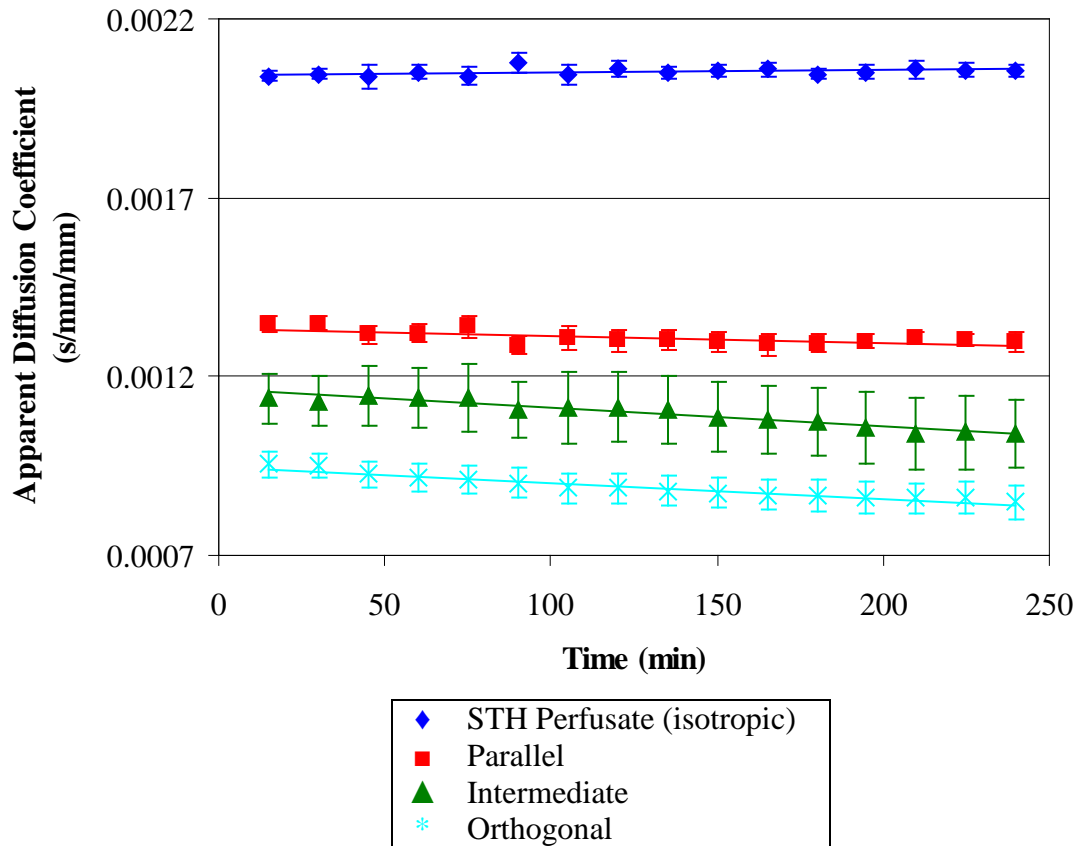


Figure 3-10. Temporal evolution of the apparent diffusion coefficient (ADC) of control hearts. Each point shows the mean and standard deviation of the selected ROIs in the left ventricular free wall. The primary eigen vectors in the orthogonal are nearly perpendicular to the diffusion gradient orientation. Ones in the parallel and the intermediate are parallel and intermediate to the diffusion gradient orientation. First eight points were measured with 5cc of STH infused every 30 min and next eight points were measured without periodic infusions. The relatively constant ADC of the STH\_perfusate over the time appears to make it unnecessary to normalize the ADCs of the regions selected for this graph.

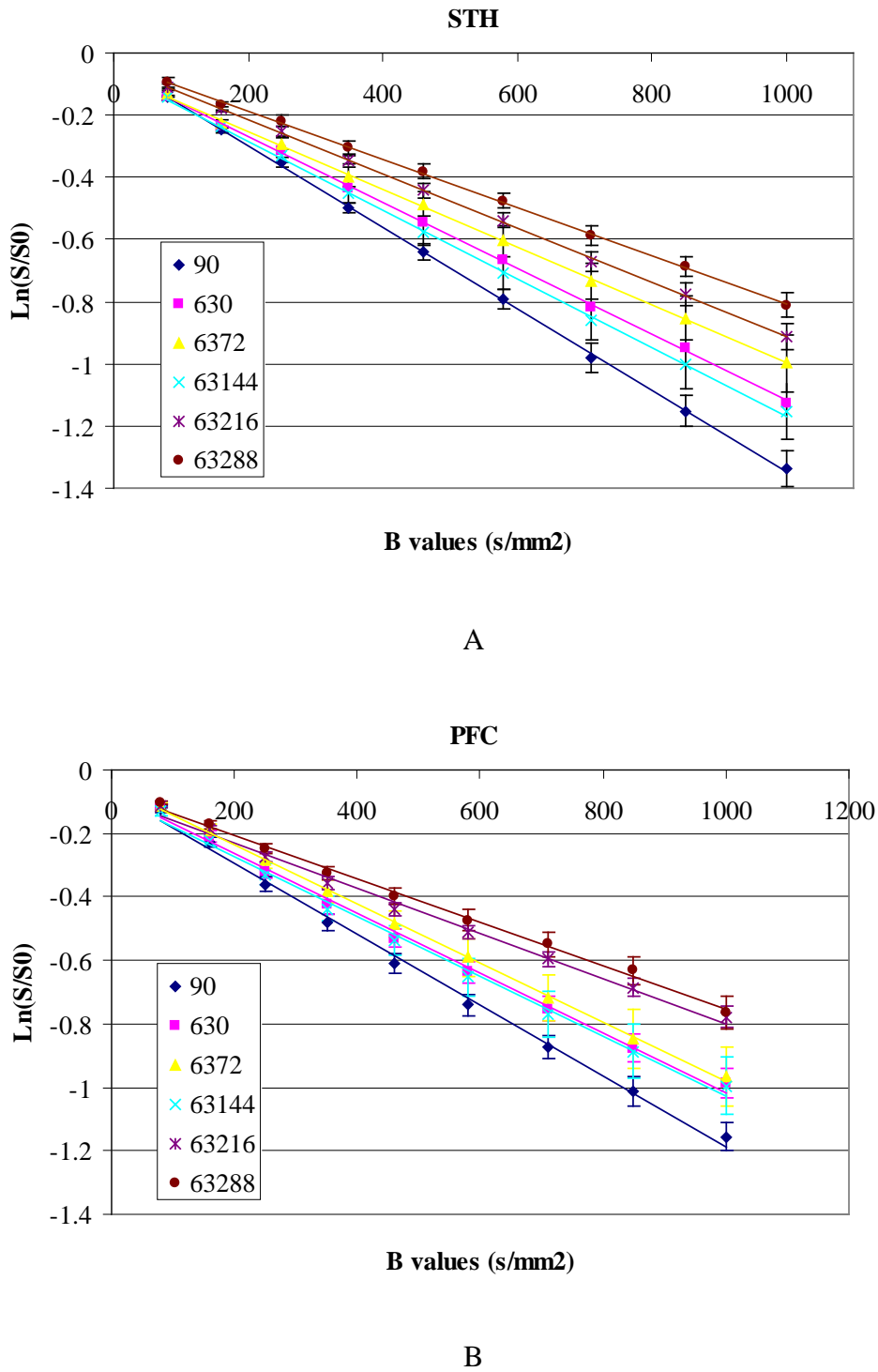
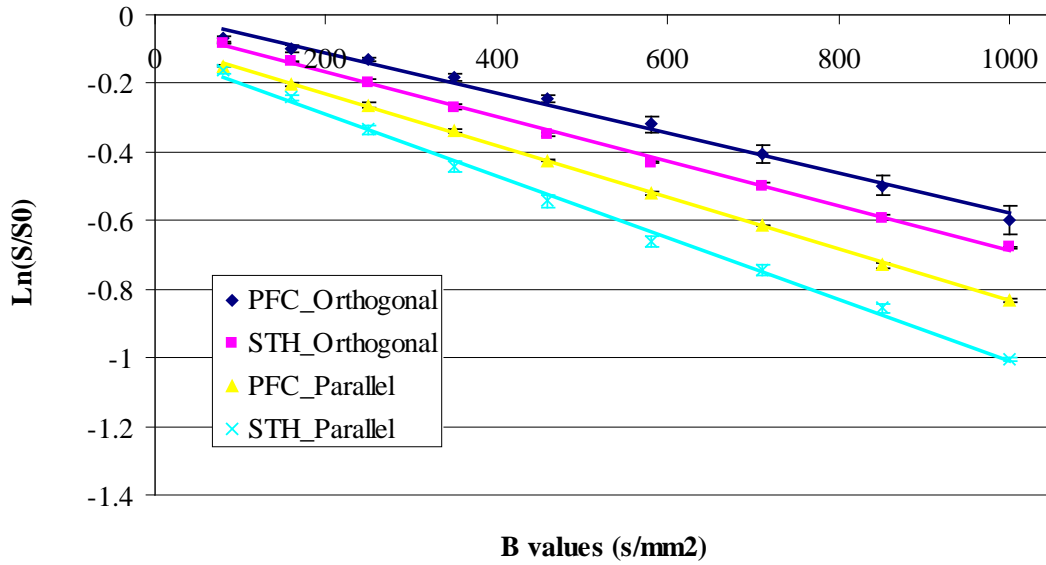
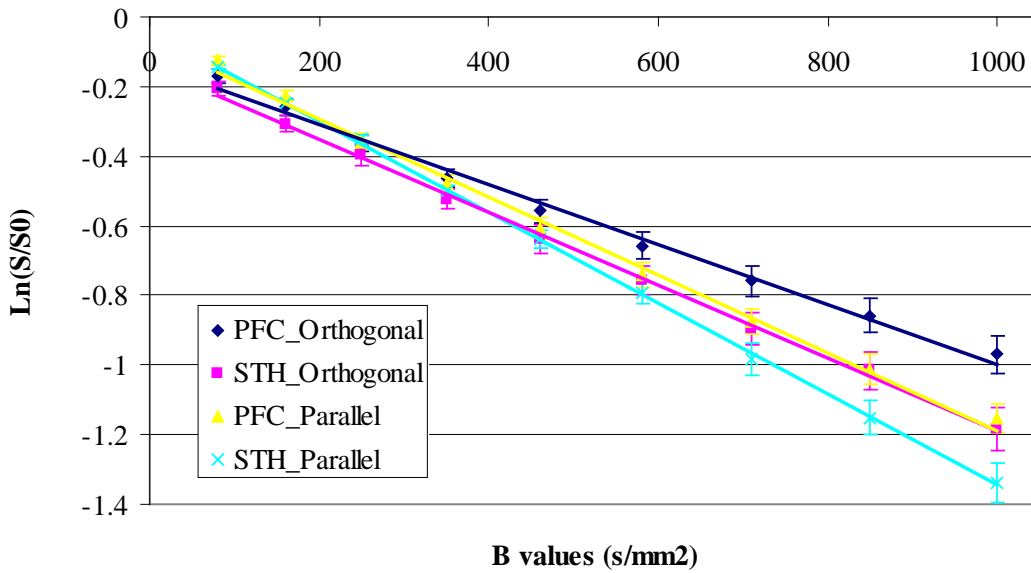


Figure 3-11. The ADC sensitivity to six diffusion encoding directions in a Free Wall region in the LV when the vascular space is filled with the STH perfusate (A) and replaced with the PFC emulsion (B)

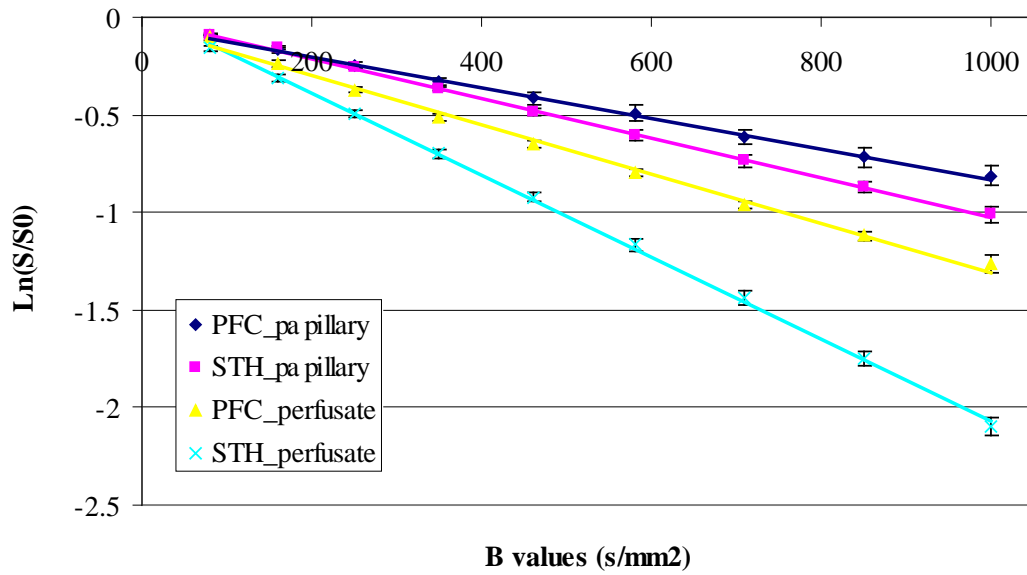


A



B

Figure 3-12. The ADC decrease when the vascular space filled with the STH perfusate is replaced with the PFC emulsion. Parallel and orthogonal myocardial fibers to diffusion encoding direction were manually selected. A) Interventricular septum. B) Free Wall in the LV. C) Papillary muscles, isotropic STH perfusate and the PFC emulsion filling in the left ventricular cavity.



C

Figure 3-12. Continued

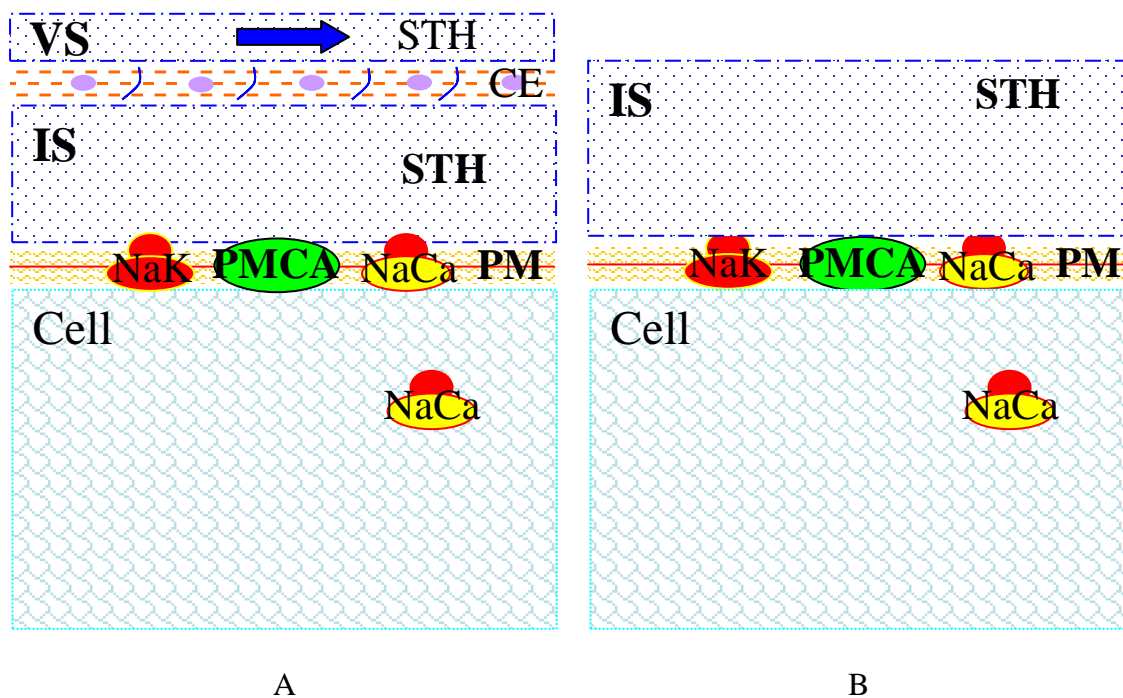


Figure 3-13. Schematic presentations of the tissue compartments. A) In a STH perfused isolated heart. B) In heart slice where vascular space collapsed. Cell: Intracellular compartment, IS: interstitial space, VS: vascular space, PM: plasma membrane, CE: capillary endothelium, NaK: Na-K pump, NaCa: Na-Ca exchanger, PMCA: plasma membrane  $\text{Ca}^{2+}$  ATPase.

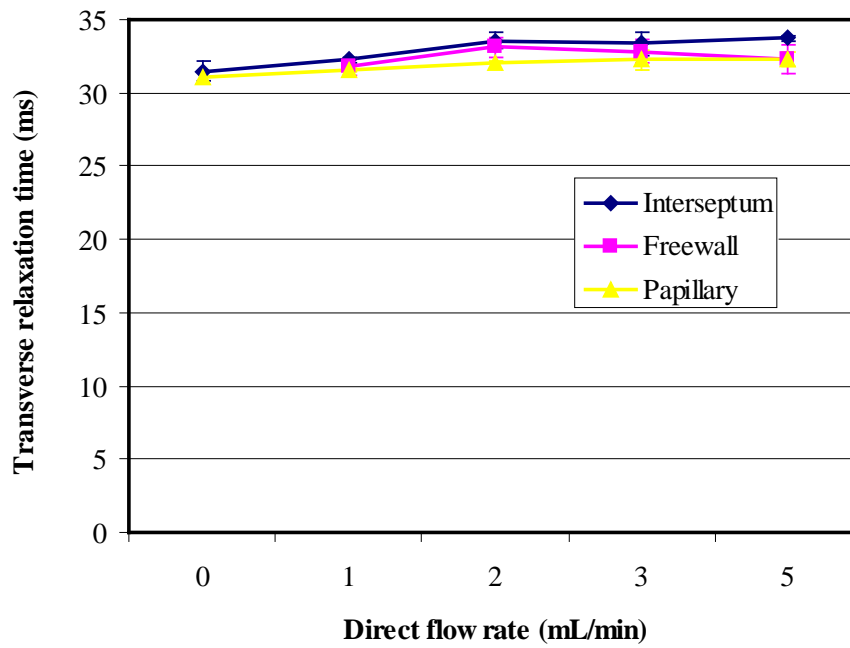
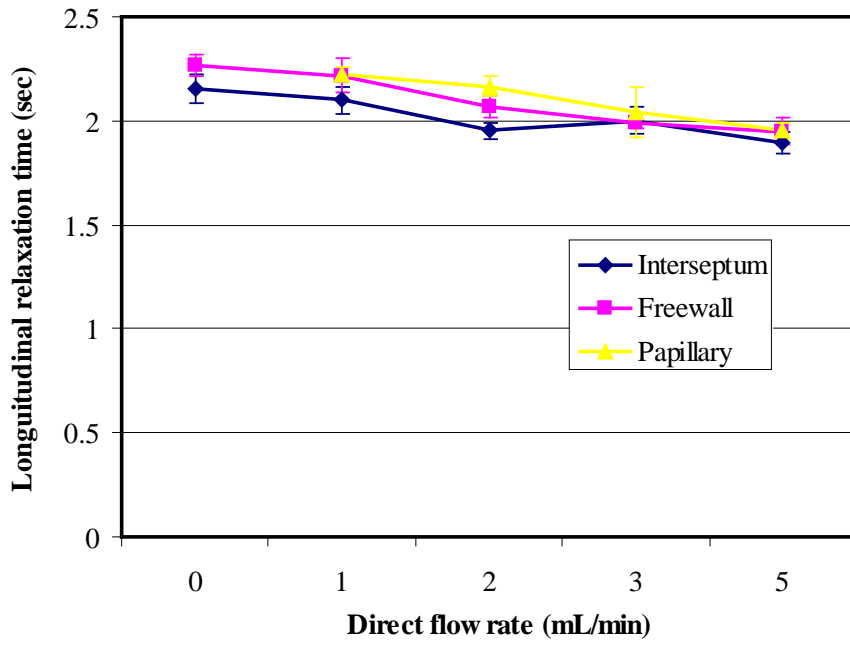


Figure 3-14. Relaxation times depending on the direct flow rate in various regions in an isolated heart.

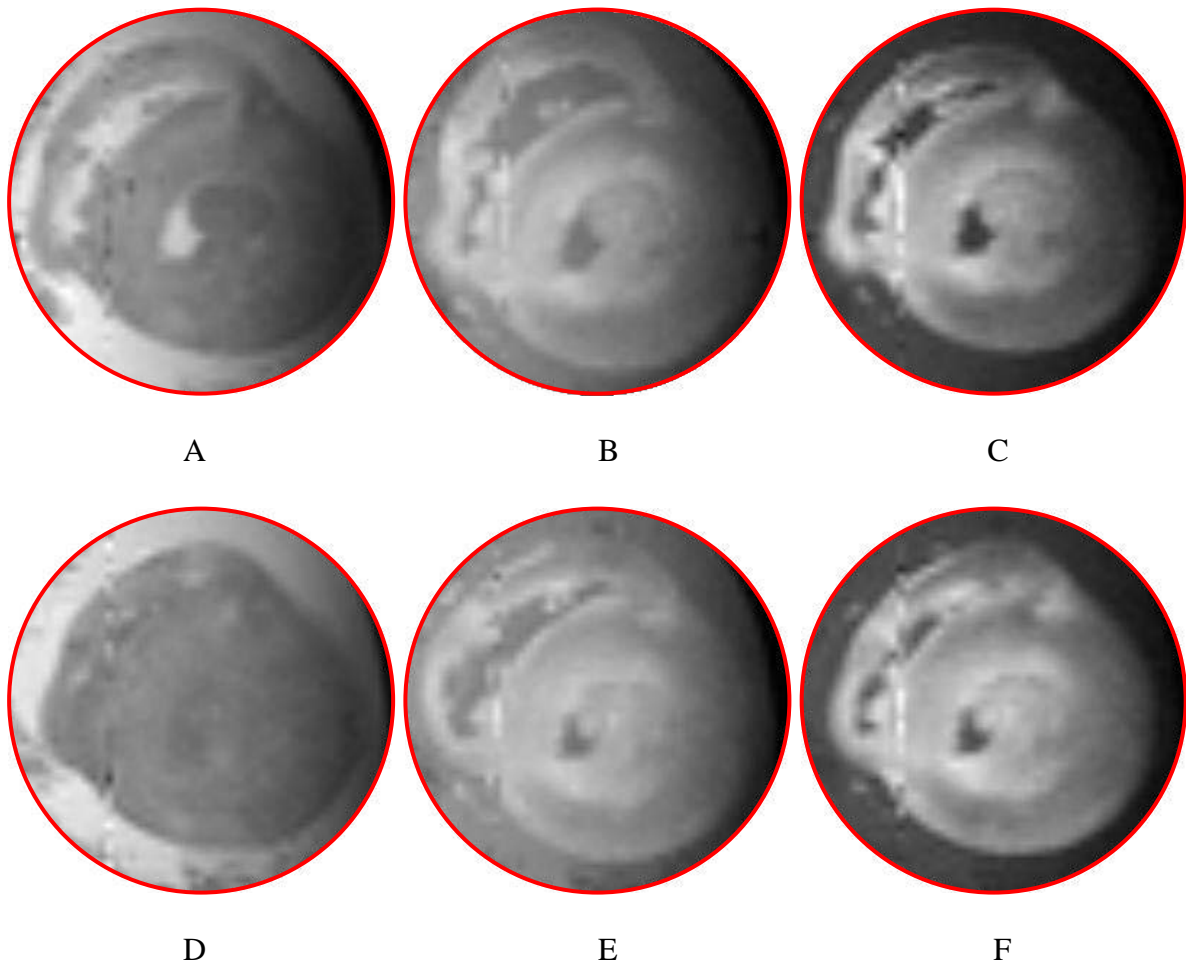


Figure 3-15. Representative MR images of an isolated rabbit heart under the STH perfusate (A, B and C) and under the PFC perfusate (D, E and F). The diffusion sensitizing factors (b values) are 0 (A, D), 450 (B, E), and 1000 (C, F)  $s/mm^2$ . Diffusion gradient is oriented vertically. Note that the left and right ventricular cavities are filled with the PFC emulsion and have lower signal intensities than ones with the STH perfusate and thus show different weighting effect on account of the lower ADC of the PFC emulsion. It may alternatively and indirectly verify that the PFC emulsion stays in the vascular space. So-called zipper artifacts are shown in the images along the vertical phase encoding direction.

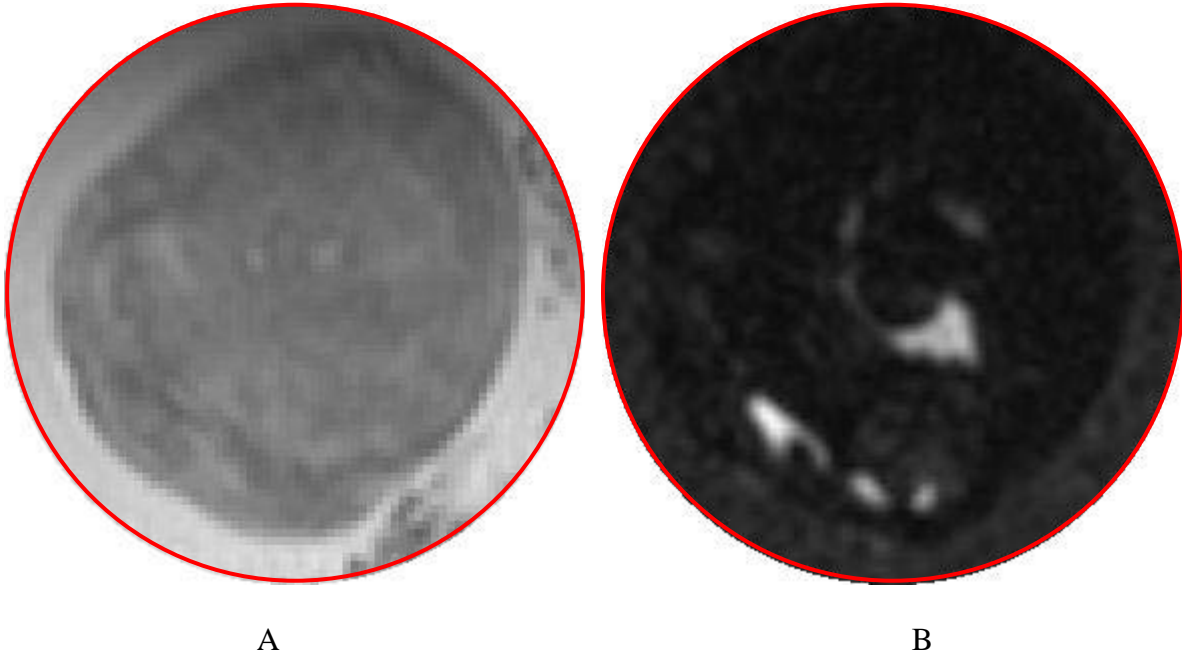
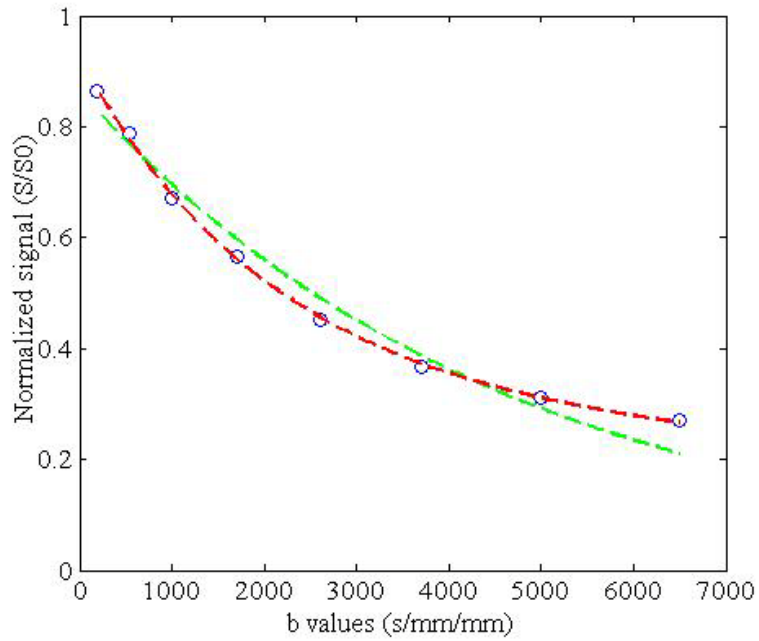
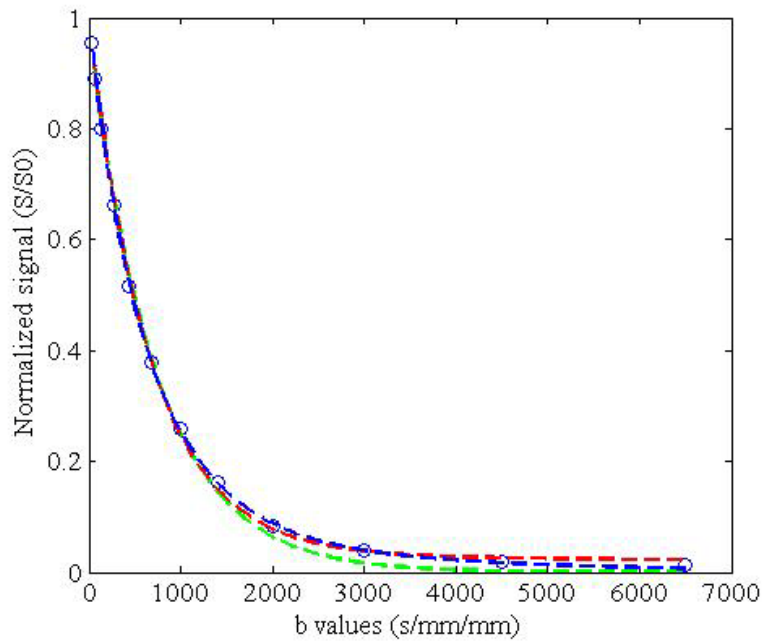


Figure 3-16. Comparison between 1H MR image (A) and 19F MR image (B) after the vascular space was replaced with PFC emulsion. Images were selected from the same slice geometry of 2 mm thickness.



A



B

Figure 3-17. Normalized signal attenuation measured. A) Heart slices. B) Isolated heart with direct flow of 1 mL/min. Data were fitted into monoexponential function (Green), biexponential function (Red), and triexponential function (Blue). A monoexponential fit to the data set gives inaccurate results.

## CHAPTER 4 NON-INVASIVE VISUALIZATION OF THE CARDIAC CONDUCTION SYSTEM USING MR MICROSCOPY

### **Introduction**

The Purkinje fibers, named after their discovery in 1845 for the man who first identified them, Jan Evangelista Purkinje, were the first part of the complex making up the cardiac conduction system (Ansari et al., 1999; Eliska, 2006). Since then, the atrioventricular bundle, the bundle of His, the atrioventricular node, the sino-atrial node, and the atrial internodal pathways were identified in that order over about seven decades. Knowledge of the conduction system was significantly expanded after Tawara (1906) demonstrated his work concerning the morphological unit of conduction transfer from the atrioventricular node to the bundle of His, bundle branching, and Purkinje fibers.

Due to the difficulty in studying the finer components of the distal conduction system, only with recent technical advances has the Purkinje-ventricular muscular junction been identified (Ansari et al., 1999). At present, the cardiac conduction system, which is able to generate spontaneous electrical impulses and conduct them to the working muscles of the whole heart, is known to start at the sino-atrial node, situated at the junction of the anterior circumference of the superior vena cava and the right auricle (Ansari et al., 1999; Dun and Boyden, 2008; Eliska, 2006). And the conduction pathways reach the atrioventricular node (AV node) localized between the coronary sinus and the septal leaflet of the tricuspid valve in the Koch triangle by so-called atrial internodal pathways. Beneath the AV node, the connecting bundle (bundle of His) starting at the atrial part penetrates into the atrioventricular membranous septum, connecting the atrium and the ventricles (Anderson and Becker, 1980). The connecting bundle then divides into the left and right branches beneath the membranous part of ventricular

septum (Sheets et al., 1983). The conduction system terminates at the Purkinje–ventricular muscular junction within the ventricular myocardium (Nakamura et al., 1986).

This impulse-conducting system that coordinates the cardiac cycle is a feature of a highly heterogeneous structure in the sense that the anatomical make-up of the system has intrinsic differences in cell size, cell type distribution, complex electromechanical properties, and activation sequence (Katz and Katz, 1989; Kohl, 2003; Davies et al., 1983). The properly integrated function of myocardial conduction system requires the well-orchestrated interplay of multiple heterogeneous components for synchronous and reliable cardiac contractions. Thus, detailed insight into the anatomy of the conduction system would be greatly essential to understand the homogeneous cardiac performance arising from well-coordinated electro-mechanical activity and further for the investigation of cardiac function and morphology in both normal and abnormal (pathophysiologic) states (Bishop et al., 2010; Burton et al., 2006; Goodyer et al., 2007; Vadakkumpadan et al., 2009, Davies et al., 1983).

To date, the techniques most commonly employed to study the cardiac conduction system include mapping from the histological serial sectioning (usually only a few micrometers in thickness), micro-dissection, endocardial staining, and direct ink injections (Burton, et al. 2006). However, these techniques are invasive, and use intrinsically destructive procedures with limitations when trying to trace the individual bundles or branches of the conduction system. Moreover, three dimensional reconstruction of the Purkinje fiber network using histological data is extremely difficult and time consuming. Consequently, the need for a non-invasive method suitable to describe the conduction system and the anatomical features of the heart makes magnetic resonance imaging (MRI) an especially promising modality (Beg et al., 2004). In this

experimental study, we performed MR microscopic (MRM) imaging using a 17.6 T magnet to demonstrate the conduction pathways as well as anatomical details of isolated rabbit hearts.

### **Materials and Method**

All animal protocols were in accordance to the guidelines approved by the Institutional Animal Care and Use Committee (IACUC) in the University of Florida.

#### **Isolated and Fixed Heart Preparation**

Isolated then arrested hearts, as described previously, were used for this experiment (Jennings, 1976). Briefly, New Zealand White male rabbits (N = 3, 2-3kg body weight, Harlan) were anesthetized using a mixture of ketamine/xylazine (40mg/kg: 10mg/kg, i.m.) followed by heparin (1000 U/kg, i.v.) and then were exsanguinated. The heart and lungs excised after sternosection were briefly placed in a bath of cold (4°C) cardioplegic solution. They next were transferred to a Langendorff apparatus and perfused retrogradely. After the descending aorta was cannulated, the lungs were ligated and removed rapidly. Tissue and perfusate were maintained at 37°C via a water-filled heat exchange unit. The perfusate was continually equilibrated with a 95% O<sub>2</sub>-5% CO<sub>2</sub> gas mixture using a membrane oxygenator. The initial perfusate was a modified Krebs Henseleit buffer, containing (in mM) 118.0 NaCl, 25.0 NaHCO<sub>3</sub>, 5.0 dextrose, 4.6 KCl, 2.5 CaCl<sub>2</sub>, 1.2 KH<sub>2</sub>PO<sub>4</sub>, 1.0 MgSO<sub>4</sub>, and insulin (50 mU/mL). An initial perfusion period of 10 min was used to wash the red blood cells out of the vascular space, permit the heart to contract normally, and the aortic valve to seat properly. A thin (1 mm in OD) polyethylene tube was inserted in the left ventricle (LV) serving as a vent to avoid excess hydrostatic pressure accumulation and distension of the LV from Thebesian flow. In order to avoid motion-induced artifacts during 3D MR imaging, the heart was arrested prior to imaging by switching perfusate to a modified St. Thomas' Hospital (STH) cardioplegic solution that consisted of (in mM) 110.0 NaCl, 16.0 MgCl<sub>2</sub>, 16.0 KCl, 10.0 NaHCO<sub>3</sub>, 5.0 dextrose, and 1.2

CaCl<sub>2</sub>. These experiments were run at ambient temperature (18 - 19°C), and equilibrated continuously with a 95% O<sub>2</sub>- 5% CO<sub>2</sub> gas mixture resulting in a pH of 7.4.

The isolated hearts were fixed in situ during an intravascular formalin-perfusion fixation procedure that was carefully standardized. And the fixed hearts were kept in a refrigerator between MR imaging experiments. Two days prior to the imaging, the hearts were transferred into phosphate buffered saline (PBS) to minimize the effect of the fixative upon T2 relaxation time, giving enough time for the water molecules to diffuse in the samples (Shepherd et al., 2009). Fluorocarbon solution (FC-43, Fluorinert, 3M, St. Paul, MN) was used as an imbedding material for the MR microscopic imaging since this non-toxic and proton-free solution prevents dehydration, decomposition, or movement of the isolated hearts during the long scan time (Benveniste and Blackband, 2002). In particular, before immersing the samples in a 25 mm NMR tube holding Fluorinert, time was spent to eliminate air bubble contamination, which might result in image artifacts due to susceptibility mismatch, by rinsing gently the inner and outer heart with the same solution. As soon as the imaging experiments were finished, the isolated hearts again were rinsed with the STH cardioplegic solution and immersed back in the formaldehyde solution until the next histological study.

### **Magnetic Resonance Imaging**

MR experiments of isolated hearts (n = 5) were performed on a 17.6 T / 89 mm vertical wide-bore magnet (Bruker Instrument spectrometer and console, Billerica, MA). The RF coil used for the in vitro imaging was an Alderman-Grant birdcage coil, diameter = 25 mm, length = 35 cm. The temperature in the magnet was maintained at 19 - 20°C. Three dimensional high resolution MR image data were collected using a fast gradient echo pulse sequence, achieving a voxel resolution of 35.2 μm x 35.2 μm x 82 μm with a matrix size = 710 x 710 x 256 in the field of view of 25 mm x 25 mm x 21 mm. Imaging parameters implementing relatively T2\*-

weighting were TR = 150 ms, TE = 18.5 ms, 1 average, sampling bandwidth = 20 k. The pilot images with three orthogonal planes were collected to check whether or not the isolated heart imbedded in the dense FC-43 solution had moved during the relatively long scans.

### **Data Analysis**

Volume renderings of the 3D MR data sets were performed using ImageJ (ver. 1.31, <http://rsbweb.nih.gov/ij/>) in the transverse, sagittal, and coronal directions to trace form the atrioventricular connecting bundle and its left and right branches in the ventricular septal muscle down to the termination of the conduction path, the so-called Purkinje-ventricular junction. Volume rendered MR images of the conduction system were compared with optical images of acetylcholine esterase staining and histological images.

### **Results**

The conduction pathways in isolated hearts were visualized from the bundle branches to Purkinje-ventricular junction using the high resolution 3D MR images sectioned non-invasively and reproducibly with appropriate views and cuts. The anatomical landmarks were used to enhance our confidence in the interpretation that the observed structures represent the conduction paths (Figure 4-1). Volume rendered MR images of isolated hearts with similar age did not show significant variations. In particular, the left ventricle showed less inter-specimen variation. Figure 4-2 demonstrates how far downward the left bundle branch(es), endocardially bound in the upper half of the ventricular interseptum, extend(s) and are associated with their divisions and terminates the path in the lower half of the left ventricle. While endocardial-bound left bundle branches in the upper half of the ventricular septum usually descend along trabeculations in relatively smooth endocardium (yellow box), the branches in the lower half do not just descend along greatly uneven trabeculations, but also anastomose across them. Figure 4-3 demonstrates that a relatively large tendinous fiber-like cord, a fascicular left bundle branch,

originates from the membranous part of the ventricular interseptum and separates into a variety of divisions approximately midway of the ventricular interseptum. Then the divisions of the left bundle branch cross freely the left ventricular chamber, or divide into twigs during flying the left ventricular cavity, or are connected with other branches in their adjacent parietal/septal inner wall portions, or reach the conical masses of the anterior or posterior papillary muscles (Figure 4-4). Seen overall, tendinous fiber-like cords that have various thickness and length form a dense polygonal reticular net in the left ventricular cavities and inner wall, the free-running Purkinje fiber network. Groups of the free-running Purkinje fibers directly attach the papillary muscles and then form the circling plexus going down toward the place in which the muscle is anchored, occasionally leaving the apical part of the papillary muscles devoid of any superficial branches of the conduction paths.

Figure 4-5 shows that a relatively thin free-running Purkinje fiber in the RV cavity, having a septal attachment in the middle of the ventricular interseptum, is visible near the medial papillary muscle. The right bundle branch appears to have a track back to where the bifurcation of the left and the right bundle branch occurs (see Discussion section). Distally, the branches divide into several twigs and spread in various directions. The free running Purkinje fibers connecting directly from the ventricular septum to the parietal wall were also observed.

### **Discussion**

The volume rendered images from the original 3D MR data, achieving a 35  $\mu\text{m}$  in-plane resolution and generating an adequate T2\*-weighted image contrast (150 ms/18.5 ms of TR/TE) made it possible to non-invasively and reproducibly trace the conduction paths in the left and right ventricles, as well as to describe the micro-anatomical features of the heart. To the best of our knowledge, this is the first instance of in situ non-invasive conduction path visualization from the left and right bundle branches to Purkinje-ventricular junction using MR microscopy.

Using the novel technique that the MRI provides, we especially tried to explore non-invasively the right bundle branch path in the ventricular interseptum.

### **Visualization of Free-running Purkinje Fiber Network**

The peculiar Purkinje fiber system in the left ventricle has recently been represented using high resolution 3D MRI for the purpose of developing image based cardiac ventricular computational model (Beg et al., 2004; Bishop et al., 2010; Burton et al., 2006; Vadakkumpadan et al., 2009). Frequency of junctions between pairs of the free-running Purkinje fibers and junctions between the free-running Purkinje fibers and the myocardium were informed, which should increase prediction accuracy using the model (Bishop et al., 2010). However, due to down-sampling for practical computation of the high resolution MR data, partial loss of anatomical features such as endocardial bound and/or free-running Purkinje fibers in the ventricular cavity might be inevitable. In our study, since MR signals from the ventricular cavity and the coronary vessels were eliminated by filling the spaces with the proton-free solution, we were able to trace and extract in situ pathways of the Purkinje fibers in the right ventricle as well as in the left ventricle without loss or confounding factor. The features of free-running Purkinje fiber network visualized using microscopic MR image showed close resemblance to the real-like pattern exposed by the optical images of acetylcholine esterase staining (Figure 4-4). This exhibits promising eligibility of microscopic MRI to monitor the micro-structural change of the network in aging or pathological condition. In addition, the integrative views of the conduction path from the base to the apex of the heart might enable systemic examination of the conduction path, which was not available with serially sectioned histological data.

The papillary muscle together with the free-running Purkinje fibers attached has been frequently used to measure the electrical conduction delay between the bundle branch and the termination of the Purkinje fibers and the Purkinje fiber-ventricular junction (Hondeghem and

Stroobandt, 1974; Trandum-Jensen et al., 1991). Histological analyses in the previous studies demonstrated that the Purkinje fibers were surrounded by a perifascicular sheath of connective tissue from the left and right bundle branches to their termination at the Purkinje fiber-ventricular myocyte junction (Ansari et al., 1999). The role of the sheath, like the myelin sheath surrounding the axon in peripheral nerves, is known to prevent the lateral propagation of the electrical impulse and only permit the conduction cascade to finish at the termination of the Purkinje fibers, the Purkinje fiber-ventricular myocyte junction.

Besides the importance for the electrophysiological studies, the free-running Purkinje fiber network shown from microscopic MR images poses a strong question about the peculiarity of the dense reticular net. Since the Purkinje fibers play essential roles in synchronizing the contraction of the normal ventricular muscle cells (Katz and Katz, 1989), the specialized fibers are not directly associated with the pumping activity that the ordinary ventricular muscles execute. However, the free-running Purkinje fibers crossing the ventricular cavities are exposed to the inflow and outflow of the blood during each cardiac cycle. Consequently, the free-running Purkinje fibers would be under cyclic forces tens of millions of times per year. Even if empty space that exists between the Purkinje fibers and the surrounding connective sheath might damp the repetitive tensile and compressive stresses imposed on the free-running Purkinje fibers, the cyclic stress at a critical frequency (fatigue stress) might arise damage to the inner Purkinje fibers and the surrounding connective tissue, similarly to the traumatic axonal damage and the demyelination, respectively. Abnormalities in the Purkinje fibers induced by the fatigue stress might affect contractions of the papillary muscles and then threaten the normal function of the mitral valve, causing mitral regurgitation or a narrowed valve. Further change in the Purkinje fibers that terminate in the ventricles, even though less drastic, might allow the wave of

activation to bypass the rapidly conducting pathways due to its lateral propagation and finally result in a fatal reduction in the synchrony of ventricular depolarization.

Studies about the mechanical property of the free-running Purkinje fibers are planned for the future study. Similarly to Indian ink injection into the space between the Purkinje fibers and the connective tissue, contrast agents such as Gd-DTPA might be injected in the space to obtain an MR image having higher resolution, which may offer greater morphological detail of the Purkinje fibers.

### **The Left Bundle Branching Forming Fan-like Structure**

The tendinous cord-like free-running Purkinje fibers that certainly make up the conduction system in the left ventricle could be traced superiorly to the site that the left bundle might ramify from the connecting bundle (Figure 4-3). This figure shows the fan-shaped arrangement that the left bundle branch makes beneath the non-coronary cusp of the aortic valve. When observed from parietal side of the left ventricle (Figure 4-4, the blue line locating serial sectioning), the left bundle branch and its small branches emerge from the septal attachment of the non-coronary cusp of the aortic valve, considered to be the membranous part of the ventricular septum. The ramifying branches move downward in the relatively smooth septal inner surface in the vicinity of the aortic valve, forming a trifascicular and further forming a fan-like structure, and continue to run anterior-inferiorly in the relatively uneven surface because of the presence of trabeculations.

Regarding the fashion in which the left bundle branch divides in the left ventricles, there have been great variations among animal species and between animals and humans. The left bundle branch of the heart of sheep, dog's, and pig's has a bifascicular structure with a cable-like arrangement. On the other hand, the left bundle branch of the rabbit heart, similarly to the patterns observed by Tawara in human hearts, radiates with three major divisions, forming a fan-

like structure in the subendocardial surface of the ventricular muscular septum (Figure 4-6). Indeed, the volume rendered images displaying the left bundle branches can be the non-invasive representation of the fan-shaped left bundle branching that Tawara (1906) and other researchers have shown using their invasive techniques (Figure 4-6). In addition, similarity of the left bundle branch of the rabbit hearts to the one of human heart may make the MRI attractive for related research using the human heart.

### **MR Images of the Connecting Bundle**

Since the atrial interseptum was not preserved during the isolated rabbit heart preparation, the atrioventricular connecting bundle (bundle of His), bridging between the atrial myocardium and the ventricular myocardium, was the most proximal part of the conduction system we tried to discriminate using the acquired MR image. Since bifurcation into the bundle branches occurs soon before the connecting bundle reached the ventricular septum, axial images that show anatomical relationships among non-coronary leaflet of aortic valve, mitral valve, and aortic-mitral continuity were explored. However, the specialized muscle fibers of the connecting bundle were hard to identify from the surrounding tissues with the achieved resolution and contrast. The 3D MR images didn't exhibit apparent differences from the ordinary ventricular muscle, which was shown in the histological image (Tawara, 1906). Thus we performed the diffusion tensor imaging to investigate whether the connecting bundle that is different from surrounding tissues in its cell size and density can be distinguished using water diffusion measurement. The result will be discussed in the next chapter.

### **Anatomical Complexity in the Ventricular Muscular Interseptum**

Volume rendered images displaying the ventricular interseptum show complex anatomical features that have never been observed in the region. Figure 4-5 shows that a free-running Purkinje fiber in the right ventricle is visible near the posterosuperior area of the medial

papillary muscle (B) and is connected to the midway of the ventricular interseptum (A). Then the Purkinje fiber embedded in the ventricular myocardium seems to have a straight track toward the base of the heart, which implies that it may be part of the right bundle branch. Similar description about the relatively thin cord-like right bundle branch has been made from the previous studies using histochemical staining (Tawara, 1906). However, possibility that the relatively large branch may be a perforating septal branch of the left descending coronary artery arises due to complex about anatomic configuration in the ventricular interseptum. Unlike tortuous other epicardial coronary branches, the perforating branch is straight and penetrates intramurally to feed the conduction system in the ventricular interseptum. Its proximity to the right bundle branch often blocks the major conduction. As a result, this implies that the branch in the ventricular interseptum of the MR images includes the perforating interseptal artery and the right bundle branches that might have very close or inter-crossed pathways (Figure 4-7).

Diffusion tensor image of the specific region in the ventricular interseptum appears to distinguish the right bundle branch from the perforating artery. Since the specialized muscle cells in the right bundle branch have structural anisotropy, directional dependency of diffusion weighted image and high fractional anisotropy may be evidenced by the existence of the conduction pathways embedded in the ventricular interseptum.

### **Non-invasive Visualization of the Intramural Purkinje Fibers**

A distinctively striped configuration was observed in the middle of the ventricular muscular septum. The lamellas of the intramural tracts were finger-like and arranged in discrete sheets side by side in the myocardium of the interseptum. The intramural tracts could be found up to the length of the myocardium in the ventricular septum. The intramural tracts appear to disappear in the top third from the base of the heart and in the bottom third toward the apex of the heart. A group of intramural tracts found in the ventricular muscular septum are suspected to

have connection with small branches from the left bundle. Hence these images imply that groups of intramural tracts might correlate with the conduction path in the region.

The Purkinje fiber-ventricular muscular junction is termination of the conduction system. With respect to the termination to date, two morphological hypotheses have been proposed in order to understand the synchrony of excitation of the big mass of the ventricular muscle by the orderly spread of depolarization waves through the small mass of the Purkinje fibers (Ansari et al., 1999). In the first model, the so-called “funnel” model, the Purkinje fiber system is seen as a branching cable, like a branching tree. Thus the conical terminal of the Purkinje fiber in the PV junction has to deliver an excitatory pulse into three dimensional ventricular myocytes (Shimada et al., 1986). This model reflects the functioning of sheep, pig, and bovine hearts. The second model, the so-called “sheet” model (Tranum-Jensen et al., 1991), suggests that the Purkinje fibers are arranged in two dimensional sheets in the subendocardium that are coupled to the deeper ventricular mass by transition areas at specific regions. Thus the resistant barrier between coupled parts would increase the propagation speed in a Purkinje fiber sheet over the endocardial surface, and thus allows synchronization of the ventricular contraction. This model reflects the perceived functioning of the human and rabbit hearts.

Considering the previous histological studies, the intramural stripes observed consistently in the current microscopic MR images might represent the intramural Purkinje fibers, which have never been observed in isolated rabbit hearts. In our case, the intramural stripes, having various shapes in different regions, were found approximately in the middle third region of the ventricular muscular septum and the free wall of the left ventricle. Since the isolated hearts were immersed in the fluorinert imbedding solution during the measurement, it is not likely that the stripes came from sample preparation or dehydration due to long scan time. A volume-rendered

image that shows a group of finger-like stripes converging on a point from that branch of the left bundle branch suggest evidence of the existence of intramural Purkinje fibers in the isolated rabbit hearts. Histochemical staining in the ventricular interseptum is currently underway in order to identify or distinguish the anatomical features shown in the MR images.

In conclusion, the MR volume rendered images with appropriate views and cut-planes demonstrate the conduction paths observed non-invasively in isolated fixed rabbit hearts. Further, those images appear to describe efficiently detailed or integrative features that are difficult to visualize with currently employed destructive techniques for identification of the Purkinje fiber because sectioning in the inappropriate direction often results in the loss of the ability to trace the desired bundle and branches. When taking into account labor and time required for sectioning of the whole heart, the intrinsic capability of MR as an efficient and integrative tool is very attractive and promising to elucidate the anatomical-function relation and to develop a working animal model, leading ultimately to application to humans.

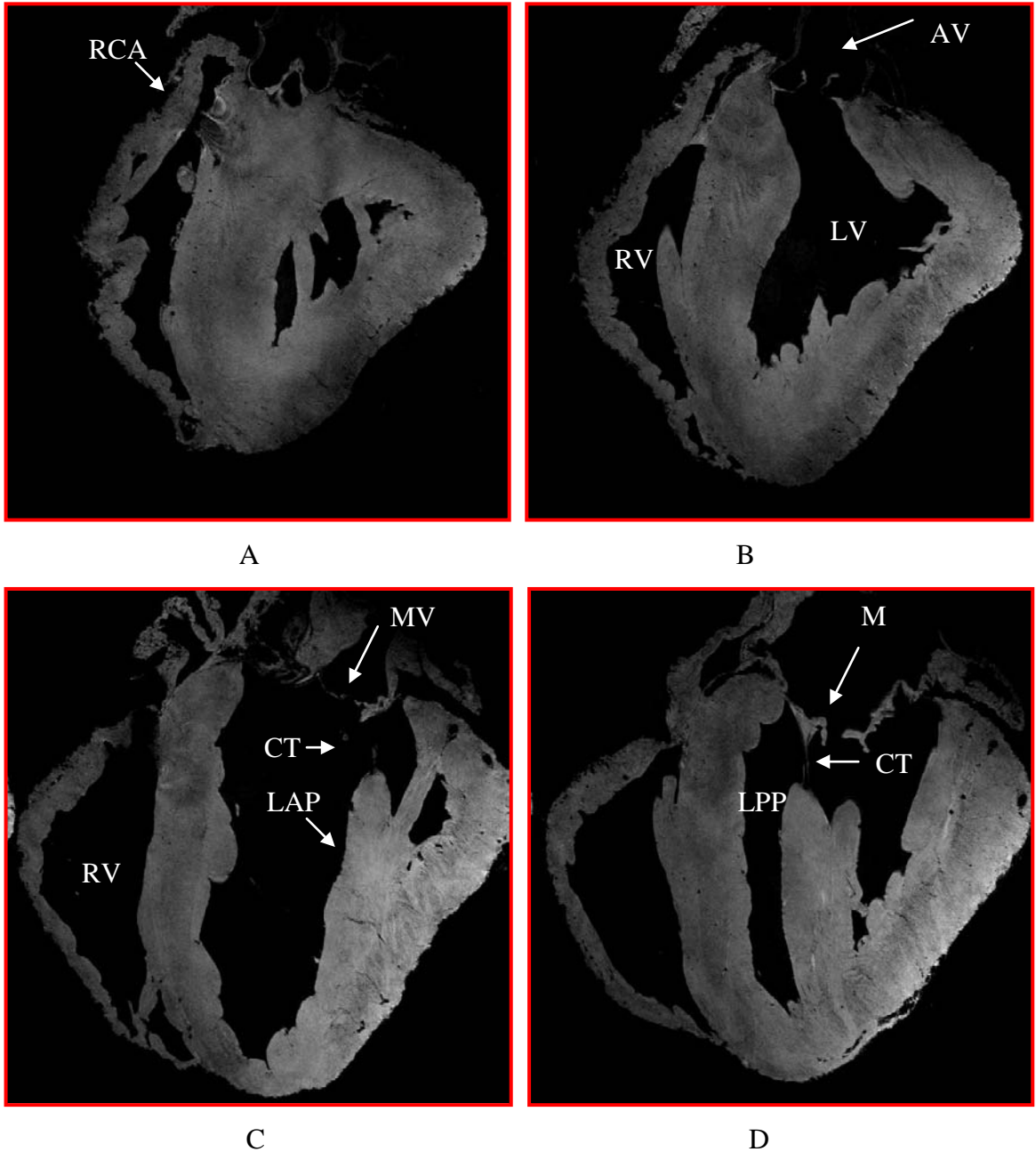


Figure 4-1. Examples of sagittal MRI slices. Individual slices from the original data sets were arranged antero-posteriorly from A to D, revealing extensive details of cardiac anatomic structures such as right coronary artery (RCA) running the right ventricle (RV), right coronary cusp (RCC) of aortic valve (AV), left coronary cusp (LCC) of AV, non-coronary cusp (NCC) of AV, anterior cusp (AC) and posterior cusp (PC) of the mitral valve (MV) and their connections to posterior papillary muscle (LPP) and anterior papillary muscle (LAP) in the left ventricular chamber by chordae tendineae (CT).

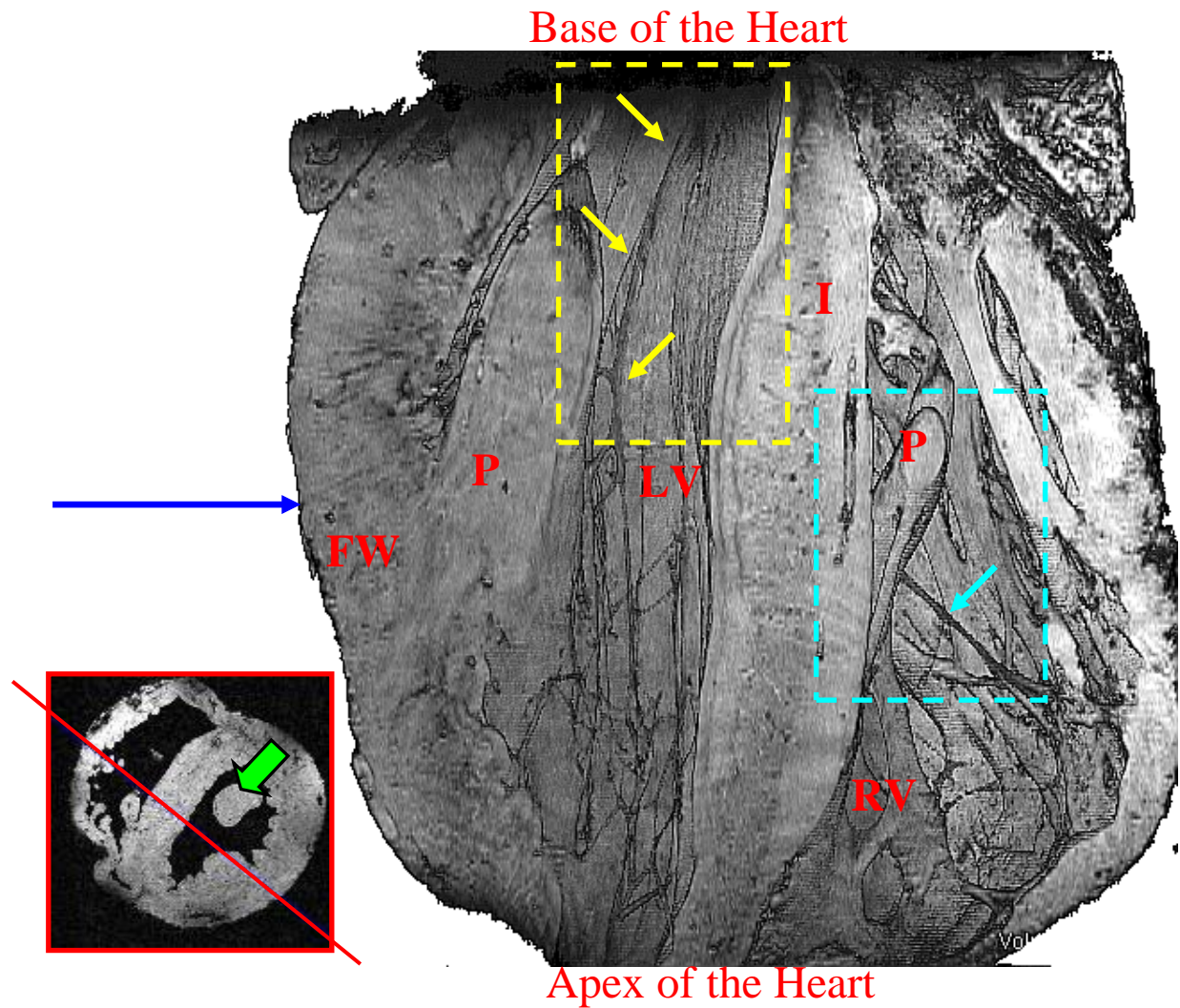


Figure 4-2. A representative volume rendered 3D MR image to visualize the conduction paths and anatomical features in an isolated heart. A red line and a green arrow in a red box indicate where sectioning occurred and viewer was located to perform the volume-rendering. Note that free-running Purkinje fibers in the left ventricular cavities, a left bundle branch (yellow arrows) in ventricular inner wall, a right bundle branch (cyan arrow) and right bundle (right, yellow circle). LV: left ventricular cavity, RV: right ventricular cavity, leaflets of the mitral valve, FW: free wall, P: papillary muscle, I: ventricular interseptum.

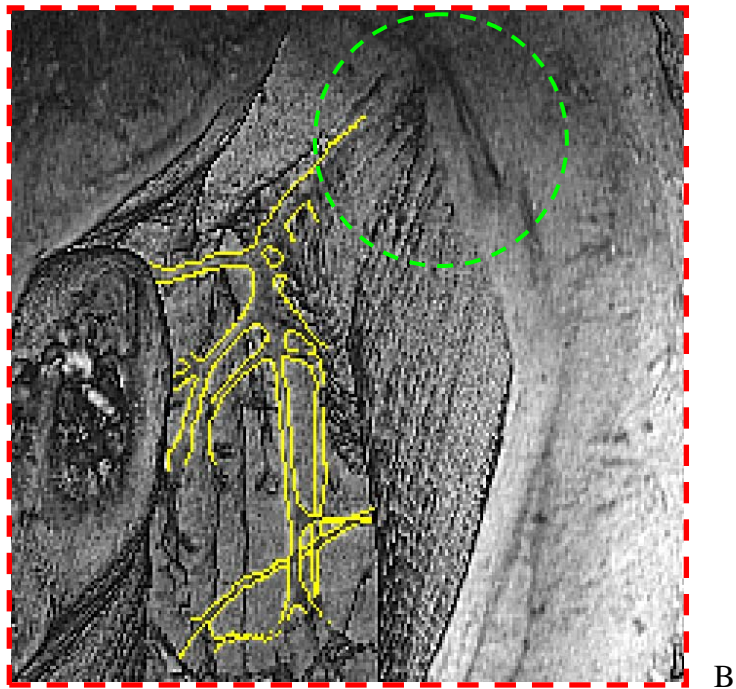
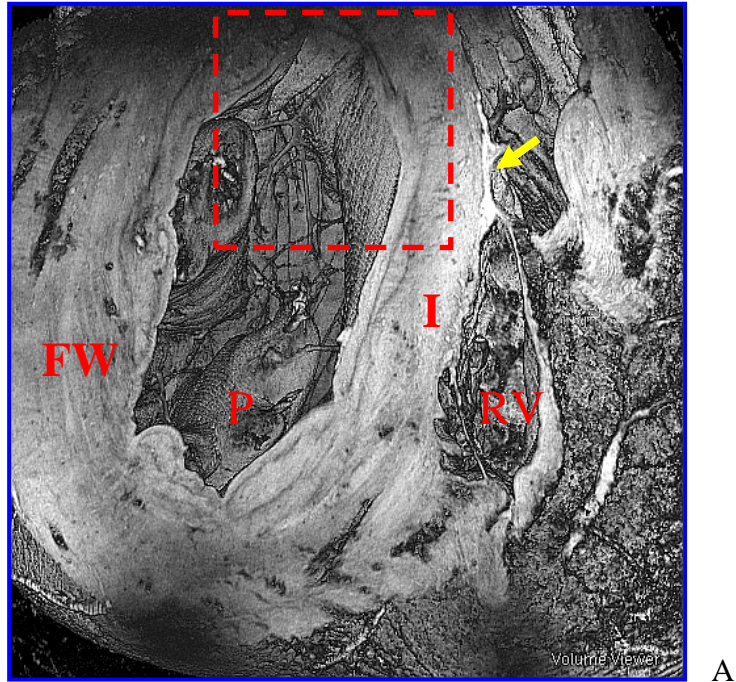
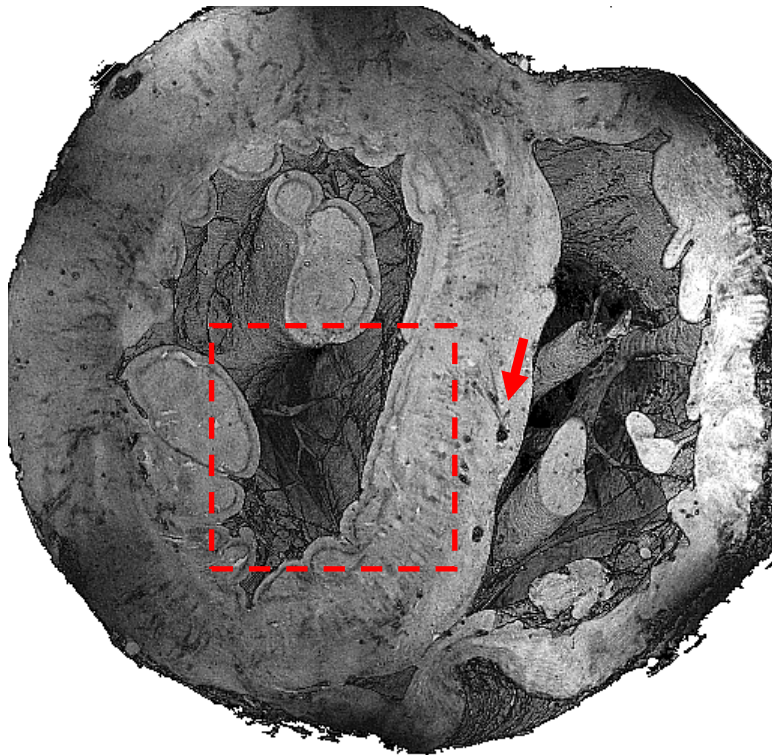
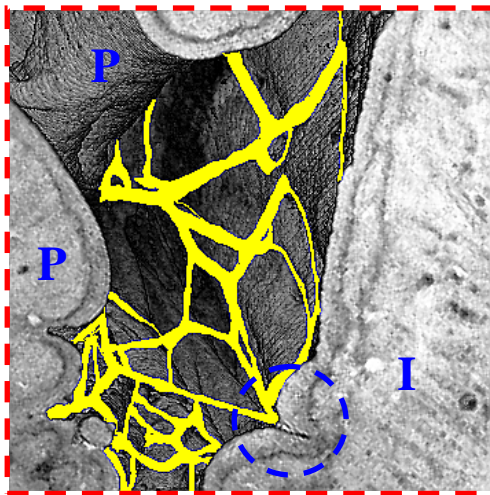


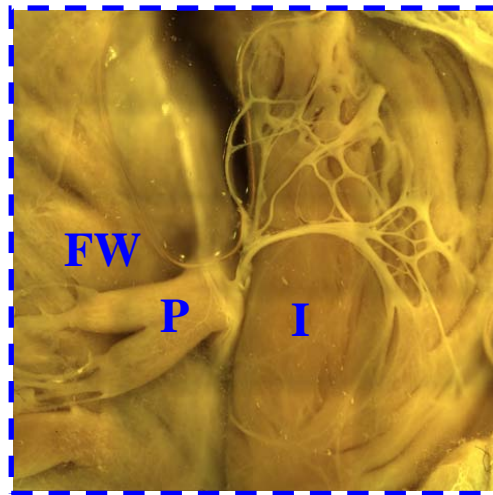
Figure 4-3. A left bundle branch bulging out of the ventricular septum (A) and its outline in an enlarged view of the small region enclosed in the dotted red box (B). Yellow arrow in A indicates the site of septal attachment of the tricuspid valve. Note the MR contrast in the green circle that may represent the fan-shaped left bundle branch. FW: free wall, P: papillary muscle, I: ventricular interseptum, RV: right ventricular cavity.



A

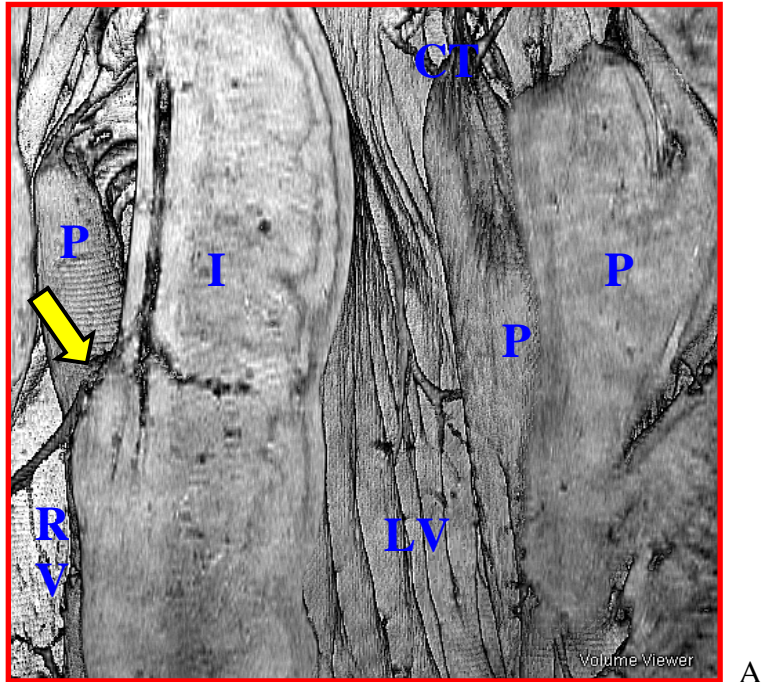


B

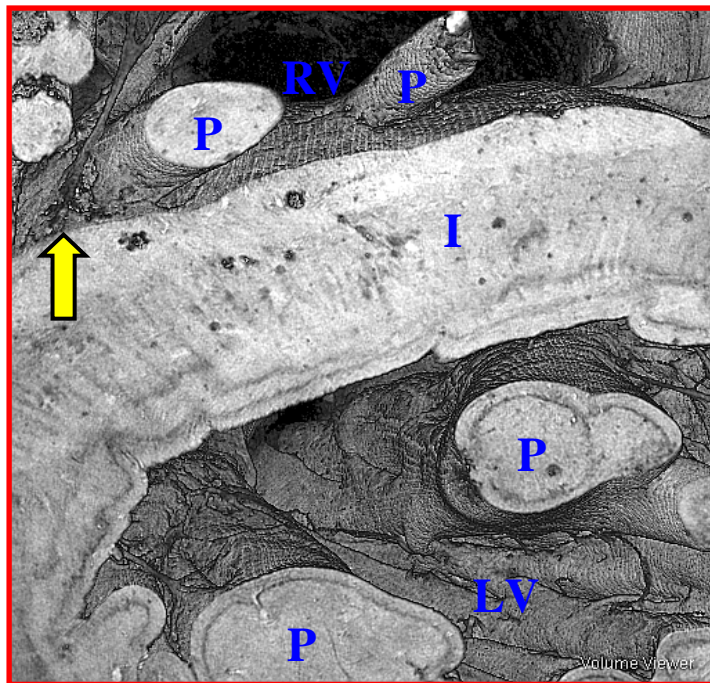


C

Figure 4-4. Demonstration of the details of polygonal free-running Purkinje fiber network in the left and right ventricular cavities. This short-axis image was viewed from the base of the heart after sectioning where the blue arrow in Figure 4-1 indicates. B) the segmented enlarged view of the small region enclosed in the dotted red box. Note how a free-running Purkinje fiber is connected with a subendocardial fringe in the ventricular interseptum (blue circle). C) An optical image of acetylcholine esterase staining around the posterior papillary muscle in the LV (folded). Note similarity of the free-running Purkinje fiber network between the segmented MR image and the stained optical image. FW: free wall, P: papillary muscle, I: ventricular interseptum.



A



B

Figure 4-5. Volume rendered images that may show septal attachment of a free-running Purkinje fiber in the RV (yellow arrows) and its continuation in the ventricular interseptum. CT: chordae tendineae, P: papillary muscle, I: ventricular interseptum, RV; right ventricular cavity, LV: left ventricular cavity.

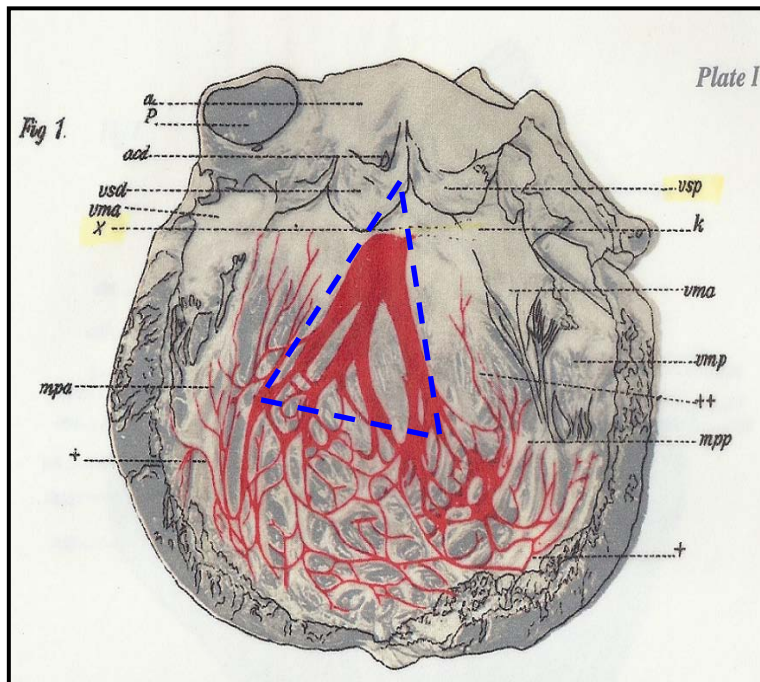
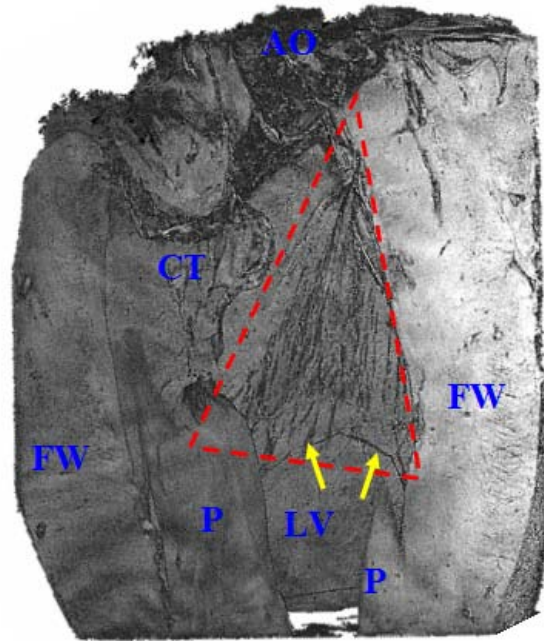


Figure 4-6. Demonstration of fan-like division of the left bundle branch of an isolated heart. A) volume rendered MR image of isolated rabbit heart. B) reproduction of illustration from the Tawara's original publication (2000). Note that fascicles of the bundle branches are connected with the free-running Purkinje fibers (arrows) in the triangle box (A). LV: left ventricle, AO: cusps of the aortic valve, FW: free wall, P: papillary muscle, CT: chordae tendineae.

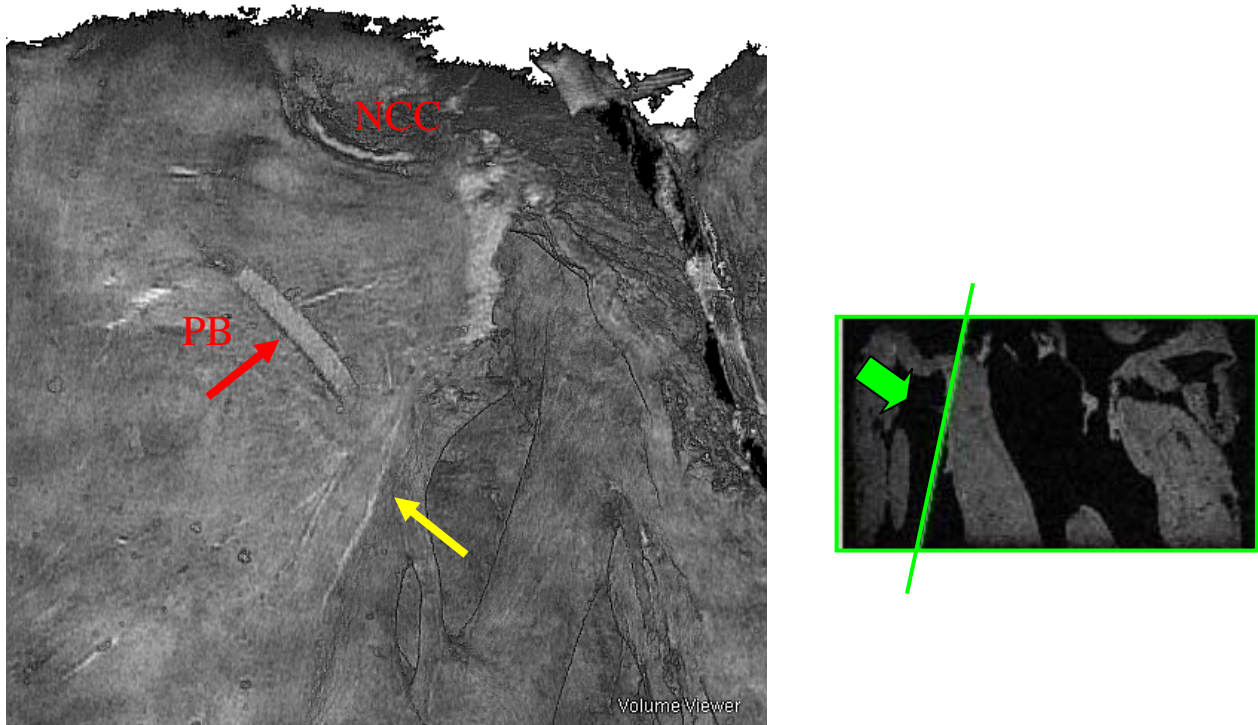


Figure 4-7. A volume rendered 3D MR image showing anatomical complexity in the interseptum contiguous to the right ventricle. This image was viewed from the right ventricle (the green arrow) after it was sectioned (the green line). Another branch (the yellow arrow) appears to exist. It is close to and/or meets with a perforating branch of the left anterior descending coronary artery (the red arrow). I: ventricular interseptum, NCC: non-coronary cusp of the aortic valve. PB: a perforating branch of the left descending coronary artery.

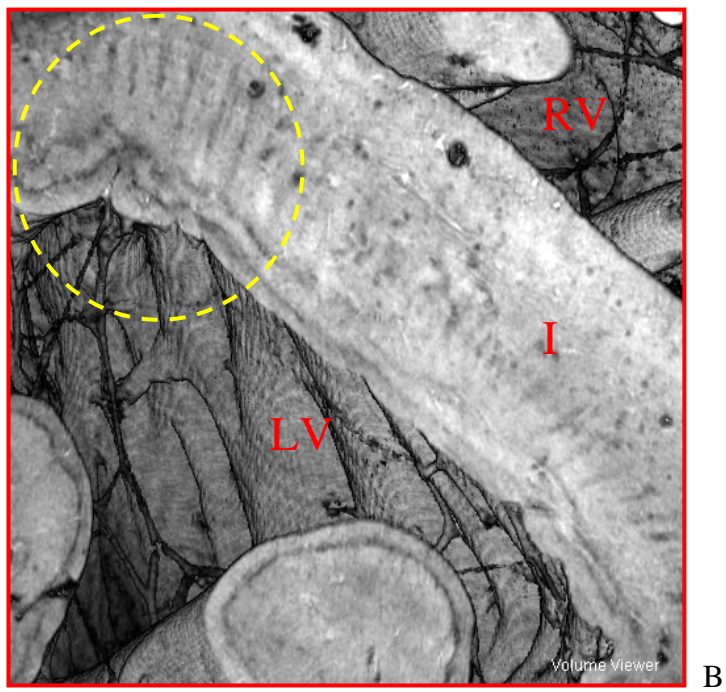
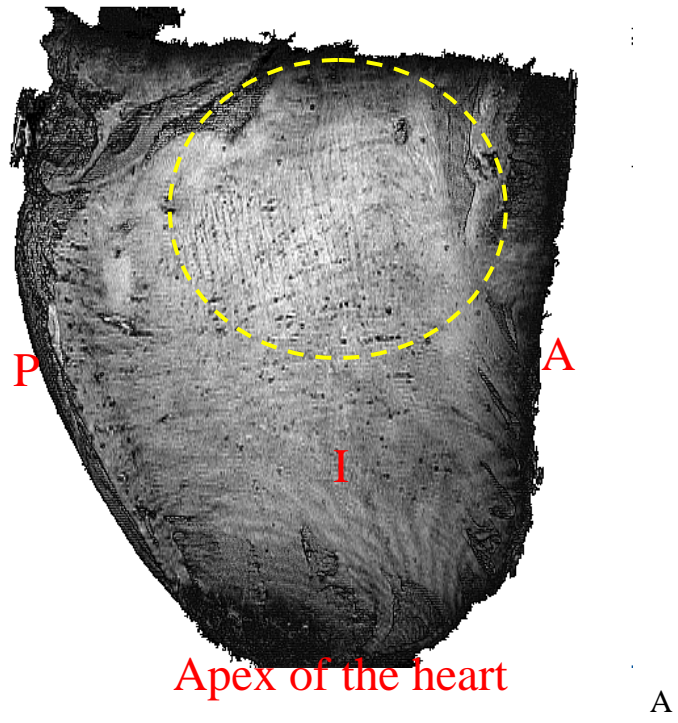


Figure 4-8. Striped patterns found intramurally in the ventricular interseptum. Note relation of the patterns with free-running Purkinje fibers in the subendocardial region (Arrow). A: anterior boundary of the ventricular interseptum (I), P: posterior boundary of I, RV: right ventricular cavity, LV: left ventricular cavity, I: ventricular interseptum.

## CHAPTER 5 MICROSCOPIC HIGH ANGULAR RESOLUTION DIFFUSION IMAGING OF ISOLATED RABBIT HEART

### **Introduction**

The heart responds to the ever-changing demands that the whole body places on the cardiovascular system. A major mechanism responsible for the spatio-temporal cardiac response over fast or slow time course is by altering myocardial contractility, called as the intricate excitation-contraction coupling orchestrated by the secondary messenger,  $\text{Ca}^{++}$  (Aliev et al., 2002). The homogeneous cardiac function is the outcome of harmonious interplay of numerous muscle cells specialized according to functions that they perform, such as contraction (normal contractile myocyte) and conduction (the Purkinje fiber) (Assaf and Cohen, 1998b; Bers, 2002; Katz and Katz, 1989; Kohl, 2003; Tranum-Jensen et al., 1991).

Those muscle cells have also various sizes, number and distributions depending on where they are located, like epicardium, myocardium, and endocardium. The complex geometry of the heart is also reflected in important heterogeneities in the mechanical conditions that govern contraction in different regions of the heart. Among the more important of it, the higher stresses developed in the endocardial regions of the ventricles. Further, considerable structural complexity exists in the extracellular space that contains blood vessels, collagen, and connective tissues, etc. (Aliev et al., 2002; Frank and Langer, 1974).

The remarkable adaptation of form to function becomes apparent when the disease alters the patterns of blood flow through the heart. For example, a narrowed valve or a defect in the ventricular interseptum creates turbulence that dissipates energy for cardiac contraction. Different hemodynamic overloads also lead to distinct abnormalities in ventricular shape, and regional wall motion abnormalities disturb the normal synchrony of contraction or relaxation, impair pump function, and reduce the mechanical efficiency of the heart. Therefore, a non-

invasive imaging that is capable of discerning the different components in the whole heart is essential for the comprehensive understanding of the structure and function of the heart in health and disease, which is a primary goal of cardiac research.

Diffusion imaging of water molecules using MR is attractive to probe the microscopic details in various cardiac cells or tissues. Diffusion tensor magnetic resonance imaging (DTMRI) has emerged to characterize structure of the cardiac tissue for a decade, with popularly spatial resolutions of tens of cellular level. This MR technique has successfully been used for nondestructive characterization of three dimensional myocardial fiber structures (Chen et al., 2005; Chen et al., 2003). Previous studies using histological data have validated that the primary eigen vector and the tertiary eigen vector derived from the diffusion tensor represent the myocardial fiber direction and the myocardial sheet structure (Assaf and Cohen, 1998b; Caravan et al., 2007; Chen et al., 2005; Hsu et al., 2001; Hsu et al., 1998b). Those have greatly contributed to understanding of the contractile myocardial fibers electrically coupled with the conductive pulses and reconstruction of the myocardial fibers that are often observed in the hearts in abnormalities. Diffusion tensor MR imaging has recently been used to develop computational models of the hearts (Vadakkumpadan et al, 2009).

In this experimental study using a 17.6 T magnet, we address the potential of microscopic high angular resolution diffusion imaging (MHARDI) achieving a cellular level spatial resolution as a non-invasive tool that is sensitive to delicate changes in the heterogeneous microstructure and arrangement of the cardiac tissues. For the first time, MHARDI of cardiac conduction pathways such as the free-running Purkinje fibers in the left ventricle and the right bundle branch in the ventricular interseptum were performed. Parameter images generated using components of the diffusion tensor were examined to follow the structures. Two MHARDI data

sets acquired with two b-values ( $1000 \text{ s/mm}^2$  and  $2000 \text{ s/mm}^2$ ) were compared to investigate whether the tensor invariants alter depending on the diffusion sensitizing factor.

### **Materials and Methods**

All animal protocols were in accordance to the guidelines approved by the Institutional Animal Care and Use Committee (IACUC) in the University of Florida.

#### **Isolated and Fixed Heart Preparation**

Isolated, then arrested hearts were used for this experiment. Briefly, New Zealand White male rabbits ( $n = 3$ , 2-3kg body weight, Harlan) were anesthetized using a mixture of ketamine/xylazine (40mg/kg: 10mg/kg, i.m.) followed by heparin (1000 U/kg, i.v.) and then were exsanguinated. A heart and lungs excised after sternosection were placed in a bath of cold cardioplegic solution ( $4^\circ\text{C}$ ). They were transferred to a Langendorff apparatus and perfused retrogradely. After the descending aorta was cannulated, the lungs were ligated and removed rapidly. Tissue and perfusate were maintained at  $37^\circ\text{C}$  via a water-filled heat exchange unit. The perfusate was continually equilibrated with a 95%  $\text{O}_2$ -5%  $\text{CO}_2$  gas mixture using a membrane oxygenator. The initial perfusate was a modified Krebs Henseleit buffer, containing (in mM) 118.0 NaCl, 25.0  $\text{NaHCO}_3$ , 5.0 dextrose, 4.6 KCl, 2.5  $\text{CaCl}_2$ , 1.2  $\text{KH}_2\text{PO}_4$ , 1.0  $\text{MgSO}_4$ , and insulin (50 mU/mL). An initial perfusion period of 10 min was used to wash the red blood cells out of the vascular space, permit the heart to contract normally, and the aortic valve to seat properly. A thin (1mm-OD) polyethylene tube was inserted in the left ventricle (LV) serving as a vent to avoid excess hydrostatic pressure accumulation and distension of the LV from Thebesian flow. In order to avoid motion induced artifact during 3D MR imaging, the heart was arrested prior to imaging by switching perfusate to a modified St. Thomas' Hospital cardioplegic solution (STH) that consists of (in mM) 110.0 NaCl, 16.0  $\text{MgCl}_2$ , 16.0 KCl, 10.0  $\text{NaHCO}_3$ , 5.0

dextrose, and 1.2 CaCl<sub>2</sub>. These experiments were run at ambient temperature (18-19°C), and equilibrated continuously with a 95% O<sub>2</sub>- 5% Co<sub>2</sub> gas mixture resulting in a pH of 7.4.

The isolated hearts was fixed in situ during intravascular formalin-perfusion fixation procedure which was carefully standardized. And the fixed hearts were kept in a refrigerator until the next MR imaging experiments. For the purpose of recovering the shortened transverse relaxation time during the fixation, at least 24 hours before the imaging experiments began, the isolated hearts in the 4 % formaldehyde solution had been moved in beakers with the STH cardioplegic solution and kept in a refrigerator, giving enough time for the water molecules to diffuse in the samples (Shepherd et al., 2009). Fluorocarbons solution (FC-43, Fluorinert, 3M, Belgium) was used as imbedding materials for the MHARDI since the non-toxic and proton-free solution prevents dehydration, decomposition and movement of the isolated hearts during long scan time (Benveniste and Blackband, 2002; Benveniste et al., 2000). In particular, before immersing the samples into a 25 mm NMR tube holding Fluoroinert, time was spent to eliminate to avoid air bubbles contamination, resulting in image artifact due to susceptibility mismatch, by rinsing inner and outer heart with the same solution. As soon as the imaging experiments were done, the isolated hearts were rinsed with the STH cardioplegic solution and immersed back in the formaldehyde solution until the following histological study.

### **Microscopic High Angular Resolution Diffusion Imaging**

High angular resolution diffusion imaging of isolated rabbit hearts was performed on a 17.6 T / 89 mm vertical wide-bore magnet (Bruker Instrument spectrometer and console, Billerica, MA). The RF coil used for the in vitro imaging was an Alderman-Grant birdcage coil, diameter = 25 mm, length = 35 mm. The temperature in the magnet was maintained at 19 - 20°C. Diffusion-weighted imaging in 21 non-collinear directions was conducted using a standard pulsed gradient spin echo (PGSE) pulse sequence, achieving an isotropic in-plane

resolution of 50  $\mu\text{m}$  and a slice thickness of 500  $\mu\text{m}$ . Diffusion sensitizing factors (b-values) were 1000  $\text{s}/\text{mm}^2$  and 2000  $\text{s}/\text{mm}^2$  using  $\Delta = 13.4$  ms and  $\delta = 1.8$  ms. Diffusion time ( $\tau$ ) was 12.8 ms. Imaging parameters were TR = 3000 ms, TE = 25.1 ms, 1 average. The pilot images with three orthogonal planes were collected to check whether or not the isolated heart imbedded in the dense FC-43 solution moved during a long scan ( $\sim 7$  hours).

### **Data Analysis**

The tensor processing of MHARDI data sets was performed using fanDTasia™ (©2008, Barmpoutis, <http://www.cise.ufl.edu/~abarmpou/>). Pixel-based analysis of selected ROIs from a variety of regions (free wall in the LV, interventricular septum, and papillary muscles in the left ventricular cavity) was conducted. The mean diffusivity (trace/3), the primary eigen value (axial diffusivity,  $\lambda//$ ), and fractional anisotropy were calculated using MATLAB (MathSoft, Cambridge, MA).

### **Results**

Magnetic resonance microscopy using a 17.6 T magnet provides successfully detailed insight into the micro-anatomical features of the whole heart, which is not available with low resolution MR images (Figure 5-1). Figure 5-2 shows twenty one diffusion weighted images of a MHARDI data set measured with b value of 1000  $\text{s}/\text{mm}^2$ . The diffusion weighted images achieving a 50  $\mu\text{m}$  in-plane resolution clearly demonstrate that diffusion weighting effect varies depending on the 21 non-collinear diffusion encoding directions. In particular, distinct pattern of stripes in the ventricular interseptum is selectively visible depending on diffusion weighted directions. Figure 5-3 shows six diffusion tensor component maps obtained from tensor estimation of the MHARDI data set (A – C, E, F, I), diffusion trace map (G), fractional anisotropy map (H). In this case  $D_{xy} = D_{yx}$ ,  $D_{xz} = D_{zx}$ , and  $D_{yz} = D_{zy}$ , resulting in the symmetric

diffusion tensor in patient coordinate system. Off-diagonal diffusion tensor images show clearly contrast regarding the discrete muscle layers in the ventricles and stripe pattern shown in the ventricular muscular septum. Figure 5-4 shows the three eigen value and the eigen vector maps derived from the six complete diffusion tensor components shown in Figure 5-3. Three discrete regions that might correlate the different muscle groups in the ventricular muscular interseptum and the free wall in the left ventricle are also observed in the color coded primary eigen vector map.

Figure 5-5 shows six diffusion tensor images (A – C, E, F, I), diffusion trace map (G), fractional anisotropy map (H) obtained from tensor estimation of a MHARDI data set measured with b value of  $2000 \text{ s/mm}^2$ . Figure 5-6 shows the parameter images derived from the six complete diffusion tensors shown in Figure 5-5. The diffusion tensor parameters depending on the two diffusion weightings are tabulated in Table 5-1. Fractional anisotropy and the primary eigen value decrease as b-value increases. On the other hand, averaged rate of water diffusion remains relatively unaffected.

Figure 5-7 and Figure 5-8 show six diffusion tensor component images (A - F) obtained from tensor estimation of a DTI data set measured in six non-collinear diffusion encoding directions with b value of  $1000 \text{ s/mm}^2$  and  $2000 \text{ s/mm}^2$ , fractional anisotropy map (G), primary eigen vector map (H), and tertiary eigen vector map (I). In-plane resolution for the images is  $500 \mu\text{m}$ . The primary eigen vector shows the spirally moving muscle fiber direction in the ventricular interseptum and the free wall. However, these images do not show the degree of details shown in the high resolution images.

Figure 5-9 and Figure 5-10 are observed to reveal structural complexity in the ventricular interseptum. Each image may reflect different structural components in the cardiac tissue such

as blood vessels, conduction tissue, and muscle fibers, all of which are contrasted differently depending on how the water molecules diffuse. When sectioning into a long axis slice adjacent to the right ventricle (the green line in H), containing only the ventricular interseptum, several branches come into sight. They seem to have different origins (Figure 5-11 and Figure 5-12).

Figure 5-13 shows the primary eigen vector map and the fractional anisotropy map of a transverse slice that display a tendinous cord of a free running Purkinje fiber that originates from a subendocardial part of the ventricular muscular interseptum and the free wall in the left ventricle. The free running Purkinje has fractional anisotropy value similar as one of the myocardium.

### **Discussion**

These results demonstrate that microscopic high angular resolution diffusion imaging (MHARDI) may be sensitive to distinguish different structural components in the isolated rabbit heart. Transmural and regional heterogeneity reflected in the six tensor components and the tensor invariants may represent the structural diversity in the cardiac tissue embedded in the proton-free Fluorinert solution. This has not been available in previous diffusion MR studies.

### **Diffusion Parameters Depending on B-values**

A bi-exponentially fitted diffusion signal attenuation curve shown in Figure 5-14 implies that the diffusion MR signal from the isolated rabbit heart can be biased to the fast component or the slow component of diffusing water pools depending on the diffusion sensitizing factors. In case of b value of  $1000 \text{ s/mm}^2$ , the fast diffusing water molecules might contribute more in the measured diffusion weighted signal. Conversely, the slow diffusing molecules contribute more to the diffusion MR signal measured using a b value of  $2000 \text{ s/mm}^2$ . Table 5-1 shows change in the diffusion parameters depending on the b-values. Since no morphological change in a cellular level would have occurred during the consecutive MHARDI measurements that took about 16

hours, decrease of the fractional anisotropy and decrease of the primary eigen value at a high b-value of  $2000 \text{ s/mm}^2$  should result from increase in contribution from the slow component to the diffusion signal. This variation in the diffusion parameters may suggest that careful attention should be paid to the analysis of diffusion parameters measured with different b-values. In particular, direct comparison among published data, when measured using different b-values, might result in incorrect assumption about cellular change and change in tissue compartments.

As shown in recent studies regarding contribution of biological tissue compartments to the diffusion MR signal (Flint et al., 2009b; Jin and Kim, 2008), mechanism in which the fast and/or the slow diffusing water molecules in the intra/extracellular compartments contribute to the diffusion MR signal is still matter of discussion. Jin et al. (2006) attributed a lack of ADC change in stimulated visual cortex to vascular effects. In contrast, Flint et al. (2009a) demonstrated that the ADC decrease in de-vascularized brain tissue could result from significant increase (around 50 %) of the slowly diffusing water molecules in activated swollen cell. Current study implies that the decreased ADC by cellular volume increase might be underestimated if the MR signal was measured with b-values less than  $1000 \text{ s/mm}^2$ . Relatively low ADC change (Le Bihan et al., 2006) or a lack of ADC change in controlled tissue suggests that effects from the vasculature (contributing to the fast diffusing pool) and the cell volume change (contributing largely to the slow diffusion pool) might be counterbalanced. Diffusion imaging using high b-values might be necessary to monitor directly change in cellular volume with higher sensitivity or separate two counter balancing effects. In this case, low signal intensity by high b-value might impact the accuracy of the diffusion parameter measurements. Acceptable signal could not be obtained in the MHARDI of using b values higher than 2000

s/mm<sup>2</sup> while maintaining the resolution. Another effective method to overcome the low diffusion signal may be necessary for a high b-value MHARDI.

### **Diffusion MR Imaging of the Free-running Purkinje Fibers**

To my knowledge, Figure 5-13 demonstrates for the first time microscopic diffusion MR image of the free-running Purkinje fiber in the left ventricles. Since the tendinous cords in the ventricular cavity truly contain the conductive Purkinje fiber cells and the connective tissue wrapping around them (Ansari et al., 1999; Tawara, 2000), the primary eigen vector might represent the Purkinje fiber direction. Compared to the contractile myocardial muscle cell, The Purkinje fiber muscle cells have relatively more isotropic and larger cell types. This may explain the lower fractional anisotropy observed in the Purkinje fibers (Eliska, 2006). These results make MHARDI be very attractive to visualize anisotropic water diffusion in the Purkinje fiber non-invasively. Progress of diffusion MR imaging of the cardiac conduction pathways will be made through future studies.

The Purkinje fibers attached to the papillary muscles may be used for non-invasive monitoring of electrophysiological function in the Purkinje fiber and papillary muscle. Flint et al. (2009b) have recently been able to generate diffusion weighted image of a mammalian neuronal cell in an activated state by combining the micro MR imaging and an advanced slice preparation technique. This advance using MR microscopy will make it feasible to acquire diffusion MR image of the Purkinje fibers, in-situ, when the fibers undergo morphological changes related with delivering conducting pulses or the conduction delay at the Purkinje fiber – papillary muscle junction (Hurst et al., 1988; Ansari et al., 1999). The relatively large Purkinje fiber cell will reduce partial volume effect that tends to enforce increase in the resolution at the cost of signal intensity or image contrast. The structural alterations of the Purkinje fibers that occur in aging or pathological heart may also be investigated using MHARDI.

## **Diffusion MR Imaging of the Ventricular Muscular Interseptum**

The primary eigen vector generated from the diffusion tensor imaging performed with a 500  $\mu\text{m}$  in plane resolution appears to follow the myocardial fiber direction that varies spirally in a short axis plane in isolated rabbit heart (Figure 5-7 and Figure 5-8). On the other hand, stripe patterns are visible transmurally in the ventricular interseptum in the diffusion weighted images performed with a 50  $\mu\text{m}$  in-plane resolution. These finger-like structures have not been observed in previous cardiac diffusion MR studies. Hence these results suggest that, in cardiac MHARDI achieving an in-plane resolution of cellular level, the primary eigen vector might not just represent the myocardial fiber directions that vary helically in the transmural direction.

The fractional anisotropy and the eigen vector maps imply that the finger-like structures may describe another tissue component that is not associated with either the myocardial muscle fiber or the myocardial muscle sheet. Size of a myocardial muscle cell in rabbit heart is approximately 120 ~ 130  $\mu\text{m}$  in length and 25 ~ 30  $\mu\text{m}$  in width (Caravan et al., 2007; Hsu et al., 2001; Hsu et al., 1998b). This means that each pixel in the MR images includes only one or two myocyte(s). Fractional anisotropy values imply that the stripe patterns have structural integrity that restricts diffusion of water molecules. Thus we suspect that the stripe patterns may be correlated with cardiac tissue components such as the Purkinje fibers or the myocardial collagen in the interstitial space.

Since isolated hearts used in current study were flushed with and embedded in the Fluorinert solution, it might penetrate into the interstitial space through through the capillary epithelium. This might make the interpretation more complicated. However, even if the penetration occurred, so the local penetration effect is still under question. Diffusion MR imaging of isolated hearts embedded in the STH cardioplegic solution or in the PBS solution

may examine the effect of the embedding materials. Histological study using the neurofilament staining is currently under way to identify the new structures observed in the MR images.

Figure 5-9 ~ Figure 5-12 show diffusion MR images that delineate anatomical structures in the ventricular interseptum. Despite the fact that the ventricular interseptum is the major site that the right bundle and the left bundle go through to deliver electrical impulses into the contractile myocardial cells, the details about this region have not been observed non-invasively. In particular, pathways of the right bundle in the ventricular interseptum have rarely been described non-invasively.

The intramurally perforating branches of the left descending coronary artery play a major role to supply the conduction path in the ventricular interseptum. The perforating arteries begin from the left coronary artery, and the right bundle begins nearby the non-coronary cusp of the aorta. Due to this close proximity in distance, the perforating artery was observed to block the conduction at the right bundle. The volume rendered MR images in Chapter 4 visualized a free-running Purkinje fiber in the right ventricular cavity as a distal part of the right bundle branch. The free-running Purkinje fiber was observed to attach directly to the ventricular interseptum, and to merge soon with a vessel in the interseptum. Then the merged branch could be traced upward along the ventricular interseptum. Thus we suspected that the volume rendered images might demonstrate the right bundle that is in close proximity to the intramural branches of the left descending coronary artery in the ventricular interseptum. The current results demonstrate that MHARDI may distinguish the tissue components in the ventricular interseptum, perforating arteries and the right bundle.

We infused the Fluorinert solution in the ventricular cavities just before the isolated heart was placed in the magnet, for the purpose of removing the MR signal from the ventricular

cavities. As a result, part of the large blood vessels, maybe located at the vicinity of the left coronary artery, might be occupied with the proton-free Fluorinert solution. These might correspond to a dark region in the MR images. However, regardless of whatever the vascular space is filled with, diffusion in the large vessel should be intrinsically isotropic during the diffusion time (12.8 ms), and low fractional anisotropy (FA) and high mean diffusivity would indicate existence of the vasculature.

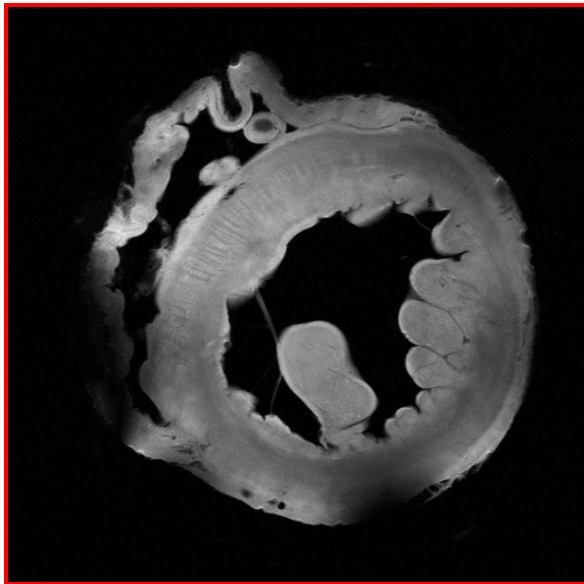
In that region, fraction anisotropy and mean diffusivity that are comparable to ones of the myocardium reflects structural integrity by restricted diffusion, and thus distinguish the specialized muscle cells comprising the right bundle from the coronary vessels. As mentioned in the previous section, the Purkinje fiber muscle cells, compared with the contractile myocardial muscle cells, are known as larger in size and isotropic in shape. Thus the FA values, which are a little lower than ones FA of surrounding muscles, may be used to discern the two cellular components, the Purkinje fiber muscle fibers and the contractile muscle fibers. Anisotropy found in the off-diagonal diffusion components may indicate the existence of the conduction fibers. The primary eigen vector in the specific region (the yellow box) may indicate the directionality induced by anisotropic water diffusion.

From these results, we suspect that the structure accompanying the perforating artery may be a branch of the right bundle branch. Integrative analysis using diffusion tensor component maps and diffusion parameters may be used to distinguish the two structures that are intermingled in the ventricular interseptum. Histological study using neurofilament is currently underway to locate the right bundle enclosed in the ventricular interseptum. This will be used to validate our analysis.

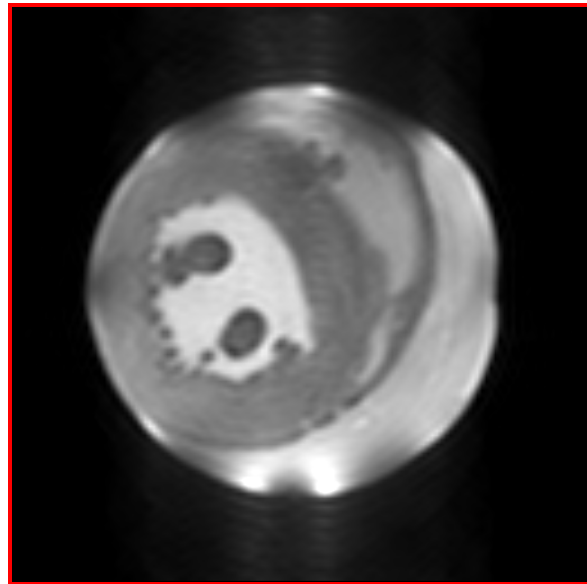
In conclusion, microscopic high angular resolution diffusion imaging achieving an in-plane resolution of 50  $\mu\text{m}$  could reveal the tissue structures such as the free-running Purkinje fibers and stripes in the ventricular interseptum as well as the heterogeneous microstructure in the myocardium. In particular, MHARDI showed the potential to trace non-invasively the conduction path buried between the working myocardium in the ventricular interseptum. Indeed, this study demonstrates that the non-invasive technique provided by MR microscopy can distinguish the cardiac tissue components and can be used to understand the cardiac conduction system, which has largely relied on the destructive technique. When combined with high resolution 3D imaging, the microscopic HARDI with an optimized b-value may be a powerful tool for comprehensive understanding of structure-function relationship in normal or pathological heart as well as aging heart. Histology of the tissue part that displays the stripe structures and MHARDI of the free-running Purkinje fibers attached the papillary muscle is planned for a future study.

Table 5-1. Diffusion parameters depending on b-values at various regions in the LV. Each value corresponds to the mean of selected ROIs. Standard deviation of parameters except the FA were less than 5% of the corresponding mean. FW: free wall, IS: interseptum, PM: papillary muscle.

Parameters	B value (s/mm <sup>2</sup> )	FW			IS		PM
		endo	myo	epi	left	right	
ADC (x 10 <sup>-3</sup> mm <sup>2</sup> /s)	1000	1.16	1.14	1.17	0.94	1.22	0.93
	2000	1.12	1.1	1.15	0.91	1.12	0.95
$\lambda_{//}$ (x 10 <sup>-3</sup> mm <sup>2</sup> /s)	1000	1.5	1.59	1.72	1.54	1.77	1.37
	2000	1.45	1.48	1.49	1.41	1.64	1.38
FA (no unit)	1000	0.28	0.34	0.39	0.51	0.39	0.39
	2000	0.27	0.30	0.32	0.45	0.33	0.37



A



B

Figure 5-1. Spin echo MR images revealing anatomical details of the heart depending on the resolutions employed. A) A transverse image measured with an in-plane resolution of  $60\ \mu\text{m} \times 60\ \mu\text{m}$  using a 17.6 T magnet. B) A transverse image with an in-plane resolution of  $500\ \mu\text{m} \times 500\ \mu\text{m}$  using an 11 T magnet (Please see Materials and Method section in Ch.3 for the details). Scan times were about 7 hours 10 min and only 2 min, respectively. Buffer solutions filling the ventricular chambers are the Fluorinert solution (A) and the STH cardioplegic solution (B), respectively.

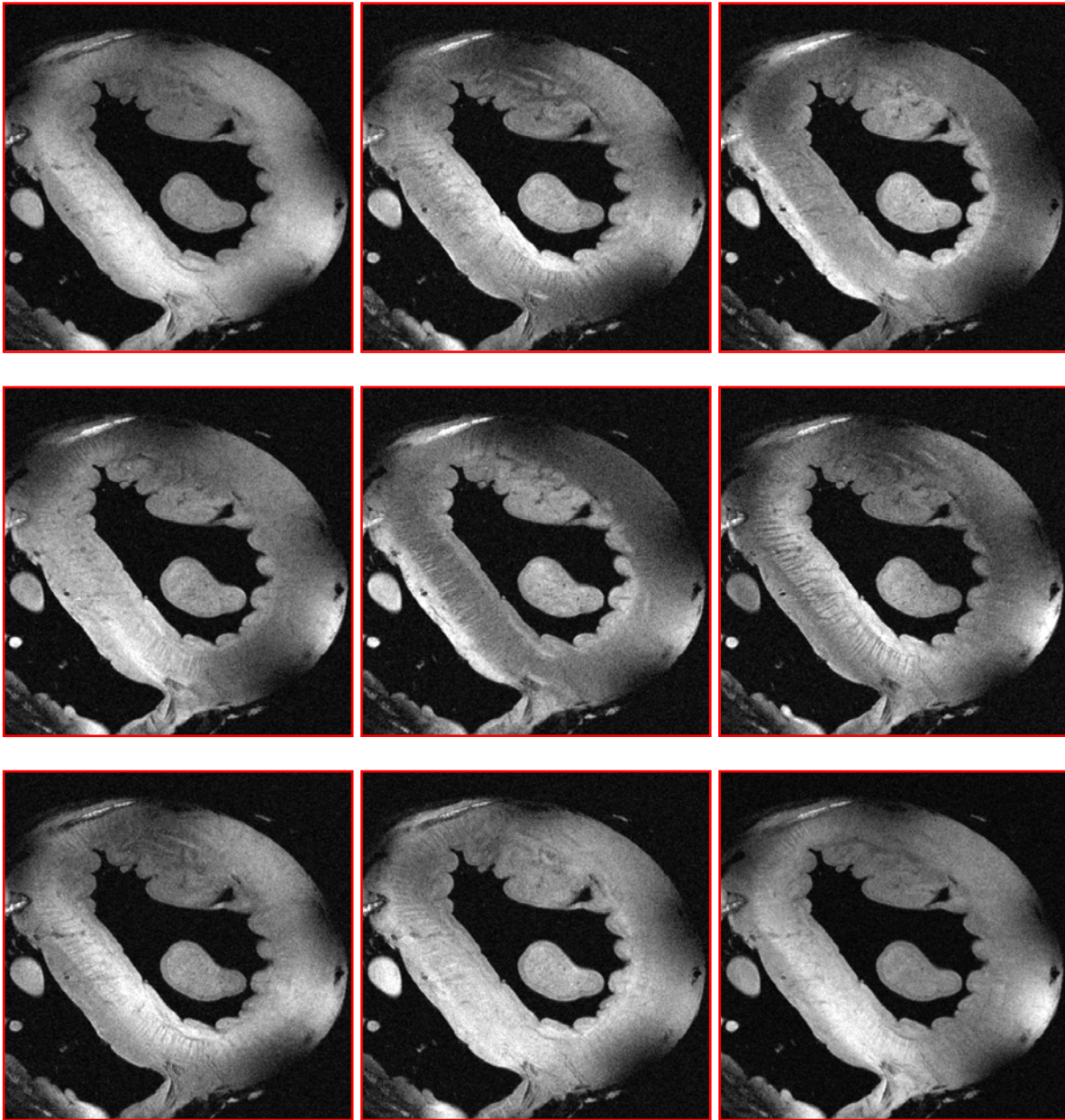


Figure 5-2. Diffusion weighted images of a HARDI data set measured in twenty one collinear diffusion encoding directions with  $1000 \text{ s/mm}^2$  of b value. Note that images show different weighting depending on the diffusion encoding directions.

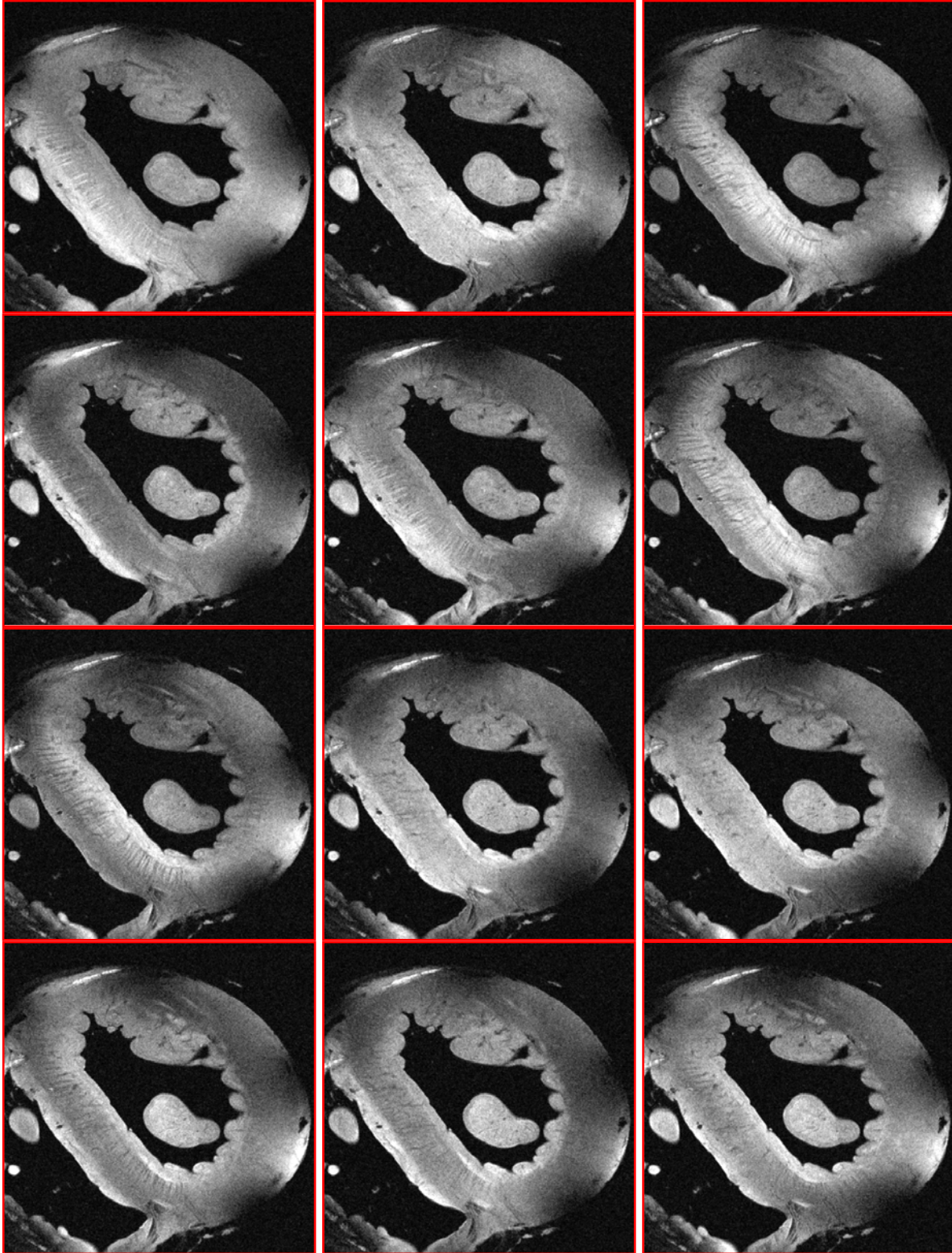


Figure 5-2. Continued

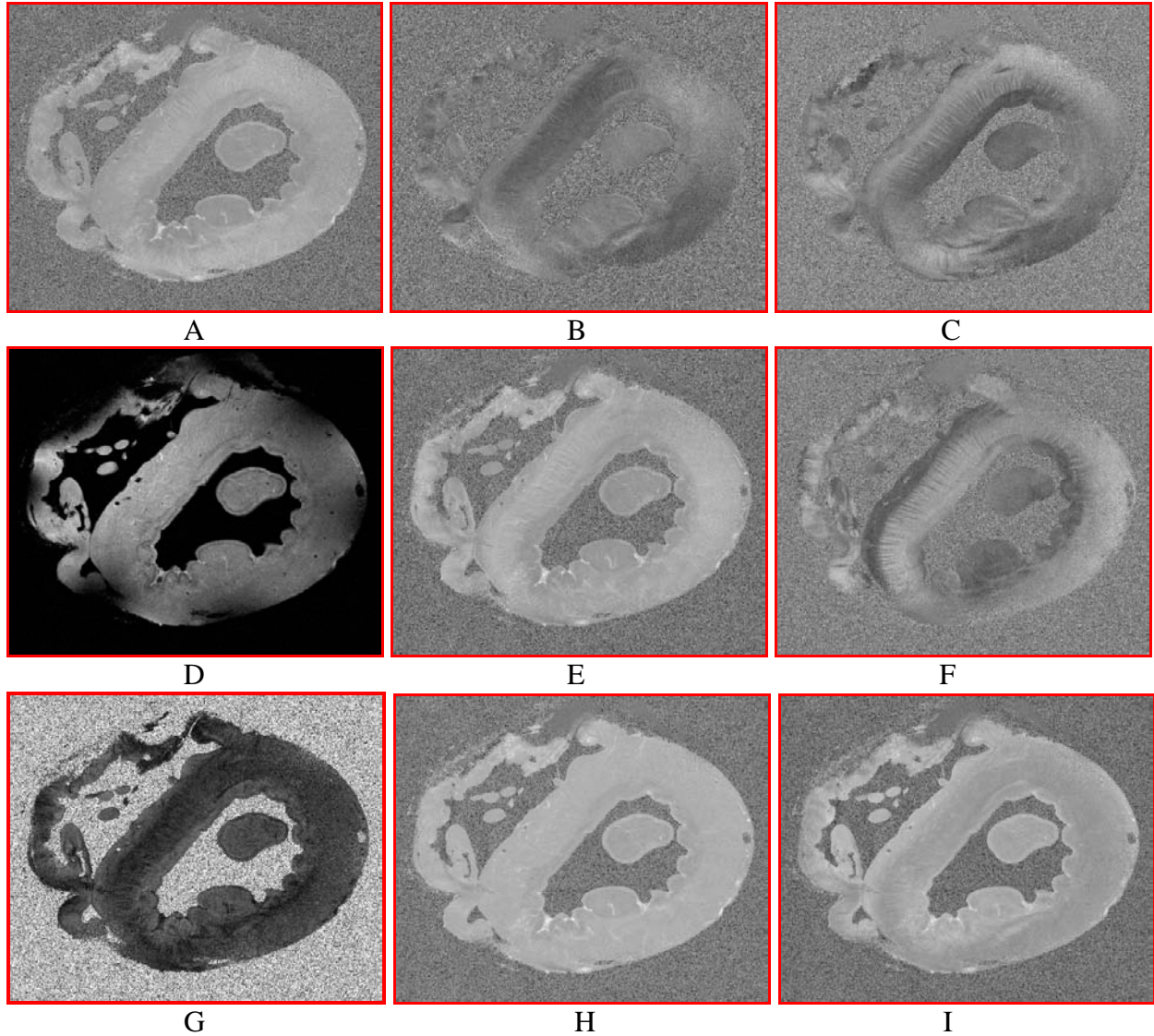


Figure 5-3. Diffusion tensor component images and images derived with the diffusion tensor components of b values of  $1000 \text{ s/mm}^2$ . A) Image of component of the diffusion tensor,  $D_{xx}$ . B) Image of component of the diffusion tensor,  $D_{xy}$ . C) Image of component of the diffusion tensor,  $D_{xz}$ . D) Intensity image without diffusion weighting. E) Image of component of the diffusion tensor,  $D_{yy}$ . F) Images of component of the diffusion tensor,  $D_{yz}$ . G) Fractional anisotropy. H) Diffusion trace. I) Image of component of the diffusion tensor,  $D_{zz}$ .

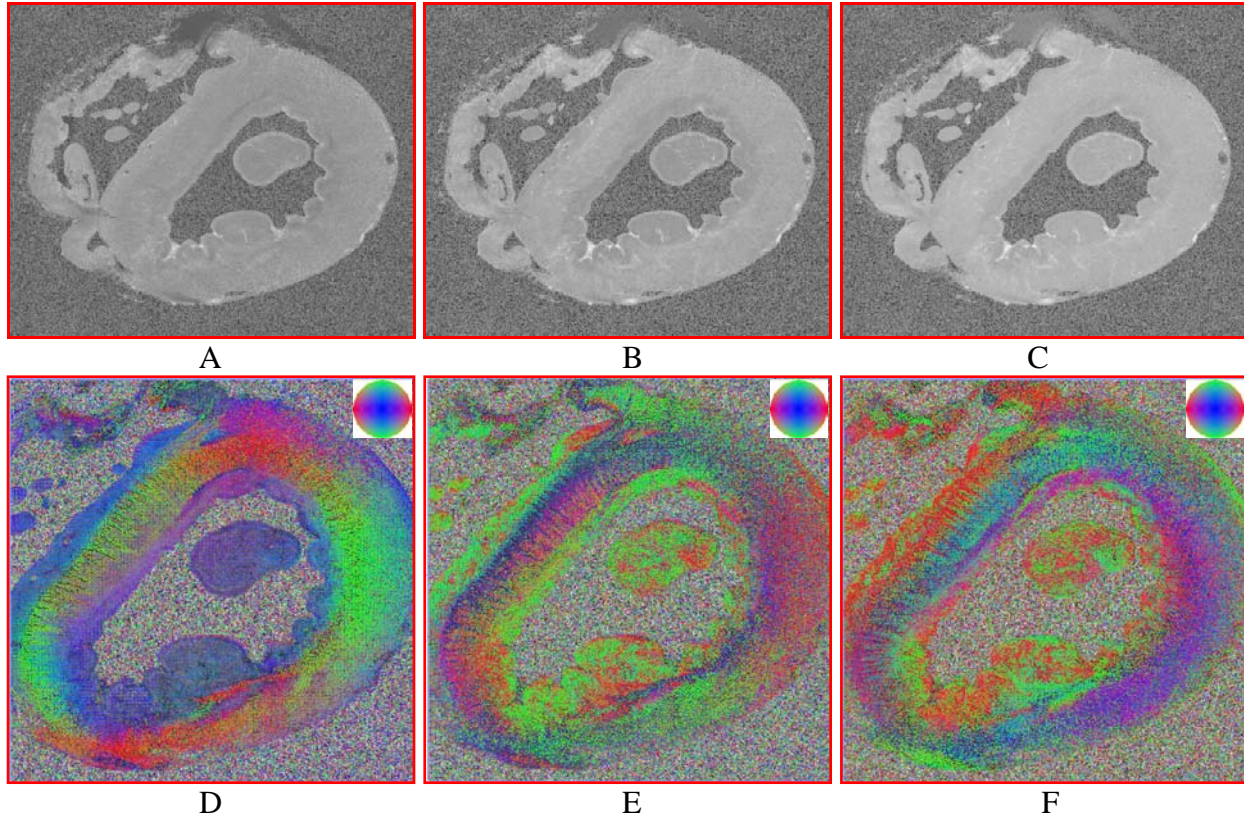


Figure 5-4. Parameter images derived from the diffusion tensor components shown in the Figure 5-3. A) Primary eigen value map. B) Secondary eigen value map. C) Tertiary eigen value map. D) Color coded primary eigen vector map. E) Color coded secondary eigen vector map. F) Color coded tertiary eigen vector map.

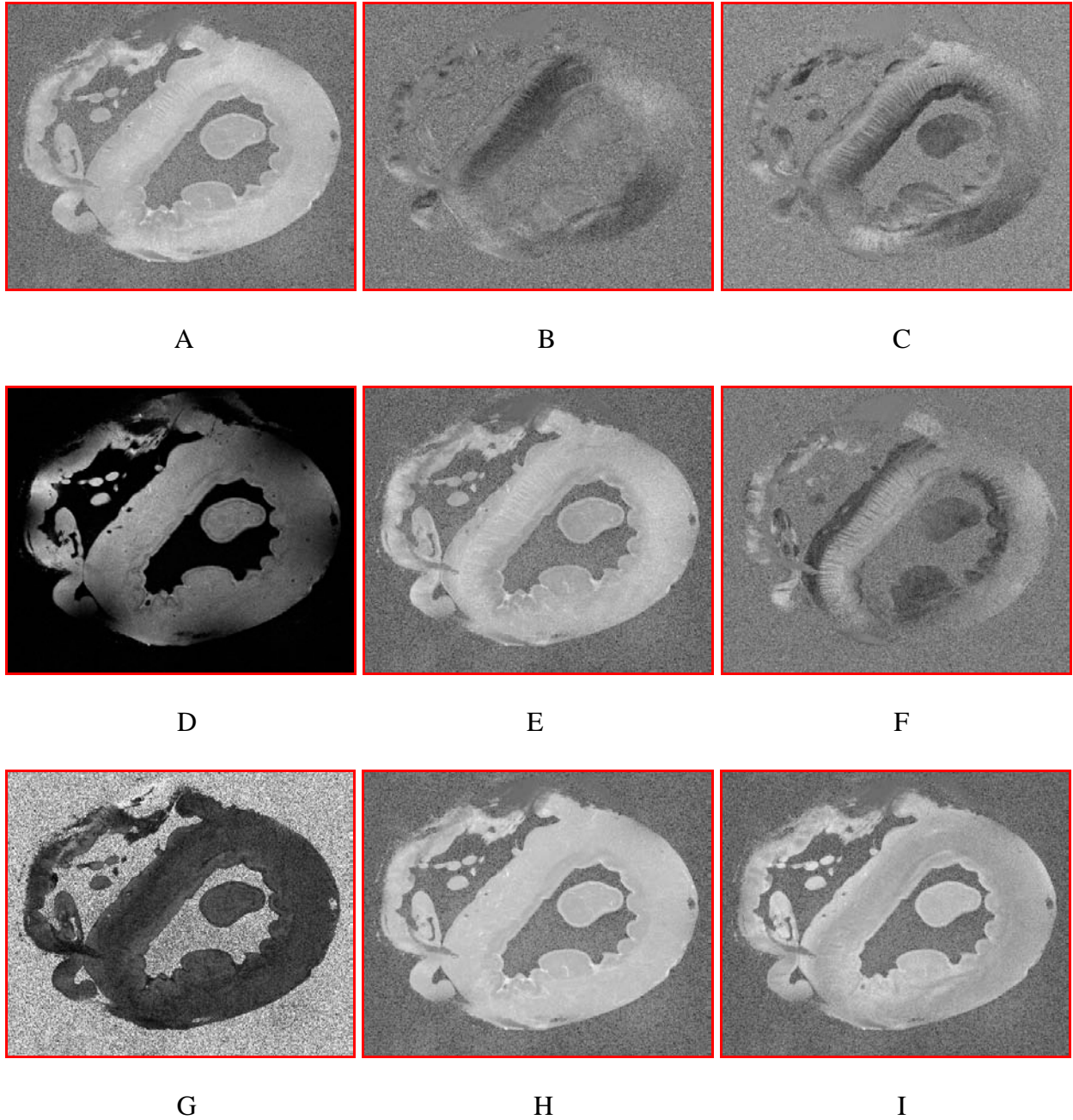


Figure 5-5. Diffusion tensor images and images derived with the diffusion tensor component of  $b$  values of  $2000 \text{ s/mm}^2$ . A) Image of component of the diffusion tensor,  $D_{xx}$ . B) Image of component of the diffusion tensor,  $D_{xy}$ . C) Image of component of the diffusion tensor,  $D_{xz}$ . D) Intensity image without diffusion weighting. E) Image of component of the diffusion tensor,  $D_{yy}$ . F) Images of component of the diffusion tensor,  $D_{yz}$ . G) Fractional anisotropy. H) Diffusion trace. I) Image of component of the diffusion tensor,  $D_{zz}$ .

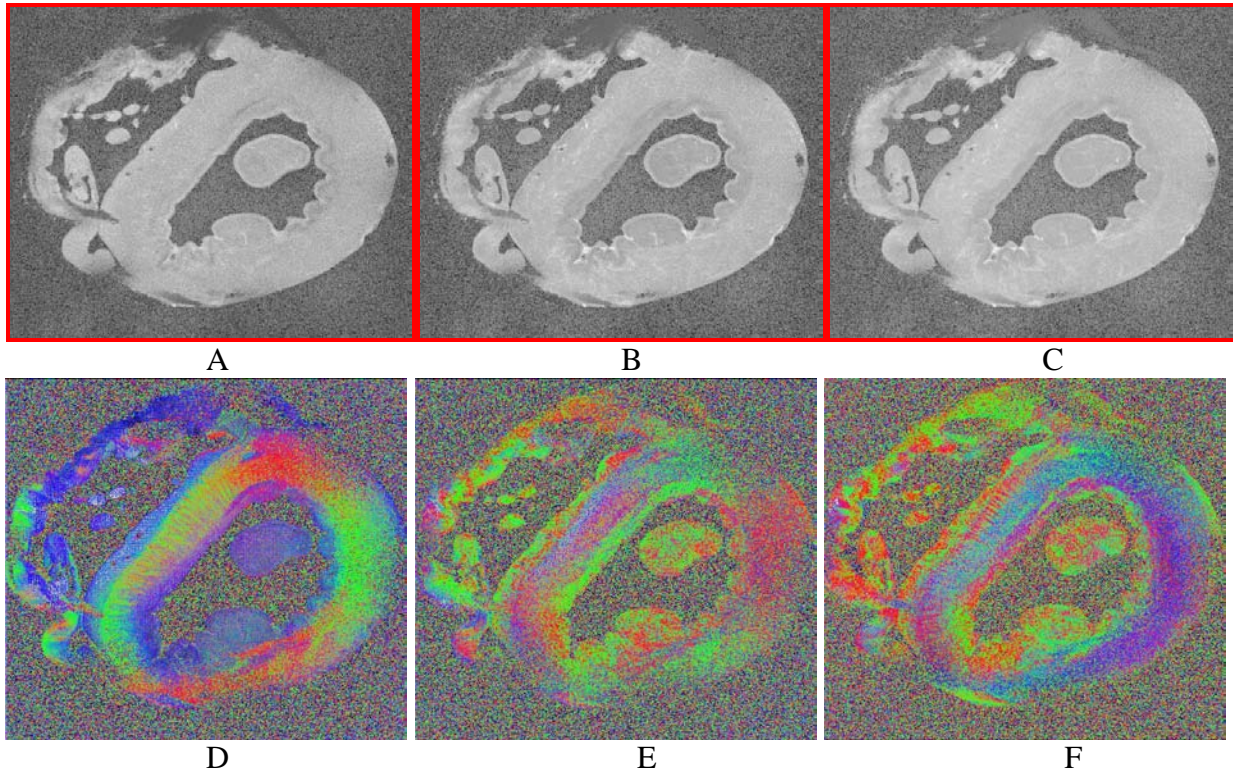


Figure 5-6. Parameter images derived from the diffusion tensor components shown in the Figure 5-5. A) Primary eigen value. B) Secondary eigen value. C) Tertiary eigen value. D) Primary eigen vecor. E) Secondary eigen vector. F) Tertiary eigen vector.

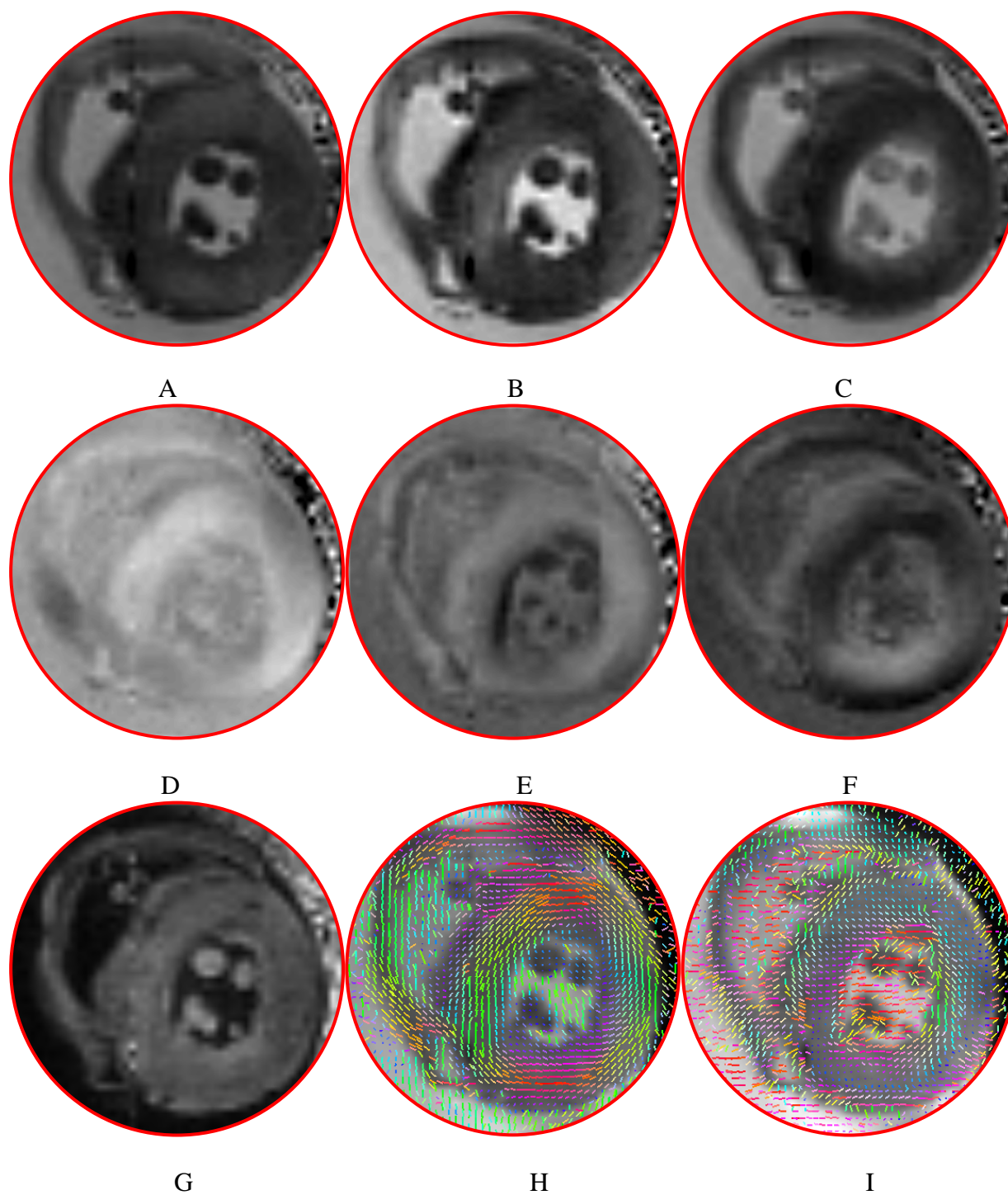


Figure 5-7. Diffusion tensor images and parameter images derived with the diffusion tensor component of  $b$  values of  $1000 \text{ s/mm}^2$ . MR images were acquired in the STH buffer using 11.1 T magnet (Please see Materials and Method section in Ch. 3). In-plane resolution was  $500 \mu\text{m} \times 500 \mu\text{m}$ . A)  $D_{xx}$ . B)  $D_{yy}$ . C)  $D_{zz}$ . D)  $D_{xy}$ . E)  $D_{xz}$ . F)  $D_{yz}$ . G) Fractional anisotropy. H) Primary eigen vector. I) Tertiary eigen vector.

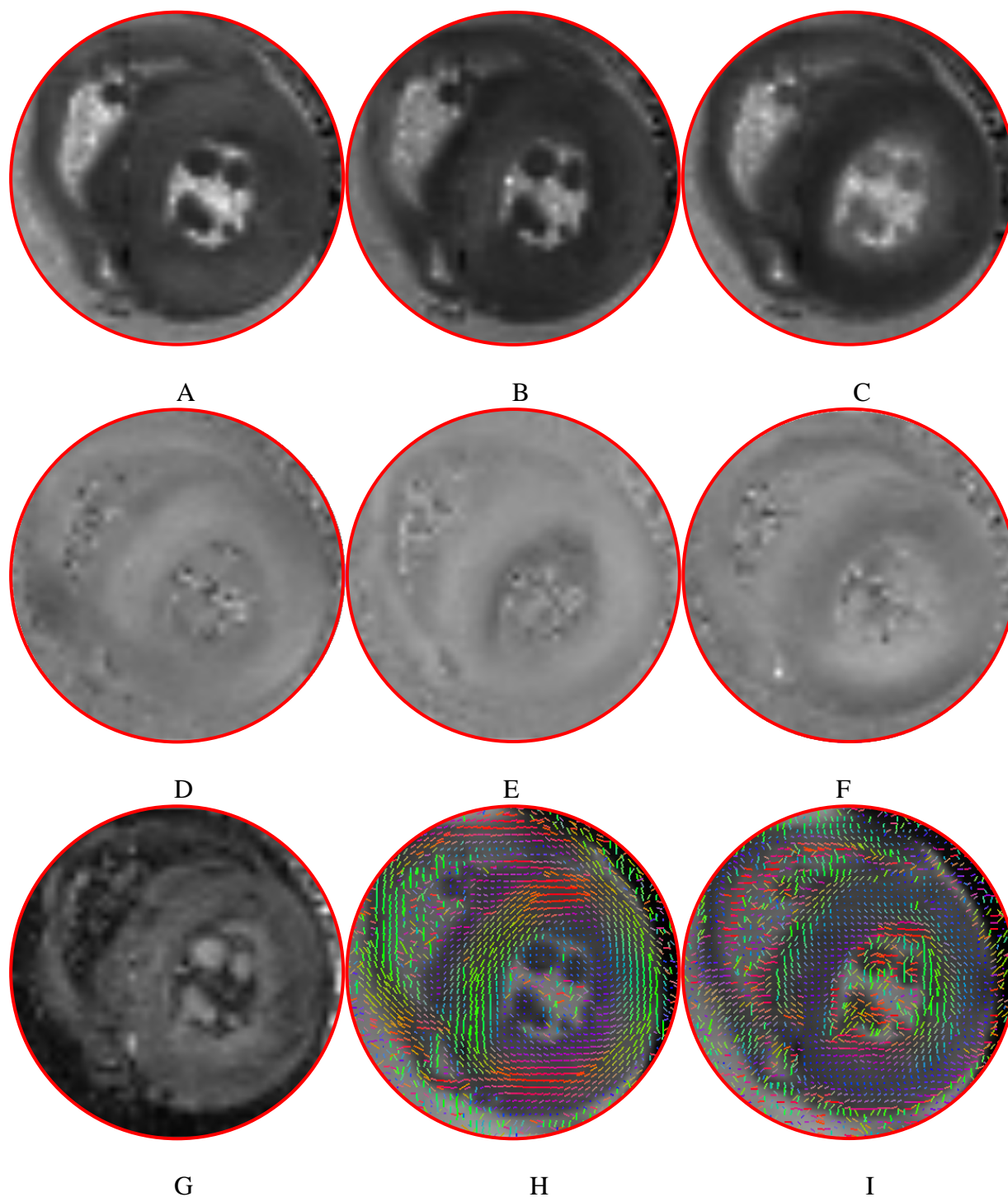


Figure 5-8. Diffusion tensor images and parameter images derived with the diffusion tensor component of  $b$  values of  $2000 \text{ s/mm}^2$ . MR images were acquired in the STH buffer using 11T magnet. (Please see Materials and Method section in Ch. 3). In-plane resolution was  $500 \mu\text{m} \times 500 \mu\text{m}$ . A)  $D_{xx}$ . B)  $D_{yy}$ . C)  $D_{zz}$ . D)  $D_{xy}$ . E)  $D_{xz}$ . F)  $D_{yz}$ . G) Fractional anisotropy. H) Primary eigen vector. I) Tertiary eigen vector.

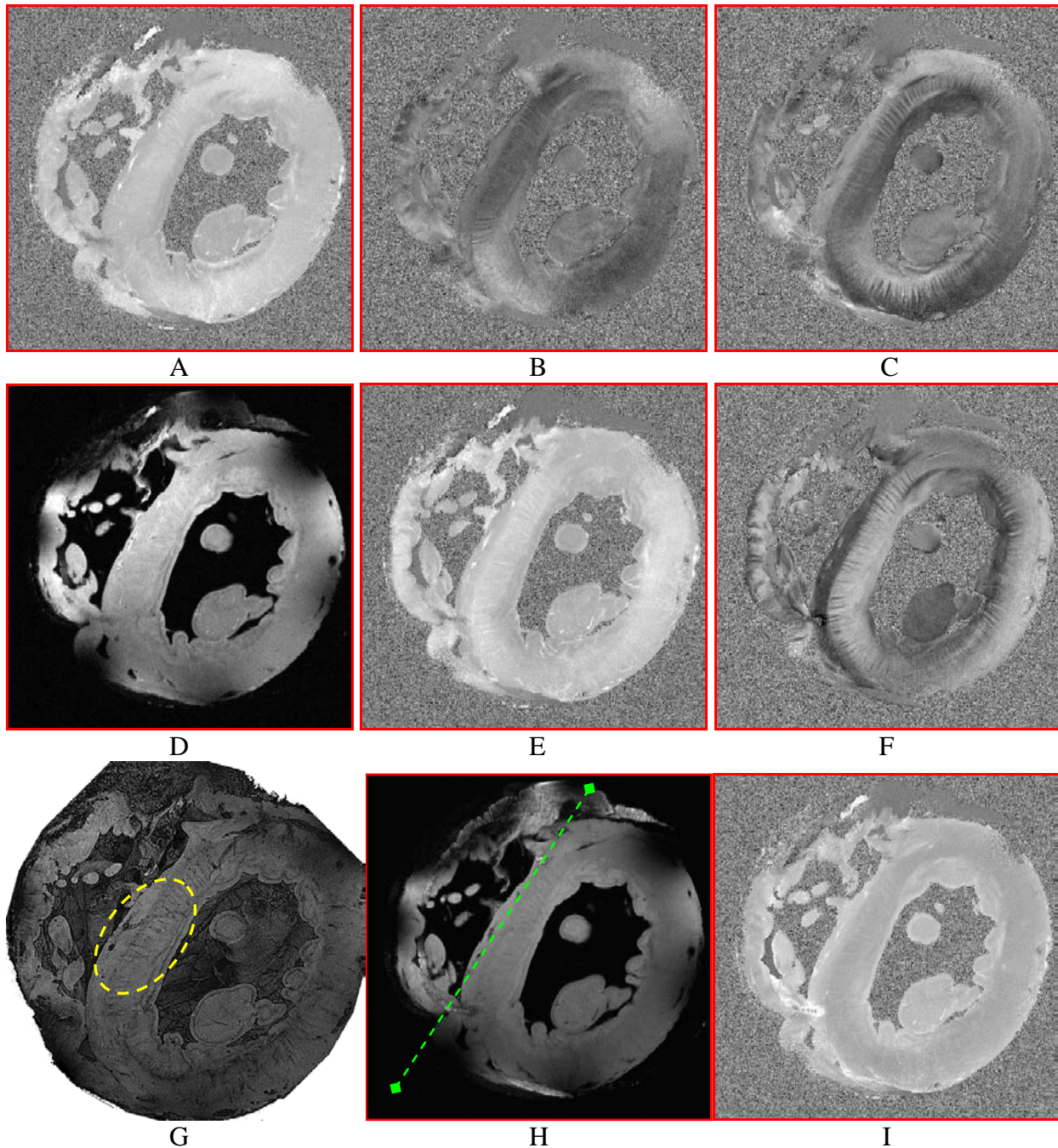
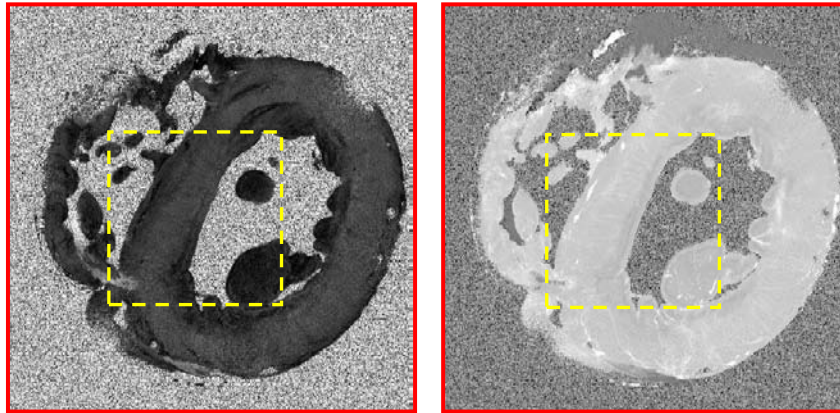
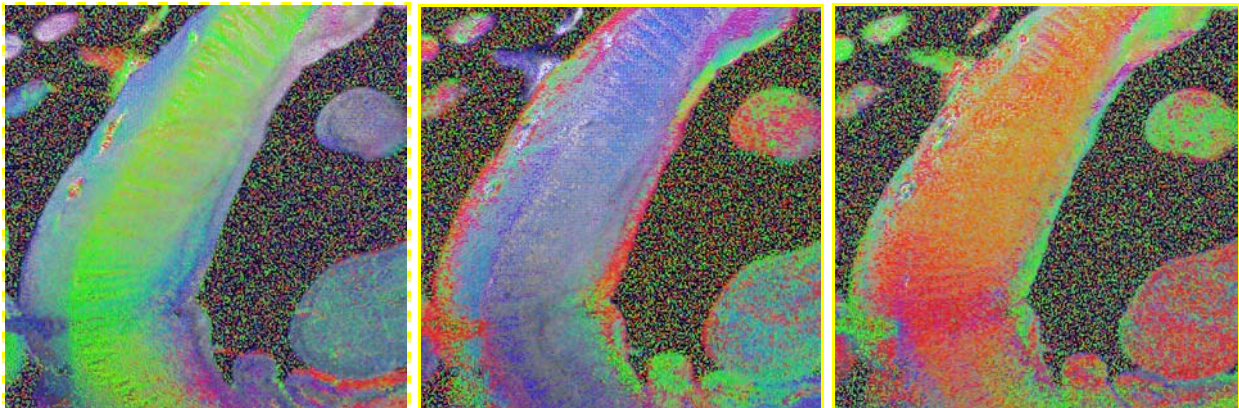


Figure 5-9. MR images revealing structural complexity in the ventricular interseptum. Diffusion tensor component images and images derived with the diffusion tensor components generated from HARDI data set measured with a  $b$  value of  $1000 \text{ s/mm}^2$ . A) Image of component of the diffusion tensor,  $D_{xx}$ . B) Image of component of the diffusion tensor,  $D_{xy}$ . C) Image of component of the diffusion tensor,  $D_{xz}$ . D) Intensity image without diffusion weighting. E) Image of component of the diffusion tensor,  $D_{yy}$ . F) Images of component of the diffusion tensor,  $D_{yz}$ . G) Volume rendered MR image. H) Diffusion trace. I) Image of component of the diffusion tensor,  $D_{zz}$ .



A

B



C

D

E

Figure 5-10. Diffusion parameter images showing components in the ventricular interseptum. These images are derived from the diffusion tensor components in the Figure 5-9. A) Fractional anisotropy. B) Mean diffusivity. C) The magnified primary eigen vector of the region in the yellow box in A). D) The magnified secondary eigen vector of the region in the yellow box in A). E) The magnified tertiary eigen vector of the region in the yellow box in A).

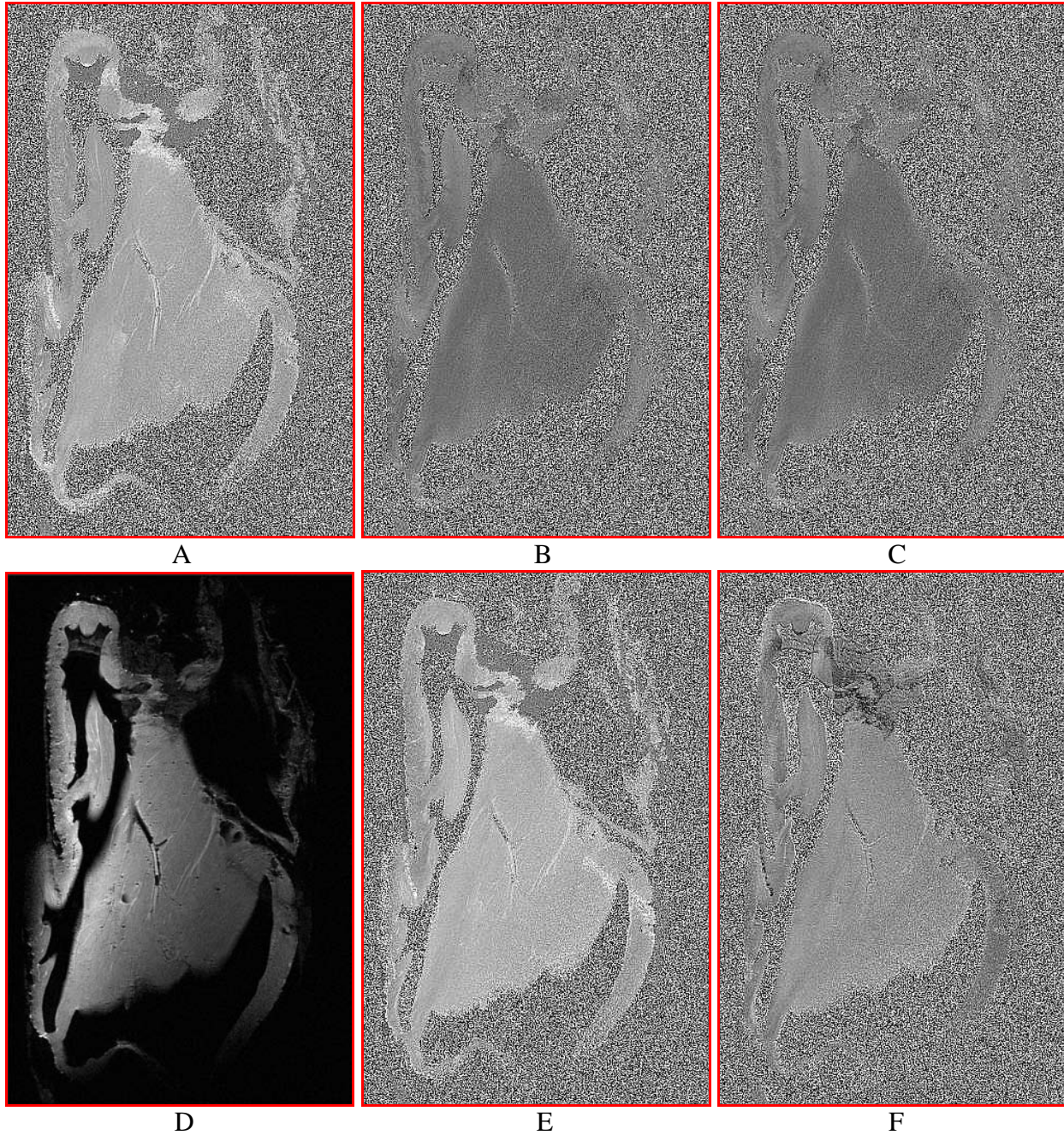


Figure 5- 11. A long axis view MR images showing the ventricular interseptum in the vicinity of the right ventricular cavity. Images correspond to where the sectioning occurs (the green dotted line, H in Figure 5-9). A) Image of component of the diffusion tensor,  $D_{xx}$ . B) Image of component of the diffusion tensor,  $D_{xy}$ . C) Image of component of the diffusion tensor,  $D_{xz}$ . D) Intensity image without diffusion weighting. E) Image of component of the diffusion tensor,  $D_{yy}$ . F) Images of component of the diffusion tensor,  $D_{yz}$ . G) Diffusion trace. H) Trace weighted image. I) Image of component of the diffusion tensor,  $D_{zz}$ .



Figure 5-11. Continued

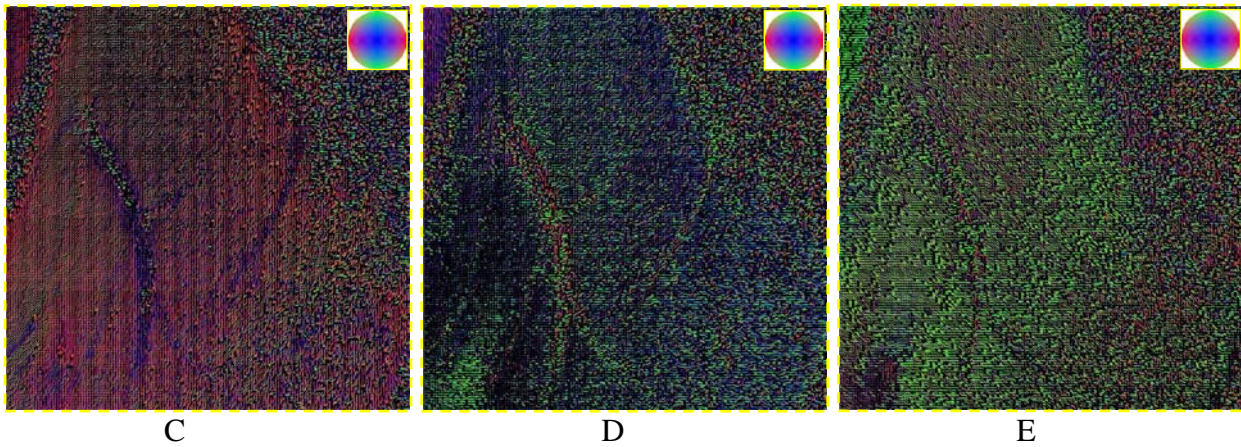
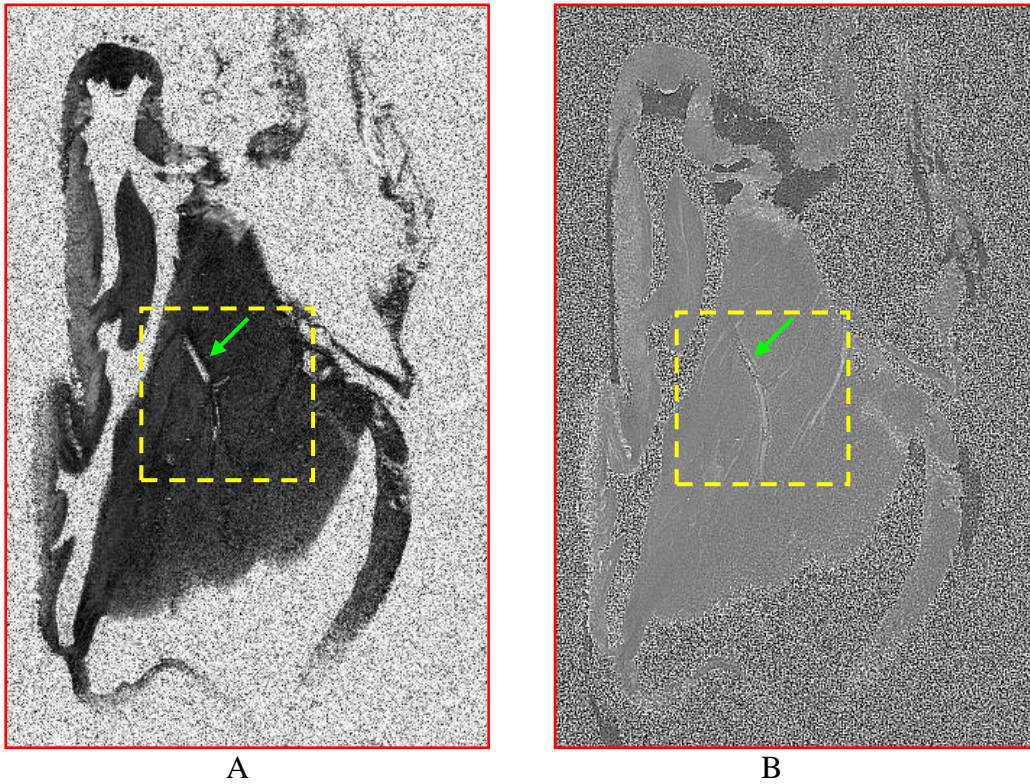
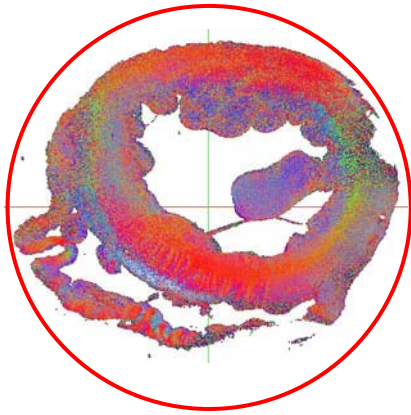
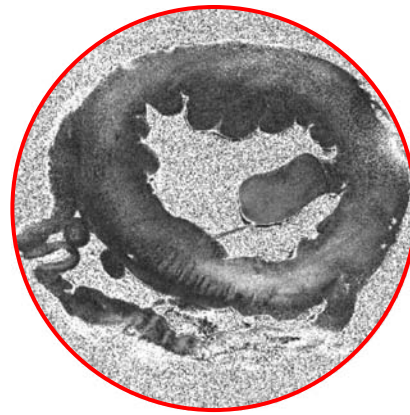


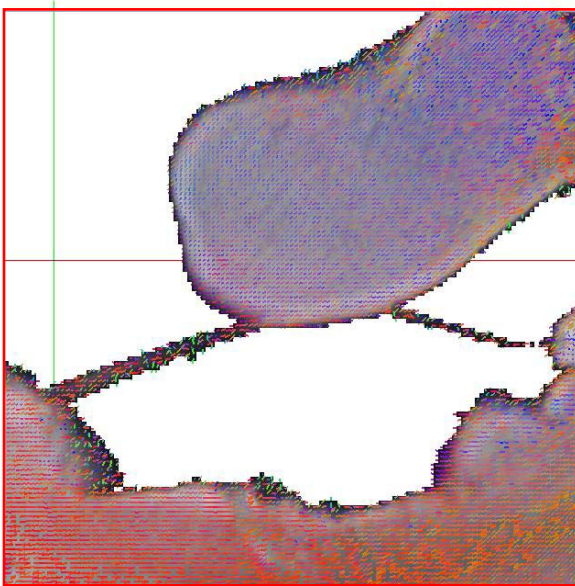
Figure 5-12. Diffusion parameter maps implying proximity at distance between the perforating artery and the right bundle branch. A) Fractional anisotropy. B) Diffusion trace. C) The magnified image of primary eigen vector of the region in the yellow dotted box. D) Magnified image of secondary eigen vector of the region in the yellow dotted box. E) Magnified image of tertiary eigen vector of the region in the yellow dotted box.



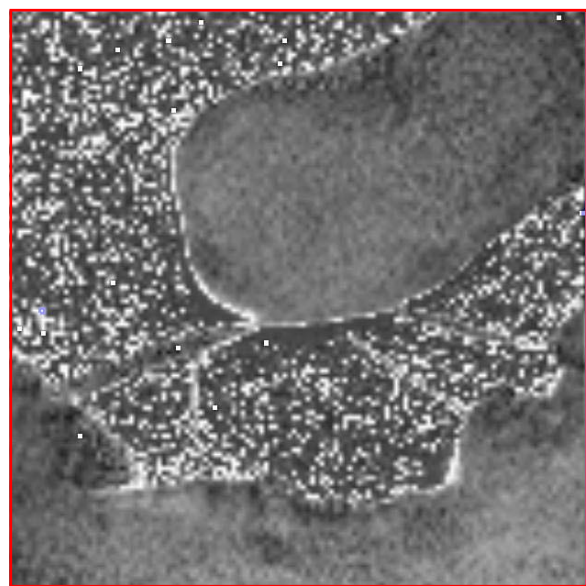
A



B



C



D

Figure 5-13. The Free-running Purkinje fibers in the left ventricular chamber. A) Primary eigen vector. B) Fractional anisotropy. C) Magnified image of primary eigen vector. D) Magnified image of fractional anisotropy.

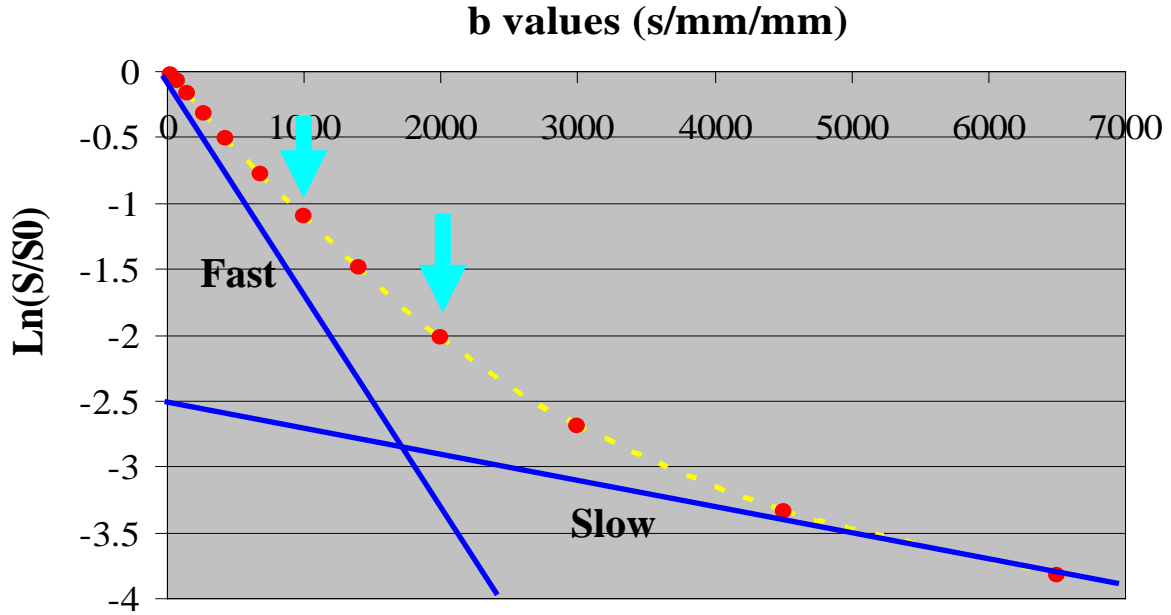


Figure 5-14. Plot of the logarithmic signal intensity as a function of b-values for an isolated rabbit heart. Arrows indicate b-values employed for MHARDI. Dotted line represents the best-fit bi-exponential function.

CHAPTER 6  
NON-INVASIVE MONITORING OF MORPHOLOGICAL ALTERATIONS IN THE RABBIT  
HEART WITH AGING

**Introduction**

Cell loss and proliferation are part and parcel of normal homeostasis (Olivetti et al., 1990). Cells have a limited life span in the living entities (Pugh and Wei, 2001). But without cell regeneration the rates of the programmed cell death would imply that all cells would die during the first few months of a rodent's life span (Olivetti et al., 1990). A mixture of young and old cells is present throughout life. Change in the proportion of these two populations is typical of aging and results in different response to external stimuli (Olivetti et al., 1990).

Although aging is a spontaneous procedure of human and living animals, age-related change in cardiovascular structure and function significantly lowers the threshold at which cardiac disease becomes apparent (Olivetti et al., 1990; Oxenham and Sharpe, 2003; Pugh and Wei, 2001). Research on aging has been attempting to elucidate the mechanisms in which aging impact the cardiovascular system. Until now, changes that are considered to result from aging have been noted in the structure and function of the cardiovascular system (Oxenham and Sharpe, 2003; Pugh and Wei, 2001). Particularly, the myocardium, composed of muscle fibers supported within a three-dimensional scaffolding of fibrillar collagen, is currently a well-known place where morphological changes in aging heart occur.

Loss of myocytes with subsequent compensatory hypertrophy of the remaining cardiac cells is a commonly observed hallmark in aging heart (Anversa et al., 2002; Anversa and Nadal-Ginard, 2002). Whether a myocyte responds to given physiological loads by hypertrophy or by replication is influenced by cell volume, which in turn reflects its age (Brooks et al., 2003). Large myocytes are old, do not tend to react with the growth stimuli, and are more subject to programmed cell death (apoptosis). Small myocytes are younger, can re-enter cell cycle or

hypertrophy, and are less susceptible to death. The large myocytes might also be coupled with a reduction in capillary density, and increase in death of myocytes with aging may explain why myocardial infarction is associated with increased failure of the aged heart.

Interstitial fibrosis in the myocardium is a common outcome found in aging hearts (de Souza, 2002). Interstitial collagen fibers surround and group myocardial muscle fibers. They also tether individual muscle fibers to another fibers and their neighboring vasculature (Janicki and Brower, 2002; Weber et al., 1994). The fibrillar connective collagen represents morphologic correlates of in-series and in-parallel elastic elements described in classic concepts of cardiac muscle mechanics (Janicki and Brower, 2002). The contractile behavior of the heart is imparted by the myocytes, whereas their extracellular matrix and collagen provide the heart with recoil and viscoelastic behavior. The myocardial fibrosis is the formation or development of excess fibrous collagen tissue, largely type I collagen, in the extracellular space as a result of a reparative or reactive process (Brooks et al., 2003; de Souza, 2002; Olivetti et al., 1990; Oxenham and Sharpe, 2003; Pugh and Wei, 2001). This collagen accumulation can occur in the absence of myocyte proliferation and result in the expansion of the extracellular space with aging.

The cardiac conduction system is also subject to alterations with aging. Loss of pacemaker cell in the SA node was observed (Pugh and Wei, 2001). Due to the calcification within the cardiac skeleton with aging, nearby structures such as the atrioventricular node or the connecting bundle (the bundle of His) may be under the influence of the stiffening. The change in the cardiac conduction system may predispose to the common rhythmic disturbances of old age including atrial fibrillation.

Biopsy has popularly been an accurate and informative means to delineate the age-related changes in the heart (de Souza, 2002; Olivetti et al., 1990; Oxenham and Sharpe, 2003; Pugh and Wei, 2001). However, it is destructive and requires staggering labor, often with severe complications for 3D reconstruction. Using a non-invasive imaging technique, investigation of morphological changes in the whole heart with aging has rarely been performed.

In this research, magnetic resonance microscopy (MRM) is used to monitor the morphological changes of the tissue components in the heart with aging. Specifically, high resolution 3D imaging and microscopic high angular resolution imaging (MHARDI) using a 17.6 T magnet are performed to investigate the aging-related morphological changes in the myocardium and in the conduction system of isolated rabbit heart. It is examined whether diffusion parameters, such as fractional anisotropy, mean diffusivity, and the primary eigen value, can reflect cellular hypertrophy and/or interstitial fibrosis, which are known as two hallmarks of aging heart. The Purkinje fiber networks in the left ventricular chamber of young hearts are compared with ones of aged hearts through volume renderings of microscopic 3D MR images.

## **Materials and Method**

### **Isolated Heart Preparation**

Isolated perfused hearts ( $n = 5$ ) of New Zealand White rabbits (3 ~ 5 kg) were prepared according to the animal protocol approved by the UF Institutional Animal Care and Use Committee. Young hearts ( $n = 3$ ) were 6 month ~ 1 year old. Old hearts ( $n = 2$ ) were 3 ~ 4 years old. The isolated hearts were fixed in situ during an intravascular formalin-perfusion fixation procedure that was carefully standardized. Fixed hearts were kept in a refrigerator until MR imaging experiments. Forty eight hours prior to the start of imaging, hearts were transferred to phosphate buffered saline solution to wash out residual fixative.

## Magnetic Resonance Imaging

MR experiments of the isolated hearts were performed on a 17.6 T / 89 mm vertical wide-bore magnet (Bruker Instrument, Inc., Billerica, MA). The RF coil used for the in vitro imaging was an Alderman-Grant birdcage coil, diameter = 25 mm, length = 35 cm. The temperature in the magnet was maintained at 19 - 20°C. Three dimensional high resolution MR image data were collected using a fast gradient echo pulse sequence, achieving a voxel resolution of 35.2  $\mu\text{m}$  x 35.2  $\mu\text{m}$  x 82  $\mu\text{m}$  with a matrix size = 710 x 710 x 256 in the field of view of 25 mm x 25 mm x 21 mm. Imaging parameters implementing relatively T2\*-weighting were TR = 150 ms, TE = 18.5 ms, 1 average, sampling bandwidth = 20 k. For direct geometrical matching with 3D imaging, the subsequent HARDI of 21 directions was performed using a standard PGSE pulse sequence, achieving an isotropic in-plane resolution of 50  $\mu\text{m}$  with a transverse slice of 500  $\mu\text{m}$ . Diffusion sensitizing factor (b-value) was 1000 s/mm<sup>2</sup> using  $\Delta$  = 13.4 ms and  $\delta$  = 1.8 ms. Imaging parameters were TR = 3000 ms, TE = 25.1 ms, 1 average. The pilot images with three orthogonal planes were collected during the experiment to determine whether an isolated heart imbedded in the dense FC-43 solution moved during long scans (~ 24 hours).

Diffusion weighted imaging of the isolated hearts were performed to study the apparent diffusion coefficient characteristic with aging by applying the gradients to give diffusion sensitizing factors (b values) of 260, 680, 1000, 1400, 2000, 3000, 4500, and 6500 s/mm<sup>2</sup> in the slice-selective direction with a pulsed gradient spin echo sequence. The selected diffusion encoding direction for the ADC analysis did not arise the significant attenuation of signal due to the cross terms. Imaging parameters were TR = 2.5 s, TE = 25.3 ms, NA = 2,  $\Delta$  = 13 ms, and  $\delta$  = 4 ms. All scans were obtained at a slice thickness of 0.5 mm, each with an in-plane resolution of 0.160 x 0.160 mm<sup>2</sup>.

## Data Analysis

Volume rendering of the 3D MR data sets was performed using ImageJ (ver. 1.31, <http://rsbweb.nih.gov/ij/>) in the transverse, sagittal, and coronal directions. Anatomical analyses of the rendered images were conducted. The tensor processing of MHARDI data sets was performed using fanDTasia™ (©2008, Barmpoutis, <http://www.cise.ufl.edu/~abarmpou/>). Pixel-based analysis of ROIs selected from the transverse slices showing the papillary muscles in the left ventricles was conducted. Averaged rate of water diffusion (AD), axial diffusivity ( $\lambda_{//}$ , the primary eigen value), radial diffusivity ( $\lambda_{\perp}$ , an average of the secondary and the tertiary eigen values), and fractional anisotropy were calculated using MATLAB (MathSoft, Cambridge, MA). Individual data were then averaged among the hearts measured and compared with the zero-mean hypothesis using the Student's t-test (Hsu et al., 1998b). A value of  $p < 0.05$  was considered to be statistically significant. The normalized signal attenuation as a function of b-values within the manually selected ROIs was fitted to a biexponential function using Levenberg-Marquardt non-linear least squares fitting routines (Shepherd et al., 2002), deriving the apparent diffusion coefficients (ADCs).

## Results

High resolution three dimensional MR imaging and microscopic high angular resolution diffusion imaging (MHARDI) are observed to reveal morphological changes associated with aging in isolated fixed rabbit hearts. Since the right ventricle showed considerable interspecific variation and its chamber shape altered while the whole heart was being fitted into a NMR tube, the left ventricle drew more attention to examine the morphological change with aging.

### Morphological Change in the Purkinje Fiber Network

Aging in rabbit heart appears to show significant impact on the interseptal thickness by increasing  $22.6 \pm 7\%$ . Figure 6-1 demonstrates increased ratio of left ventricular wall thickness

to the chamber size. Difference in the free-running Purkinje network in the left ventricular chamber could be pronounced by the volume renderings of three dimensional high resolution MR imaging. Young hearts form denser reticular net in the ventricular cavity. With aging, rabbit hearts seem to lose the solid Purkinje fiber network and the free-running Purkinje fibers become thinner. Density of the free-running Purkinje fibers connected with the papillary muscles also alters with aging.

A tensor component map of a young heart ( $D_{yz}$ ) shows a conspicuous stripe pattern in the interseptum and freewall (Figure 6-2). In contrast, the directional patterns seem to be confined to small area of aging hearts (Figure 6-3). A volume rendered image of the interseptum, having a long axis view, shows that the stripe patterns are oriented longitudinally. The primary eigen vector and fractional anisotropy maps also appear to reflect alteration in the myocardium with aging.

### **Change in MR Diffusion Characteristics**

Aging in rabbit hearts was associated with increased diffusivity (Table 6-1). Specifically, mean diffusivity, axial diffusivity, and radial diffusivity of the papillary muscles in young hearts were  $0.955 \pm 0.075 \times 10^{-3} \text{ mm}^2/\text{s}$ ,  $1.39 \pm 0.09 \times 10^{-3} \text{ mm}^2/\text{s}$ , and  $0.738 \pm 0.068 \times 10^{-3} \text{ mm}^2/\text{s}$ , respectively. In aged hearts, those diffusivities increased to  $1.271 \pm 0.087 \times 10^{-3} \text{ mm}^2/\text{s}$ ,  $1.87 \pm 0.16 \times 10^{-3} \text{ mm}^2/\text{s}$ , and  $0.971 \pm 0.062 \times 10^{-3} \text{ mm}^2/\text{s}$ , respectively. The aged hearts also showed slight increase in fractional anisotropy from  $0.386 \pm 0.033$  to  $0.401 \pm 0.029$ .

Figure 6-3 demonstrates the influence of aging upon the logarithmic bi-exponential decline in signal intensity plotted as a function of b-values up to  $6500 \text{ s}/\text{mm}^2$  in the papillary muscles of the left ventricle, where the muscle fibers would be nearby parallel to diffusion encoded direction. The change in the ADC curve in the papillaries correlates with relative

change of two water pools (fast and slow components), which results from the variation of tissue compartments (extracellular/intracellular) with aging.

### **Discussion**

These results demonstrate that the morphological effect of aging can be examined by high resolution MR imaging using isolated rabbit heart model. Although translation of animal data to the human model can not certainly be assumed, the high resolution MRI regarding aging in isolation using isolated rabbit heart model appears to overcome limitation placed on non-invasive imaging techniques of human heart in aging, specifically in terms of resolution or penetration depth. From a simple physical relationship by the Laplace equation, the thickness of the heart at any place bears direct proportion to the relative tension at that place (Pugh and Wei, 2001). The increase in the thickness of the ventricular interseptum and its ratio to the size of the left ventricular chamber may explain the high left ventricular pressure in the aging heart.

Previous electrophysiological studies observed slowing of conduction in the His-Purkinje-Ventricular system, beginning at the bundle of His and reaching the ventricular myocardium via the Purkinje fibers (Eloff et al., 2001). Loss of Purkinje fibers in the network is suspected as one reason for a slowing of the His-Purkinje-Ventricular conduction. Hence macroscopic changes in the left ventricular Purkinje network in young vs. aged hearts shown in the volume rendered MR images might represent the suspected reason. The macroscopic change might also correlate with stiffened Purkinje fibers by increased collagen content, which has been observed in aging heart (Pugh and Wei, 2002). Extensive analysis of the whole conduction system in the two populations is currently underway. Overlay of these three dimensionally reconstructed MR images with optical mapping images of the measured hearts may lead to identify the Purkinje fiber's possible role in age-related change of the conduction. The ability of high resolution 3D MR imaging in reconstructing the Purkinje network may be extended to

elucidate the role of the Purkinje network in other pathological conditions such as the arrhythmogenesis (Brunner et al., 2008).

Stripe patterns observed in the mid-wall of the left ventricular myocardium are separated from the adjacent myocardium by the primary eigen vector. The patterns that imply structural integrity by the corresponding FA values apparently become dilute or disappear in aged hearts. From location where the patterns are observed in the ventricular interseptum, the patterns are suspected of being correlated with change in conduction fibers. This may also indicate change in the myocardial fiber orientation with aging. Identification of the stripe patterns by histochemical staining is necessary to understand the source responsible for the alteration in aging hearts, and the work is currently underway.

Typical changes in aging hearts would contain myocyte loss subsequently followed by the compensatory cellular hypertrophy, and interstitial fibrosis that results in the expansion of the extracellular space. The extracellular expansion was previously observed by histological examination. The two dominating alterations in cellular level with aging may well be represented by alterations in diffusion. However, contribution of increased cellular volume and increased interstitial volume to the diffusion MR signal would be counterbalancing. This might be evidenced in Chapter 3. For instance, in heart slices superfused with hypotonic solution, resulting in cellular volume increase, the signal attenuation curve moved in a fashion that the slow component increasingly contributes (Figure 3-6). On the other hand, in isolated hearts having increased extracellular space due to secured vasculature, the ADC curve was shifted in the opposite direction.

The results from MHARDI and the bi-exponential signal attenuation as a function of b values appear to reflect increase in the extracellular space with aging, previously observed by

histological examination. Since the water diffusion in the interstitial space is in general described as fast as free diffusion under a slow limit assumption, the expanded extracellular space would impose less restriction on water diffusion, leading to an increase in water diffusivity (Nicholson and Sykova, 1998). Hence increase in contribution of the fast component due to the expanded extracellular space may be responsible for increase in the ADC curve with aging. Furthermore, increased diffusivity observed from MHARDI of aged hearts might also be associated with expansion of the extracellular space,

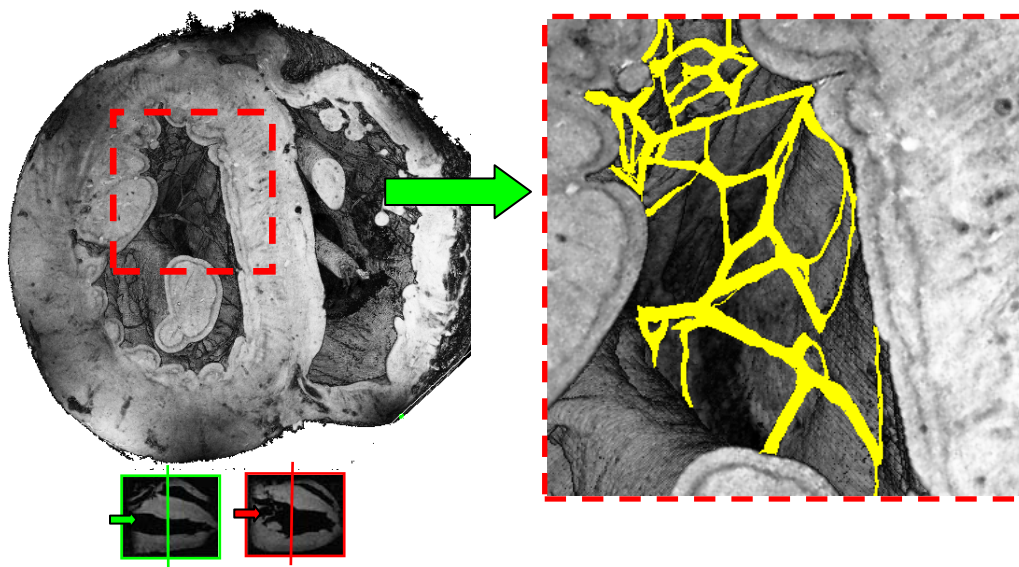
In general, increase in mean diffusivity is an ensuing result of loss of diffusion anisotropy (FA), vice versa (Li et al., 2009). Interestingly, our results show slight increase of FA and increase of AD in the papillary muscle of aged rabbit hearts, which is inconsistent with a recent publication that observed reduced MR diffusion anisotropy in aged hamster hearts (Li et al., 2009). This might result from the expansion of both the myocyte and the non-myocyte compartments of the myocardium while sustaining the proportion of these two structural constituents (Oxenham and Sharpe, 2003). As shown in Table 6-2, slight increase in fractional anisotropy (FA) with aging results from the greater increase of the primary eigen value than increase of the secondary and tertiary eigen values. This implies that an isotropic diffusion environment derived by the expanded extracellular space may be restricted in part by the increased fibrillar collagen content in the extracellular space. Otherwise if the replacing interstitial fibrosis plays a major role in the extracellular expansion, increased collagen fiber may provide additional yet at most minor barriers to water diffusion. Variation in the tensor invariants may correlate with potential differences in the fibrosis content of young and aged hearts and differences in the fiber orientation by the age-related fibrosis, which is currently under investigation. In addition, those diffusion parameters and the ADC curve may correlate slowing

of the conduction velocity observed in aged hearts, which may be explained by loose myocyte junction that the expanded extracellular space may impose.

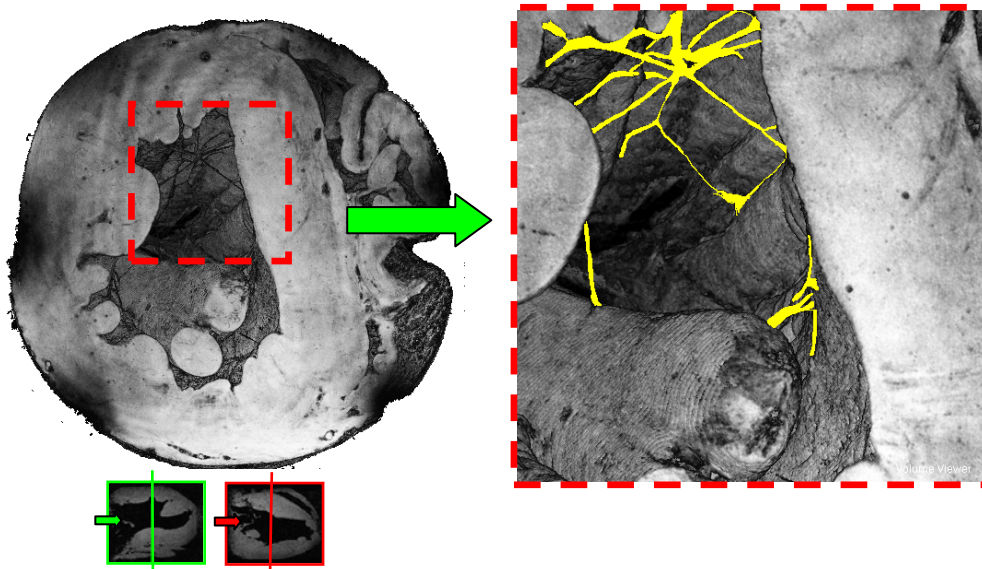
In conclusion, alteration in the free-running Purkinje fiber network with aging could be non-invasively pronounced using MR microscopy. Microscopic high angular resolution diffusion imaging showed the potential to follow age-related structural changes in the myocardium. In particular, the diffusion tensor invariants and the signal attenuation curve as a function of b values might be good indicators to the changes in the aged hearts. Combined analysis of the MR techniques using a high magnetic field is a promising tool to investigate the microscopic alterations in the cardiac tissue compartments and the components with aging.

Table 6-1. Diffusion parameters of the papillary muscles in the left ventricles of young and old rabbit hearts. Each value corresponds to the mean (standard deviation) of selected ROIs. AD is mean diffusivity, the averaged rate of water diffusion.  $\lambda_{//}$  is the axial diffusivity (the primary eigen value),  $\lambda_{\perp}$  is the radial diffusivity, an average of the secondary and the tertiary eigen values. FA is fractional anisotropy. Note that AD and FA are orientation-independent measure of water diffusion.

Parameters	AD ( $\times 10^{-3} \text{ mm}^2/\text{s}$ )	$\lambda_{//}$ ( $\times 10^{-3} \text{ mm}^2/\text{s}$ )	$\lambda_{\perp}$ ( $\times 10^{-3} \text{ mm}^2/\text{s}$ )	FA (no unit)
Young heart	0.96 (0.08)	1.39 (0.09)	0.74 (0.07)	0.38 (0.03)
Old heart	1.27 (0.09)	1.87 (0.17)	0.97 (0.06)	0.40 (0.03)



A



B

Figure 6-1. Volume rendered transverse images and manual segmentation (magnified) of the free-running Purkinje fiber network in the LV of a young rabbit heart (A) and an old rabbit heart (B). Lines and arrows in the green and red boxes indicate where sectioning occurred and viewer was located. Interseptal thickness is approximately 3.93 mm (young) and 4.82 mm (old). I: ventricular interseptum, P: papillary muscle, FW: free wall.

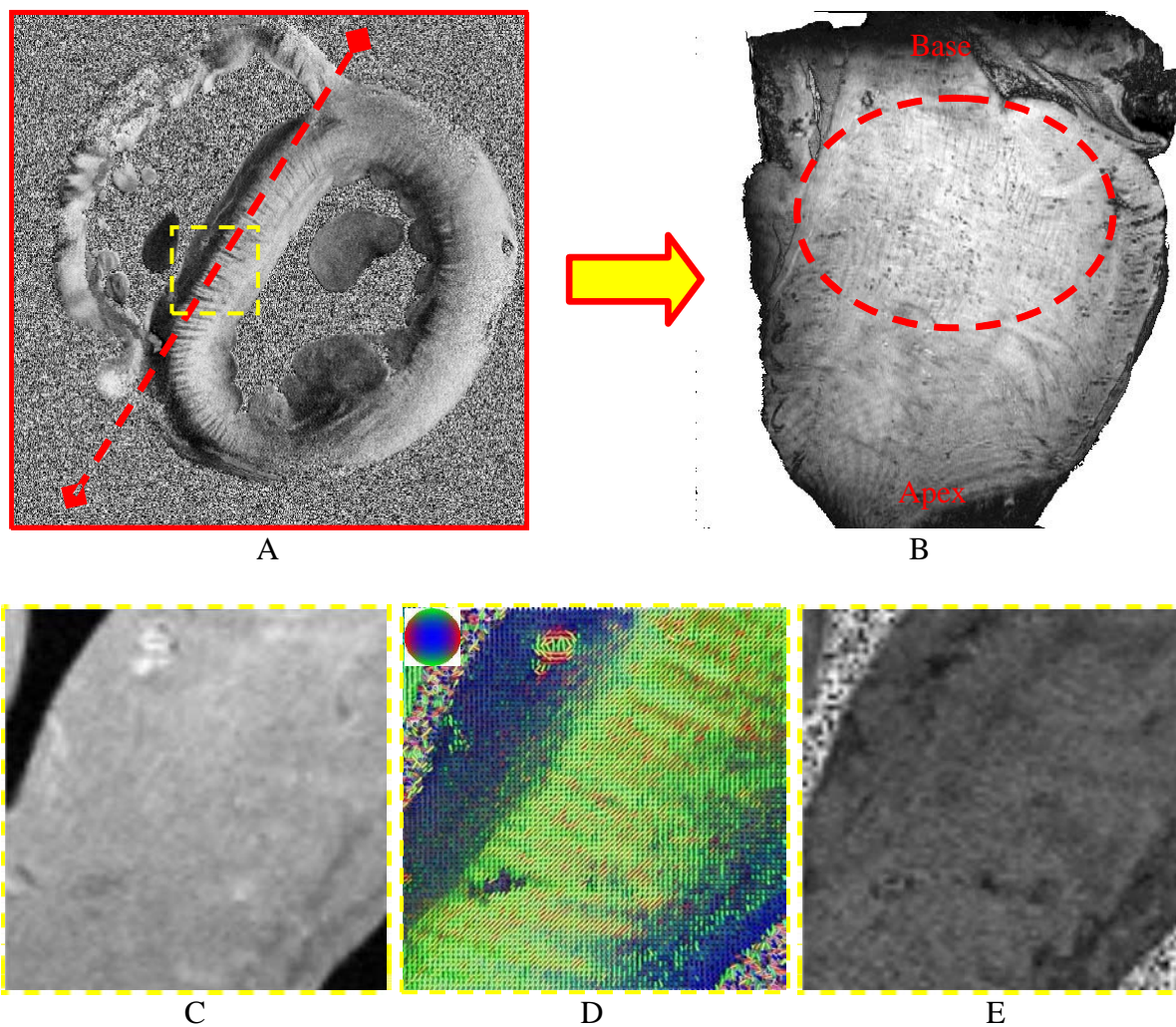


Figure 6-2. Diffusion parameter maps from MHARDI and a volume rendered image of the interseptum of a young rabbit heart. A) Tensor component ( $D_{yz}$ ) map; B) a volume rendered image of a long axis view generated from the cut that the dotted red line in A indicates. C (intensity map), D (the primary eigen vector map), and E (fractional anisotropy map) are the magnified images of the dotted yellow box in A.

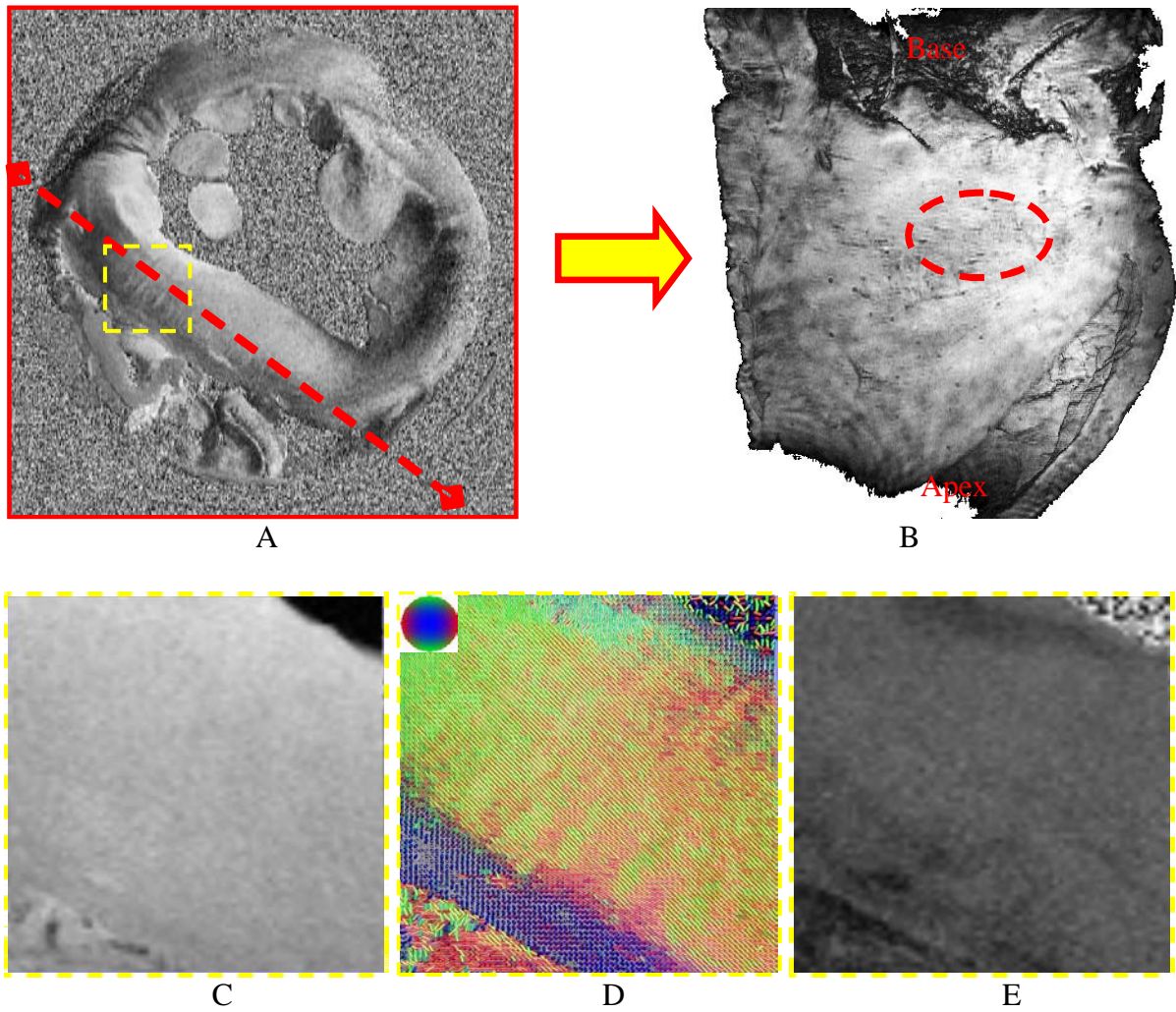


Figure 6-3. Diffusion parameter maps from MHARDI and a volume rendered image of the interseptum of an old rabbit heart. A) Tensor component ( $D_{yz}$ ) map, B) a volume rendered image of a long axis view generated from the cut that the dotted red line in A) indicates. C) Signal intensity map without diffusion-weighting, D) the primary eigen vector map, E) fractional anisotropy map. C) ~ E) are the magnified images of the dotted yellow box in A).

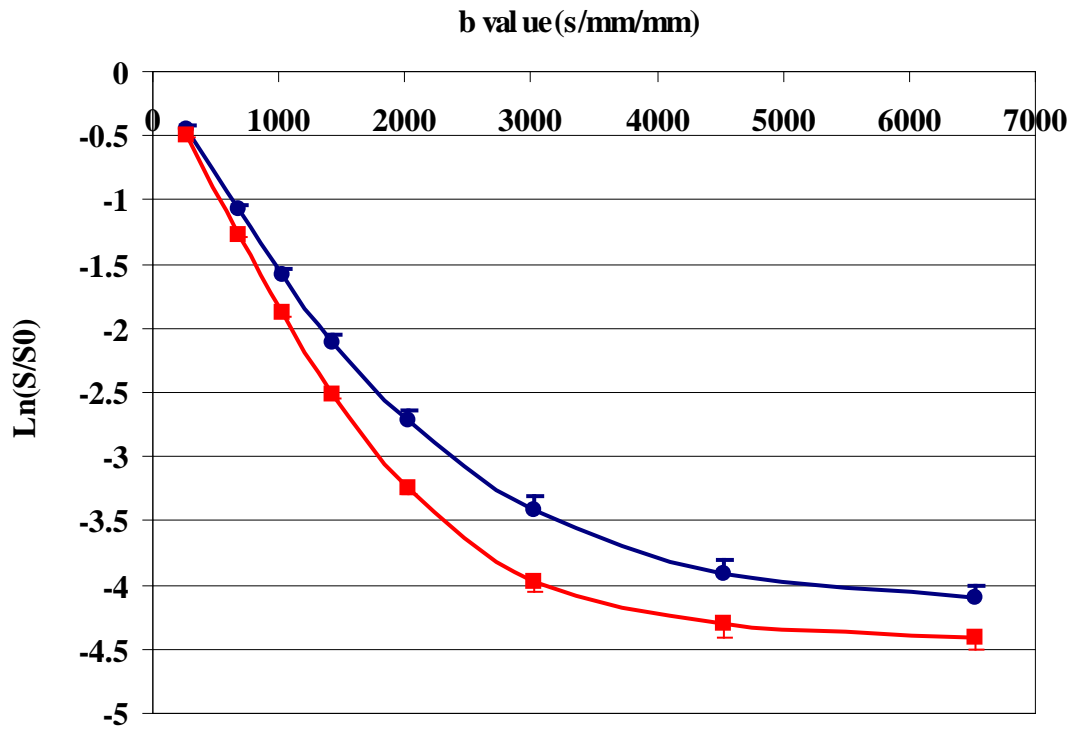


Figure 6-4. Logarithmic normalized diffusion signal attenuation depending on aging. Blue and red colors correspond to the ROIs in the papillaries of young and old hearts, respectively.

## CHAPTER 7 CONCLUSIONS

Magnetic resonance imaging has advanced quickly with ever increasing strengths of magnetic fields. Obtaining a higher signal to noise ratio (SNR) and/or reduced partial volume effect allows microscopic anatomical features of the heart to be visualized non-invasively. These improvements have also made it possible to probe water diffusion in cardiac tissue with more flexibility and accuracy. With these technical advances in looking at cardiac tissue comes the responsibility of understanding exactly where the acquired MR signal comes from and to scrutinize what can be newly visualized with the methods that the advanced techniques provide.

The research presented in this thesis attempted to distinguish changes in tissue compartments and cellular components in the rabbit heart and monitor their pathophysiological alterations, in-situ, using 17.6 T and 11.1 T magnets located at the University of Florida. The results demonstrated that diffusion-weighted imaging using b-values up to  $6500 \text{ s/mm}^2$ , three-dimensional high resolution MRI, and microscopic high angular resolution diffusion imaging (MHARDI) can non-invasively discern tissue compartments and cellular components comprising the heart.

In Chapter 2, a modified experimental setup was described that rendered heavy diffusion weighted MR imaging of isolated fresh rabbit hearts. This setup included 1) a birdcage RF coil giving acceptable SNR with an appropriate filling factor for the isolated rabbit hearts, 2) a compact, reusable, and portable perfusion system that enables control of temperature and flow rate of the perfusate, and 3) a long cradle fitted with a minimum margin into a gradient coil that allows sufficient diffusion gradient strength to obtain desired images. Samples in the long cradle were not susceptible to non-diffusional motion during heavy diffusion weighted imaging. This experimental setup was successfully applied to high resolution diffusion tensor imaging (DTI) of

isolated and fixed rabbit hearts measured using a b value of 2000 s/mm<sup>2</sup> and high angular resolution diffusion imaging (HARDI) of in vivo rat brain measured using a b value of 1000 s/mm<sup>2</sup>.

In Chapter 3, the MR diffusion signal intensity as a function of b-values up to 6500 s/mm<sup>2</sup> was used to reflect changes in the tissue compartments. The tissue compartments, the physiological sources responsible for the apparent diffusion coefficient of water molecules, were observed to significantly contribute to a measured diffusion MR signal. The focus of this research was on understanding the contribution of the vascular compartment by modifying the vasculature in the cardiac tissue. The modification included 1) collapsing the vascular space by slicing the tissue, 2) replacing a modified St. Thomas' Hospital (STH) cardioplegic solution in the vascular space with the proton-free solution (perfluorocarbons-emulsion), and 3) changing the direct flow rate of STH cardioplegic solution in the vascular space. Diffusion-weighted MR imaging of isolated hearts and heart slices demonstrated that the vascular compartment in the myocardium is a significant contributor to the fast moving water pool of water diffusion signal that has bi-exponential behavior as a function of b-values. First, from the MR diffusion measurement using the PFC emulsion, the presence of the secured vasculature in the isolated heart contributed to the apparent diffusion coefficient (ADC) for the fast component as well as the volume fraction for that component. Second, from the MR diffusion measurement using direct flow, attenuation of signal intensity with b values up to 6500 s/mm<sup>2</sup> was modulated by vascular flow, especially at lower flow rates. For the fast component, the variation of the vascular flow rate is observed to contribute to the ADC rather than the volume fraction. Relaxation times in the intracellular and extracellular compartments using single-cell MR imaging need to be measured for more accurate quantifications of their contributions.

In Chapter 4, the volume-rendered images gained from three-dimensional high resolution MR imaging made it possible to non-invasively and reproducibly trace the conduction pathways in the left and right ventricles, as well as to describe the micro-anatomical features of the heart. To the best of our knowledge, this is the first instance of an in situ non-invasive visualization of the cardiac conduction pathways from the left and right bundle branches to the Purkinje-ventricular junction. We also explored the anatomical relationship among constituents in the ventricular muscular interseptum, such as the perforating vasculature, the right bundle, and the contractile muscles, which to date may be a non-invasive approach that only magnetic resonance microscopy can provide. Very few studies have been performed regarding this so-called ‘Purkinje fiber MR imaging’, but this research shows great promise. Furthermore, similarity of the Purkinje fibers in the left ventricle of the rabbit heart and of the human heart increases the possibility of clinical application of this research. Histochemical staining is currently underway to bolster confidence in our current interpretation.

The results in Chapter 5 demonstrate that microscopic high angular resolution diffusion imaging (MHARDI) could reveal such tissue structures as the free-running Purkinje fibers and the stripes in the ventricular interseptum, as well as the heterogeneous microstructure in the myocardium. In particular, MHARDI showed the potential to non-invasively trace the conduction path buried in the ventricular interseptum. Derived diffusion parameters and tensor invariants were employed to disentangle anatomical complexities imposed by perforating interseptal branches of the coronary arteries in the ventricular interseptum. MR imaging of a Purkinje fiber cell and MHARDI of the free-running Purkinje fibers attached to the papillary muscle are planned as future study.

In Chapter 6, age-related changes in isolated hearts were monitored using high resolution 3D imaging and MHARDI. This research was conducted as an application of results obtained from the previous chapters. Alterations in the free-running Purkinje fiber network, the tensor invariants, and the ADC curve with aging were observed. Combined analysis of the two MR modalities may be a promising tool to understand the microscopic alterations in the aging heart. A study relating these MR findings to ones observed using such other modalities as optic imaging and conduction velocity measurement will be performed. When combined with high resolution 3D imaging, the MHARDI with an optimized b-value can be a powerful tool for comprehensive understanding of the structure-function relationship in the normal or pathological heart as well as the aging heart.

## LIST OF REFERENCES

- Aguayo, J.B., Blackband, S.J., Schoeniger, J., Mattingly, M.A., Hintermann, M., 1986. Nuclear magnetic resonance imaging of a single cell. *Nature* 322, 190-191.
- Aliev, M.K., Dos Santos, P., Hoerter, J.A., Soboll, S., Tikhonov, A.N., Saks, V.A., 2002. Water content and its intracellular distribution in intact and saline perfused rat hearts revisited. *Cardiovasc Res* 53, 48-58.
- Anderson, R.H., Becker, A.E., 1980, *Cardiac anatomy: an integrated text and color atlas*. Gower Medical Publishing, London.
- Ansari, A., Ho, S.Y., Anderson, R.H., 1999. Distribution of the Purkinje fibres in the sheep heart. *Anat Rec* 254, 92-97.
- Anversa, P., Leri, A., Kajstura, J., Nadal-Ginard, B., 2002. Myocyte growth and cardiac repair. *J Mol Cell Cardiol* 34, 91-105.
- Anversa, P., Nadal-Ginard, B., 2002. Myocyte renewal and ventricular remodelling. *Nature* 415, 240-243.
- Assaf, Y., Cohen, Y., 1998a. In vivo and in vitro bi-exponential diffusion of N-acetyl aspartate (NAA) in rat brain: a potential structural probe? *NMR Biomed* 11, 67-74.
- Assaf, Y., Cohen, Y., 1998b. Non-mono-exponential attenuation of water and N-acetyl aspartate signals due to diffusion in brain tissue. *J Magn Reson* 131, 69-85.
- Bammer, R., 2003. Basic principles of diffusion-weighted imaging. *Eur J Radiol* 45, 169-184.
- Barmpoutis, A., Hwang, M.S., Howland, D., Forder, J.R., Vemuri, B.C., 2009. Regularized positive-definite fourth order tensor field estimation from DW-MRI. *Neuroimage* 45, S153-162.
- Barmpoutis, A., Vemuri, B.C., Forder, J.R., 2007a. Registration of high angular resolution diffusion MRI images using 4th order tensors. *Med Image Comput Comput Assist Interv* 10, 908-915.
- Barmpoutis, A., Vemuri, B.C., Howland, D., Forder, J.R., 2008. Extracting tractosemas from a displacement probability field for tractography in DW-MRI. *Med Image Comput Comput Assist Interv Int Conf Med Image Comput Comput Assist Interv* 11, 9-16.
- Barmpoutis, A., Vemuri, B.C., Shepherd, T.M., Forder, J.R., 2007b. Tensor splines for interpolation and approximation of DT-MRI with applications to segmentation of isolated rat hippocampi. *IEEE Trans Med Imaging* 26, 1537-1546.
- Barmpoutis, A., FanDTasia, 2008, <http://www.cise.ufl.edu/~abarmpous/>, April 15, 2009

- Basser, P.J., 1995. Inferring microstructural features and the physiological state of tissues from diffusion-weighted images. *NMR Biomed* 8, 333-344.
- Basser, P.J., Jones, D.K., 2002. Diffusion-tensor MRI: theory, experimental design and data analysis - a technical review. *NMR Biomed* 15, 456-467.
- Basser, P.J., Mattiello, J., LeBihan, D., 1994a. Estimation of the effective self-diffusion tensor from the NMR spin echo. *J Magn Reson B* 103, 247-254.
- Basser, P.J., Mattiello, J., LeBihan, D., 1994b. MR diffusion tensor spectroscopy and imaging. *Biophys J* 66, 259-267.
- Basser, P.J., Pierpaoli, C., 1996. Microstructural and physiological features of tissues elucidated by quantitative-diffusion-tensor MRI. *J Magn Reson B* 111, 209-219.
- Basser, P.J., Pierpaoli, C., 1998. A simplified method to measure the diffusion tensor from seven MR images. *Magn Reson Med* 39, 928-934.
- Baumgarten, C.M., 2006. Cell volume regulation in cardiac myocytes: a leaky boat gets a new bilge pump. *J Gen Physiol* 128, 487-489.
- Beck, B., Plant, D.H., Grant, S.C., Thelwall, P.E., Silver, X., Mareci, T.H., Benveniste, H., Smith, M., Collins, C., Crozier, S., Blackband, S.J., 2002. Progress in high field MRI at the University of Florida. *Magma* 13, 152-157.
- Beg, M.F., Helm, P.A., McVeigh, E., Miller, M.I., Winslow, R.L., 2004. Computational cardiac anatomy using MRI. *Magn Reson Med* 52, 1167-1174.
- Benveniste, H., Blackband, S., 2002. MR microscopy and high resolution small animal MRI: applications in neuroscience research. *Prog Neurobiol* 67, 393-420.
- Benveniste, H., Blackband, S.J., 2006. Translational neuroscience and magnetic-resonance microscopy. *Lancet Neurol* 5, 536-544.
- Benveniste, H., Kim, K., Zhang, L., Johnson, G.A., 2000. Magnetic resonance microscopy of the C57BL mouse brain. *Neuroimage* 11, 601-611.
- Bernstein, M.A., King, K.F., Zhou, X.J., 2004. Handbook of MRI pulse sequences. Elsevier Academic Press, Burlington, MA.
- Bers, D.M., 2002. Cardiac excitation-contraction coupling. *Nature* 415, 198-205.
- Bishop, M.J., Plank, G., Burton, R.A., Schneider, J.E., Gavaghan, D.J., Grau, V., Kohl, P., 2010. Development of an anatomically detailed MRI-derived rabbit ventricular model and assessment of its impact on simulations of electrophysiological function. *Am J Physiol Heart Circ Physiol* 298, H699-718.

- Bloch, F., 1946. Nuclear Induction. *Physical Review* 70, 460-474.
- Bloch, F., Hansen, W.W., Packard, M., 1946. The Nuclear Induction Experiment. *Phys Rev* 70, 474-485
- Bloembergen, N., Purcell, E.M., Pound, R.V., 1948. Relaxation Effects in Nuclear Magnetic Resonance Absorption. *Phys Rev* 73, 679-712.
- Boron, W.F., Boulpaep, E.L., 2005. *Medical physiology*. Elsevier Saunders, Philadelphia, PA.
- Bowtell, R.W., Peters, A., Sharp, J.C., Mansfield, P., Hsu, E.W., Aiken, N., Horsman, A., Blackband, S.J., 1995. NMR microscopy of single neurons using spin echo and line narrowed 2DFT imaging. *Magn Reson Med* 33, 790-794.
- Brooks, A., Schinde, V., Bateman, A.C., Gallagher, P.J., 2003. Interstitial fibrosis in the dilated non-ischaemic myocardium. *Heart* 89, 1255-1256.
- Brown, R., 1827. A brief account of microscopical observations in the months June, July and August 1827 on the particles contained in pollen. *Edin New Phil J* 5, 358-371.
- Brunner, M., Peng, X., Liu, G.X., Ren, X.Q., Ziv, O., Choi, B.R., Mathur, R., Hajjiri, M., Odening, K.E., Steinberg, E., Folco, E.J., Pringa, E., Centracchio, J., Macharzina, R.R., Donahay, T., Schofield, L., Rana, N., Kirk, M., Mitchell, G.F., Poppas, A., Zehender, M., Koren, G., 2008. Mechanisms of cardiac arrhythmias and sudden death in transgenic rabbits with long QT syndrome. *J Clin Invest* 118, 2246-2259.
- Buckberg, G.D., 2005. Imaging, models, and reality: a basis for anatomic-physiologic planning. *J Thorac Cardiovasc Surg* 129, 243-245.
- Buckley, D.L., Bui, J.D., Phillips, M.I., Blackband, S.J., 1999a. MRI measurement of cell volume fraction in the perfused rat hippocampal slice. *Magn Reson Med* 42, 603-607.
- Buckley, D.L., Bui, J.D., Phillips, M.I., Zelles, T., Inglis, B.A., Plant, H.D., Blackband, S.J., 1999b. The effect of ouabain on water diffusion in the rat hippocampal slice measured by high resolution NMR imaging. *Magn Reson Med* 41, 137-142.
- Bui, J.D., Buckley, D.L., Phillips, M.I., Blackband, S.J., 1999. Nuclear magnetic resonance imaging measurements of water diffusion in the perfused hippocampal slice during N-methyl-D-aspartate-induced excitotoxicity. *Neuroscience* 93, 487-490.
- Burton, R.A., Plank, G., Schneider, J.E., Grau, V., Ahammer, H., Keeling, S.L., Lee, J., Smith, N.P., Gavaghan, D., Trayanova, N., Kohl, P., 2006. Three-dimensional models of individual cardiac histoanatomy: tools and challenges. *Ann N Y Acad Sci* 1080, 301-319.
- Callaghan, P.T., 1991. *Principles of Nuclear Magnetic Resonance Microscopy*. Clarendon Press, Oxford.

- Callaghan, P.T., 1997. A Simple Matrix Formalism for Spin Echo Analysis of Restricted Diffusion under Generalized Gradient Waveforms. *J Magn Reson* 129, 74-84.
- Caravan, P., Das, B., Dumas, S., Epstein, F.H., Helm, P.A., Jacques, V., Koerner, S., Kolodziej, A., Shen, L., Sun, W.C., Zhang, Z., 2007. Collagen-targeted MRI contrast agent for molecular imaging of fibrosis. *Angew Chem Int Ed Engl* 46, 8171-8173.
- Carr, H.Y., 1954. Effects of diffusion on free precession in nuclear magnetic resonance experiments. *Phys Rev* 94, 630-638.
- Chen, J., Liu, W., Zhang, H., Lacy, L., Yang, X., Song, S.K., Wickline, S.A., Yu, X., 2005. Regional ventricular wall thickening reflects changes in cardiac fiber and sheet structure during contraction: quantification with diffusion tensor MRI. *Am J Physiol Heart Circ Physiol* 289, H1898-1907.
- Chen, J., Song, S.K., Liu, W., McLean, M., Allen, J.S., Tan, J., Wickline, S.A., Yu, X., 2003. Remodeling of cardiac fiber structure after infarction in rats quantified with diffusion tensor MRI. *Am J Physiol Heart Circ Physiol* 285, H946-954.
- Cieslar, J., Huang, M.T., Dobson, G.P., 1998. Tissue spaces in rat heart, liver, and skeletal muscle in vivo. *Am J Physiol* 275, R1530-1536.
- Clark, C.A., Barker, G.J., Tofts, P.S., 2000. Improved reduction of motion artifacts in diffusion imaging using navigator echoes and velocity compensation. *J Magn Reson* 142, 358-363.
- Collins, M.J., Ozeki, T., Zhuo, J., Gu, J., Gullapalli, R., Pierson, R.N., Griffith, B.P., Fedak, P.W., Poston, R.S., 2007. Use of diffusion tensor imaging to predict myocardial viability after warm global ischemia: possible avenue for use of non-beating donor hearts. *J Heart Lung Transplant* 26, 376-383.
- Croisille, P., 2009. [Cardiac diffusion imaging: toward new insights in myocardial ischemia]. *J Radiol* 90, 455-457.
- Davies, M.J., Anderson, R.H., Becker, A.E., 1983. The conduction system of the heart. Butterworths, London.
- de Souza, R.R., 2002. Aging of myocardial collagen. *Biogerontology* 3, 325-335.
- Dobson, G.P., Cieslar, J.H., 1997. Intracellular, interstitial and plasma spaces in the rat myocardium in vivo. *J Mol Cell Cardiol* 29, 3357-3363.
- Dou, J., Reese, T.G., Tseng, W.Y., Wedeen, V.J., 2002. Cardiac diffusion MRI without motion effects. *Magn Reson Med* 48, 105-114.

- Dou, J., Tseng, W.Y., Reese, T.G., Wedeen, V.J., 2003. Combined diffusion and strain MRI reveals structure and function of human myocardial laminar sheets in vivo. *Magn Reson Med* 50, 107-113.
- Dun, W., Boyden, P.A., 2008. The Purkinje cell; 2008 style. *J Mol Cell Cardiol* 45, 617-624.
- Einstein, A., 1906. Zur Theorie der Brownschen Bewegung [On the theory of Brownian Motion]. *Annalen der Physik* 19, 371-381.
- Eliska, O., 2006. [Purkynje fibers of the heart conduction system--history and the present time]. *Cas Lek Cesk* 145, 329-335.
- Eloff, B.C., Lerner, D.L., Yamada, K.A., Schuessler, R.B., Saffitz, J.E., Rosenbaum, D.S., 2001. High resolution optical mapping reveals conduction slowing in connexin43 deficient mice. *Cardiovasc Res* 51, 681-690.
- Fick, A., 1855. Ueber Diffusion [On Diffusion]. *Poggendorff's Annalen der Physik* 94, 59-86. 1855
- Finney, J.L., 2004. Water? What's so special about it? *Philos Trans R Soc Lond B Biol Sci* 359, 1145-1163; discussion 1163-1145, 1323-1148.
- Fischer, S.E., Stuber, M., Scheidegger, M.B., Boesiger, P., 1995. Limitations of stimulated echo acquisition mode (STEAM) techniques in cardiac applications. *Magn Reson Med* 34, 80-91.
- Flint, J., Hansen, B., Vestergaard-Poulsen, P., Blackband, S.J., 2009a. Diffusion weighted magnetic resonance imaging of neuronal activity in the hippocampal slice model. *Neuroimage* 46, 411-418.
- Flint, J.J., Lee, C.H., Hansen, B., Fey, M., Schmidig, D., Bui, J.D., King, M.A., Vestergaard-Poulsen, P., Blackband, S.J., 2009b. Magnetic resonance microscopy of mammalian neurons. *Neuroimage* 46, 1037-1040.
- Flogel, U., Ding, Z., Hardung, H., Jander, S., Reichmann, G., Jacoby, C., Schubert, R., Schrader, J., 2008. In vivo monitoring of inflammation after cardiac and cerebral ischemia by fluorine magnetic resonance imaging. *Circulation* 118, 140-148.
- Forder, J.R., Bui, J.D., Buckley, D.L., Blackband, S.J., 2001. MR imaging measurement of compartmental water diffusion in perfused heart slices. *Am J Physiol Heart Circ Physiol* 281, H1280-1285.
- Forder, J.R., Pohost, G.M., 2003. Cardiovascular nuclear magnetic resonance: basic and clinical applications. *J Clin Invest* 111, 1630-1639.
- Frank, J.S., Langer, G.A., 1974. The myocardial interstitium: its structure and its role in ionic exchange. *J Cell Biol* 60, 586-601.

- Frank, L.R., 2002. Characterization of anisotropy in high angular resolution diffusion-weighted MRI. *Magn Reson Med* 47, 1083-1099.
- Gamcsik, M.P., Forder, J.R., Millis, K.K., McGovern, K.A., 1996. A versatile oxygenator and perfusion system for magnetic resonance studies. *Biotechnol Bioeng* 49, 348-354.
- Gamper, U., Boesiger, P., Kozerke, S., 2007. Diffusion imaging of the in vivo heart using spin echoes--considerations on bulk motion sensitivity. *Magn Reson Med* 57, 331-337.
- Ganote, C.E., Jennings, R.B., Hill, M.L., Grochowski, E., 1976. Experimental myocardial ischemic injury. II. Effect of in vivo ischemia on dog heart slice function in vitro. *J Mol Cell Cardiol* 8, 189-204.
- Gill, J., 1991. The pathophysiology and epidemiology of myocardial infarction. A review. *Drugs* 42 Suppl 2, 1-7.
- Goodyer, C.E., Grau, V., Mansoori, T., Schneider, J.E., Brodlie, K.W., Kohl, P., 2007. 3D visualization of cardiac anatomical MRI data with para-cellular resolution. *Conf Proc IEEE Eng Med Biol Soc* 2007, 147-151.
- Grant, S.C., Aiken, N.R., Plant, H.D., Gibbs, S., Mareci, T.H., Webb, A.G., Blackband, S.J., 2000. NMR spectroscopy of single neurons. *Magn Reson Med* 44, 19-22.
- Grant, S.C., Buckley, D.L., Gibbs, S., Webb, A.G., Blackband, S.J., 2001. MR microscopy of multicomponent diffusion in single neurons. *Magn Reson Med* 46, 1107-1112.
- Hahn, E.L., 1950. Spin Echoes. *Physical Review* 80, 580-594.
- Hasse, A., Odoj, F., Kienlin, M.V., Warnking, J., Fidler, F., Weisser, A., Nittka, M., Rommel, E., Lanz, T., Kalusche, B., Griswold, M., 2000. NMR probeheads for in vivo applications. *Concepts Magn Reson* 12, 361-388.
- Helm, P.A., Tseng, H.J., Younes, L., McVeigh, E.R., Winslow, R.L., 2005. Ex vivo 3D diffusion tensor imaging and quantification of cardiac laminar structure. *Magn Reson Med* 54, 850-859.
- Hondeghem, L.M., Stroobandt, R., 1974. Purkinje fibers of sheep papillary muscle: occurrence of discontinuous fibers. *Am J Anat* 141, 251-261.
- Hsu, E.W., Aiken, N.R., Blackband, S.J., 1997. A study of diffusion isotropy in single neurons by using NMR microscopy. *Magn Reson Med* 37, 624-627.
- Hsu, E.W., Buckley, D.L., Bui, J.D., Blackband, S.J., Forder, J.R., 2001. Two-component diffusion tensor MRI of isolated perfused hearts. *Magn Reson Med* 45, 1039-1045.

- Hsu, E.W., Henriquez, C.S., 2001. Myocardial fiber orientation mapping using reduced encoding diffusion tensor imaging. *J Cardiovasc Magn Reson* 3, 339-347.
- Hsu, E.W., Muzikant, A.L., Matulevicius, S.A., Penland, R.C., Henriquez, C.S., 1998a. Magnetic resonance myocardial fiber-orientation mapping with direct histological correlation. *Am J Physiol* 274, H1627-1634.
- Hsu, E.W., Xue, R., Holmes, A., Forder, J.R., 1998b. Delayed reduction of tissue water diffusion after myocardial ischemia. *Am J Physiol* 275, H697-702.
- Hurst, J.W., Anderson, R.H., Becker, A.E., Wilcox, B.R., 1988. *Atlas of the heart*. Gower Medical Publishing, New York, NY.
- Inglis, B.A., Bossart, E.L., Buckley, D.L., Wirth, E.D., 3rd, Mareci, T.H., 2001. Visualization of neural tissue water compartments using biexponential diffusion tensor MRI. *Magn Reson Med* 45, 580-587.
- Janicki, J.S., Brower, G.L., 2002. The role of myocardial fibrillar collagen in ventricular remodeling and function. *J Card Fail* 8, S319-325.
- Jennings, R.B., 1976. Cell volume regulation in acute myocardial ischemic injury. *Acta Med Scand Suppl* 587, 83-93.
- Jiang, Y., Pandya, K., Smithies, O., Hsu, E.W., 2004. Three-dimensional diffusion tensor microscopy of fixed mouse hearts. *Magn Reson Med* 52, 453-460.
- Jin, T., Kim, S.G., 2008. Functional changes of apparent diffusion coefficient during visual stimulation investigated by diffusion-weighted gradient-echo fMRI. *Neuroimage* 41, 801-812.
- Jin, T., Zhao, F., Kim, S.G., 2006. Sources of functional apparent diffusion coefficient changes investigated by diffusion-weighted spin-echo fMRI. *Magn Reson Med* 56, 1283-1292.
- Judd, R.M., Rottman, G.A., Forder, J.R., Yin, F.C., Blackband, S.J., 1992. Feasibility of 19F imaging of perfluorochemical emulsions to measure myocardial vascular volume. *Magn Reson Med* 28, 129-136.
- Kanai, A., Salama, G., 1995. Optical mapping reveals that repolarization spreads anisotropically and is guided by fiber orientation in guinea pig hearts. *Circ Res* 77, 784-802.
- Karger, J., Pfeifer, H., Vojta, G., 1988. Time correlation during anomalous diffusion in fractal systems and signal attenuation in NMR field-gradient spectroscopy. *Phys Rev A* 37, 4514-4517.
- Katz, A.M., 1977. *Physiology of the heart*. Raven Press, New York, NY.
- Katz, A.M., Katz, P.B., 1989. Homogeneity out of heterogeneity. *Circulation* 79, 712-717.

- Kohl, P., 2003. Heterogeneous cell coupling in the heart: an electrophysiological role for fibroblasts. *Circ Res* 93, 381-383.
- Kumar, A., Kaur, H., Devi, P., Mohan, V., 2009. Role of coenzyme Q10 (CoQ10) in cardiac disease, hypertension and Meniere-like syndrome. *Pharmacol Ther* 124, 259-268.
- Latour, L.L., Svoboda, K., Mitra, P.P., Sotak, C.H., 1994. Time-dependent diffusion of water in a biological model system. *Proc Natl Acad Sci U S A* 91, 1229-1233.
- Lauterbur, P.C., 1973. Image formation by induced local interactions: Examples employing nuclear magnetic resonance. *Nature* 242, 190-191.
- Le Bihan, D., 1995a. [Diffusion, perfusion and functional magnetic resonance imaging.]. *J Mal Vasc* 20, 203-214.
- Le Bihan, D., 1995b. Molecular diffusion, tissue microdynamics and microstructure. *NMR Biomed* 8, 375-386.
- Le Bihan, D., 2006. [From Brownian motion to mind imaging: diffusion MRI]. *Bull Acad Natl Med* 190, 1605-1627; discussion 1627.
- Le Bihan, D., 2007. The 'wet mind': water and functional neuroimaging. *Phys Med Biol* 52, R57-90.
- Le Bihan, D., Breton, E., Lallemand, D., Aubin, M.L., Vignaud, J., Laval-Jeantet, M., 1988. Separation of diffusion and perfusion in intravoxel incoherent motion MR imaging. *Radiology* 168, 497-505.
- Le Bihan, D., Breton, E., Lallemand, D., Grenier, P., Cabanis, E., Laval-Jeantet, M., 1986. MR imaging of intravoxel incoherent motions: application to diffusion and perfusion in neurologic disorders. *Radiology* 161, 401-407.
- Le Bihan, D., Mangin, J.F., Poupon, C., Clark, C.A., Pappata, S., Molko, N., Chabriat, H., 2001. Diffusion tensor imaging: concepts and applications. *J Magn Reson Imaging* 13, 534-546.
- Le Bihan, D., Poupon, C., Amadon, A., Lethimonnier, F., 2006a. Artifacts and pitfalls in diffusion MRI. *J Magn Reson Imaging* 24, 478-488.
- Le Bihan, D., Turner, R., Douek, P., Patronas, N., 1992. Diffusion MR imaging: clinical applications. *AJR Am J Roentgenol* 159, 591-599.
- Le Bihan, D., Urayama, S., Aso, T., Hanakawa, T., Fukuyama, H., 2006b. Direct and fast detection of neuronal activation in the human brain with diffusion MRI. *Proc Natl Acad Sci U S A* 103, 8263-8268.

- Le Bihan, D., van Zijl, P., 2002. From the diffusion coefficient to the diffusion tensor. *NMR Biomed* 15, 431-434.
- Le Bihan, D., 1995. *Diffusion and perfusion magnetic resonance imaging: applications to functional MRI*. Raven Press, New York, NY.
- Leemans, A., Jones, D.K., 2009. The B-matrix must be rotated when correcting for subject motion in DTI data. *Magn Reson Med* 61, 1336-1349.
- Legrice, I.J., Hunter, P.J., Smaill, B.H., 1997. Laminar structure of the heart: a mathematical model. *Am J Physiol* 272, H2466-2476.
- Li, W., Lu, M., Banerjee, S., Zhong, J., Ye, A., Molter, J., Yu, X., 2009. Ex vivo diffusion tensor MRI reflects microscopic structural remodeling associated with aging and disease progression in normal and cardiomyopathic Syrian hamsters. *NMR Biomed* 22, 819-825.
- Ma, Y., Smith, D., Hof, P.R., Foerster, B., Hamilton, S., Blackband, S.J., Yu, M., Benveniste, H., 2008. In Vivo 3D Digital Atlas Database of the Adult C57BL/6J Mouse Brain by Magnetic Resonance Microscopy. *Front Neuroanat* 2, 1.
- Mansfield, P., Grannell, P. K., 1973. NMR 'diffraction' in solids? *J Phys C: Solid State Phys* 6, L422-426.
- Mattiello, J., Basser, P.J., Le Bihan, D., 1997. The b matrix in diffusion tensor echo-planar imaging. *Magn Reson Med* 37, 292-300.
- Miller, K.L., Bulte, D.P., Devlin, H., Robson, M.D., Wise, R.G., Woolrich, M.W., Jezzard, P., Behrens, T.E., 2007. Evidence for a vascular contribution to diffusion FMRI at high b value. *Proc Natl Acad Sci U S A* 104, 20967-20972.
- Mori, S., van Zijl, P.C., 2002. Fiber tracking: principles and strategies - a technical review. *NMR Biomed* 15, 468-480.
- Mori, S., Zhang, J., 2006. Principles of diffusion tensor imaging and its applications to basic neuroscience research. *Neuron* 51, 527-539.
- Moseley, M.E., Cohen, Y., Mintorovitch, J., Chileuitt, L., Shimizu, H., Kucharczyk, J., Wendland, M.F., Weinstein, P.R., 1990. Early detection of regional cerebral ischemia in cats: comparison of diffusion- and T2-weighted MRI and spectroscopy. *Magn Reson Med* 14, 330-346.
- Moseley, M.E., Kucharczyk, J., Mintorovitch, J., Cohen, Y., Kurhanewicz, J., Derugin, N., 1990. Diffusion-weighted MR imaging of acute stroke: correlation with T2-weighted and magnetic susceptibility-enhanced MR imaging in cats. *Am J Neuroradiol* 11, 423-429.

- Nakamura, S., Hama, K., Asai, J., Irisawa, H., 1986. Observations on the fine structure of nodal, Purkinje and working myocardial cells isolated from rabbit hearts. *Arch Histol Jpn* 49, 105-116.
- National Institute of Health, ImageJ, 2009, <http://rsbweb.nih.gov/ij/>, January 15, 2009.
- Neeman, M., Freyer, J.P., Sillerud, L.O., 1991a. A simple method for obtaining cross-term-free images for diffusion anisotropy studies in NMR microimaging. *Magn Reson Med* 21, 138-143.
- Neeman, M., Jarrett, K.A., Sillerud, L.O., Freyer, J.P., 1991b. Self-diffusion of water in multicellular spheroids measured by magnetic resonance microimaging. *Cancer Res* 51, 4072-4079.
- Nicholson, C., Sykova, E., 1998. Extracellular space structure revealed by diffusion analysis. *Trends Neurosci* 21, 207-215.
- Niendorf, T., Dijkhuizen, R.M., Norris, D.G., van Lookeren Campagne, M., Nicolay, K., 1996. Biexponential diffusion attenuation in various states of brain tissue: implications for diffusion-weighted imaging. *Magn Reson Med* 36, 847-857.
- Norris, D.G., 2001. The effects of microscopic tissue parameters on the diffusion weighted magnetic resonance imaging experiment. *NMR Biomed* 14, 77-93.
- Norris, D.G., Niendorf, T., 1995. Interpretation of DW-NMR data: dependence on experimental conditions. *NMR Biomed* 8, 280-288.
- Norris, D.G., Niendorf, T., Leibfritz, D., 1994. Health and infarcted brain tissues studied at short diffusion times: the origins of apparent restriction and the reduction in apparent diffusion coefficient. *NMR Biomed* 7, 304-310.
- Olivetti, G., Capasso, J.M., Sonnenblick, E.H., Anversa, P., 1990. Side-to-side slippage of myocytes participates in ventricular wall remodeling acutely after myocardial infarction in rats. *Circ Res* 67, 23-34.
- Oosthoek, P.W., Viragh, S., Lamers, W.H., Moorman, A.F., 1993. Immunohistochemical delineation of the conduction system. II: The atrioventricular node and Purkinje fibers. *Circ Res* 73, 482-491.
- Oxenham, H., Sharpe, N., 2003. Cardiovascular aging and heart failure. *Eur J Heart Fail* 5, 427-434.
- Ozarslan, E., Basser, P.J., Shepherd, T.M., Thelwall, P.E., Vemuri, B.C., Blackband, S.J., 2006. Observation of anomalous diffusion in excised tissue by characterizing the diffusion-time dependence of the MR signal. *J Magn Reson* 183, 315-323.

- Ozarslan, E., Mareci, T.H., 2003. Generalized diffusion tensor imaging and analytical relationships between diffusion tensor imaging and high angular resolution diffusion imaging. *Magn Reson Med* 50, 955-965.
- Ozarslan, E., Vemuri, B.C., Mareci, T.H., 2005. Generalized scalar measures for diffusion MRI using trace, variance, and entropy. *Magn Reson Med* 53, 866-876.
- Pfeuffer, J., Provencher, S.W., Gruetter, R., 1999. Water diffusion in rat brain in vivo as detected at very large b values is multicompartmental. *Magma* 8, 98-108.
- Pierpaoli, C., Alger, J.R., Righini, A., Mattiello, J., Dickerson, R., Des Pres, D., Barnett, A., Di Chiro, G., 1996. High temporal resolution diffusion MRI of global cerebral ischemia and reperfusion. *J Cereb Blood Flow Metab* 16, 892-905.
- Pierpaoli, C., Basser, P.J., 1996. Toward a quantitative assessment of diffusion anisotropy. *Magn Reson Med* 36, 893-906.
- Plank, G., Burton, R.A., Hales, P., Bishop, M., Mansoori, T., Bernabeu, M.O., Garny, A., Prassl, A.J., Bollensdorff, C., Mason, F., Mahmood, F., Rodriguez, B., Grau, V., Schneider, J.E., Gavaghan, D., Kohl, P., 2009. Generation of histo-anatomically representative models of the individual heart: tools and application. *Philos Transact A Math Phys Eng Sci* 367, 2257-2292.
- Poole, D.C., Mathieu-Costello, O., 1990. Analysis of capillary geometry in rat subepicardium and subendocardium. *Am J Physiol* 259, H204-210.
- Pugh, K.G., Wei, J.Y., 2001. Clinical implications of physiological changes in the aging heart. *Drugs Aging* 18, 263-276.
- Purcell, E.M., Torrey, H.C., Pound, R.V., 1946. Resonance absorption by nuclear magnetic moments in a solid. *Phys Rev* 69, 37-38.
- Reese, T.G., Weisskoff, R.M., Smith, R.N., Rosen, B.R., Dinsmore, R.E., Wedeen, V.J., 1995. Imaging myocardial fiber architecture in vivo with magnetic resonance. *Magn Reson Med* 34, 786-791.
- Schumpe, A., Adler, I., Deckwer, W. D., 2004. Solubility of oxygen in electrolyte solutions. *Biotechnology and Bioengineering* 20, 145-150.
- Scollan, D.F., Holmes, A., Winslow, R., Forder, J., 1998. Histological validation of myocardial microstructure obtained from diffusion tensor magnetic resonance imaging. *Am J Physiol* 275, H2308-2318.
- Scollan, D.F., Holmes, A., Zhang, J., Winslow, R.L., 2000. Reconstruction of cardiac ventricular geometry and fiber orientation using magnetic resonance imaging. *Ann Biomed Eng* 28, 934-944.

- Sehy, J.V., Ackerman, J.J., Neil, J.J., 2002. Evidence that both fast and slow water ADC components arise from intracellular space. *Magn Reson Med* 48, 765-770.
- Sheets, M.F., January, C.T., Fozzard, H.A., 1983. Isolation and characterization of single canine cardiac purkinje cells. *Circ Res* 53, 544-548.
- Shepherd, T.M., Blackband, S.J., Wirth, E.D., 3rd, 2002. Simultaneous diffusion MRI measurements from multiple perfused rat hippocampal slices. *Magn Reson Med* 48, 565-569.
- Shepherd, T.M., Flint, J.J., Thelwall, P.E., Stanisiz, G.J., Mareci, T.H., Yachnis, A.T., Blackband, S.J., 2009. Postmortem interval alters the water relaxation and diffusion properties of rat nervous tissue--implications for MRI studies of human autopsy samples. *Neuroimage* 44, 820-826.
- Shimada, T., Noguchi, T., Asami, I., Campbell, G.R., 1986. Functional morphology of the conduction system and the myocardium in the sheep heart as revealed by scanning and transmission electron microscopic analyses. *Arch Histol Jpn* 49, 283-295.
- Stanisiz, G.J., Szafer, A., Wright, G.A., Henkelman, R.M., 1997. An analytical model of restricted diffusion in bovine optic nerve. *Magn Reson Med* 37, 103-111.
- Stejskal, E.O., Tanner, J.E., 1965. Spin diffusion measurements: Spin echoes in the presence of a time-dependent field gradient. *Journal of Chemical Physics* 42, 288-292.
- Szafer, A., Zhong, J., Gore, J.C., 1995. Theoretical model for water diffusion in tissues. *Magn Reson Med* 33, 697-712.
- Tawara, S., 2000. The conduction system of the mammalian heart: an anatomico-histological study of the atrioventricular bundle and the Purkinje fibers. Imperial College Press, London.
- Torrey, H.C., 1956. Bloch equations with diffusion terms. *Phys Rev* 104, 563-565.
- Tranum-Jensen, J., Wilde, A.A., Vermeulen, J.T., Janse, M.J., 1991. Morphology of electrophysiologically identified junctions between Purkinje fibers and ventricular muscle in rabbit and pig hearts. *Circ Res* 69, 429-437.
- Tropp, J., 1997. Mutual Inductance in the Bird-Cage Resonator. *J Magn Reson* 126, 9-17.
- Tuch, D.S., 2004. Q-ball imaging. *Magn Reson Med* 52, 1358-1372.
- Tuch, D.S., Reese, T.G., Wiegell, M.R., Makris, N., Belliveau, J.W., Wedeen, V.J., 2002. High angular resolution diffusion imaging reveals intravoxel white matter fiber heterogeneity. *Magn Reson Med* 48, 577-582.

- Vadakkumpadan, F., Rantner, L.J., Tice, B., Boyle, P., Prassl, A.J., Vigmond, E., Plank, G., Trayanova, N., 2009. Image-based models of cardiac structure with applications in arrhythmia and defibrillation studies. *J Electrocardiol* 42, 157 e151-110.
- von dem Hagen, E.A., Henkelman, R.M., 2002. Orientational diffusion reflects fiber structure within a voxel. *Magn Reson Med* 48, 454-459.
- Waldman, L.K., Nosan, D., Villarreal, F., Covell, J.W., 1988. Relation between transmural deformation and local myofiber direction in canine left ventricle. *Circ Res* 63, 550-562.
- Weber, K.T., Sun, Y., Tyagi, S.C., Cleutjens, J.P., 1994. Collagen network of the myocardium: function, structural remodeling and regulatory mechanisms. *J Mol Cell Cardiol* 26, 279-292.
- Wedeen, V.J., Hagmann, P., Tseng, W.Y., Reese, T.G., Weisskoff, R.M., 2005. Mapping complex tissue architecture with diffusion spectrum magnetic resonance imaging. *Magn Reson Med* 54, 1377-1386.
- Wedeen, V.J., Wang, R.P., Schmahmann, J.D., Benner, T., Tseng, W.Y., Dai, G., Pandya, D.N., Hagmann, P., D'Arceuil, H., de Crespigny, A.J., 2008. Diffusion spectrum magnetic resonance imaging (DSI) tractography of crossing fibers. *Neuroimage* 41, 1267-1277.
- Wedeen, V.J., Weisskoff, R.M., Poncelet, B.P., 1994. MRI signal void due to in-plane motion is all-or-none. *Magn Reson Med* 32, 116-120.
- Wesbey, G.E., Moseley, M.E., Ehman, R.L., 1984a. Translational molecular self-diffusion in magnetic resonance imaging. I. Effects on observed spin-spin relaxation. *Invest Radiol* 19, 484-490.
- Wesbey, G.E., Moseley, M.E., Ehman, R.L., 1984b. Translational molecular self-diffusion in magnetic resonance imaging. II. Measurement of the self-diffusion coefficient. *Invest Radiol* 19, 491-498.
- Wu, M.T., Tseng, W.Y., Su, M.Y., Liu, C.P., Chiou, K.R., Wedeen, V.J., Reese, T.G., Yang, C.F., 2006. Diffusion tensor magnetic resonance imaging mapping the fiber architecture remodeling in human myocardium after infarction: correlation with viability and wall motion. *Circulation* 114, 1036-1045.
- Yoneda, Y., Tokui, K., Hanihara, T., Kitagaki, H., Tabuchi, M., Mori, E., 1999. Diffusion-weighted magnetic resonance imaging: detection of ischemic injury 39 minutes after onset in a stroke patient. *Ann Neurol* 45, 794-797.

## BIOGRAPHICAL SKETCH

Min Sig Hwang completed his Bachelor of Science in Metallurgical engineering at Yon-Se University in 1998. He received the degree of Master of Science in Materials Science and Engineering from Korea Institute of Science and Technology (KAIST) in 2001. In 2001, he began his career as a researcher at LG Electronics Co. Ltd., a global leading technology company in South Korea. He began his Ph.D. studies at the University of Florida in 2003. He plans to continue his career in academic field as a professional biomedical engineer with knowledge and experience he gained through his Ph.D study.